

**SYNTHESIS AND CHARACTERIZATION OF SILICON
OXIDE AND SILICON CARBIDE NANOSTRUCTURES**

MAJID BIN SALIM BIN MOHAMMED AL-RUQIESHI

**DEPARTMENT OF PHYSICS
FACULTY OF SCIENCE
UNIVERSITY OF MALAYA**

2010

SYNTHESIS AND CHARACTERIZATION OF SILICON OXIDE AND SILICON CARBIDE NANOSTRUCTURES

By

**MAJID BIN SALIM BIN MOHAMMED
AL-RUQIESHI**

**THESIS SUBMITTED IN FULFILLMENT OF
THE REQUIREMENTS FOR THE DEGREE OF
DOCTOR OF PHILOSOPHY**

UNIVERSITY OF MALAYA

2010

ABSTRACT

Silicon oxide nanostructures have attracted extensive interests in recent years due to their physical and optical properties. SiO_x nanostructures are synthesized by catalytic and non-catalytic approaches. With catalytic approach, long and uniform amorphous silicon oxide nanowires, nanofibers (comet and tree like), nanocakes and nanocages were synthesized on Si substrate by carbothermal evaporation reactions of TiO_2 at high temperature. The SiO_x nanowires were about 13 nm to 243 nm in diameters and 194 nm to several microns in length and the nanofibres with diameter between 8 nm to 30 nm and around 50 nm to 2.5 μm in length. The diameter and density of SiO_x nanostructures were modified by controlling the size, distribution and thickness layer of the Au particles on substrate surface by annealing process. The average lowest diameter was found as 37 nm with 6.8 nm gold layer thickness. In non-catalytic part the obtained SiO_x nanostructures diameters were about from 60 nm to 300 nm and several microns in length. The formation of cracks on the silicon substrate surface found to be due to the evaporation of silicon monoxide at $\geq 900^\circ\text{C}$.

It was found that increased temperature, C: TiO_2 ratio and deposition time increases the yield of the growth of SiO_x nanostructures. The highest yield for SiO_x nanowires growth is obtained at 10 sccm Ar flow rate. The XRD and FTIR results confirmed that the obtained SiO_x nanowires are amorphous.

The SiO_x nanostructures PL consist of UV peak centred at 350 nm (3.54 eV), one wide peak in the blue and green regions (400-600 nm) and red band centered at 730 nm. A broad emission band from 290 to 600 nm is observed in the photoluminescence (PL) spectrum of these nanostructures. There are four PL peaks:

one UV, two emissions in green bluish region and one red emission. PL higher intensity in the case of non catalytic wires is due to the higher oxygen vacancies.

We believed that the assistance of carbon is the most important factor to enhance the fabrication of beta-type silicon carbide nanowires. The grown β -SiC nanowires were aligned in shape with almost same height and with diameter ranged between 40 to 500 nm. The majority of crystal planes are planes of β -SiC (111) with other less intensity of (200), (220) and (311). The effect of parametric studies (substrate location, Ar and O₂ flowrate, rapid heating rate) on the growth of β -SiC nanowires was carried out. The FTIR results reveal that the most chemical bonds were single Si-C, which can be related to the obtained β -SiC nanostructure.

DEDICATIONS

To whom I need invocation, my mother and father

ACKNOWLEDGMENTS

In the name of Allah, most gracious, most merciful

(O company of jinn and men, if ye have power to penetrate (all) regions of the heavens and the earth, then penetrate (them)! Ye will never penetrate them save with (Our) sanction)

The author would like to thank Allah ‘Subhanah Wa Talla’ for his help and guidance to complete this thesis. I would like to express my sincere thanks to my advisor Associate Prof. Dr. Roslan Md Nor for his numerous support, scientific guidance, and continuous encouragement during my research and thesis completion.

I gratefully acknowledge my co-supervisor Prof Dr. Yusoff Mohd Amin for his patience and assistance and I would like to extend thanks to my teachers, friends, colleagues in physics department, university of Malaya. I cannot accomplish the requirements of doctoral degree successfully without their kind helps and constructive suggestions. Particularly, I am grateful to Pn. Zurina Marzuki, En. Mohammed Aruf, En. Azman Mat Nor and En. Shahril Bahrudinn for their assistances in the practical part.

This thesis would not be possible if sultanate of Oman government support did not exist. For that, the author would like to thank Ministry of Education for their efforts under the wise and strategic plans of his majesty Sultan Qaboos bin Said, the modern Omani civilization builder.

Additionally I would like to thank my parents for their solitudes and supports, to my wife for her love and understanding throughout my studies. Finally I am grateful to my kids (Ahmed, Anwaar, Mohammed, Osama, Ruam and small baby Qabas), for them brings lots joy and happiness in my life. There are too many others who may not mentioned over these acknowledgments, so I am very thankful for them.

This work was financially supported by Institute of Research Management and Consultancy, University Malaya, under grant No. PS2007/118B.

CONTENTS	PAGE
ABSTRACT	I
DEDICATION	III
ACKNOWLEDGMENTS	IV
TABLE OF CONTENTS	VI
LIST OF FIGURES	XI
LIST OF TABLES	XIX
Chapter 1	INTRODUCTION
	1
1.1. Introduction	1
1.2. Thesis Objectives	3
1.3. Layout of the Thesis	3
Chapter 2	LITERATURE REVIEW OF SILICON OXIDE AND SILICON CARBIDE NANOSTRUCTURES
	4
2.1. Introduction	4
2.1.1. Inorganic One Dimensional Nanowires	5
2.1.2. One Dimensional Silicon Oxide Nanostructures	7
2.2. Fabrication of Silicon Oxide Nanostructures	8
2.2.1. Crystal Structures of Silicon and Silicon Oxides	8
2.2.2. Synthesis Methods of Silicon oxide nanostructures	15
2.2.2.1. Thermal Evaporation Method	16
2.2.3. Non-catalytic Growth of Silicon Oxide Nanostructures	19
2.2.4. Catalytic growth of Silicon Oxide Nanostructures	20
2.2.5. Growth Mechanisms of Silicon Oxide Nanostructures	26
(i) Vapour–Liquid–Solid Growth Mechanism	26
(ii) Solid Liquid Solid Growth Mechanism	29
(iii) Vapour - Solid Growth Mechanism	30
(iv) Solid - Vapour – Liquid - Solid Growth Mechanism	33

(v) Carbothermal Reactions	34
(vi) Oxygen Assisted Growth	37
2.2.6. Morphology of Silicon Oxides Nanostructures	40
2.2.7. Photoluminescence of Silicon Oxide Nanowires	42
2.3. Fabrication of beta-Silicon carbide nanowires	47
2.3.1. Introduction	47
2.3.2. Structure of β -SiC crystal	49
2.3.3. β -SiC Nanowires Properties	50
2.3.4. Synthesis Methods and growth mechanisms of β -SiCNWs	51
2.4. Preparation and Characterization Techniques of SiO_x and SiC Nanostructures	53
2.4.1. DC Sputter Coater	53
2.4.2. Field Emission Scanning Electron Microscope	55
2.4.3. Electron Dispersive X-ray Analysis	59
2.4.4. X-ray Diffraction Technique (XRD)	63
2.4.5. Transmission Electron Microscope (TEM)	66
2.4.6. Optical Characterization	68
2.4.6.1. Fourier Transformed Infra-Red (FTIR)	68
2.4.6.2. Photoluminescence Spectrometer	71
Chapter 3 EXPERIMENTAL SETUP AND METHODOLOGY	77
3.1. Introduction	77
3.2. Synthesis of Silicon Oxide and Silicon Carbide Nanostructures	78
3.2.1. Substrate preparation	78
3.2.2. Substrate coater	78
3.2.3. The Tube Furnace	80

3.3. Experimental setup	82
3.4. Characterization Techniques	84
3.4.1. Field Emission Scanning Electron Microscope (FESEM)	84
3.4.1.1. Energy Dispersive X-Ray (EDX) Analysis	85
3.4.2. X-ray diffraction (XRD)	86
3.4.3. High Resolution TEM	88
3.4.4. Optical Characterization	89
3.4.4.1. Photoluminescence Spectroscopy System	89
3.4.4.2. Fourier Transform Infra-Red (FTIR)	90
Chapter 4 RESULTS AND DISCUSSIONS	92
4.1. Introduction	92
4.2. Fabrications of SiO _x Nanostructures without Catalyst	93
4.2.1. Effect of Temperature on the Growth of SiO _x NWs	93
4.2.2. Effect of Deposition Time on the Growth of SiO _x NWs	98
4.2.3. Effect of Argon Gas Flowrate on the Growth of SiO _x NWs	104
4.2.4. Discussion of non-catalyst Growth of SiO _x NWs	110
4.2.5. Summary	112
4.3. Fabrications of Silicon Oxide Nanostructures on Au Coated Si Substrate	113
4.3.1. Parametric Studies of SiO _x Nanostructures on Au Coated Si Substrate	115
4.3.1.1. Effect of Temperature on the Growth of SiO _x NWs	115
4.3.1.1.1. Silicon Nanostructures Observed at Temperature 1200°C	120
4.3.1.2. Effect of Oxygen and Argon Gases on the Growth of SiO _x NWs	128
4.3.1.3. Effect of (TiO ₂ : C) Mass Ratio on the Growth of SiO _x NWs	131
4.3.1.4. Effect of Argon Flowrate on the Growth of SiO _x NWs	133

4.3.1.5.	Effect of Deposition Time on the Growth of SiO _x NWs	136
4.3.1.6.	Effect of Gold Layer Thickness on the Growth of SiO _x NWs	138
4.3.1.7.	Effect of Rapid Heating Rate on the Growth of SiO _x NWs	142
4.3.2.	Catalytic Growth of SiO _x Nanostructures	144
4.3.2.1.	Tip Growth Process of SiO _x NWs Grown on Au coated Silicon substrate	144
4.3.2.2.	Root Growth of SiO _x NWs	148
4.3.2.3.	Growth Model of SiO _x Nano-cages	150
4.3.2.4.	Growth Model of SiO _x Nano-cakes	151
4.3.3.	Summary	152
4.4.	HRTEM Characterizations	153
4.5.	Optical Properties of Silicon Oxide Nanostructures	155
4.5.1.	Photoluminescence (PL) of SiO _x Nanostructures	155
4.5.1.1.	Effect of Temperature on the PL of SiO _x Nanostructures	157
4.5.1.2.	Effect of Au Catalyst on the PL of the SiO _x Nanostructures	158
4.5.1.3.	Effect of Annealing Temperature on the PL of SiO _x Nanostructures	159
4.5.2.	Discussion on PL spectrum of SiO _x NWs	160
4.5.3.	Fourier Transform Infrared Spectroscopy Characterization of Silicon Oxide Nanostructures	162
4.6.	Growth of Beta-Silicon Carbide Nanowires	165
4.6.1.	Introduction	165
4.6.2.	Parametric Studies on the Growth of β -SiCNWs	171
4.6.2.1.	Effect of the Substrate Location using Argon Gas on the Growth of β -SiCNWs	171
4.6.2.2.	Effect of the Substrate Location using Oxygen Gas on the Growth of β -SiCNWs	173
4.6.2.3.	Effect of Rapid Heating Rate on the Growth of β -SiCNWs	76
4.6.3.	Growth Mechanism of β -SiCNWs	179

4.6.4.	Fourier Transform Infrared Spectroscopy Characterization of β -SiCNWs	180
4.6.5.	Summary	181
4.7.	General Discussion on the Growth of SiO_x Nanostructures	182
4.8.	General Discussion on the Growth of β -SiCNWs	190
Chapter 5	CONCLUSION AND FUTURE WORK	192
5.1.	Conclusion	192
5.2.	Suggestions for Future Research	195
References		196
List of Publications		209

List of Figures

FIGURE	CHAPTER TWO	PAGE
2.1.	Single Silicon Crystal	8
2.2.	Bonded structure for one silicate	9
2.3.	Silicon ions bond to oxygen atoms, forming tetrahedral structures and the angle at which the two tetrahedra are connected also varies.	10
2.4.	Schematic diagram showing surface atoms shifting either inwardly or laterally so as to reduce the surface energy.	12
2.5.	Schematic diagram illustrating the (2×1) restructure of silicon (100) surface	13
2.6.	Schematic diagram showing the surface of diamond is covered with hydrogen and that of silicon is covered with hydroxyl groups through chemisorption before restructuring	13
2.7.	Schematic diagram illustration of laser ablation growth system.	15
2.8.	Thermal evaporation set up.	17
2.9.	The relationship between particle size and melting point of gold nanoparticles.	21
2.10.	Phase Diagram of (a) Au-Si and (b) Different alloys eutectic temperatures.	22
2.11.	SEM of (a) Au catalysts prepared by annealing a thin Au film. (b) Au patterns prepared by e-beam lithography. (c) Splitting of the Au particles by annealing.	23
2.12.	The formation mechanism of Au embedded SiO _x NWs by furnace annealing: (a) Au nanoparticles deposited by argon ion sputtering are attached on the surface of a Si nanowire, (b) oxidation of Si nanowires and diffusion of Au nanoparticles into Si nanowires under heating, (c) diffusion of Au nanoparticles in the SiO _x matrix of the nanowire at elevated temperature (e.g. 880 °C), and (d) formation of Au embedded SiO _x NW.	25
2.13.	Schematic diagram of (a) The diffusion path of the source materials through a metal droplet; (b) the whisker growth can be catalyzed with a solid catalyst.	27

2.14.	A Sketch of the temperature gradient (TEMPGRAD) growth model of (A) droplet and (B) the evolving nanowire.	30
2.15.	Schematic diagram of (a) Nanorods formed due to anisotropic growth of crystals. (b) Unidirectional growth of single crystals due to screw dislocation. (c) Growth induced by twining.	31
2.16.	Schematic diagram of VLS, SLS and SVLS mechanisms for tip and root growth.	34
2.17.	TEM of (a) Si nanowires synthesized by oxide-assisted growth. (b) Yield of Si nanowires vs. the percentage of SiO ₂ in the target.	38
2.18.	Oxygen assisted growth mechanism.	39
2.19.	Beta type of Silicon carbide crystal structure.	49
2.20.	Schematic diagram of (a) DC sputtering device and (b) the working mechanism inside the chamber.	54
2.21.	Schematic of a typical scanning electron microscope and imaging process.	56
2.22.	Schematic diagram of SEM image in analog optical camera.	57
2.23.	A simple diagram of the first three shells of an atom.	60
2.24.	EDX spectrum for phosphorous with fluorine.	61
2.25.	X-ray with wave length between 0.5 and 2 °Å is incident on specimen according to Bragg's Law.	63
2.26.	X-ray diffraction device showing the X-ray tube generate X-ray beam that hit the examined sample on the stage and the emitted electrons collected by the moving detector.	64
2.27.	HRTEM (a) internal constructions (b) image.	67
2.28.	FTIR operation method and resultant spectrum.	70
2.29.	Schematic diagram of PL measurements experimental set up.	71

2.30.	A schematic diagram of experimental apparatus for low temperature photoluminescence	72
2.31.	A schematic diagram of (a-c) Radiative recombination paths: (a) band-to-band; (b) donor to valence band; (c) conduction band to acceptor. (d) Nonradiative recombination via an intermediate state.	75

CHAPTER THREE

3.1.	Sputtering device (a) the SIP sputter coater and SPI control (b) the instrument labels.[79
3.2.	Carbolite MTF tube furnace	80
3.3.	A schematic diagram of uniform temperature curve	81
3.4.	A schematic diagram of experimental setup	82
3.5.	A schematic diagram illustrate the synthesis of SiO _x nanowires.	83
3.6.	FESEM image of SiO _x nanowires grown on pure silicon substrate at 1200°C with 10 sccm Ar gas flowrate for one hour.	84
3.7.	EDX spectrum and elements weight percentage of selected spot on the SiO _x nanowire grown at 1200°C with 10 sccm Ar gas flowrate for one hour.	85
3.8.	XRD spectrum of β-SiC nanowires showing the crystal planes (111), (200), (220) and (311) at 2θ= 35.75°, 41.5°, 60.1° and 72.0° respectively, grown under 1200°C with 10 sccm for 1h.	87
3.9.	HRTEM of (A) core SiO _x NW grown under 1200°C with 10 sccm of Ar flowrate gas for 1h and (B) the outer shell.	88
3.10.	Room temperature PL spectrum of Au-SiO _x nanowires grown under 1200°C with 10 sccm for 1h.	89
3.11.	Absorption IR spectrum of SiO _x nanowires grown under 1200°C with 10 sccm for 1h.	91

Chapter 4

4.1.	FESEM image of sample center (a), edge (b) and (c) in-between. The corresponding EDX spectrum with mass ratios (a1) and (b1) after heating by 950°C for 1h.	94
------	---	----

4.2.	FESEM image of (a) pits formation under 60 sccm Ar flow rate at 1200°C for 1h and (b) enlarged image of (a).	95
4.3.	FESEM images of SiO _x nanowires grown on pure silicon substrate at (a) 1000°C, (b) 1100°C and 1200°C temperatures with 10 sccm Ar flowrate for one hour.	97
4.4.	FESEM of (a) SiO _x NWs (8k) at 1200°C for 5 minutes, (b) magnified image of the nanoballs (100k) and (c) EDX spectrum of image (a).	98
4.5.	FESEM images of SiO _x NWs grown in (a) 5, (b) 10, (c) 40 and (d) 60 minutes at 1200°C temperature with 10 sccm Ar flow rate	100
4.6.	FESEM image of tow single SiO _x NW (a) and (b) grown on Si(100) substrate for 5 minutes deposition time at 1200°C and 10 sccm flowrate of Ar.	101
4.7.	Two examples of the variation of SiO _x NWs diameter at different length fabricated for 5 minutes at 1200°C with Ar gas of 10sccm flowrate.	102
4.8.	XRD spectrums of SiO _x NWs for 5, 10, 40, 60 mins deposition time at 1200°C heating temperature with 10sccm Ar flowrate.	103
4.9.	FESEM image of SiO _x nanowires deposited at Ar flowrate, (a) 60, (b) 40, (c) 20 and (d)10 sccm using temperature of 1200°C for 1h.	105
4.10.	Graphs of argon flow rate versus (a) average nucleated seed diameter and (b) average SiO _x NWs length.	107
4.11.	A schematic diagram of SiO _x NWs densities at different Ar flow rates	108
4.12.	XRD spectrum of SiO _x NWs at 10, 20, 40 and 60 sccm flow rates using 1200°C heating temperature and 30 mins deposition time.	109
4.13.	A schematic diagram of non-catalytic growth of SiO _x nanowires by SVLS mechanism.	111
4.14.	FESEM of gold thin film over Si substrate heated at (a) 450°C and (b) 550°C temperatures.	113
4.15.	FESEM images of SiO _x nanowires grown on coated gold Si substrate at (a) 900°C, (b) 1000°C and (c) 1100°C using Ar gas with 10 sccm flowrate for 1h.	116
4.16.	FESEM of (a) SiO _x nanowires grown at 1100°C from base Au-Si alloy (b) enlarge image of two Au-Si alloys with attached SiO _x NWs and (c) EDX spectra of image (a).	118
4.17.	EDX spectrum of (a) FESEM image a2, centre of the nucleated ball and (b) EDX spectrum of FESEM image b2, the ball surrounding SiO _x layer.	119

4.18.	FESEM of (a) SiO _x nanostructures grown at 1200°C under 10 sccm Ar flowrate and 1h deposition time, (b) EDX spectrum of sample (a) and (c) EDX spectrum of one nanowire's cap inset image.	120
4.19.	FESEM image of SiO _x nanowires embedded with gold (a) and (b) at 1200°C under 10 sccm Ar flowrate and 1h deposition time, (c) the EDX spectrum in the middle of the wire.	122
4.20.	FESEM of SiO _x comet-like objects low and high magnifications at 1200°C under 10 sccm Ar flowrate for 1h deposition time (a) and (b), (c) tree-like nanostructure attached to a rod (white), (d) SiO _x nanowires tree-roots base formation.	124
4.21.	FESEM of (a, b) SiO _x nano-cages obtained on Au/Si substrate at 6cm apart from the furnace centre at 1200°C and under 10 sccm Ar flowrate for 1h, (C) EDX spectrum of SiO _x nano-cages.	126
4.22.	XRD spectrum of (A) SiO ₂ /Si, (B) Au/ SiO ₂ /Si and (C) SiO _x Nanowires at 1200°C heating temperature for 1h.	127
4.23.	FESEM image of SiO _x nanowires grown at 1200°C under 10 sccm Ar flowrate for 5, 6, 7 and 8 mins deposition time for (a) image (1) to (d) image (1) and using oxygen gas for (a) image (2) to (d) image (2).	129
4.24.	FESEM of SiO _x NWs at 1200°C under 10 sccm Ar flowrate for 1h deposition time using TiO ₂ :C mass ratios at (a)–(c) 1:1-1:3 and (d)-(e) 2:1-3:1 respectively.	132
4.25.	FESEM image of SiO _x NWs at (a) 40, (b) 30, (c) 20 and (d) 10 sccm flow rates with 1200°C heating temperature for 1h deposition time.	133
4.26.	XRD spectrum for (A) Au coated Si substrate and (B) SiO _x NWs grown at 1200°C under 10 sccm Ar flowrate for 1h deposition time.	135
4.27.	FESEM of SiO _x nanowires grown at 1200°C for (a) 10 (b) 20 (c) 40 (d) 60 and (e) 80 minutes deposition time under 10sccm Ar flow rate.	136
4.28.	FESEM of SiO _x NWs grown using Au coated silicon substrate deposited for (a) 20, (b) 30 and (c) 40 seconds, the wires were grown out from the Au-Si alloys for (a) and (b) while in (c) the nanowires have Au tips at the far end of the wire.	137
4.29.	Au thickness layer versus average SiO _x NWs diameter	139
4.30.	FESEM of SiO _x Nano-cakes grown on Au coated Si substrate which was inserted directly to the furnace at 1200°C with 10 sccm Ar flowrate for 8 mins, (a) 8k, (b) 16k and (c) 30k.	141
4.31.	EDX spectrums of SiO _x nano-cakes grown on Au coated Si substrate which was inserted directly to the furnace at 1200°C with 10 sccm Ar flowrate for 8 mins, (a) low magnification and (b) high magnification.	142

4.32.	XRD spectrum of SiO _x nano-cakes grown on Au coated Si substrate which was inserted directly to the furnace at 1200°C with 10 sccm Ar flowrate for 8 mins.	143
4.33.	A schematic diagram of Au –SiO _x NWs growth mechanism.	143
4.34.	A schematic drawing for root growth group of SiO _x NWs by SVLS mechanism.	145
4.35.	A Schematic diagram of SiO _x nano-cages growth model by assistance of SVLS mechanism.	149
4.36.	A schematic model of SiO _x nano-cakes growth at 1200°C with rapid heating rate. Growth steps: Stage (1) formation of Au nano-balls, stage (2) Formation of SiO _x NWs by SLS and stage (3) Formation of SiO _x nano-cakes.	150
4.37.	HTEM image of Au-SiO _x nanowire tip and stem grown under 1200°C with 10 sccm of Ar flowrate gas for 1h.	151
4.38.	HRTEM image of (a) SiO _x NWs grown at 1200°C and under 10 sccm Ar flowrate gas for 1h (b) magnified image of the tip of the wire.	153
4.39.	HRTEM of (A) core SiO _x NW grown under 1200°C with 10 sccm of Ar flowrate gas for 1h and (B) the outer shell.	154
4.40.	Room temperature PL spectrum of Au-SiO _x nanowires grown under 1200°C with 10 sccm of Ar flowrate gas for 1h recorded with excitation at 325nm.	154
4.41.	Room temperature PL spectrums of SiO _x NWs grown at 1200°C and 1100°C under 10sccm Ar flowrate for 1h.	155
4.42.	Room temperature PL spectrums of catalytic and non-catalytic SiO _x nanowires grown under 1200°C with 10 sccm of Ar gas flowrate for 1h.	157
4.43.	Room temperature PL spectrum of Au-SiO _x nanowires grown at 1200°C under 10 sccm of Ar gas flowrate for 1h with excitation at 325nm recorded before and after annealing.	158
4.44.	The formation of non-bridging oxygen centers	159
4.45.	Absorption IR spectrum of non-catalytic SiO _x nanowires grown under 1200°C with 10 sccm of Ar flowrate gas for 1h.	160
4.46.	IR spectrums of SiO _x NWs grown under 1200°C deposited for 1h at Ar flowrates (a-f) 60, 50, 40, 30, 20 and 10 sccm respectively.	162
4.47.	A schematic diagram of experiment setup for SiC fabrication at certain positions using Ar /O ₂ .	164

4.48.	XRD spectrums for as prepared samples (A-E) at 2, 4, 6, 8 and 10 cm locations from the furnace centre respectively under 1200°C with 10 sccm for 1h.	165
4.49.	FESEM image of β -SiC nanowires at (A 2cm) and (B 4cm) locations from the furnace centre under 1200°C with 10 sccm for 1h with inset image of EDX element mass percentages for A and B. (C) is magnified image (15k) of B.	166
4.50.	XRD spectrum for β -SiC nanowires grown at 2cm and 4cm locations respectively under 1200°C with 10 sccm for 1h.	167
4.51.	FESEM of aligned β -SiC nanowires obtained at location B, 4cm apart from the furnace centre under 1200°C with 10 sccm for 1h.	168
4.52.	FESEM of β -SiC NWs diameters at (A=2cm and B= 4cm) at 1200°C in 10 sccm Ar flowrate gas for 1h. (C) enlarged image of B.	169
4.53.	FESEM of β -SiC nanowires grown at (A-E), 2 -8 cm locations respectively, and (E (1, 2) at 10 cm from the furnace centre under 1200°C with 10 sccm Ar flowrate for 1h.	170
4.54.	XRD spectrums of β -SiC nanowires at (A-B, 2-8 cm from the furnace centre) using Ar as an ambient gas at 1200°C for 1h.	172
4.55.	FESEM of substrate locations from the graphite boat at (A-D), (2 -8 cm) and E (1, 2) at 10 cm using 10 sccm of O ₂ flowrate gas under 1200°C with for 1h.	173
4.56.	XRD spectrums of β -SiC nanowires using 10 sccm of O ₂ flowrate gas at locations 2cm, 4cm, 6cm and 8cm under 1200°C for 1h.	174
4.57.	FESEM of β -SiC bunch-like nanostructures (A-C) (with 0.1k, 0.5 and 3k magnifications, respectively) gown with rapid heat rate by loading the silicon substrates directly to the furnace centre with 1200°C and 10 sccm of Ar flowrate gas for 1h.	175
4.58.	FESEM image of ultra-long β -SiC nanowires obtained at the samples edge under 1200°C with 10 sccm of Ar flowrate gas for 1h.	176
4.59.	A schematic diagram showing the OAG mechanism of SiC nanowires growth.	177
4.60.	FTIR spectrum of SiC nanowires peaks corresponding to Si–C stretching vibration at 798, 810 and 820 cm ⁻¹ and stretching vibration of Si–O for samples grown at 2, 4 and 6 cm from the furnace center respectively.	179
4.61.	A schematic drawing of non-catalytic growth of SiO _x nanowires via carbo-thermal reactions.	180
4.62.	A schematic drawing of catalytic SiO _x nanowires (tip, root) growth and the relative carbo-thermal suggested reactions.	182

- 4.63. A schematic drawing of the formation process of β -SiC nanowires and the relative carbo-thermal suggested reactions. 186

List of Tables

TABLE		PAGE
CHAPTER TWO		
2.1.	Parameters of unit cells of 3C-SiC, 2H-SiC, 4H-SiC, 6H-SiC	48
2.2.	Chemical and mechanical properties of β -SiC	51
CHAPTER THREE		
3.1.	Specification of the Carbolite MTF Tube Furnace	80
CHAPTER FOUR		
4.1.	The Au layer thickness and the SiO _x NWs diameter data.	102
4.2.	The collection of data for different argon flow rates, the average nucleation seed diameters and the average SiO _x NWs lengths	107
4.3.	The Si:O mass ratio for different spots on the SiO _x nanostructures	125
4.4.	The SiO _x NW diameters and lengths data.	140
4.5.	FTIR data of SiO _x NWs, the bond types, vibration modes and related wavenumber.	163

Chapter 1

1.1 Introduction

One-dimensional nanostructures have attracted significant attention in recent years, due to their physical and chemical properties that could lead to novel devices in electronics, chemistry and biomedical applications [1,2,3,4,5,6]. Among these, silicon oxide (SiO_x) and silicon carbide (SiC) nanostructures are two examples of such materials.

SiO_x nanostructures have stimulated much interest because of their different electronic and optical characteristics compared with bulk materials [7- 10]. Potential novel applications of SiO_xNWs have also been reported, including p–n junction [11] and chemical sensors [12]. The electrical transport properties [13] and noise characteristics [14] of SiO_xNWs have been reported. Silicon oxide nanowires have been used in Li-ion batteries as an electrode [15]. Among the materials, silicon has the highest specific capacity of about 4200 mAh g^{-1} [16-19] and has stimulated extensive interest in preparing silicon nanowires (SiO_xNWs) to be used as an anode instead of graphite. These wires have also attracted considerable attention due to their potential applications in interconnects and basic components in future nanoelectronic and, especially, optoelectronic devices [20].

An extensive work has been done to synthesize these wires from laser ablation [22] to thermal evaporation methods [23, 24]. The main function of these methods is to evaporate silicon, which functioned as a source of building blocks for SiO_x

INTRODUCTION

nanostructures. There are three techniques used to generate silicon in vapor form. They are using saline (SiH_4) gas, silicon powder evaporation at high temperatures and evaporation of solid silicon substrate. The advantages of evaporating silicon direct from the substrate over other techniques are easy to handle, valid at atmospheric pressure, easy to control and low cost.

To the best of our knowledge, no previous studies have been reported on the parametric studies of SiO_x nanostructures growth using the evaporation of silicon from the substrate. In this study, the effect of experimental parameters such as (furnace temperature, Ar gas flowrates, O_2 gas flowrates, deposition time and carbon to titanium oxide mass ratio) on the growth of SiO_x nanostructures grown on Au-coated and bare Si substrate have been investigated as well as the study of their optical properties.

Silicon carbide (β -SiC) nanowires which has very unique properties, such as wide band gap, excellent thermal conductivity, chemical inertness, high electron mobility, and biocompatibility [25-27] has been synthesized. Thus, in the last few years, much effort has been made to the synthesis of 1D β -SiC nanostructures. Several techniques were reported, including carbon nanotubes-confined growth [28], chemical vapour deposition (CVD) [29–31], carbo-thermal evaporation [32, 33]. In this work β -SiC nanowires were grown on bare silicon substrate using carbo-thermal evaporation method. For the first time, β -SiC nanowires synthesized using carbo-thermal by evaporating carbon powder at temperature around 1200°C . Moreover, parametric studies of the effect of substrate location, Ar gas flowrate, oxygen gas flowrates and rapid heating rate on the growth of β -SiC nanowires have been examined. The related

INTRODUCTION

FTIR transmission spectrums were applied for β -SiC samples to examine their functional groups.

1.2 Thesis Objectives

The objectives of our study can be summarized as follows:

- 1- To study the effect of parametric studies on the growth of SiO_x nanostructures using carbo-thermal evaporation method on pure and gold coated silicon substrates.
- 2- To investigate the optical properties of SiO_x nanostructures.
- 3- To synthesize β -SiC nanowires on bare silicon substrate by carbo-thermal evaporation method and study the effect of parametric conditions on their growth.

1.3 Layout of the Thesis

This thesis is divided into five chapters, started with introduction about SiO_x and β -SiC nanostructures. The literature review in chapter two gives background about on SiO_x and β -SiC nanostructures and their structure in bulk form, the synthesis method, discussion on different growth mechanisms followed with their photoluminescence property. In chapter three the instruments used and techniques to characterize SiO_x and β -SiC will be discussed. Results and related discussions are revealed in chapter four. Conclusions and future work suggestions will be presented in chapter five.

Chapter 2

Silicon Oxide and Silicon Carbide Nanostructures

2.1 Introduction

Silicon oxide and silicon carbide nanostructures have attracted more interest due to their enormous applications. Literature review on these nanostructures has been discussed in this chapter in detail.

The fabrication of silicon oxide (SiO_x) nanostructures will be presented, which include the silicon oxide structures and related main synthesis methods, the laser ablation and thermal evaporation. Then, the non-catalytic and catalytic growths of SiO_x nanostructures with related mechanisms will be outlined and followed with discussion on physical background of SiO_x nanostructure's photoluminescence.

The part of the fabrication of silicon carbide nanowires will be handled afterward, which is followed by crystal structure and its properties. After that, a collection of synthesis methods of SiC will be discussed. At the end of this chapter, the characterization techniques of SiO_x and SiC nanostructures will be presented.

LITERATURE REVIEW OF SILICON OXIDE AND SILICON CARBIDE NANOSTRUCTURES

2.1.1 Inorganic One Dimensional Nanowires

Since the discovery of carbon nanotubes by Iijima [34], there has been great interest in the synthesis and characterization of one-dimensional (1-D) materials. A nanowire is a wire of dimensions of the order of a nanometer (10^{-9} meters). Alternatively, nanowires can be defined as structures that have a lateral size constrained to tens of nanometers or less and an unconstrained longitudinal size.

The inorganic nanowires can also act as active components in devices as revealed by recent investigations. In the last 3–4 years, a variety of inorganic material nanowires has been synthesized and characterized. Many different types of nanowires exist, including metallic (e.g., Ni, Pt, Au), semiconducting (e.g., Si, InP, GaN, etc.), and insulating (e.g., SiO_2 , TiO_2).

The nanowires could be used, in the near future, to link tiny components into extremely small circuits. Using nanotechnology, such components could be created out of chemical compounds. Typical nanowires exhibit aspect ratios (length-to-width ratio) of 1000 or more. As such they are often referred to as 1-D materials. Nanowires have many interesting properties that are not seen in bulk or 3-D materials. This is because electrons in nanowires are quantum confined laterally and thus occupy energy levels that are different from the traditional continuum of energy levels or bands found in bulk materials.

Thus, nanowires of oxides have been generated by employing various strategies. One of the crucial factors in the synthesis of nanowires is the control of composition, size and crystallinity. Among the methods employed, some are based on vapour phase techniques, while others are solution techniques.

LITERATURE REVIEW OF SILICON OXIDE AND SILICON CARBIDE NANOSTRUCTURES

Compared to physical methods such as nanolithography and other patterning techniques, chemical methods have been more versatile and effective in the synthesis of these nanowires. Thus, techniques involving chemical vapor deposition (CVD), precursor decomposition, as well as solvothermal, hydrothermal and carbothermal methods have been widely employed. Several physical methods, especially microscopic techniques such as scanning electron microscopy (SEM), transmission electron microscopy (TEM), and X-ray diffraction (XRD) are commonly used to characterize nanowires.

LITERATURE REVIEW OF SILICON OXIDE AND SILICON CARBIDE NANOSTRUCTURES

2.1.2 One Dimensional Silicon Oxide Nanostructures

The most abundant oxides in the earth's crust, silica and its related oxides are also known for their outstanding structural features. Silica is an important material in many technological and scientific areas. In the past decades, considerable progress has been made in growing 1D nanomaterials of silicon dioxide, including nanowires and nanotubes, because of their potential applications in electronics, optics, and nanodevices.

2.2 Fabrications of Silicon Oxide Nanostructures

2.2.1 Crystal Structures of Silicon and Silicon Oxides

Bulk silicon is the second most abundant element in the Earth's crust, making up 25.7% of it by weight. It occurs in clay, feldspar, granite, quartz and sand, mainly in the form of silicon dioxide (also known as silica) and silicates (compounds containing silicon, oxygen and metals). Silicon can be either crystalline or amorphous depending upon percentage of purity. The Silicon that is pulled as a single crystal will make a perfect structure. The internal crystalline structure is completely homogenous, which can be recognized by an even external coloring, see Fig. 2.1.

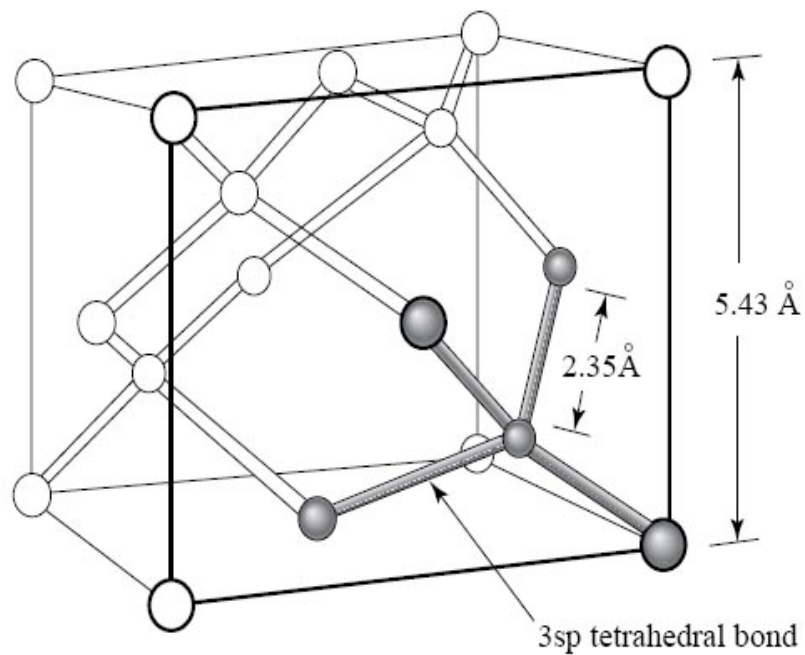


Figure 2.1 Single Silicon Crystal

The silicon density, melting point and boiling point are 2.33 g.cm^{-3} at 20°C , 1410°C and 3265°C respectively. Silicon is an intrinsic semiconductor in its purest form, although the intensity of its semiconduction is highly increased by introducing small quantities of impurities. Amorphous silicon (a-Si) is the non-crystalline allotropic form

LITERATURE REVIEW OF SILICON OXIDE AND SILICON CARBIDE NANOSTRUCTURES

of silicon. Silicon is a four-fold coordinated atom that is normally tetrahedrally bonded to four neighboring silicon atoms. In crystalline silicon this tetrahedral structure is continued over a large range, forming a well-ordered lattice (crystal). In amorphous silicon this long range order is not present and the atoms form a continuous random network. The silicate tetrahedron is a central silicon atom surrounded by four oxygen atoms at the corners of a tetrahedron. Three of the oxygen atoms of each tetrahedron are shared with other tetrahedrons, but no two tetrahedrons have more than one oxygen atom in common; each tetrahedron, therefore, is linked to three others. The silicon atoms are arranged at the corners of hexagons as in Fig. 2.2, and the unshared oxygen atoms are commonly oriented on the same side of the sheet. Because these are capable of forming chemical bonds with other metal atoms, the silicate sheets are interleaved with layers of other elements.

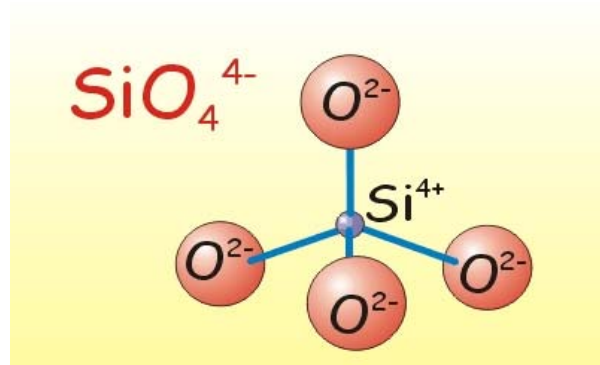


Figure 2.2 Bonded structure for one silicate

Not all the atoms within amorphous silicon are four-fold coordinated. Due to the disordered nature of the material some atoms have a dangling bond. These dangling bonds are defects in the continuous random network, which cause electrical behavior. If desired, the material can be passivated by hydrogen, which bonds to the dangling bonds and can reduce the dangling bond density by several orders of magnitude. Silica is an important material in many technological and scientific areas. In the past decades,

LITERATURE REVIEW OF SILICON OXIDE AND SILICON CARBIDE NANOSTRUCTURES

considerable progress has been made in growing 1D nanomaterials of silicon dioxide, including nanowires [35–39] and nanotubes [40–44], because of their potential applications in electronics, optics, and nanodevices. Silicon dioxide is formed when silicon is exposed to oxygen (or air) at high temperature. A very thin layer (approximately 1 nm or 10 Å) of so-called 'native oxide' is formed on the surface when silicon is exposed to air under ambient conditions as in Fig. 2.3.

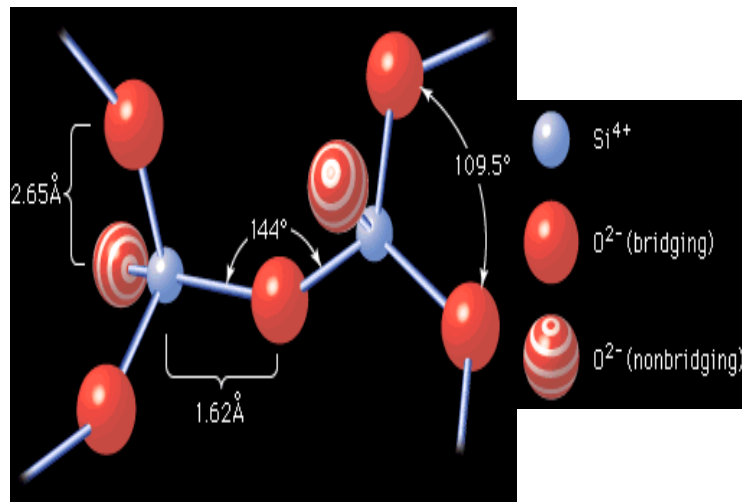


Figure 2.3 Silicon ions bond to oxygen atoms, forming tetrahedral structures and the angle at which the two tetrahedra are connected also varies.

Higher temperatures and alternate environments are used to grow well-controlled layers of silicon dioxide on silicon, for example at temperatures of 600 -1200 °C so-called "dry" or "wet" oxidation using O₂ or H₂O respectively. There are more than two types of amorphous silicon when focusing on nano-scale. The number of oxygen atoms played an important role in the determination of the final shape of silicon oxide (SiO_x) nanostructures.

LITERATURE REVIEW OF SILICON OXIDE AND SILICON CARBIDE NANOSTRUCTURES

The nano-scale silicon structure will be affected due to change in its surface free energy. Thermodynamics tells us that any material or system is stable only when it is in a state with the lowest Gibbs free energy. Therefore, there is a strong tendency for a solid or a liquid to minimize the total surface energy. There are a variety of mechanisms to reduce the overall surface energy. The various mechanisms can be grouped into atomic or surface level, individual structures and the overall system.

For a given surface with a fixed surface area, the surface energy can be reduced through (i) surface relaxation, the surface atoms or ions shift inwardly which occur more readily in liquid phase than in solid surface due to rigid structure in solids, (ii) surface restructuring through combining surface dangling bonds into strained new chemical bonds, (iii) surface adsorption through chemical or physical adsorption of terminal chemical species onto the surface by forming chemical bonds or weak attraction forces such as electrostatic or van der Waals forces, and (iv) composition segregation or impurity enrichment on the surface through solid-state diffusion.

Let us take the surface atoms on an atomic flat (100) surface as an example, assuming the crystal has a simple cubic structure and each atom has a coordination number of six. The surface atoms are linked with one atom directly beneath and four other surrounding surface atoms. It is reasonable to consider each chemical bond acting as an attractive force; all the surface atoms are under the influence of a net force pointing inwardly and perpendicular to the surface.

Understandably, under such a force, the distance between the surface atomic layer and the subsurface atomic layer would be smaller than that inside the bulk, though the structure of the surface atomic layer remains unchanged. In addition, the distance between the atomic layers under the surface would also be reduced. Such surface relaxation has been well established. Furthermore, the surface atoms may also shift

LITERATURE REVIEW OF SILICON OXIDE AND SILICON CARBIDE NANOSTRUCTURES

laterally relative to the subsurface atomic layer.

Figure 2.4 schematically depicts such surface atomic shift or relaxation. For bulk materials, such a reduction in the lattice dimension is too small to exhibit any appreciable influence on the overall crystal lattice constant and, therefore, can be ignored. However, such an inward or lateral shift of surface atoms would result in a reduction of the surface energy. Such a surface relaxation becomes more pronounced in less rigid crystals, and can result in a noticeable reduction of bond length in nanoparticles.

If a surface atom has more than one broken bonds, surface restructuring is a possible mechanism in which surface atoms combine to form a highly strained bond to reduce the surface energy [45]. The broken bonds from neighboring surface atoms combine to form a highly strained bond.

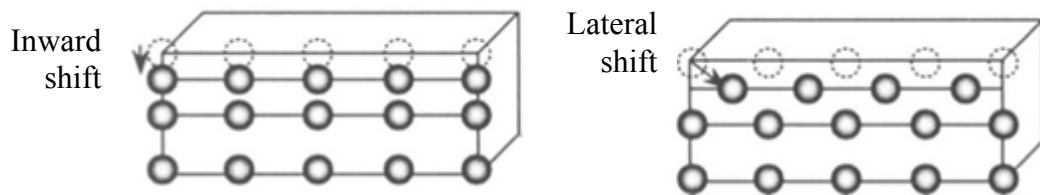


Fig. 2.4 Schematic showing surface atoms shifting either inwardly or laterally so as to reduce the surface energy.

For example, such surface restructuring is found in the (100) surface of silicon crystals. Surface energy of (100) faces in diamond and silicon crystals before restructuring is higher than of both (111) and (110) faces [46]. However, restructured (100) faces have the lowest surface energy among three low indices faces,[47-49] and such surface restructuring can have a significant impact on the crystal.

Figure 2.5 shows the original (100) surface and 2×1 restructured (100) surface of diamond crystal. Another way to reduce the surface energy is chemical and physical adsorption on solid surfaces, which can effectively lower the surface energy.

LITERATURE REVIEW OF SILICON OXIDE AND SILICON CARBIDE NANOSTRUCTURES

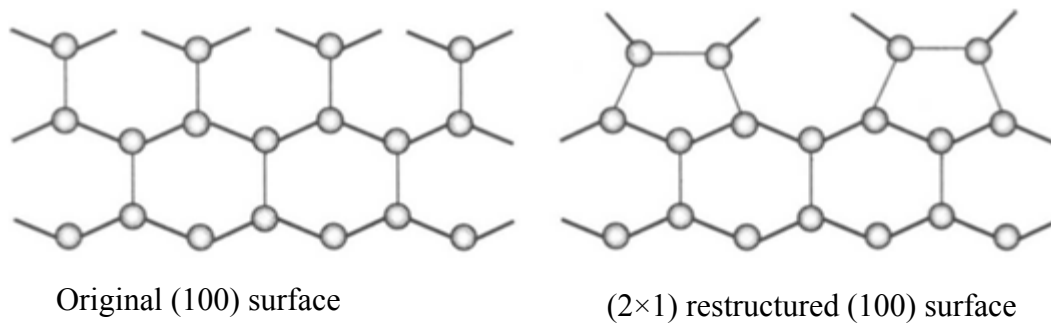


Fig. 2.5 Schematic illustrating the (2×1) restructure of silicon (100) surface.

For example, the surface of diamond is terminated with hydrogen and that of silicon is covered with hydroxyl groups before restructuring as schematically shown in Fig. 2.6. These are considered as chemical adsorption. Yet another approach to reduce the surface energy is composition segregation or enrichment of impurities on the surfaces. Although composition segregation, such as enrichment of surfactants on the surface of a liquid is an effective way to reduce the surface energy, it is not common in a solid surface. In bulk solids, composition segregation is not significant, since the activation energy required for solid-state diffusion is high and the diffusion distance is large. In nanostructures and nanomaterials, however, phase segregation may play a significant role in the reduction of surface energy, considering the great impact of surface energy and the short diffusion distance.

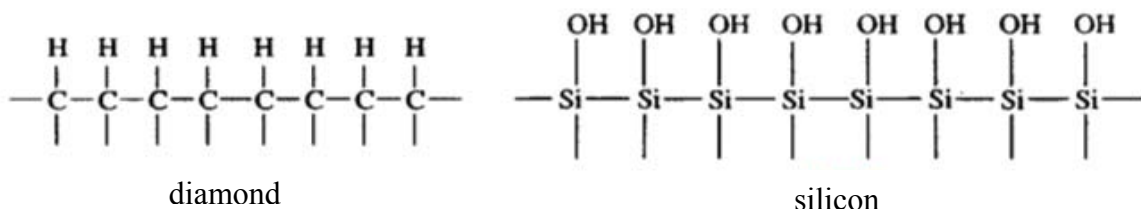


Fig. 2.6 Schematic showing the surface of diamond is covered with hydrogen and that of silicon is covered with hydroxyl groups through chemisorption before restructuring.

LITERATURE REVIEW OF SILICON OXIDE AND SILICON CARBIDE NANOSTRUCTURES

The same is also found for a glass. When heating a piece of glass to temperatures above its glass transition point, sharp corners will round up. For liquid and amorphous solids, they have isotropic microstructure and, thus, isotropic surface energy. For such materials, reduction of the overall surface area is the way to reduce the overall surface energy. However, for a crystalline solid, different crystal facets possess different surface energy. Therefore, a crystalline particle normally forms facets, instead of having a spherical shape, which in general, possesses a surface energy higher than a faceted particle.

2.2.2 Synthesis Methods of Silicon oxide nanostructures

Recently, an intensive work has led to the establishment of general field of manufacturing 1D silicon or silicon oxide nanostructures (SiO_x nanostructures). SiO_x nanostructures have been produced by physical and chemical routes including those structures composed of amorphous and crystalline silicon, amorphous silicon dioxide, crystalline silicon core with an amorphous silicon dioxide sheath, and SiO_x .

SiO_x nanostructures can be fabricated using pulsed laser ablation. The pulsed laser ablation [22] with apparatus design as in Fig. 2.7, which consist of a quartz tube installed inside a furnace and then heated to more than 1150 °C. An inner quartz tube was placed inside the outer tube. The laser target (pure Si or mixed Si–5% Au) was put inside the inner tube. The substrates on which the SiO_x nanostructures were supposed to grow were placed along the inner and the outer tubes. The laser beam hits the target and evaporates growth species, which make 15 nm Si nanowires at 1200°C. However, the nanowires made with this method were not as long and uniform as those produced at higher temperatures where high quality Si-based nanowires free of additional amorphous coating and up to several millimetres long were made.

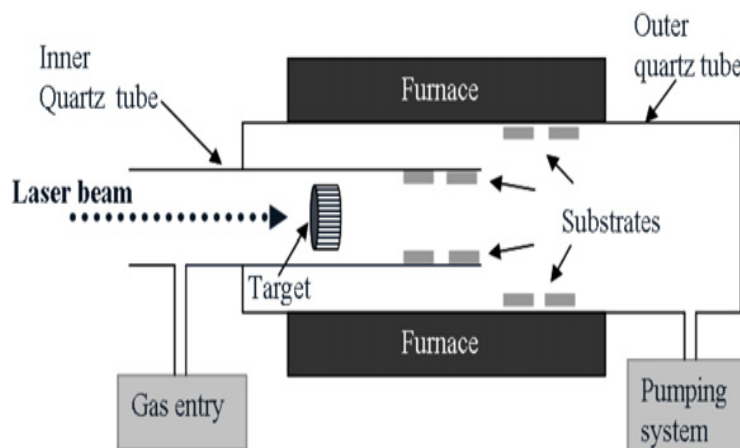


Figure 2.7 Schematic illustration of laser ablation growth system.

2.2.2.1. Thermal Evaporation Method

Among physical vapour deposition techniques thermal evaporation (TE) is the one with the longest standing tradition. However, during the last 30 years of booming semiconductor industry which involves a great deal of thin film technology, deposition techniques like CVD (chemical vapor deposition) or sputtering which often offer unquestionable advantages have been developed to perfection and TE has largely been replaced in production lines. On the laboratory scale, due to their simplicity, techniques like TE, pulsed laser deposition or sputtering were much more promising to realize fast results.

However, as time went by it became clear that using TE method over various deposition methods strongly depends on material issues as well as economic aspects. With progressive commercialization, cost effective volume production and reproducibility became the driving forces and the intrinsic advantages of TE turned the scales.

The TE method is used to fabricate SiO_xNWs which is a part of chemical vapor deposition (CVD). Here, the temperature gradient and the vacuum conditions are two critical parameters for the formation of nanostructures.

The fabrication is simply through evaporating commercial metal oxide powders at elevated temperatures under a vacuum or in an inert gas, mainly argon, atmosphere with a negative pressure. Nanostructures products form in the low temperature regions where materials deposit from the vapour phase. Fig. 2.8 illustrates the common thermal evaporation set up.

LITERATURE REVIEW OF SILICON OXIDE AND SILICON CARBIDE NANOSTRUCTURES

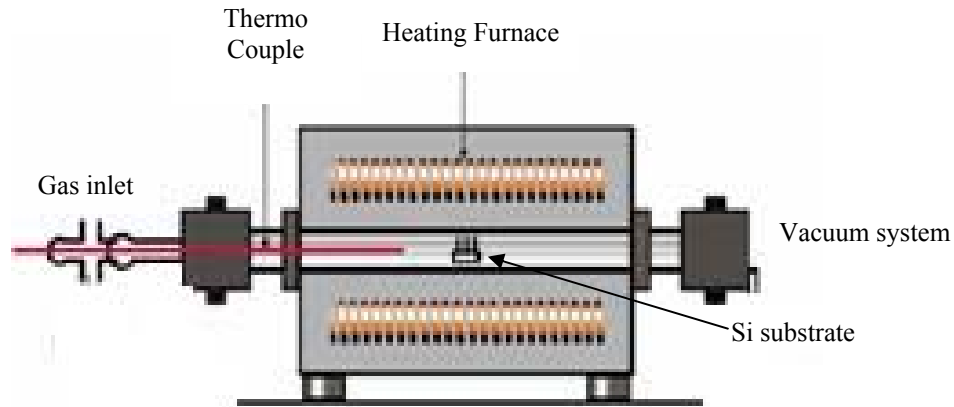


Figure 2.8 Thermal evaporation set up.

The thermal evaporation deposition technique consists of heating until evaporation of the material to be deposited. The material vapour finally condenses in form of thin film or micro and nano structures on the cold substrate surface and on the vacuum chamber walls. Usually low pressures are used, about 10^{-6} or 10^{-5} Torr, to avoid reaction between the vapour and atmosphere. At these low pressures, the mean free path of vapour atoms is the same order as the vacuum chamber dimensions, so these particles travel in straight lines from the evaporation source towards the substrate.

Besides, in thermal evaporation techniques the average energy of vapour atoms reaching the substrate surface is generally low (order of kT , i.e. tenths of eV). This affects seriously the morphology of the products (nanostructures). Resistance heating (Joule effect) equipments is mostly used in thermal evaporation method which applied to heat the material.

In addition, the source to substrate distance can be varied and automatically results deferent deposited nanostructures morphologies. This important parameter is certainly one of the essential and unquestionable advantages of TE over other methods to study the effect of temperature fluctuations on the growth of nanostructures. Due to the fact

LITERATURE REVIEW OF SILICON OXIDE AND SILICON CARBIDE NANOSTRUCTURES

that a nearest location to the source receives high growth species and therefore dense growth yield.

In SiO_x nanostructures synthesis process many researchers depend on this method. For example, Pure SiNWs without SiO_2 sheath were made by Yan et al. [50] in which hydrogen was used to prevent the formation of a SiO_2 surface layer. However, it is unclear whether the sample would be stable in air after exposure to oxygen. SiO_x nanowires were made by Tang et al. [51] was conducted through thermal evaporation method, and SiO was suggested as the catalyst in that work. Ni thin films were used as catalysts by Jin et al. to produce amorphous SiNW at 1200°C heating temperature [52].

No external supplies of Si were needed, but argon gas was used.

This method is simple, so it does not need complicated electronic networks or different gas piping. Instead of voltage controlling in laser ablation, here controlling the Ar or O_2 flow rates, deposition times and substrate temperature can give an ultra-long SiO_x nanowires and many different unique nanostructures shapes.

Moreover, the substrate in thermal evaporation will be the source of Si and place of growth at the same time. Therefore, this method was used in this thesis to produce SiO_x nanostructures, which will be explained deeply in chapter three.

2.2.3 Non-catalytic Growth of Silicon Oxide Nanostructures

Only a few papers have been devoted to the non-catalyst-based method [53-57]. Peng et al. [53] suggested that by thermal CVD long amorphous nanowires were synthesized with diameters between 20-100 nm. In this case, usually Si wafers, SiO₂ nanoparticles, and a mixture of Si and SiO₂ powder [57] were used as the source materials, and the oxygen came from either the O₂ gas flow [43,55] or the source materials (e.g., SiO₂) [42,44] or was attributed to the residue O₂ gas in the chamber or carrier gas. When SiO_x was used as a catalyst, no aliened nanoparticles were found at the tip of the nanowires. Strings of SiO nanoparticles were found in the sample, providing critical information regarding the growth mechanisms. The growth mechanisms for the non-catalyst method are not yet well understood.

2.2.4 Catalytic Growth of Silicon Oxide Nanostructures

The majority of SiO_x nanowires fabrication methods are catalyst-based methods. The identification of catalysts has been straightforward. In most cases, they are metal nanoparticles that are found either at the tip of the nanowires, or are enclosed at the tip of or along the nanowires, suggesting tip growth. Different kinds of catalysts have been used, such as Au [58,59], Fe [60], Co [61], Ni [62], Ge [63,64], and other metal alloys [65]. In many cases, metal silicides may very well be the catalysts. It is also possible that during the catalytic processes that silicon diffuses relatively freely through the metal catalyst and consequently, the observed silicides at the end of reaction may be different from those during the catalytic reaction. No direct evidence is available to show whether metal or metal silicide nanoparticles are the true catalyst. For example, with catalysts, the reaction temperature can be as low as 300 to 400°C. The diameter of the nanowires is more controllable with the use of catalysts. The difference between the diameters of long SiO_xNW and the catalysts forming them is comparable to that between long carbon nanotubes and the corresponding catalysts, and the correlation between the two in both cases is strong. The extent of correlation is also temperature and catalyst dependent. A comparison with the growth results on Si(111) and Si(100) reference templates (Au droplets) yields similar SiNW arrays [66]. That means, the substrate lattice planes are not affecting the growth of SiO_xNWs .

The first indication that gold might be a useful catalyst came through the work of Haruta et al. when he discovered in the late 1980s that gold becomes considerably stickier when spread in tiny dots on certain metal and oxide compounds [67]. The choices for nano-Au catalyst depend upon the activities of irreducible oxide supports such as Al_2O_3 and reducible transition metals oxides such as TiO_2 . When the reducible metals are coupled with gold, the catalytic activity of the system will be one order

LITERATURE REVIEW OF SILICON OXIDE AND SILICON CARBIDE NANOSTRUCTURES

higher than that of Au coupled with irreducible supports. Goodman et al. suggested that the primary source of the catalytic activity of gold was non-metallic nanoparticle clusters [68]. The relationship between particle size and melting point of gold nanoparticles can be seen in Fig. 2.9.

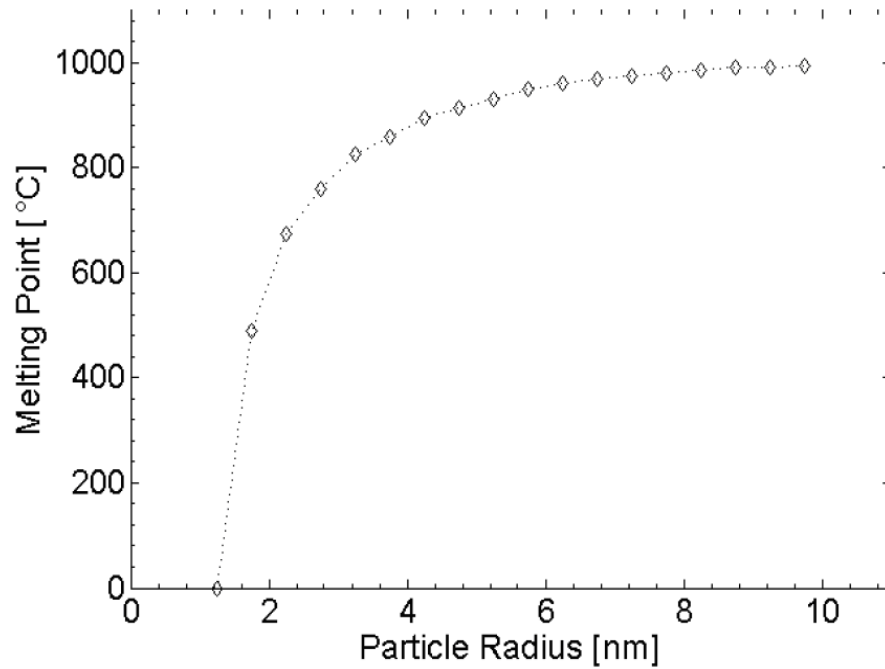


Figure 2.9 The relationship between particle size and melting point of gold nanoparticles.[69]

The Au-Si assessed by Massalski [70] presents a deep eutectic temperature, which is the indication of a strong attractive interaction between Au and Si in the liquid state, in contrast with the strong repulsive interaction between Au and Si in the solid state. The temperature for SiNW formation must be above the eutectic point as liquid droplets can form under this condition; see Fig. 2.10 (a). From the diagram the melting (T_m) temperatures for Au and Si are 1046°C and 1414°C respectively. But both Au and Si at certain percentage of Si reach a eutectic alloy temperature around 363°. The

LITERATURE REVIEW OF SILICON OXIDE AND SILICON CARBIDE NANOSTRUCTURES

catalyst gold has very low eutectic temperature with silicon, when comparing to other metals, see Fig. 2.10 (b).

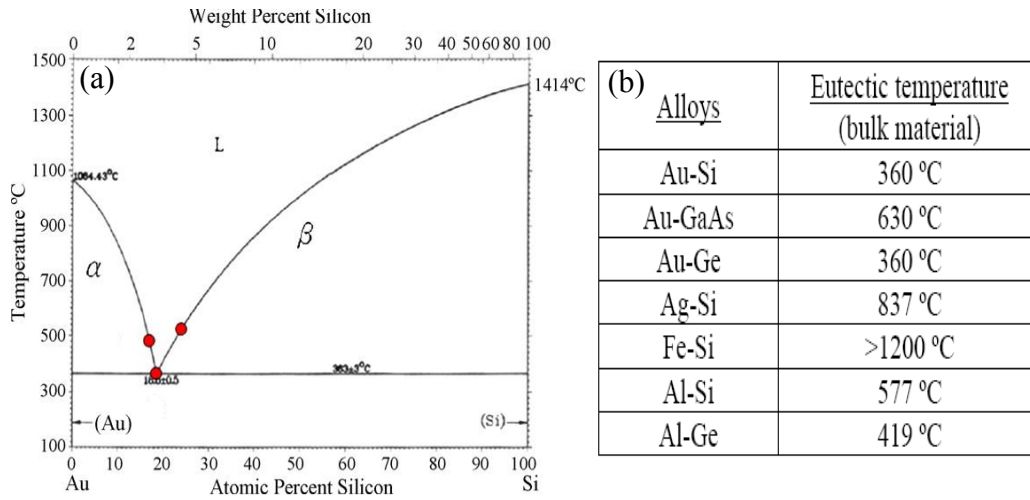


Figure 2.10 Phase Diagram of (a) Au-Si and (b) Different alloys eutectic temperatures [70].

If the reaction temperature is increased to be above the eutectic point of 363 °C, a liquid alloy can form and will assist the growth. Au has also been used to make very thin Si-based nanowires in heated supercritical solution.

Usually, Au nanoparticles can be prepared simply by first depositing Au thin film on a Si substrate using sputtering (sputter coater) or thermal evaporation and then annealing the thin film to form droplets. Fig. 2.11(a) shows uniform Au nanoparticles formed by annealing Au thin film (thickness = 1 nm) at 500 °C. A thick film results in large diameters of Au particles [71]. Au particles arrays can be prepared by lithography techniques. Fig. 2.11(b) shows Au disc array prepared by e-beam lithography. The thickness of the Au pattern is critical to the final sizes of the nanoparticles generated by the subsequent annealing. Au films that are too thin always result in splitting of the Au pattern (Fig. 2.11 (c)).

LITERATURE REVIEW OF SILICON OXIDE AND SILICON CARBIDE NANOSTRUCTURES

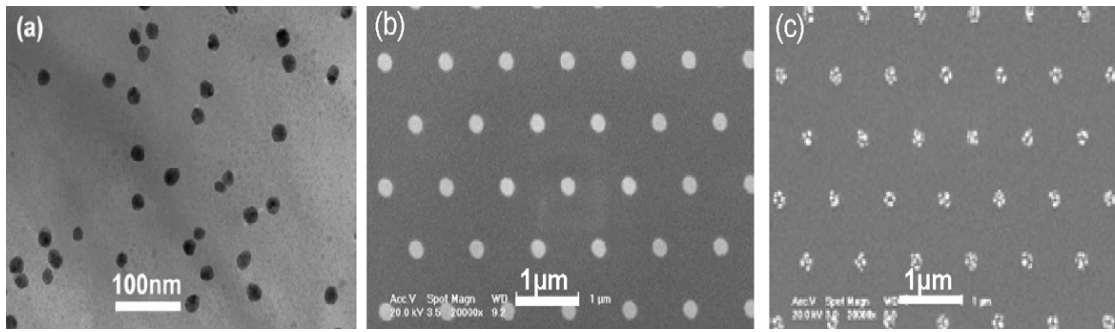


Figure 2.11 SEM of (a) Au catalysts prepared by annealing a thin Au film. (b) Au patterns prepared by e-beam lithography. (c) Splitting of the Au particles by annealing [71].

A proper treatment of the substrate surface by chemical etching and cleaning can result in the catalyst totally wetting the substrate surface, which is important for later growth of the nanowires epitaxially on the substrate.

Because of the oxide layer on the substrate surface or impurities on the catalyst surface induced by the lithography technique, Au catalysts may not wet the substrate surface. In this case, Si nanowires may not have orientation relationship with the substrate and grow along random directions [71].

Due to the softening of Si nanowires upon oxidation and the increasing Au diffusion at elevated temperatures, the embedded SiO_xNW was formed, and the formation mechanism of these wires is shown in Fig. 2.12.

First, the deposited Au nanoparticles attached on the surface of a Si nanowire. Upon heating the coated Si nanowires, the Au nanoparticles tended to move into the core, together with the motion of the Si– SiO_x interface of the wire so as to reduce the surface area and thus the surface energy. As the annealing temperature was slightly below the melting point of Au, the Au nanoparticles would be in a semi-liquid state.

The crystalline structure of silicon was changed to an amorphous structure soft enough to allow the diffusion of Au nanoparticles into the core of the nanowire. The SiO_x over

LITERATURE REVIEW OF SILICON OXIDE AND SILICON CARBIDE NANOSTRUCTURES

layer of Au nanoparticles can be readily removed by HF etching to expose the SiO_xNWs, if necessary.

Thus, the furnace annealing of Au-coated Si nanowires offers a simple method of synthesizing thin and large quantity crystalline Au nanowires. The synthesized Au embedded SiO_xNWs should find interesting applications in nanodevices.

Metal silicides are promising candidates as electrical contacts for silicon nanowires because of their excellent properties, such as high thermal stability, good compatibility with Si and no electron migration effect. Several methods have been developed to convert the nanowires to metal silicides.

LITERATURE REVIEW OF SILICON OXIDE AND SILICON CARBIDE NANOSTRUCTURES

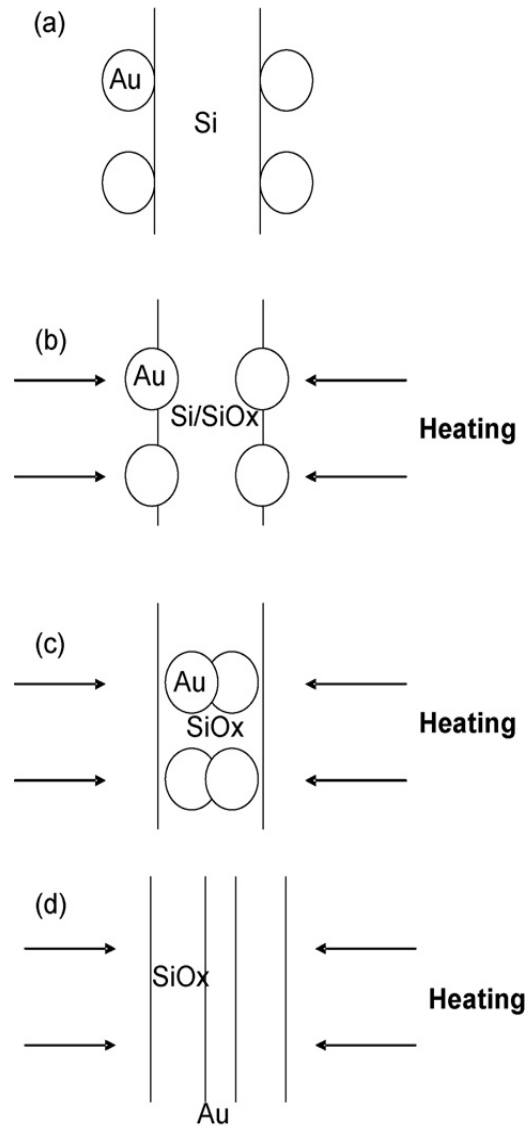


Figure 2.12 The formation mechanism of Au embedded SiO_xNWs by furnace annealing: (a) Au nanoparticles deposited by argon ion sputtering are attached on the surface of a Si nanowire, (b) oxidation of Si nanowires and diffusion of Au nanoparticles into Si nanowires under heating, (c) diffusion of Au nanoparticles in the SiO_x matrix of the nanowire at elevated temperature (e.g. 880 °C), and (d) formation of Au embedded SiO_xNW [71].

2.2.5 Growth Mechanisms of Silicon Oxide Nanostructures

The SiO_x nanostructure growths are possible to categorize based on the source of feedstock. In CVD and laser vaporization methods, gaseous stock materials are used, which lead to the well-known vapour–liquid–solid (VLS) growth mechanism, referring to the gas feedstock, liquid catalysts and solid nanowires.

In solution synthesis, the Si feedstock comes from the solution, leading to the solution–liquid–solid growth model. This should not be confused with the solid–liquid–solid (SLS) model, which suggests that bulk solid materials are used to produce nanostructures via catalytic processes. Moreover, the synthesis of SiO_xNWs without catalyst can be explained also by vapour–solid growth mechanism. These mechanisms will be discussed as follows.

(i) Vapour–Liquid–Solid Growth Mechanism

In different semiconductor material systems, whiskers with similar morphologies and structures have been fabricated by the vapour–liquid–solid (VLS) reaction and a variety of whisker forms have been obtained.

Although the VLS technique has been widely used for the fabrication of nanowires in recent years, the real absorption, reaction and diffusion processes of source atoms through the catalyst are complicated and largely depend on the experimental conditions and the material systems.

Many experiments have shown the deviation of some nanowire growth from the classical VLS mechanism. The absorption, diffusion and precipitation processes of Si as schematically shown by the path 1, 2 and 3 in Fig. 2.13 (a) involve vapor, liquid and solid phases. There has been a long-standing debate on whether the metal catalysts in these cases are solid particles (see Fig. 2.13 (a, b)) or liquid droplets [72]. There are two main uncertainties in this debate: (1) because of the nanosize effect, the melting

LITERATURE REVIEW OF SILICON OXIDE AND SILICON CARBIDE NANOSTRUCTURES

temperatures of nanoparticles are always lower than those of bulk materials and (2) it is not possible to measure the real temperature at the catalyst tips. In fact, in some cases, nanosized metal droplets are in a partially molten state [73].

Silicon nanostructures were synthesized by the Vapour-Liquid-Solid (VLS) method by standard Chemical Vapour Deposition (CVD) [74-76]. With the purpose of revealing the intrinsic structural characteristics of the nanowires and to decouple those from the influence of the substrate, synthesis was carried out on an oxidized substrate (as opposed to a crystalline silicon wafer). Gold nanoparticles of sizes ranging from 10 to 100 nm were used as catalysts for the nucleation and growth of silicon nanowires.

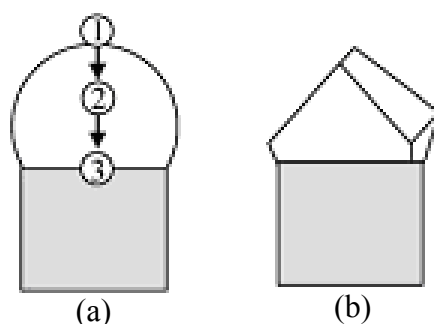


Figure 2.13 Schematic diagram of (a) The diffusion path of the source materials through a metal droplet; (b) the whisker growth can be catalyzed with a solid catalyst.

Growth mechanisms have been investigated, and several theories have been proposed. There are two general models that are used to explain catalytic synthesis of nanowires or nanotubes.

The first is called tip growth, in which gas-phase reaction feedstock such as silane (SiH_4) deposits on nanoparticle tips on growing nanowires. The sources can be SiH_4 mixed in H_2 at a typical ratio of 1:10. The reaction gases have to be diluted to about 2% in an Ar atmosphere. The pressure for the reaction is about 200 Torr, and the flow rate is kept at 1500 standard cubic centimetre per minutes (sccm). The breakdown and dissolution of silane and subsequent migration and precipitation of Si after

LITERATURE REVIEW OF SILICON OXIDE AND SILICON CARBIDE NANOSTRUCTURES

saturation in the metal catalyst leads to the formation of SiO_xNW . Many images have shown that metal nanoparticles are at the tip of nanowires or nanotubes [77, 78].

The second model is termed root growth. In this case, Si feedstock, either coming directly from the substrate or coming from the gas phase, migrates and diffuses to the locations of nanoparticle catalysts on the surface or substrate. The feedstock is then converted to SiO_xNW by the catalysts. In both cases, the size of the nanoparticles has to be comparable to the diameter of the nanowires so that nanoparticles can efficiently absorb feedstock. For root growth, nanoparticles are found near the root or anchor of the nanowires, as contrasted to tip growth in which nanoparticles are found at the suspended end of the nanowires growing in space.

During growth, Au or Au silicide nanoparticles are considered molten. Molten metal catalysts are considered to be spherical or near spherical because of the surface tension. They may also take in silicon feedstock more readily than solid form catalysts. The melting point of metal nanoparticles is size dependent. For example, 2 to 3-nm gold nanoparticles can produce SiO_xNW at 500°C [79].

For larger gold nanoparticles, the reaction temperatures are higher, and the diameters of the SiO_xNW are bigger [55]. For transition metal nanoparticles of medium sizes (10 to 50 nm), the lowering of the melting temperature due to the size effect may not be significant, and growth temperatures are generally close to the eutectic temperatures of their respective alloys with Si. When Si in Au nanoparticles becomes supersaturated, it will precipitate out.

For small size nanoparticles (<100 nm), the interactions between Au nanoparticles and the Si substrate may not be strong enough to hold the nanoparticles onto the Si surface, as results have shown that these nanoparticles are at the tip of SiO_xNW . The precipitation of Si then pushes the nanoparticles in the opposite direction to the growth

LITERATURE REVIEW OF SILICON OXIDE AND SILICON CARBIDE NANOSTRUCTURES

of the SiO_xNW , resulting in tip growth. This may be why small nanoparticles are usually involved in tip growth. When nanoparticles are larger, the growth rate is slower and the interaction between nanoparticles and the substrate is stronger, and most likely the growth of nanowires will not cause the nanoparticles to move. Most of the results on SiNW have shown tip growth, and they often yield 15-nm diameter nanowires.

Due to the presence of gold metal catalyst in the VLS growth, the geometry and atomic structure of the interface between the metal catalyst and the nanowire have been found to be very critical to the nanowire growth and formation of defects, particularly the growth direction or crystal orientation in ultrathin nanowires.

(ii) Solid Liquid Solid Growth Mechanism

On the other hand, the work by Yan et al. [50] and Jin et al. [52] using silicon wafers and Ni as catalysts have suggested that bulk silicon would diffuse through the nanoparticles to produce SiO_xNW . In this case, solid silicon in the wafer reacts with Ni catalysts to directly make SiO_xNW . If this is true, it falls into the category of root growth. However, the use of hydrogen in the presence of metal catalysts may activate a new reaction pathway that converts Si in the substrate into silane. As a result, the suggested solid–liquid–solid (SLS) [80, 81] model may actually be the VLS model at work.

The SLS mechanism was successfully used to explain the formation of SiO_xNWs from silicon–metal alloy droplets [82]. On the base of SLS and vapor–liquid–solid (VLS) mechanisms, a growth model is given.

During CVD process, the temperatures of silicon–metal alloy droplets can be divided into several ranges, as shown in Fig. 2.14. The temperature in the interface range is highest and that in the top range is lowest. From the bottom to the top of a droplet, the

LITERATURE REVIEW OF SILICON OXIDE AND SILICON CARBIDE NANOSTRUCTURES

temperature decreases gradually ($a \rightarrow b \rightarrow c \rightarrow d \rightarrow e \rightarrow f$). Therefore, the saturation concentration of silicon in the alloy decreases also gradually from bottom to top. At the top of the droplet, the temperature is lowest and saturation concentration is lowest. In the beginning of SiNW formation, the top region (f) reaches supersaturation at first and Si atoms are precipitated out of the droplet to upward side. Then, silicon concentration in the region (f) becomes under-saturated so that Si atoms transfer from the region (e) into the region (f) because of the concentration gradient. Finally, Si atoms originate from the silicon substrate and continually transfer to the top from the bottom ($a \rightarrow b \rightarrow c \rightarrow d \rightarrow e \rightarrow f$) to precipitate there. Therefore, SiNWs grow upward from the center of the top but not from other directions, see Fig. 214. (B).

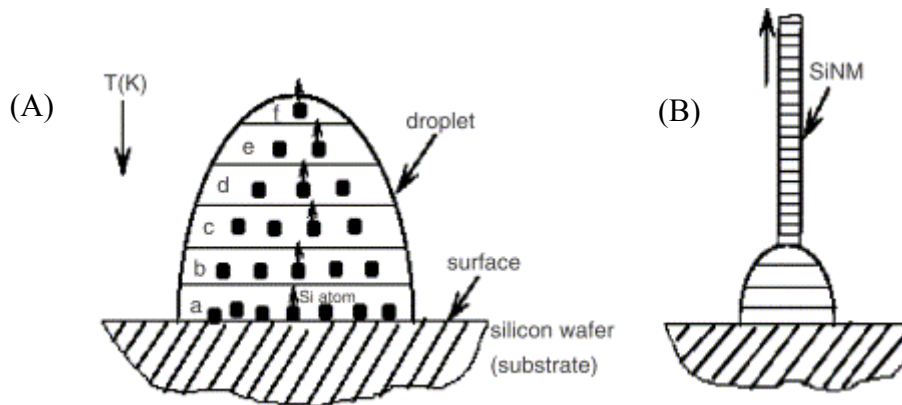


Figure 2.14 Sketch graph of the temperature gradient (TEMPGRAD) growth model of (A) droplet and (B) the evolving nanowire.

(iii) Vapour - Solid Growth Mechanism

Without the aid of metal catalysts, the vapour–solid (VS) growth has been mainly used to synthesize metal oxide and some semiconductor nanomaterials. It is often called self catalytic growth since the nanostructures grow directly from vapor phases. Plausible growth mechanisms such as the anisotropic growth, defect-induced growth (e.g., through a screw dislocation), and self-catalytic growth have been suggested based on

LITERATURE REVIEW OF SILICON OXIDE AND SILICON CARBIDE NANOSTRUCTURES

electron microscopy studies, According to the classical theories of crystal growth from liquid or vapour phases, the growth fronts play a crucial role for the deposition of atoms. There are two kinds of microscopic surfaces: (1) rough surfaces on which atoms of about several layers are not well arranged. Deposition of atoms is relatively easy compared to a flat surface and crystal growth can continue if enough source atoms are continuously provided; (2) atomically flat surfaces on which atoms are well arranged. Atoms from the source have a weak bonding with flat surfaces and can easily return to the liquid/vapour phase.

Atoms deposition occurs only on the atomic steps. There are three ways to generate atomic steps on a flat surface: (1) nucleation of new two-dimensional islands which is difficult because the nucleation barrier is high, and there is almost no super-cooling. The islands will be exhausted eventually (see Fig. 2.15(a)); (2) screw dislocations which generate atomic steps to help atoms to deposit continuously (Fig. 2.15(b)); and (3) twining structures which contain ditches at the cross of two grain surfaces. Atoms deposit at the ditches resulting in atomic steps along twining surfaces. The resulting growth can be continuous along the direction of the twining plane (Fig. 2.15(c)).

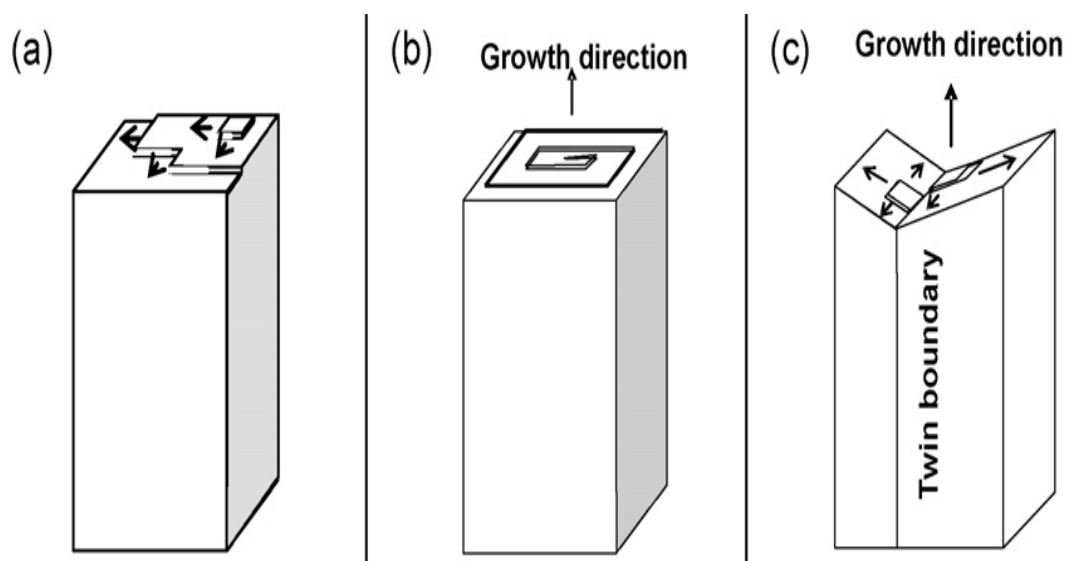


Figure 2.15 Schematic diagram of (a) Nanorods formed due to anisotropic growth of crystals. (b) Unidirectional growth of single crystals due to screw dislocation. (c) Growth induced by twining.

LITERATURE REVIEW OF SILICON OXIDE AND SILICON CARBIDE NANOSTRUCTURES

Followings are important factors for the nanocrystal growth in the VS process. Because of anisotropic properties of different surfaces in a crystal, such as the preferential reactivity and binding of gas reactants on specific surfaces and all crystals tend to minimize their total surface energy, rod- or wire-like shapes are frequently resulted. Screw dislocations (the well known Burton–Cabrera–Frank theory) are known to significantly enhance the crystal growth of metals and some molecular materials [83].

This classical mechanism is based on the fact that the growth of a crystal proceeds by adding atoms at the kink sites of a surface step. Kink sites always exist on the steps even at the thermal equilibrium state. Due to the advance of the kink along the surface by the addition of atoms, the crystal grows perpendicularly to the surface. In thermal equilibrium state, a perfect crystal should eventually contain no surface steps. Then, the growth of a perfect crystal depends on the nucleation of surface steps. For the growth of a real crystal, however, the growth rate is much faster than that predicted for a perfect crystal because real crystals contain defects, e.g., dislocations and twins.

A dislocation cannot terminate inside a perfect crystal. They can terminate on a defect inside the crystal or on a surface. If a dislocation ends on a surface and its Burgers vector has a component normal to the surface (the screw component), a step forms starting from the emerging point of the dislocation. Leading by the dislocation, steps can winds into a spiral, and the growth of the crystal is largely enhanced without the need of nucleation for fresh surface steps.

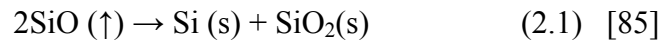
There are many reasons for the formation of a dislocation in a crystal. For Si nanowires, oxygen atoms may cause the nucleation of a dislocation [84]. Thus it is clear that the VLS model can enable either tip or root growth mechanisms, whereas the solid–liquid–solid model only applies to the root growth mechanism. The amount of diffused silicon atoms absorb from the substrate by molten Au-Si alloy will be reduced as the alloy

LITERATURE REVIEW OF SILICON OXIDE AND SILICON CARBIDE NANOSTRUCTURES

reached the equilibrium stage. Therefore, the SLS mechanism still poorly understood because, there are no chemical forces responsible for the growth of SiNWs after the alloy reaching the equilibrium stage or saturated. The SLS and oxygen assisted growth mechanisms were used to explain the non catalytic growth of the SiO_x and SiC nanostructures.

(iv) Solid - Vapour – Liquid - Solid Growth Mechanism

Other mechanisms have also been proposed. For example, SiO has been used to produce SiNW. In this case, disproportionation reactions between SiO nanoparticles produce Si and SiO_2 nanoparticles. These nanoparticles then coalesce to form SiO_xNW . SiO powders were also used as Si sources. During the evaporation at 1100°C , SiO vapour was continually generated and was then transported by the flowing Ar to the relatively low temperature region ($900\text{--}1000^\circ\text{C}$) to decompose on substrates as follows:



This gives rise for Solid-Vapour-Liquid-Solid (SVLS) mechanism, which was suggested by Bahloul et al [86]. SVLS is similar to VLS mechanism, but differs in the starting phase of silicon whether it is solid or vapour. Therefore, silicon (feedstock) may come from either solid substrate or SiO gas or both of them. This study concentrated on the thermodynamic of the Au-Si-O systems and it showed the possibility of forming the SiO in gas phase when the substrate heated $>1100^\circ\text{C}$. A schematic diagram in Fig. 2.16 shows all three growth mechanisms.

LITERATURE REVIEW OF SILICON OXIDE AND SILICON CARBIDE NANOSTRUCTURES

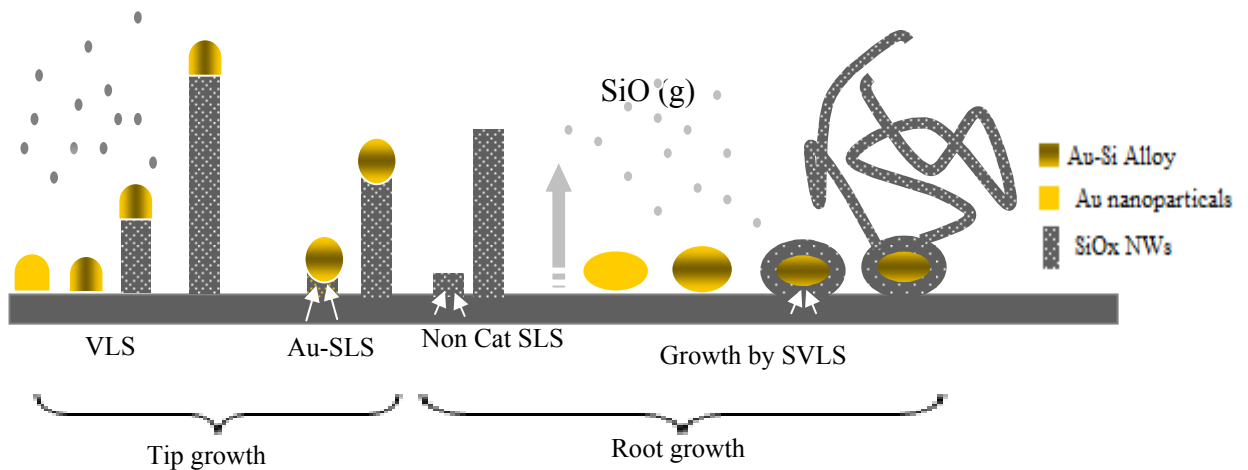


Figure 2.16 Schematic diagram of VLS, SLS and SVLS mechanisms for tip and root growth.

It has been shown that the nanometric decreases the melting point of pure Au and Si and more generally the liquid's temperatures. Moreover, the presence of SiO in the gaseous phase is a necessary but not sufficient condition for the formation of nanowires. The nanowires growth cannot be explained by the modification of the Au-Si phase diagram with the size of the particles, neither by the presence of SiO, but by the existence of a metastable equilibrium involving the silicon of the wafer, the deposit of vitreous silica and supersaturated SiO in the gaseous phase [86]. Therefore in our study, the SVLS mechanism will be used as the main mechanism to explain the growth of the obtained nanostructures in our results.

(v) Carbothermal Reactions

The carbothermal reduction process has been employed to synthesize nanowires of functional oxides such as ZnO [87, 88]. Interestingly, in an effort to grow ZnO and MgO nanowires via carbothermal reduction of ZnO and MgO powders, respectively, the accidental formation of SiO_xNWs on Au-coated Si substrate was observed and no SiO_xNWs were grown without introducing those powders [24]. However, with the carbothermal reduction of WO₃ powders crystalline core-shell Si-SiO_x nanowires

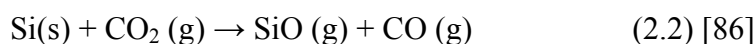
LITERATURE REVIEW OF SILICON OXIDE AND SILICON CARBIDE NANOSTRUCTURES

instead of SiONWs were grown, and conversely SiO_xNWs were grown without using WO₃/carbon powders [89].

The proposed mechanisms for the growth of SiO_xNWs via carbothermal reduction of WO₃ and ZnO powders are quite different even though in both mechanisms it is indicated that the generation of CO plays an important role in forming core-shell Si-SiO_x nanowires and SiO_xNWs, respectively. As a consequence, viable mechanisms for the growth of SiO_xNWs via carbothermal reduction of metal oxide powders remain to be explored.

The CuO powders can be reduced to Cu and CO₂ by carbon at temperatures higher than 600 °C [90]. It is known that CO₂ acts as an oxidant in the growth of SiO_xNWs [91]. Zhu et al. have reported the formation of SiO₂ nanoflowers by mixing SiC and cobalt powders when heated to 1500°C. They used a graphite heater, and concluded that the CO liberated from the graphite heater played an important role. They demonstrated that SiO₂ nanowires can be grown successfully by the direct flow of CO gas (mixed with Ar) into the chamber [92].

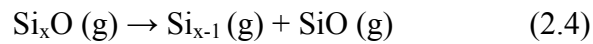
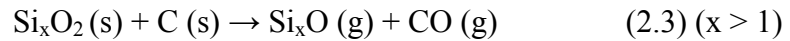
Carter et al. [61] also showed crystalline SiO₂ nanofibers grown from the Ni-Si and Co-Si alloy surface by exposing the alloys to Ar/CO₂ and Ar/CO/CO₂ gases at 1130°C. They proposed that CO₂, not O₂, nor CO, was the decisive factor for the growth through the following reaction.



The formation of SiO gas make both SVLS and the carbothermal work to accomplish the growth of SiO_x nanowires. Saulig-Wenger et al. have reported the synthesis of amorphous silicon dioxide nanowires with the presence of graphite in the furnace [91]. The source materials were Si powder (no Au), the Ar: O₂ carrier gas ratio was 99.2 mol %:0.8 mol %, and the growth temperature was 1200 °C. They found the

LITERATURE REVIEW OF SILICON OXIDE AND SILICON CARBIDE NANOSTRUCTURES

relative O₂ flow rate played a very important role in the formation of the nanowires: having either no O₂ or a large amount of O₂ did actually hinder the nanowire growth. They postulated a nanowire growth mechanism similar to that of Carter et al. The majority of SiO_x nanowire fabrication methods are catalyst-based methods, only a few papers have been devoted to the non-catalyst-based method [39, 93, and 94], among those, the carbon-assisted SiO_x nanowire growth methods [24, 61, 95, and 96] are particularly of our interest. Li et al. [24] have reported the graphite-assisted SiO_x nanowire growth on Au-coated Si substrate. Zhu et al. [96] have demonstrated that SiO₂ nanowires can be grown successfully by the direct flow of CO gas (mixed with Ar) into the chamber. They used a graphite heater and concluded that the CO liberated from the graphite played an important role. Karine et al. [95] have reported the synthesis of amorphous SiO₂ nanowires with the presence of graphite. During the RTP process at 1200°C, first, CO₂ is formed by the reaction of residue O₂ with the sp² structured carbon at grain boundaries and reacts with silicon substrates to form silicon oxide SiO (g). As Gundiah et al. [97] proposed the growth mechanism of SiNWs stated in the equations below contributed a great deal in understanding the growth process. The oxide layer is generally covered the silicon substrate may be reduced to silicon monoxide by action of carbon through the following reaction:



But S. H. Li et al. demonstrated that CO (g) played more important than CO₂ on the reactions involving the formation of precipitating Si solid atoms [24]. Initially, we tried to grow titanium dioxide nanowires by using a mixture of graphite and TiO₂ powders at 1200°C but suddenly we obtained, as reveals in chapter 4 with details. In the present study, the growth of SiO_xNWs as functions of the carbon concentration in TiO₂/carbon

LITERATURE REVIEW OF SILICON OXIDE AND SILICON CARBIDE NANOSTRUCTURES

powders was studied. From these results, viable mechanisms for the growth of SiO_xNWs via carbothermal reduction of metal oxide powders can be elucidated.

(vi) Oxygen Assisted Growth

Wang et al. [98-100] reported that SiO_2 largely enhanced Si nanowire growth (Fig. 2.17(a)). A model called oxide-assisted growth (OAG) was therefore proposed with evidence from experiments not only on Si but also on Ge [101] and III-V [102-104] semiconductor nanowire growth. As shown in Fig. 2.17(b), the presence of SiO_2 in the source significantly increases the yield of Si nanowire product. The Si nanowire product obtained using a powder source composed of 50% SiO_2 and 50% Si is 30 times larger than the amount generated by using a metal-containing target [98].

The (OAG) reaction is special because no metal elements or catalysts are involved either in the source materials or the nanowire itself. The starting material is oxide and the nanowires are in non-oxide form. In OAG using SiO , the nanowires are pure Si (not Si-oxide), and Si itself does not have a self-catalyst effect. This means that Si nanowires are formed by the assistance of Si-oxide.

The OAG model has been tested by a simple experiment [105], which was carried out by simply sealing highly pure SiO powder or a mixture of Si and SiO_2 (1:1, Si reacts with SiO_2 to form SiO or Si_xO ($x > 1$) vapour phase) in an evacuated quartz tube and then inserting the tube into a preheated furnace (1250–1300 °C).

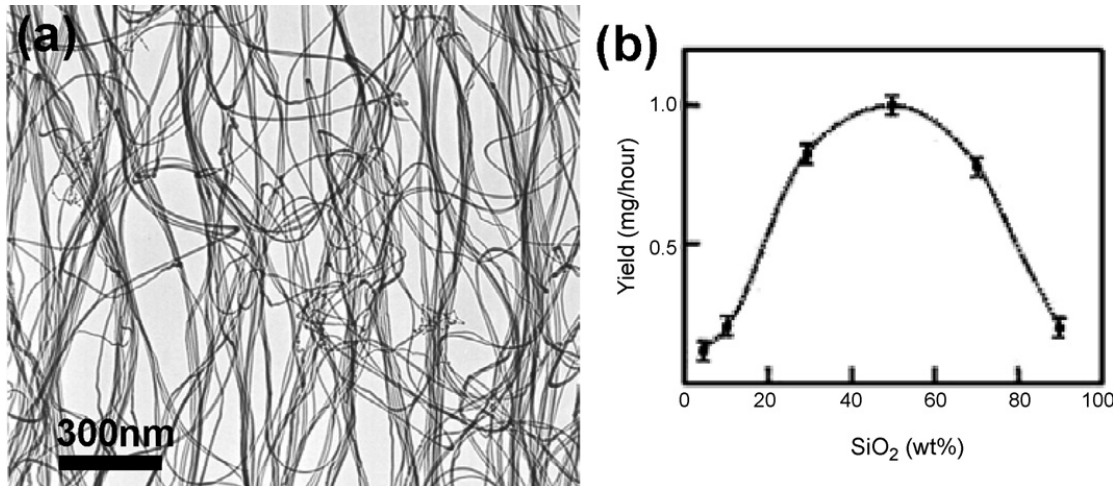


Figure. 2.17 TEM of (a) Si nanowires synthesized by oxide-assisted growth. (b) Yield of Si nanowires vs. the percentage of SiO₂ in the target [98].

Studies show that high quality silicon nanowires could be produced by an oxide-assisted growth (OAG) approach [106, 107]. It has been proven that at the initial nucleation stage, silicon oxide vapour condensed on the substrate and formed Si nanoparticles. Each Si nanowire nucleus consists of a polycrystalline Si core containing a high density of defects and a silicon oxide shell. Compared to the VLS mechanism, the nucleation and growth of Si nanowires from the oxide-assisted mechanism appears to be novel. The oxide-assisted nanowire growth is described by reactions (2.1) and (2.4). The vapour phase of SiO and Si_xO ($x > 1$) generated by the thermal effect is the key factor. Silicon oxide clusters generated and present in the gas phase in Si nanowire synthesis play an important role in the nucleation and growth. The catalytic effect of the Si_xO ($x > 1$) layers on the nanowire tips is an important driving force for the nanowire growth. Among the number of different forms of Si sub-oxides, some of them are very reactive. The materials at the Si nanowire tips (similar to the case of nanoparticles) may be in or near their molten states. This is because that the surface melting temperatures of nanoparticles can be much lower than that of their bulk materials. The atomic absorption, diffusion, and reaction are thus largely enhanced at the tips. They act as the

LITERATURE REVIEW OF SILICON OXIDE AND SILICON CARBIDE NANOSTRUCTURES

nuclei to absorb reactive silicon oxide clusters and facilitate the formation of the Si nanowires with a certain crystalline orientation. The schematic diagrams on Fig.2.18 describe the formation of Si or SiO_x nanowires. In (a) silicon monoxide vapour is deposited first and forms the matrix within which the Si nanoparticles are precipitated. Then, the nanoparticles in a preferred orientation grow to form nanowires.

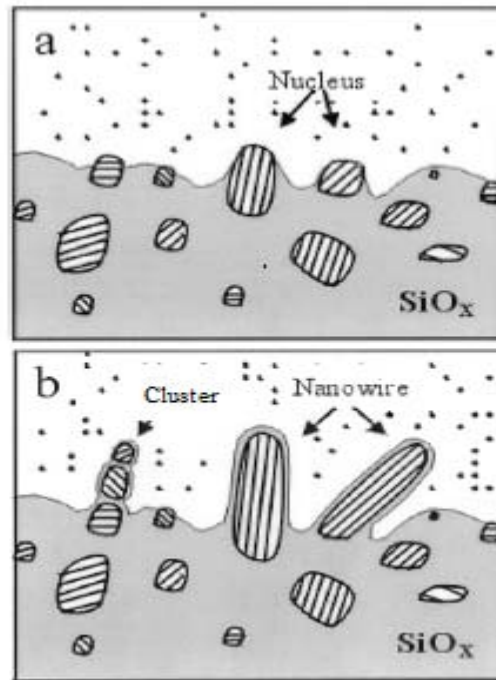


Figure 2.18 Oxygen assisted growth mechanism [108].

We can conclude that the catalytic VLS method offers better control of diameter and patterning of SiO_x NWs but relatively low yield of production; whereas the OAG method can produce SiO_x NWs in large quantities and without metal contamination, but with less control in wire pattern and diameter. Recently, SiO_x NWs have been grown by combining the OAG method and metal catalysts.

2.2.6 Morphology of Silicon Oxides Nanostructures.

The overall diameters of silicon oxide nanowires produced so far range from 3 nm to 100 nm, and many methods have yielded a frequently occurring diameter of 15 nm when they are made between the temperature of 1100°C and 1200°C. This size of nanowires, as speculated at the end of this chapter, may be determined by the selected growth temperature. Pure silicon nanowires can be made when the nanowires are reduced by hydrogen while growing. However, it has been shown that these pure Si nanowires are generally more difficult to make or preserve because Si in those nanowires is readily oxidized in air. Therefore, Si nanowires are normally covered with SiO₂. Under special conditions, SiO_x ($x < 2$) nanowires can be made. SiNWs (made of silicon, silicon-covered with silica, or silica) can be either crystalline or amorphous.

The interaction of silicon and metal catalysts, the evolution of silicon precipitating out of the catalysts, and the reactions followed the precipitation determine the morphology and crystallinity of SiNWs. In many cases, SiNWs have been observed with a silicon core covered with an amorphous silicon dioxide sheath.

The crystalline core can make SiNWs either fairly straight, or coiled or curly. It was discovered that CH₄ may affect the helicity. This may be caused by a more complicated phase diagram that involves carbon, silicon, and metal.

Other morphologies have also been made and observed for SiNWs. Although straight nanowires dominate, other forms such as string beans (strings of pearls), shells, cones, nanoflowers, and elongated volcanoes have been reported [109]. Coiled nanowires represent another category, and have been reported by several groups [110, 111]. Milligram quantity SiNWs have been obtained, although no stand-alone materials have been generated for easy handling. In general, nanowires so produced are attached to the substrate, and removal has been difficult or nearly impossible due to the small quantities

LITERATURE REVIEW OF SILICON OXIDE AND SILICON CARBIDE NANOSTRUCTURES

available. For different experimental conditions different morphologies than just a wire have been synthesized.

Various silica morphologies, such as carrot-shaped rods whose walls are composed of highly aligned silica nanowires, with diameters in the range of 15–30 nm and lengths of 10–40 μm , as well as comet-like structures composed of highly oriented silica nanowires, with diameters of 50–100 nm and lengths of 10–50 μm were thus formed. A variety of silica nanostructures consisting of nanowire bundles and brush-like arrays, as shown have been prepared by heating equimolar mixtures of Si/SiO₂ in argon/nitrogen atmospheres at about 1400 °C for 12 h [111].

Another simple route has been developed for the synthesis of SiO_x nanoflowers and Si or SiC nanowires wrapped in SiO_x sheaths [112]. These materials are produced by heating SiC under CO in the presence of fine Co or Fe powders, or ferrocene at a temperature of ~1500 °C. The different types of nanostructures are formed due to the presence of different catalysts. Amorphous SiO_x nanowires have also been synthesized on a Si substrate, by the vapor transport reaction using pure silicon powder as the Si source in the presence of a Au catalyst, under a constant flow of Ar/O₂ at 1100 °C by the VLS growth mechanism [113]. The nanowires have a uniform diameter of about 20 nm and lengths up to several tens of micrometers.

2.2.7 Photoluminescence of Silicon Oxide Nanowires

Photoluminescence (PL) analysis is a powerful tool in the characterization of surfaces and interfaces. Although a number of experimental techniques can provide detailed mechanical information about interfaces, the optoelectronics industry that drives most interface investigations is ultimately concerned with optical and electronic properties. The PL signal is characterized by three essential features: energy, intensity, and polarization. Because PL is the result of optical transitions between electronic states, the PL spectrum gives precise information on the energy levels available to electrons in the material. As dimensions are decreased the physical properties of a semiconductor are changed from that of bulk material. Below are a few examples of physical properties that change when dimensions are decreased. Some of these properties can be used in various applications and some simply need to be taken into account as one move into the nano regime. As bulk silicon is reduced to nano dimensions the band gap changes according to

$$E_G = E_G (\text{bulk}) + \pi^2 \hbar^2 / 2m \square (n_x^2 / L_x^2 + n_y^2 / L_y^2 + n_z^2 / L_z^2) (1/m_e + 1/m_h) \quad (2.16)$$

The symbols and letters used in equation 2.1.6 are E_G which is the calculated band gap of the nanostructures, E_{bulk} is the band gap of bulk silicon, m_h , m_e are the hole and electron masses, n_x , n_y , n_z are the state occupation numbers and L_x , L_y , L_z are the lengths for the x, y and z directions respectively. This formula represents an effective mass approximation solving the Schrödinger equation in three dimensions. As can be seen in the formula the effect of decreased nanostructures dimensions increases or widens the energy band gap of these nanostructures. This effect can be used for instance in photonics to tune the band gap for various applications. For nanowires this effect becomes prominent as dimensions reach sub 5 nm and is therefore of no concern in this work.

LITERATURE REVIEW OF SILICON OXIDE AND SILICON CARBIDE NANOSTRUCTURES

The photoluminescence (PL) is the spontaneous emission of light from a material under optical excitation. PL emission wavelength is determined by the gap between two energy levels. The band gap is the sum of interatomic potentials that depends on the atomic separations and quantity of charge of the neighbouring atoms.

The width of the band gap depends on the crystal field or size and reaction repopulate, valence band electrons. The crystal size depends upon increasing its surface to volume ratio and surface bond contraction. Therefore, the PL depends on the shape of the nanostructures particle size, chemical treatment process, mechanism of quantum confinement effect, PL centre formation and surface alloying.

A shorter bond length and positively charged ions enhanced the crystal field and also the band gap. Reactions also enhanced the crystal field due to charge transfer. The process of charge transfer widens the band gap directly by emptying the occupied density of state (DOS) below E_f . It has been shown that electronegative elements such as oxygen and nitrogen possess the special ability to widen the band gap by producing the holes below E_f through charge transportation during bond formation. There are three factors control the PL intensity: the PL efficiency, particle density and size distribution.

Silicon is an indirect band gap semiconductor (~ 1.1 eV), making it a poor light emitter. The development of efficient light-emitting silicon devices could enable optical interconnects on a new generation of chips, and extends the use of Si technology from electronics into optoelectronics. Towards this goal, efficient room temperature photoluminescence (PL) has been observed in porous silicon and silicon wires, and since the early '90s much effort has been put into understanding and controlling the PL observed in such nanoscale silicon structures. Many approaches have been taken to produce Si nanowires, ranging from laser ablation methods to solution techniques. These generally produce wires with an oxide sheath surrounding a crystalline Si core.

LITERATURE REVIEW OF SILICON OXIDE AND SILICON CARBIDE NANOSTRUCTURES

The PL emission energy increases with decreasing wire diameter, ranging from about 1 eV up towards 4 eV in the narrowest wires. These nanowires possess very intense photoluminescence (PL) due to oxygen vacancies compared to that of pure SiO₂. In contrast, crystalline silicon nanowires possess little PL because silicon has an indirect band gap. Although amorphous Si nanowires in principle should photoluminesce, no direct evidence is available yet. The influence of ionizing radiation on optical properties of amorphous-SiO₂ (silica) is a timely research field strongly motivated by the large use of silica materials in many technologies requiring a good maintenance of transparency (e.g. fibers, laser optics and radioactive environments) [114, 115].

A huge number of works over the last decades have illustrated that irradiation induces intrinsic defects (dangling bonds, oxygen-deficiency or oxygen-excess) which cause optical transitions of absorption (OA) and photoluminescence (PL) (see review papers by Griscom [116] and Skuja et al. [117]). Owing to the complexity of OA and PL spectra over a wide range extending from visible to vacuum-ultraviolet (UV), the identification of defects and the assignment of the optical bands to their electronic structure remains a still incompletely solved problem. One of the most controversial aspects regards the optical transitions associated with the paramagnetic non-bridging oxygen hole center (NBOHC) whose structure is identified by its paramagnetic properties and is denoted by $\equiv\text{Si-O}\bullet$ [118]; (\equiv) stands for bonds with three oxygen and (\bullet) indicates an unpaired electron.

The red weak emission of SiO_x NWs was reported [98], which arises because of nonbridging oxygen hole centres (NBOHCs, $\equiv\text{Si-O}\bullet$) [119]. Unlike bulk Silica, silicon oxide nanostructures have very large surface to volume ratio, which allow the molecules (oxygen, hydrogen, hydroxide and water) to be adsorb, and diffuse to SiO_x nanowires during growth process as well as when the sample exposed to air. There are two radicals

LITERATURE REVIEW OF SILICON OXIDE AND SILICON CARBIDE NANOSTRUCTURES

that may form intrinsic defects:

1- The hydroxyl radicals $\equiv\text{Si}-\text{O}-\text{H}$

2- The peroxy linkage $\equiv\text{Si}-\text{O}-\text{O}-\text{Si}\equiv$ [120]

These intrinsic defects may change (NBOHCs, $\equiv\text{Si}-\text{O}\bullet$) to be new oxygen centres ($\equiv\text{Si}\bullet + \text{O}\cdot$) due to the high-energy photon excitation (3.8 eV used in our PL measurement).

Then, the red emission start to degrade and stabilize, which is consistent with observations on bulk crystalline and amorphous SiO_2 [121]. The emission of the blue light (2.6 eV – 2.8 eV) has been suggested due to oxygen deficient centres (ODCs) such as neutral oxygen vacancies, $\equiv\text{Si}-\text{Si}\equiv$, and some intrinsic diamagnetic defect centres, such as the twofold coordinated silicon lone pair centres ($=\text{Si}$: i.e. $\equiv\text{Si}-\text{O}-\text{Si}-\text{O}-\text{Si}\equiv$) and self trapped excitons (STEs) [122,123].

Nishikawa et al [123] observed several bands in various types of high purity silica glass, with different peak energies ranging from 1.9 to 4.3 eV under 7.9 eV excitation. It was revealed that the 2.7 eV band was ascribable to the neutral oxygen vacancy ($\equiv\text{Si}-\text{Si}\equiv$), while the 3.1 eV band corresponded to twofold-coordinated silicon lone-pair centres ($\text{O}-\text{Si}-\text{O}$). As radiative recombination centres, these structure defects were due to the oxygen deficiency of the SiO_x sample. Therefore, it is reasonable to believe that the blue emission from the SiO_x nanowire arrays can be attributed to the above mentioned defect centres [123].

Detailed photoluminescence measurements at room temperature revealed that the a-SiNW film emitted blue-green light, peaked at 445 and 480 nm, respectively. According to our recent work on the physical origin of the full visible-band light emission from crystalline Si nanowires [124], however, such a photoluminescence from the a-SiNWs was ascribed as arising from defect centers in the amorphous SiO_x layer sheathing the nanowires as well. The silicon nanowires are interesting to evaluate the

LITERATURE REVIEW OF SILICON OXIDE AND SILICON CARBIDE NANOSTRUCTURES

quantum confinement effect related to low dimensionality [124]. A-SiNWs grown on substrate have a remarkable surface/volume ratio, possibly showing physical-chemical properties completely different from the bulk.

In fact, it was recently revealed that the lithium battery using silicon nanowires as material for electrodes showed a capacity as high as 8 times that of the ordinary material [125, 126]. UV light emission with a wavelength around 360–370 nm from porous silicon prepared by high temperature oxidation has been reported [127], and it was believed that the UV light emission occurred in the luminescence centres in silicon oxide. Kanashima et al [128] reported that photoluminescence peaks at 3.4 -3.5 eV for the silicon oxide film were observed. In addition, there exist a large quantity of different types of unsaturated bond in the large volume fraction interface in the nanostructures, which produce some defect energy level in the energy gap, and cause some new luminescence bands. These characteristics are important because they help define both applications and methods of characterization of these nanowires.

2.3 Fabrication of beta-Silicon carbide nanowires

2.3.1 Introduction

Silicon carbide (SiC) is the only chemical compound of carbon and silicon. It was originally produced by a high temperature electro-chemical reaction of sand and carbon. SiC is one of the most important materials for industrial application and basic research, and has been applied in many areas, from cutting tools to nanoscale electrical devices.

Silicon carbide has very unique properties, such as large band gap, excellent thermal conductivity, chemical inertness, high electron mobility, and biocompatibility, which promise well for applications in microelectronics and optoelectronics and have thus attracted much interest from the materials and devices communities[129-131]. In particular, silicon carbide nanowires are expected for the reinforcement of various nanocomposite materials or as nanocontacts in harsh environment, due mainly to their super mechanical properties and high electrical conductance. Research on silicon carbide 1D nanowires would be highlighted both from the fundamental research standpoint and for what concerns the potential application in nanodevices and nanocomposites. In this study, to produce SiC nanowires, we used a simple method to directly fabricate 1D SiC nanostructures from carbon powder at relative low temperature without catalyst. We also reveal how the temperature and rapid heating rate affect properties of the final product.

However, SiC may exist in the form of numerous of polytypes. More than 170 different polytypes have been identified [132]. The most common polytypes are 3C-SiC, 2H-SiC, 4H-SiC, and 6H-SiC, and their parameters are listed in Table 2.1.

LITERATURE REVIEW OF SILICON OXIDE AND SILICON CARBIDE NANOSTRUCTURES

Table 2.1 Parameters of unit cells of 3C-SiC, 2H-SiC, 4H-SiC, 6H-SiC.

	Cell Parameters						System
	a	b	c	α	β	γ	
6H-SiC	3.073Å	3.073Å	15.080Å	90	90	90	Hexagonal
4H-SiC	3.081Å	3.081Å	10.061Å	90	90	90	Cubic
3C-SiC	4.3589Å	4.3589Å	5.031Å	90	90	90	Hexagonal
2H-SiC	3.081Å	3.081Å	4.3589Å	90	90	90	Hexagonal

In polytype notation system, the first number denotes the periodicity and the following letters C or H refer to cubic and hexagonal structures, respectively. 3C-SiC is referred to β -SiC, and all other polytypes are notated as α -SiC.

In 1824 Jöns Jacob Berzelius reported the first observation of SiC [133]. However, only after the invention of electric smelting furnace and its application to produce some carbonaceous compounds, the attention started to be attracted onto the production of SiC material [134, 135]. Initially SiC was used as hard material substituting diamond to produce cutting, drilling and polishing tools. Shortly afterwards the interests in electronic properties of SiC came into focus. Today SiC is a fascinating semiconductor that can be operated in harsh environments [136].

SiC nanorods were first synthesized successfully in 1995, in the process in which carbon nanotubes were converted to SiC nanorods by reaction with SiO vapour [137].

Subsequently, a number of methods of synthesis of 1D SiC nanostructures have been developed.

2.3.2 Structure of β -SiC crystal

Silicon carbide occurs in many different crystal structures, called polytypes. Despite the fact that all SiC polytypes consist of carbon atoms covalently bonded with equal numbers of silicon atoms, each SiC polytype has its own distinct set of electrical semiconductor properties. While there are more than 100 known polytypes of SiC, only two of them are presently grown and commercially available in forms acceptable for the use as an electronic semiconductor. Both of them, denoted 4H-SiC and 6H-SiC, have hexagonal crystal structure. Another polytype, denoted 3C-SiC or beta silicon carbide (β -SiC) has cubic crystal structure and, with respect to use in electronic devices, offers significant benefits over conventional hexagonal SiC polytypes. Beta silicon carbide is considered an attractive candidate window material for adverse environments, due to its isotropic properties, i.e. cubic structure, low mass density and thermal expansion, high-thermal conductivity and flexural strength, thermal shock resistance, oxidation and rain erosion resistance potential [138]. The β -SiC structure is shown in Fig 2.19.

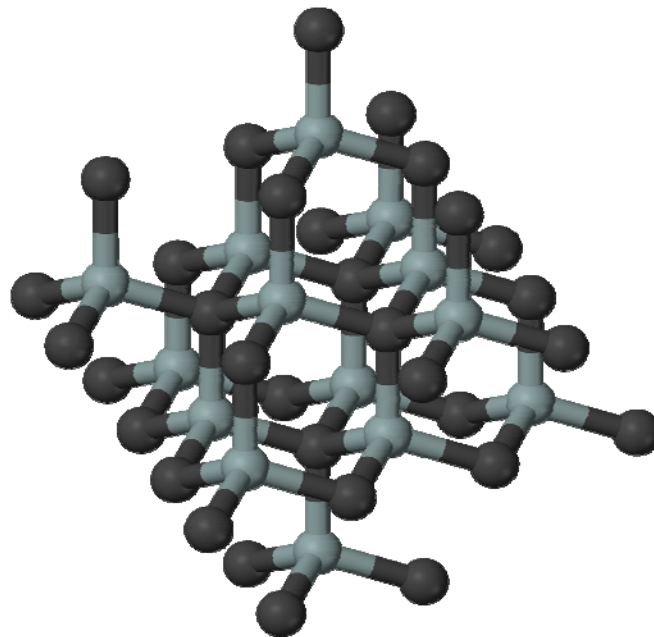


Figure 2.19 Beta type of Silicon carbide crystal structure.

2.3.3 β -SiC Nanowires Properties

Silicon carbide is not attacked by any acids or alkalis or molten salts up to 800°C. In air, SiC forms a protective silicon oxide coating at 1200°C and is able to be used up to 1600°C. The high thermal conductivity coupled with low thermal expansion and high strength gives this material exceptional thermal shock resistant qualities.

Silicon carbide ceramics with little or no grain boundary impurities maintain their strength to very high temperatures, approaching 1600°C with no strength loss. Chemical purity, resistance to chemical attack at temperature, and strength retention at high temperatures has made this material very popular as wafer tray supports and paddles in semiconductor furnaces.

The electrical conduction of the material has lead to its use in resistance heating elements for electric furnaces, and as a key component in thermistors (temperature variable resistors) and in varistors (voltage variable resistors) [139].

As a wide band gap semiconducting material, silicon carbide (SiC) exhibits many excellent properties for high temperature, high frequency and high power applications [140]. SiC 1D nanostructures have shown many outstanding performances except for excellent mechanical properties. It can be used in field emission display, nanosensors and nanoscale electro-devices [141–144]. The chemical and mechanical properties are listed in table 2.2.

LITERATURE REVIEW OF SILICON OXIDE AND SILICON CARBIDE NANOSTRUCTURES

Table 2.2 Chemical and mechanical properties of β -SiC [10]

Properties	
Molecular formula	SiC
Molar mass	40.097 g/mol
Appearance	black-green odourless powder
Density	3.22 g/cm ³ , solid
Melting point	2730°C
Thermal Conductivity	120 W/m•°K
Coefficient of Thermal Expansion	4.0 10 ⁻⁶ /°C
Specific Heat	750 J/kg•K

2.3.4 Synthesis Methods and growth mechanisms of β -SiC nanowires

Thus, in the last few years, much effort has been made to the synthesis of 1D SiC nanostructures. Several techniques were demonstrated, including carbon nanotubes-confined growth [145], chemical vapor deposition (CVD) [146–148], carbo-thermal reduction [1149, 150], polymeric precursor pyrolysis method [151], etc. However, most of these synthetic approaches involved complex processes and manipulation. The usage of metal catalyst for the vapor–liquid–solid growth mechanism makes it difficult to remove the resident catalyst after the synthetic process.

SiCNWs were synthesized at 900 °C by the laser ablation of a SiC target, by means of the VLS growth mechanism, [152]. Bulk quantities of β -SiC nanowires have been produced from a mixture of activated carbon and sol-gel derived silica embedded with Fe nanoparticles [153]. The nanowires consist of a 10–30 nm diameter single-crystalline core wrapped with an amorphous silicon oxide layer, and have lengths up to several tens of microns. Reaction of SiO vapor, generated by the reduction of silica, with CNTs

LITERATURE REVIEW OF SILICON OXIDE AND SILICON CARBIDE NANOSTRUCTURES

forms SiC nanowires [154]. Heating a mixture of SiC powder and Al catalyst at 1700 °C in Ar produces SiC nanowires by the VLS growth mechanism [155]. These had diameters in the range of 10–50 nm and lengths in the 1–2 millilitres range. Nanojunctions of SiC were obtained by a similar procedure [156]. The SiC core had a diameter between 10 and 40 nm (with a helical periodicity of 40 to 80 nm) and was covered by a uniform layer of 30–60 nm thick amorphous silica.

The VLS process has been used to synthesize BN-coated β -SiC nanowires [157]. β -SiC nanowires have been grown by the thermal treatment of commercial Si particles disposed in a graphite crucible under N₂ atmosphere [158]. Oriented SiCNWs are obtained on reacting aligned CNTs with SiO by a carbon nanotube confined reaction [159]. These have diameters between 10 and 40 nm and lengths up to 2 mm.

Aligned SiCNWs have also been synthesized from Si substrates via a catalytic reaction with methane and hydrogen mixture at 1100 °C [160]. Thermal evaporation of SiC powders with Fe catalyst has been used to synthesize needle-shaped SiCNWs and their field emission properties studied [161].

So the thermal evaporation method depending on carbo-thermal reactions seems to be one of the preferred methods among others, which is cheaper, gives resultant high crystal purity and easy to control the experimental variables or conditions.

2.4 Preparation and Characterization Techniques of SiO_x and SiC Nanostructures

Depending on the nature of the material being investigated, suitable techniques may be utilized to assess its structure and properties. Whereas some techniques are qualitative, such as providing an image of a surface, others yield quantitative information such as the relative concentrations of atoms that comprise the material. The ability to focus the extremely small incident wavelengths of energetic electrons results in an unprecedented spatial resolution compared to optical based microscopy techniques. In this thesis, one group of silicon substrates were coated with gold using sputter coater and after doing all experiments these samples were examined by two microscopes, Scanning electron microscope and Transmission electron microscope. X-Ray diffraction (XRD) and Photoluminescence (PL) was used to test related composition and optical properties respectively.

2.4.1 DC Sputter Coater

When a target is bombarded with fast heavy particles, erosion of the target material occurs, the process, when occurring in the conditions of a gaseous glow discharge, between an anode and cathode is termed sputtering. Enhancement of this process for EM sample coating is obtained by the choice of a suitable ionisation gas and target material [162]. The deposition by sputtering is a physical vapor deposition (PVD) method of ejecting, material from a target, i.e., source, which then deposits onto a substrate. Magnetron Sputter Deposition based on DC sputtering that utilizes strong electric and magnetic fields to trap electrons close to the surface of the magnetron, which is known as the target.

In Fig 2.20 (a) the sputter voltage applied to the target is around 2-5 kV. In our experiment we used a tiny thin gold sheet as a target. The treated substrates were placed on the anode plate, where we can control the substrate temperature by bias

LITERATURE REVIEW OF SILICON OXIDE AND SILICON CARBIDE NANOSTRUCTURES

voltage. By increasing the sputtering voltage, the Ar ions will form and increase, which collide with target (gold). As results a lot of Au ions are produced [163]. The treated substrate is being bombarded by electrons and ions from target and plasmas as in Fig 2.20 (b). The Ar pressure can be varied as well as sputtering voltage to control the deposition rate or time.

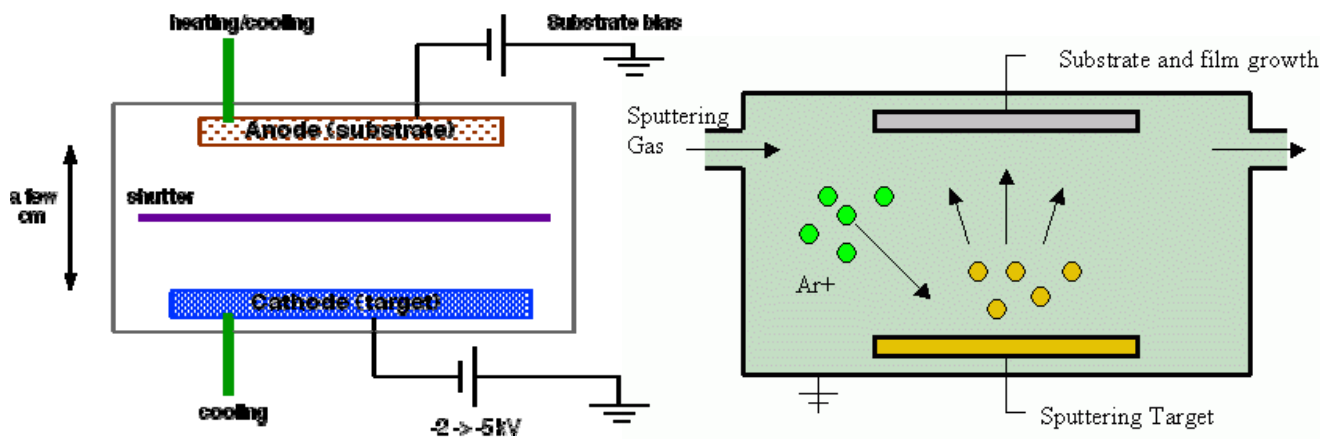


Figure 2.20 Schematic diagram of (a) DC sputtering device and (b) the working mechanism inside the chamber [163].

Generally a gold film of thickness 100-300 angstroms is used for investigations [164]. Usually gold is used to coat silicon substrates but other targets give different sputtering rates (e.g. a platinum target gives approximately half the sputtering rate of gold). The sputtering rate will also depend on the cleanliness of the sputtering system.

2.4.2 Field Emission Scanning Electron Microscope

Field emission scanning electron microscope (FESEM) technique is most often used to provide a topographic image of the sample surface. However, the electron beam is not confined to the top of the surface, but also interacts with lower depths of the sample. Figure 2.21 shows a schematic of a typical SEM system. A sample is mounted on a mobile stage and electrons emitted by the electron gun are focused through a series of electromagnetic lenses onto the specimen surface.

When electrons impinge upon the specimen surface, they interact with the atomic structure. The volume affected by incident electrons is the “interaction volume.” The radiation emitted during the interaction includes (a) secondary electrons, (b) backscattered electrons and (c) additional components such as visible light, auger electrons, and X-rays. Though all these components are produced simultaneously; they are analyzed independently to generate the type of information desired [165].

When an incident electron passes through a material, it may transmit a part of its energy to the electron cloud of the specimen atoms, inducing ejection of a secondary electron. Because of their weak energy (<50 eV), secondary electrons are only ejected from the specimen and detected by the SE detector. Since small variations of topography will modify the number of secondary electrons emitted, the information obtained with the SE detector is mainly correlated to the topography of the specimen. BSE emissions are created when an incident electron is elastically scattered by the atoms of the specimen. The amount of back-scattered electrons collected depends primarily on the charge, hence, the atomic number of the material, rather than the atomic mass.

In contrast with the SE signal, the BSE signal represents not only the local topography of the specimen but also information about the local atomic composition of the specimen. The Quanta has a Schottky field-emission source gun and three modes of

LITERATURE REVIEW OF SILICON OXIDE AND SILICON CARBIDE NANOSTRUCTURES

imaging and analysis: High vacuum for characterisation of conductive samples, Low vacuum (<200 Pa), for analysis of non-conductive samples and environmental mode (<4000 Pa) for studying wet organic or inorganic materials. The microscope is equipped with an array of X-ray and electron detectors for the comprehensive morphological, microstructural, chemical and crystallographic characterisation of materials. An infra-red CCD camera that provides real-time images of the interior of the microscope chamber.

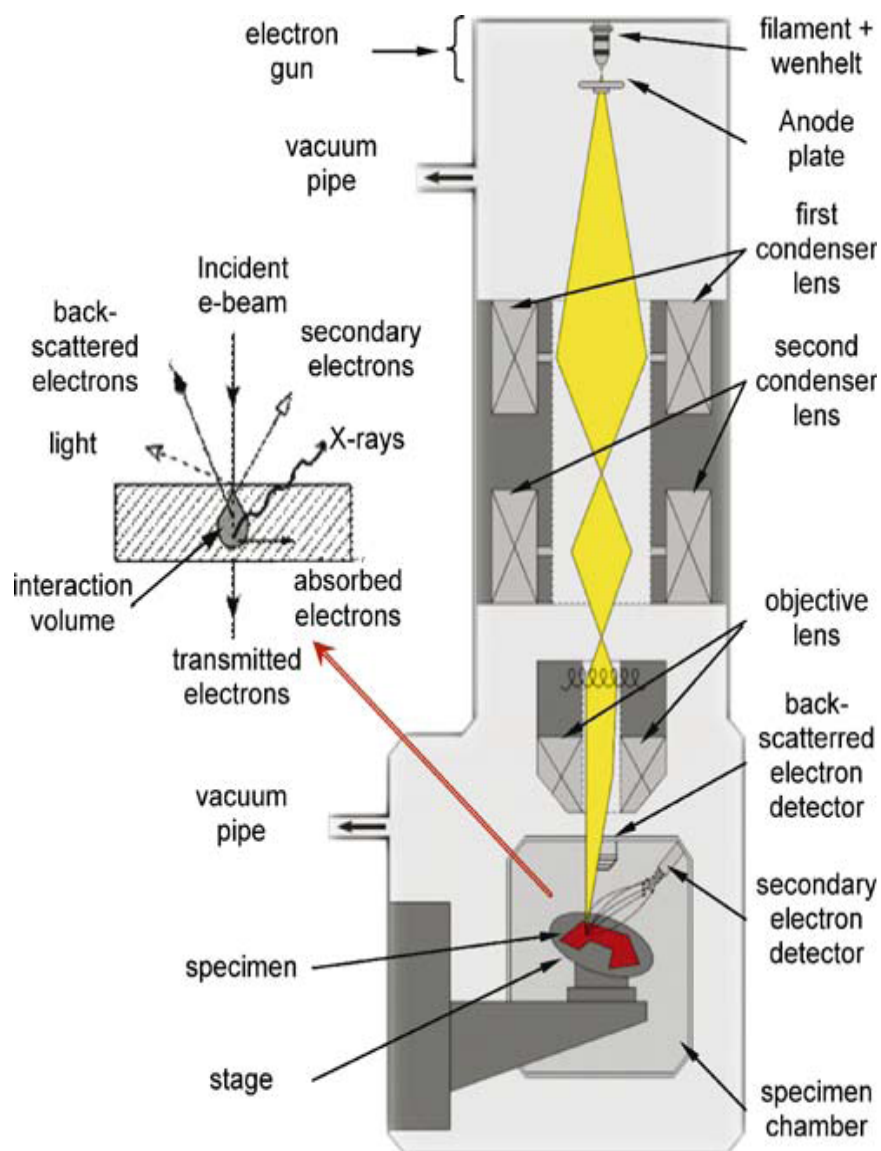


Fig. 2.21 Schematic of a typical scanning electron microscope and imaging process [166].

LITERATURE REVIEW OF SILICON OXIDE AND SILICON CARBIDE NANOSTRUCTURES

As shown in Fig. 2.22, a digital representation of the specimen is produced by the SEM through a raster process. In a manner that is similar to the approach used to acquire images using an early analog optical camera system to either image a specimen or digitize a photograph, the image is acquired through a series of line-scans. Fig 2.22 shows schematic of typical image formation process in an SEM.

The e-beam is rastering horizontally with a dwell time that is a function of preset scan time to obtain a row of “intensity” data in the digitized image. A delay time between rows is required to reset the e-beam. Either secondary electron detector or back-scattered electron detector is used to record the “intensity” data.

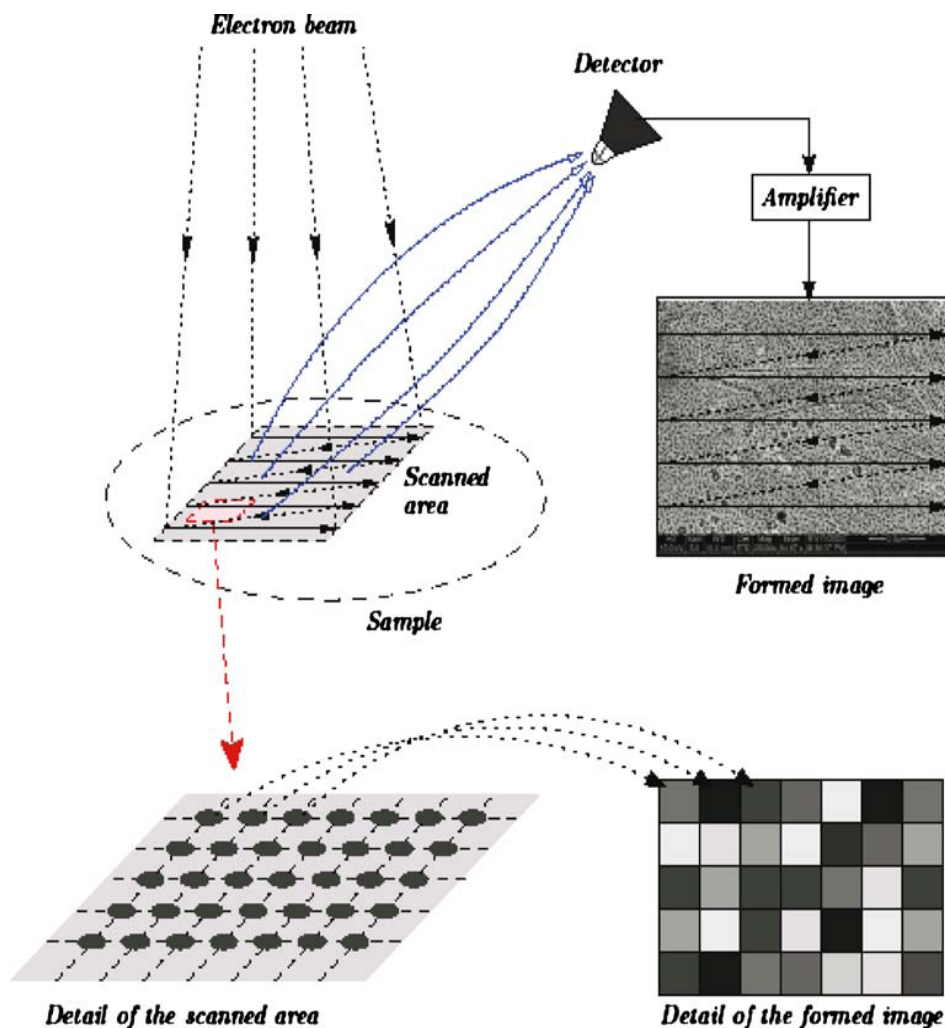


Figure 2.22 Schematic diagram of SEM image in analog optical camera.[166]

LITERATURE REVIEW OF SILICON OXIDE AND SILICON CARBIDE NANOSTRUCTURES

The spatial resolution of the SEM depends on the size of the electron spot which in turn depends on the magnetic electron-optical system which produces the scanning beam. The resolution is also limited by the size of the interaction volume, or the extent to which the material interacts with the electron beam [166]. On the other hand the FESEM can magnify up to 100k, which give a high resolution and defined images.

2.4.3 Electron Dispersive X-ray

Energy dispersive X-ray spectroscopy (EDS, EDX or EDXRF) is an analytical technique used for the elemental analysis or chemical characterization of a sample. As a type of spectroscopy, it relies on the investigation of a sample through interactions between electromagnetic radiation and matter, analyzing x-rays emitted by the matter in response to being hit with charged particles. Its characterization capabilities are due in large part to the fundamental principle that each element has a unique atomic structure allowing x-rays that are characteristic of an element's atomic structure to be identified uniquely from each other [167].

The displacement of target material electrons by primary electrons triggers the release of an x-ray photon, which is characteristic of the atom (element) from which it was released. Atoms hold electrons in orbit around their nuclei as a result of electrical charge differences between them, the nucleus carrying a positive charge and the electrons carrying a negative charge. These charges exactly balance each other. The arrangement of electrons around the nucleus of an atom is conventionally considered as a sequence of 'electron shells', with the innermost shell electrons possessing the lowest energy but with higher bonding energies, and the outermost electrons possessing the highest energies with lower binding energies.

The shells are, also conventionally, labeled K, L, M, N, O, P, and Q from innermost to outermost. Because of the differing binding energy levels of the electrons around the nucleus, primary electrons of a higher potential energy (electron volts - eV) are required to displace K-shell electrons than are required to displace L-shell electrons, which is higher than that required for M-shell electrons etc.

A simple diagram of the first three shells is illustrated in Fig. 4.23. Primary electrons bombarding the atom are able to 'knock' shell electrons out of their orbits, which can be

LITERATURE REVIEW OF SILICON OXIDE AND SILICON CARBIDE NANOSTRUCTURES

replaced by electrons from shells further out, that are able to 'jump' into the inner shell vacancies. There are a number of reactions that occur as a result of this, but for the purposes of explaining the generation of x-rays, only the following points are considered. The knocking out of an inner shell electron causes the atom to take on an excited, high energy state until the missing electron is replaced and the atom relaxes. There is therefore a difference in energy states.

This difference can be large, and if it is, the excess energy can be released in the form of an x-ray (it can also be released in the form of an Auger electron, but is not considered here), which carries this energy difference, and has a wavelength that is characteristic of the atomic species from which it came as in Fig. 2.23.

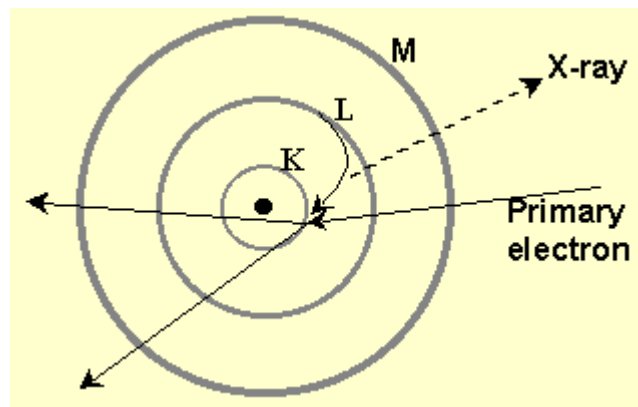


Figure 2.23 A simple diagram of the first three shells of an atom

It should be noted that replacement of L and M shell (etc.) electrons can also be achieved by electrons jumping in from shells that are further out again, and can lead to a large number of generated x-rays of differing wavelengths. There are therefore a number of possible lines of x-rays available for analysis.

The most significant issue to note from this is that the x-rays generated from any particular element are characteristic of that element, and as such, can be used to identify which elements are actually present under the electron probe. This is achieved by

LITERATURE REVIEW OF SILICON OXIDE AND SILICON CARBIDE NANOSTRUCTURES

constructing an index of x-rays collected from a particular spot on the specimen surface, which is known as a spectrum. For an example, spectrum for phosphorous with fluorine is shown in Fig. 2.24. The element peaks for analysis have been marked in red. Where two peaks are shown for the same element, the smaller peak corresponds to one of the other lines of electron replacement, such as an 'M' shell electron jumping into the 'K' shell. The y-axis is an arbitrary pixel count [168].

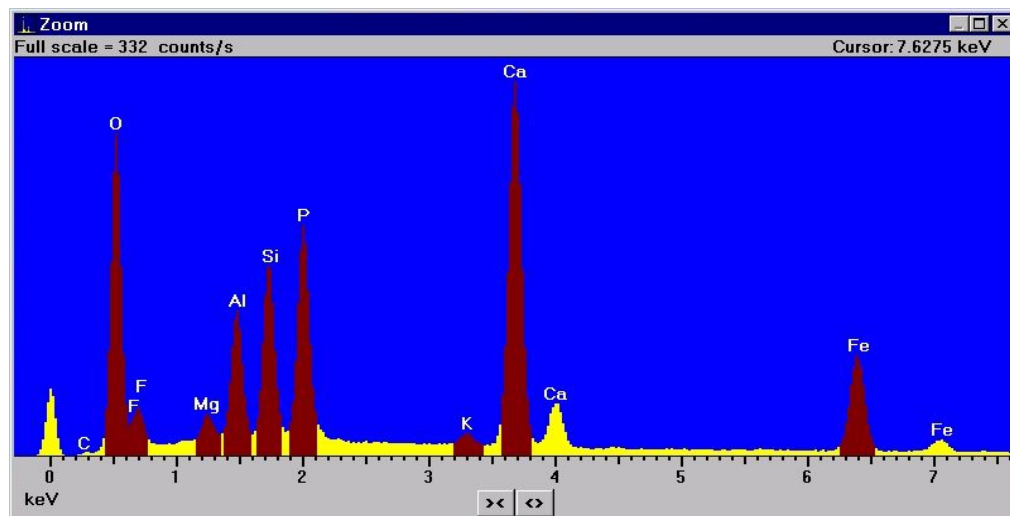


Figure 2.24 EDX spectrum for phosphorous with fluorine.

The x-axis of the spectrum is the x-ray energy scale, along which x-rays collected from various elements are registered, and which in turn form a series of peaks along the x-axis where each peak corresponds to a particular element. With modern software, it is possible to collect a series of spectrums for each point (pixel) analysed by the electron beam probe, as it is scanned across the surface of the specimen. If one spot only is analysed, quantification of the relative proportions of elements under that spot is possible, which is known as a point analysis.

If however a line of pixels is analysed, a line-traverse analysis can be performed which highlight changing proportions of elements with distance along the line. This is known

LITERATURE REVIEW OF SILICON OXIDE AND SILICON CARBIDE NANOSTRUCTURES

as line scanning. Finally, each pixel in an image can also be analysed, which illustrates the distribution of a chosen element across the image. This is known as dot-mapping of the elements, and can take up some considerable time as the electron probe is required to dwell on each separate point for a pre-determined period of time in order to collect enough data for analysis.

In many applications of the technique to concrete petrography this is normally done in conjunction with a backscattered electron image, where each pixel of the image has an exact and corresponding pixel on each of the element maps, which are collected at the same time and at the same resolution. Another reason for choosing this image type is that efficient x-ray analysis requires a flat polished surface where there are few obstructions to x-rays leaving the surface of the specimen that may cause contamination of the signal. The software requires calibration to known standards before normal use.

2.4.4 X-ray Diffraction Technique (XRD)

An X-ray which reflects from the surface of a substance has travelled less distance than an X-ray which reflects from a plane of atoms inside the crystal. The penetrating X-ray travels down to the internal layer, reflects, and travels back over the same distance before being back at the surface. The distance travelled depends on the separation of the layers and the angle at which the X-ray entered the material [169]. For this wave to be in phase with the wave which reflected from the surface it needs to have travelled a whole number of wavelengths while inside the material.

An X-ray with wave length 1.5418°A is incident on specimen elastically according to Bragg's equation now known as Bragg's Law, see Fig 2.25.

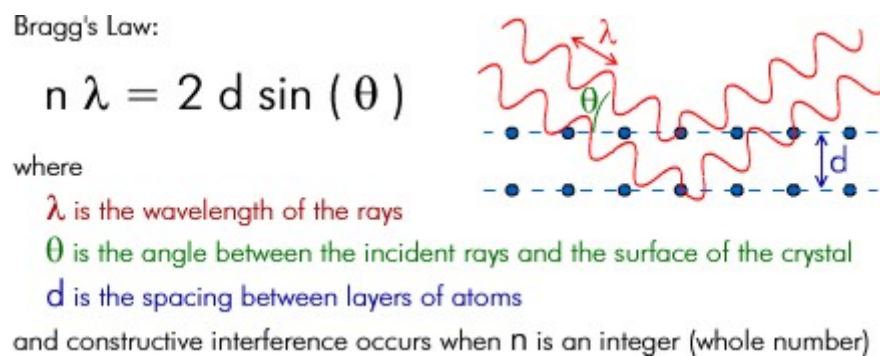


Figure 2.25 X-ray with wave length between 0.5 and 2 °A is incident on specimen according to Bragg's Law

When n is an integer (1, 2, 3 etc.) the reflected waves from different layers are perfectly in phase with each other and produce a bright point on a piece of photographic film. Otherwise the waves are not in phase, and will either be missing. X-ray Diffraction device like that in Fig. 2.26 is an efficient analytical technique used to identify and characterize unknown crystalline materials.

LITERATURE REVIEW OF SILICON OXIDE AND SILICON CARBIDE NANOSTRUCTURES

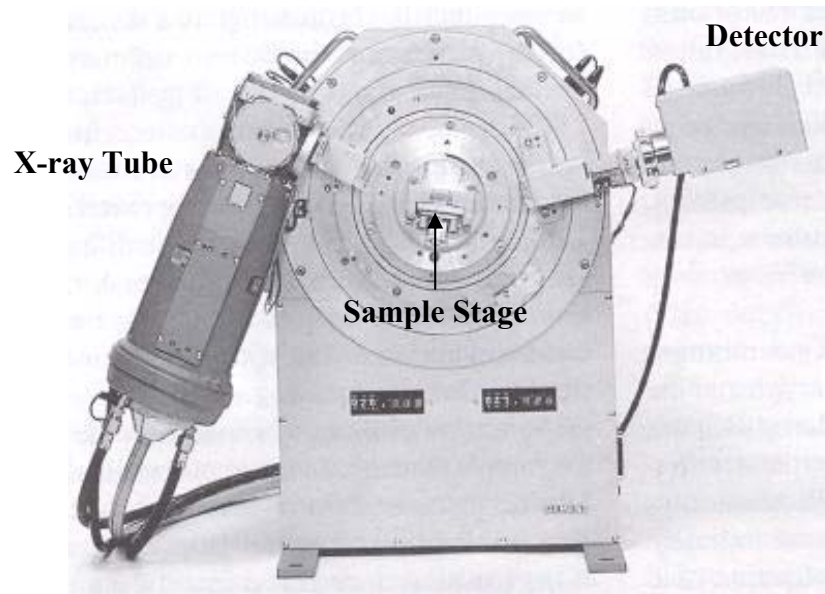


Figure 2.26 X-ray diffraction device showing the X-ray tube generate X-ray beam that hit the examined sample on the stage and the emitted electrons collected by the moving detector.

Monochromatic x-rays are used to determine the interplanar spacings of the unknown materials. Samples are analyzed as powders with grains in random orientations to insure that all crystallographic directions are "sampled" by the beam. When the Bragg conditions for constructive interference are obtained, a "reflection" is produced, and the relative peak height is generally proportional to the number of grains in a preferred orientation.

The X-ray spectra generated by this technique, thus, provide a structural fingerprint of the unknown. Mixtures of crystalline materials can also be analyzed and relative peak heights of multiple materials may be used to obtain semi-quantitative estimates of abundances. A glancing x-ray beam may also be used to obtain structural information of thin films on surfaces.

In addition, changes in peak position that represent either compositional variation (solid solution) or structure-state information (e.g. order-disorder transitions, exsolution, etc.) are readily detectable. Peak positions are reproducible to 0.02 degrees.

LITERATURE REVIEW OF SILICON OXIDE AND SILICON CARBIDE NANOSTRUCTURES

An x-ray diffractometer illuminates a sample of material with x-rays of known wavelength, moving the sample and detector in order to measure the intensity of the diffracted radiation as a function of beam angle.

From the results the x-ray intensities versus reflected angles are plotted to reveal the structure of the material (crystalline, amorphous ect..). The measurement is generally not straightforward, and the inference required to make useful observations on the sample is quite subtle. All the diffractometer can tell us is the spacing between atomic layers:

For example if the diffracted beam is reflected directly back into the x-ray source we know there are crystal planes D-spacing exactly two times the incident wavelength 1.5418 angstroms or, possibly, some integer multiple of that spacing. When combined with enough other information, in particular knowledge of crystal symmetries, remarkably complete understanding of the sample can be achieved.

Indeed, in a sufficiently ordered sample (i.e., a good single crystal) molecular structures can be worked out. Conversely, if the structure is known a measurement of the structure's disorder becomes possible. This has important applications in process control, since epitaxial growth of well known materials is crucial to microelectronic fabrication and x-ray diffraction provides a relatively precise measurement of crystal growth quality.

2.4.5 Transmission Electron Microscope (TEM)

Transmission electron microscopy (TEM) is an imaging mode that allows the imaging of the crystallographic structure of a sample at an atomic scale [170]. A TEM works much like a slide projector. A projector shines a beam of light through (transmits) the slide, as the light passes through it is affected by the structures and objects on the slide. These effects result in only certain parts of the light beam being transmitted through certain parts of the slide. This transmitted beam is then projected onto the viewing screen, forming an enlarged image of the slide.

In Fig 2.27 (a) [171] and reveals the construction of the HRTEM with its image. The working steps of HRTEM can be summarized as follows:

1. The "Virtual Source" at the top represents the electron gun, producing a stream of monochromatic electrons.
2. This stream is focused to a small, thin, coherent beam by the use of condenser lenses 1 and 2. The first lens largely determines the "spot size"; the general size range of the final spot that strikes the sample. The second lens changes the size of the spot on the sample; changing it from a wide dispersed spot to a pinpoint beam.
3. The beam is restricted by the condenser aperture (usually user selectable), knocking out high angle electrons (those far from the optic axis, the dotted line down the center)
4. The beam strikes the specimen and parts of it are transmitted.
5. This transmitted portion is focused by the objective lens into an image.
6. Optional objective and selected area metal apertures can restrict the beam; the objective aperture enhancing contrast by blocking out high-angle diffracted electrons, the selected area aperture enabling the user to examine the periodic diffraction of electrons by ordered arrangements of atoms in the sample.

LITERATURE REVIEW OF SILICON OXIDE AND SILICON CARBIDE NANOSTRUCTURES

7. The image is passed down the column through the intermediate and projector lenses, being enlarged all the way.
8. The image strikes the phosphor image screen and light is generated, allowing the user to see the image. The darker areas of the image represent those areas of the sample that fewer electrons were transmitted through (they are thicker or denser). The lighter areas of the image represent those areas of the sample that more electrons were transmitted through (they are thinner or less dense).

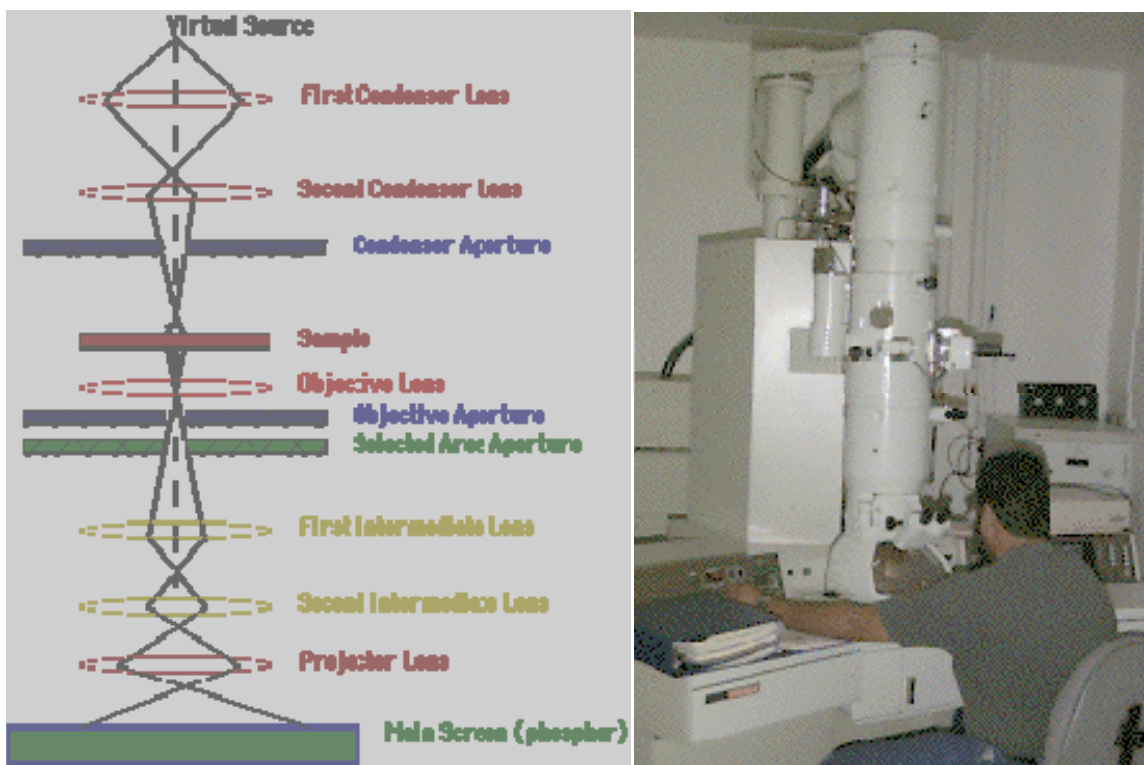


Figure 2.27 HRTEM (a) internal constructions (b) image [171].

2.4.6 Optical Characterization

2.4.6.1 Fourier Transform Infra-Red (FTIR) Spectroscopy.

In infrared spectroscopy, IR radiation is passed through a sample. Some of the infrared radiation is absorbed by the sample and some of it is passed through (transmitted). The resulting spectrum represents the molecular absorption and transmission, creating a molecular fingerprint of the sample. Like a fingerprint no two unique molecular structures produce the same infrared spectrum. This makes infrared spectroscopy useful for several types of analysis.

Fourier Transform Infrared (FT-IR) spectrometry was developed in order to overcome the limitations encountered with dispersive instruments. The main difficulty was the slow scanning process. A method for measuring all of the infrared frequencies simultaneously, rather than individually, was needed. A solution was developed which employed a very simple optical device called an interferometer. The interferometer produces a unique type of signal which has all of the infrared frequencies “encoded” into it. The signal can be measured very quickly, usually on the order of one second or so. Thus, the time element per sample is reduced to a matter of a few seconds rather than several minutes. Most interferometers employ a beam splitter which takes the incoming infrared beam and divides it into two optical beams. One beam reflects off of a flat mirror which is fixed in place. The other beam reflects off of a flat mirror which is on a mechanism which allows this mirror to move a very short distance (typically a few millimeters) away from the beam splitter. The two beams reflect off of their respective mirrors and are recombined when they meet back at the beam splitter. Because the path that one beam travels is a fixed length and the other is constantly changing as its mirror moves, the signal which exits the interferometer is the result of these two beams “interfering” with each other.

LITERATURE REVIEW OF SILICON OXIDE AND SILICON CARBIDE NANOSTRUCTURES

The resulting signal is called an interferogram which has the unique property that every data point (a function of the moving mirror position) which makes up the signal has information about every infrared frequency which comes from the source. This means that as the interferogram is measured; all frequencies are being measured simultaneously. Thus, the use of the interferometer results in extremely fast measurements. Because the analyst requires a frequency spectrum (a plot of the intensity at each individual frequency) in order to make identification, the measured interferogram signal can not be interpreted directly.

A device is required for decoding the individual frequencies. This can be accomplished via a well-known mathematical technique called the Fourier transformation. This transformation is performed by the computer which then presents the user with the desired spectral information for analysis. The normal instrumental process is as follows:

1. The Source: Infrared energy is emitted from a glowing black-body source. This beam passes through an aperture which controls the amount of energy presented to the sample (and, ultimately, to the detector).
2. The Interferometer: The beam enters the interferometer where the “spectral encoding” takes place. The resulting interferogram signal then exits the interferometer.
3. The Sample: The beam enters the sample compartment where it is transmitted through or reflected off of the surface of the sample, depending on the type of analysis being accomplished. This is where specific frequencies of energy, which are uniquely characteristic of the sample, are absorbed.
4. The Detector: The beam finally passes to the detector for final measurement. The detectors used are specially designed to measure the special interferogram signal.
5. The Computer: The measured signal is digitized and sent to the computer where the Fourier transformation takes place. The final infrared spectrum is then presented to the

LITERATURE REVIEW OF SILICON OXIDE AND SILICON CARBIDE NANOSTRUCTURES

user for interpretation and any further manipulation. All these processes are summarized in Fig. 2.28. [172]

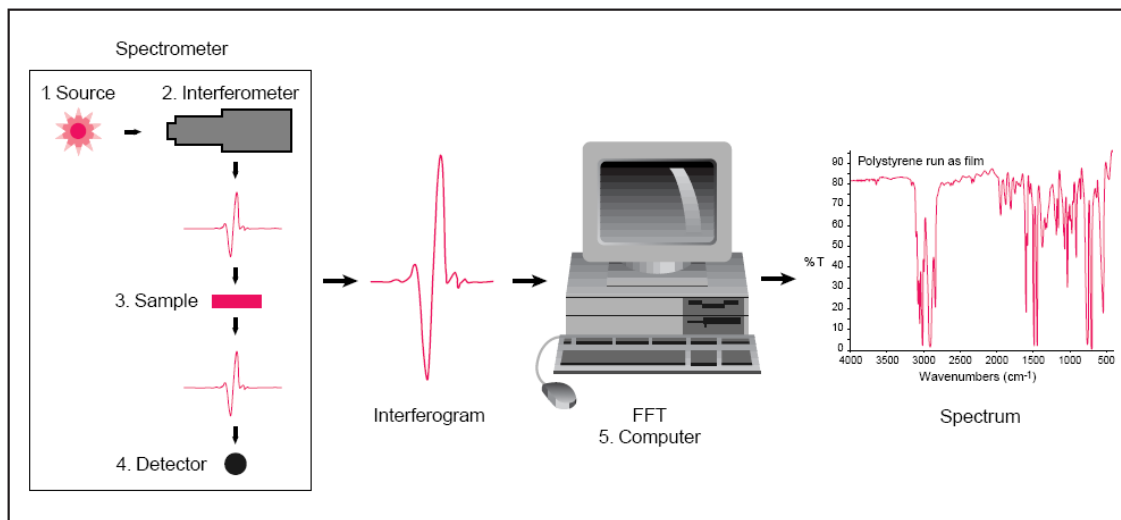


Figure 2.28 FTIR operation method and resultant spectrum.

The IR absorption characteristic of amorphous SiO₂ has also been studied for many years [173]. Three major absorption bands centered at 460, 810, and 1070 cm⁻¹ have been confirmed by Kirk et al. [174]. These three absorption peaks reflect the rocking of an oxygen atom about an axis through the two silicon, the symmetrical stretching of an oxygen atom along a line bisecting the axis through the two silicon atoms and asymmetrical stretching of an oxygen atom along a line parallel to the axis through the two silicon atoms, respectively.

In addition, an increase in the structural disorder could enhance the relative intensity of the absorption band at a higher-frequency side [175]. Among these absorption bands, the intensity of 1070 cm⁻¹ is much stronger than the features at its high-frequency side even when the structural disorder of amorphous SiO₂ has been increased by different ways [176]. The nanostructural effect on the IR absorption properties may be investigated by studying the vibration modes of Si–O on the surface of the SiO_x nanowires and in their interfaces.

2.4.6.2 Photoluminescence Spectrometer

When light of sufficient energy is incident on a material, photons are absorbed and electronic excitations are created. Eventually, these excitations relax and the electrons return to the ground state. If radiative relaxation occurs, the emitted light is called PL. This light can be collected and analyzed to yield a wealth of information about the photoexcited material.

The PL spectrum provides the transition energies, which can be used to determine electronic energy levels. The PL intensity gives a measure of the relative rates of radiative and nonradiative recombination. Variation of the PL intensity with external parameters like temperature and applied voltage can be used to characterize further the underlying electronic states and bands. Because PL often originates near the surface of a material, PL analysis is an important tool in the characterization of nanostructures on the surfaces.

PL is simple, versatile, and nondestructive. The instrumentation that is required for ordinary PL work is modest: an optical source and an optical power meter or spectrophotometer. A typical PL set-up is shown in Fig. 2.29.

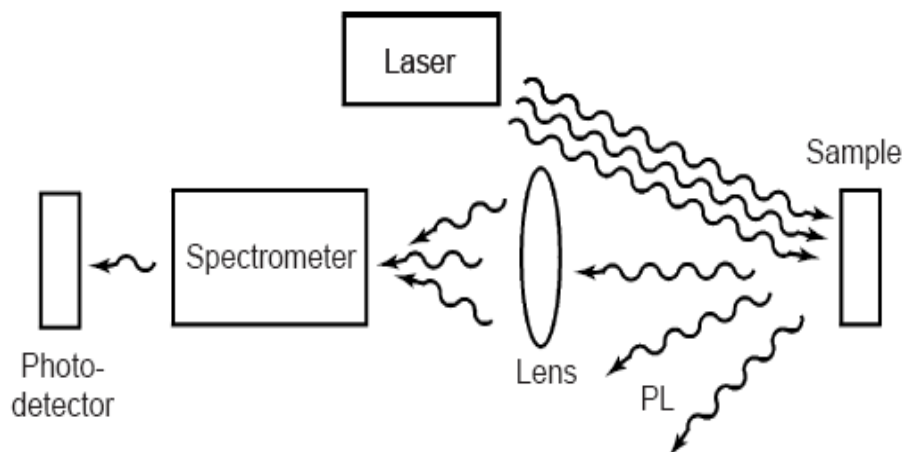


Figure 2.29 Schematic diagram of PL measurements experimental set up.

LITERATURE REVIEW OF SILICON OXIDE AND SILICON CARBIDE NANOSTRUCTURES

PL is the optical radiation emitted by a semiconducting crystal after excitation with incident light source (usually a laser). Most of the light results from the difference in energy of the excited electron (in the conduction energy band) returning to its ground state (valence energy band).

At low temperatures (4-77K) the excited electrons return to their initial energy through more complex mechanisms involving mainly point (0-D) defects and interactions with the vibrational energy states (phonons) of the crystal [177]. Inside the photoluminescence spectrometer apparatus laser hit the specimen. The photoluminescence rays were collected by L1 and L2 lenses, which is then focused as a beam, see Fig 2.30.

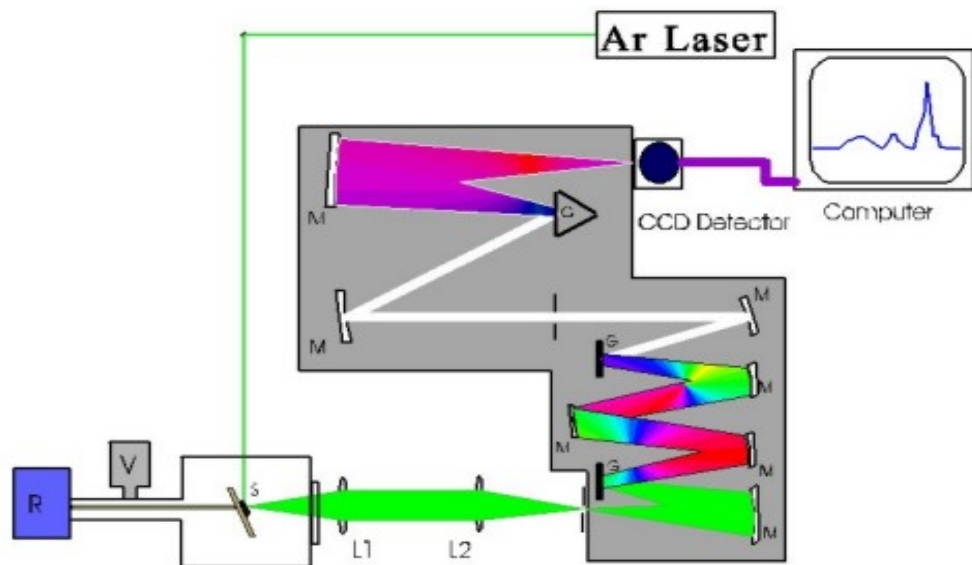


Figure 2.30 A schematic diagram of experimental apparatus for low temperature photoluminescence [177].

This beam is magnified and then detected by CCD detector. The final step is analyzing the resultant spectrum in the computer by special programme. The PL spectra have narrow bands (peaks) which make analysis possible. The PL is a complementary technique to the absorption spectra. The emission spectrum contains "fingerprint"-type

LITERATURE REVIEW OF SILICON OXIDE AND SILICON CARBIDE NANOSTRUCTURES

peaks related to the energy of each excited level and can be used as a sensitive probe to find impurities and other defects in semiconductors. Because the measurement does not rely on electrical excitation or detection, sample preparation is minimal. This feature makes PL particularly attractive for material systems having poor conductivity or undeveloped contact/junction technology.

Measuring the continuous wave PL intensity and spectrum is quick and straightforward. Because PL can be used to study virtually any surface in any environment, it can be used to monitor changes induced by surface modification in real time. For example, unlike most surface characterization techniques, PL is generally not sensitive to the pressure in the sample chamber.

Hence, it can be used to study surface properties in relatively high-pressure semiconductor growth reactors. Although PL does depend quite strongly on temperature, liquid helium temperatures being required for the highest spectral resolution, room-temperature measurements are sufficient for many purposes. In addition, PL has little effect on the surface under investigation.

Photoinduced changes and sample heating are possible, but low excitation can minimize these effects. In situ PL measurements do require optical access to the sample chamber. Yet, compared with other optical methods of characterization like reflection and absorption, PL is less stringent about beam alignment, surface flatness, and sample thickness.

The advantages of PL analysis listed above derived from the simplicity of optical measurements and the power to probe fundamental electronic properties. In the bulk of a crystalline material, translational symmetry leads to the formation of electronic energy bands. Defects and impurities break the periodicity of the lattice and perturb the band structure locally. The perturbation usually can be characterized by a discrete energy

LITERATURE REVIEW OF SILICON OXIDE AND SILICON CARBIDE NANOSTRUCTURES

level that lies within the band gap. Depending on the defect or impurity, the state acts as a donor or acceptor of excess electrons in the crystal. Electrons or holes are attracted to the excess or deficiency of local charge due to the impurity nucleus or defect, and Coulomb binding occurs.

The situation can be modeled as a hydrogenic system where the binding energy is reduced by the dielectric constant of the material. Because electrons and holes have different effective masses, donors and acceptors have different binding energies. When the temperature is sufficiently low, carriers will be trapped at these states. If these carriers recombine radiatively, the energy of the emitted light can be analyzed to determine the energy of the defect or impurity level.

Shallow levels, which lie near the conduction or valence band edge, are more likely to participate in radiative recombination, but the sample temperature must be small enough to discourage thermal activation of carriers out of the traps.

Deep levels tend to facilitate non-radiative recombination by providing a stop-over for electrons making their way between the conduction and valence bands by emitting phonons. Several intrinsic and impurity transitions are illustrated in Fig 2.31. Of all the properties that characterize PL, the intensity of the PL signal has received the most attention in the analysis of interfaces. This interest is due to the fact that, large PL signals correlate with good interface properties.

A useful review of the dominant mechanisms and the relationship between them has been provided by Chang et al. [178]

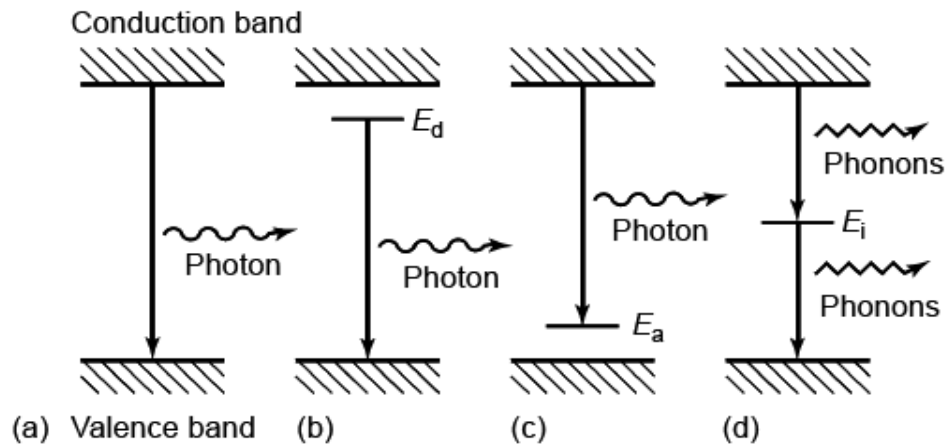


Figure 2.31 A schematic diagram of (a-c) Radiative recombination paths: (a) band-to-band; (b) donor to valence band; (c) conduction band to acceptor. (d) Nonradiative recombination via an intermediate state.

In particular, they discuss the roles of the surface recombination velocity S and band bending at the surface in the PL measurement. Because surface recombination is usually non-radiative, and band bending can lead to the formation of a depletion region or “dead layer” where PL is effectively quenched, both of these phenomena tend to reduce the PL intensity.

Distinguishing between the two effects is difficult and usually requires a supplementary measurement of the surface potential. All else being constant, the surface recombination velocity is proportional to the density of surface states. However, changes in the surface-state density can affect the accumulation of charge at the surface, thereby altering the depletion thickness. If increasing the surface-state density enhances the depletion layer, both mechanisms suppress the PL intensity and the surface recombination velocity increases rapidly.

Conversely, if the space-charge region is reduced by an increase in the density of surface states, the two mechanisms will have opposite effects on the PL signal and tend to cancel each other out. It should also be noted that, even though changes in surface-

LITERATURE REVIEW OF SILICON OXIDE AND SILICON CARBIDE NANOSTRUCTURES

state density usually affect band bending, the inverse is not necessarily true. For example, the electric field at the surface can be modified by adsorption of molecules that shift the distribution of electrons between bulk and surface states but leave the surface-state density unchanged. Hence, the coupling of the two phenomena is quite complex.

The intensity of the PL signal depends on the rate of radiative and nonradiative events, which depends in turn on the density of nonradiative interface states. PL measurements are not sensitive to the pressure in the sample chamber and can be performed at virtually any temperature. These features make PL an excellent in situ probe of surface or interface modification.

Chapter 3

Experimental setup and methodology

3.1 Introduction

For the synthesis of silicon oxide and silicon carbide nanostructures used in this thesis, thermal evaporation method is preferred to provide the synthesis process with growth species in vapor form. Therefore, in this chapter the preparation setup of tube furnace will be presented first. After that, the setup of the experimental work is build, which includes an attached inlet gases at left side and an exhausted outlet at the other end where the system is vacuumed. Then, the substrate is prepared by cleaning the substrate surface and sputtering catalyst gold over the substrate as required. In last section, the characterization equipments used in our work was outlined.

3.2 Synthesis of Silicon Oxide and Silicon Carbide Nanostructures.

3.2.1 Substrate preparation

N-type Si (100) of resistivity $5.15 \Omega\cdot\text{cm}^{-2}$ substrates were ultrasonically cleaned in acetone for 5 minutes and then immersed in methanol solution for another 5 minutes to remove unwanted materials. These substrates were cleaned with running distilled water and dried in air at 50°C . After that, treated substrates were isolated from the outside environment and divided into two groups. The first group was taken to the DC sputtering and coated with a thin layer of gold, which was named catalytic group and the remaining substrates made the second group called as non catalytic.

3.2.2 Substrate coater

The thickness of the deposited layer has been controlled by time. The deposition time was varied between 10 s to 100 s as required. The sputtering instruments (SPI) sputter coater module and SPI module control [164] was performed in our thesis experiments. The sputtering variables kept are as 2 Torr pressure, half gas leak and 20 mA for different duration of time (20 to 80 sec). The instrument image used in this study is shown in Fig 3.1 (a). The construction labels can be seen in Fig. 3.1(b).

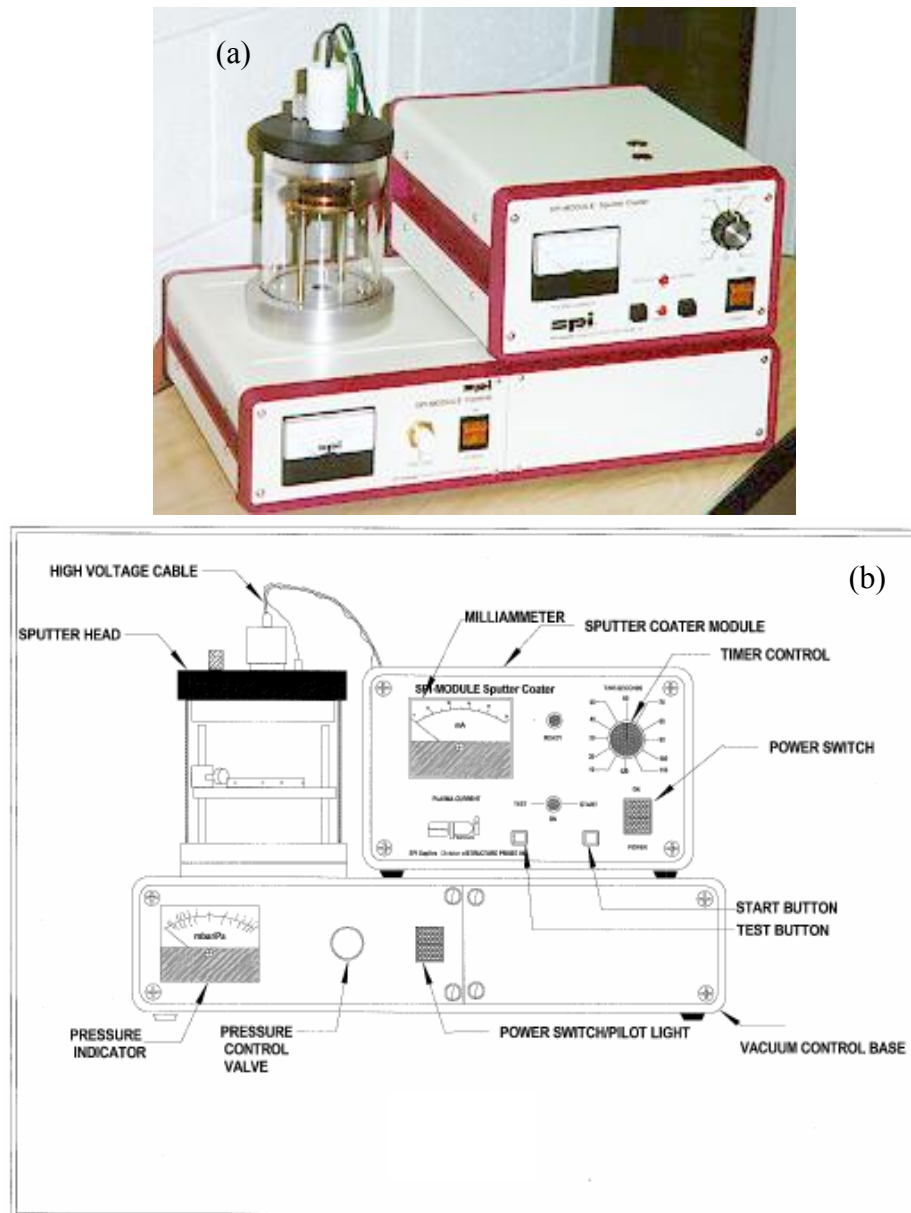


Figure 3.1 Sputtering device (a) the sputtering instruments (SPI) sputter coater and SPI control (b) the instrument labels.[164]

3.2.3 The Tube Furnace

Thermal evaporation method required a furnace of sufficient heating temperature. Horizontal tube furnace with maximum 1200°C was chosen to evaporate the materials needed to be in vapor phase as growth species to accomplish the synthesis process. The furnace configuration allows the attachment of horizontal quartz tube from one end and vacuum system at the other end. Carbolite MTF tube furnace (12/38/250) model with 1200°C and 1.5°C/s heating rate was chosen to run the temperature for all our experiments. The relative characteristics can be seen in table 3.1 [179].

Table 3.1 Specification of the Carbolite MTF Tube Furnace.

Model	MTF 12/38/250
Maximum temperature (°C)	1200
Ceramic Tube length (mm)	300
Heated length (mm)	250
Tube inside diameter (mm)	38
Power rating (kW)	1
Uniform Zone Length (mm)	110

This model in Fig. 3.2 utilise a resistance wire heating element wound around a ceramic work tube, forming an integral part of the heating element to ensure excellent thermal uniformity.



Figure 3.2 Carbolite MTF tube furnace [179].

The temperature inside the furnace has uniform value ($T \pm 10^\circ\text{C}$) for certain length.

Tube furnace cross section and uniformly curve are shown in Fig. 3.3.

The temperature is uniform over 14 cm tube length as illustrated in Fig. 3.3. The quartz tube with 2.2 cm inner diameter was mounted inside the ceramic tube by two standing holders. A marked rod was used for the substrates handles to choose the substrate locations with good precision.

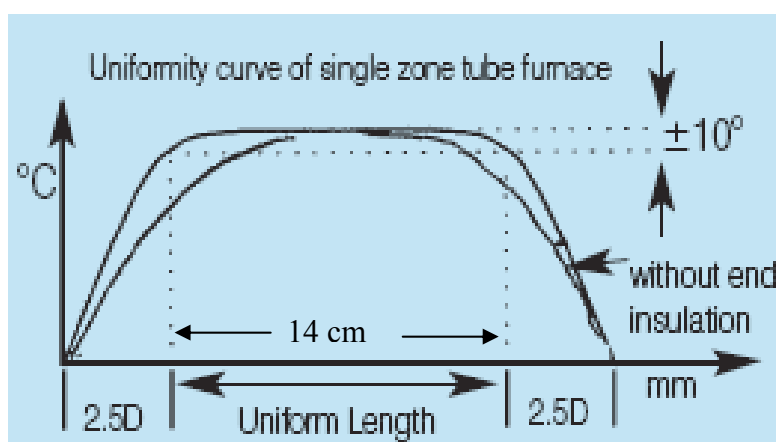


Figure 3.3 A schematic diagram of uniform temperature curve [179]

3.3 Experimental setup

In the synthesis of silicon oxide nanostructures, titanium dioxide (TiO_2) and graphite powder (ALDRICH) with (1:1) ratio were mixed together. 2g of the TiO_2 +C mixture or pure carbon was loaded into the center of a 2.2 cm-inner diameter quartz tube, which was placed inside the tube furnace at 1200°C achieved by heating at 1.4°C/s . Then, in each experiment trial the substrates were placed 2 cm apart from the mixture as shown in Fig 3.4. The gas flow meter controlled the amount of argon gas entered the chamber between 0-100 standard cubic centimeter (sccm) and the vacuum in the deposition region was achieved using a rotary pump. The vacuum achieved during the experiments was typically 150 mTorr.

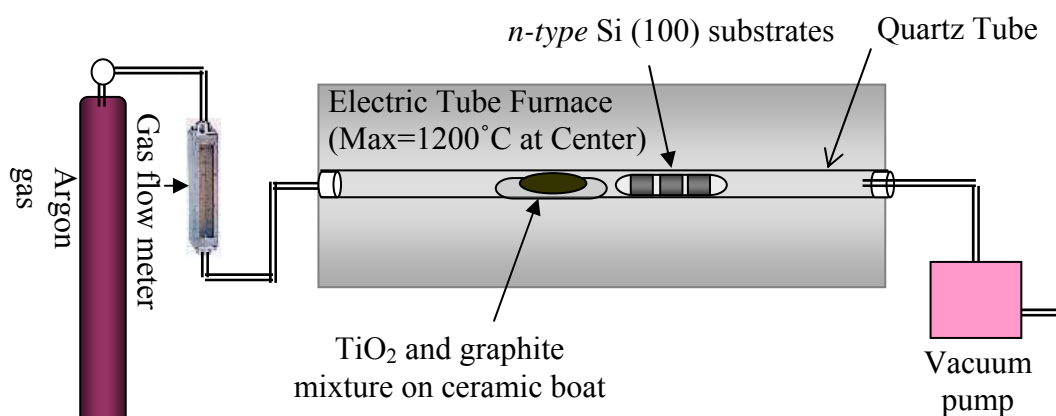


Figure 3.4 A schematic diagram of experimental setup

The schematic diagram in Fig. 3.5 shows the temperature is uniform at 1200°C for about 14 cm. The substrate was placed 2 cm from the porcelain boat containing the TiO_2 /C mixture all in the region of uniform temperature of 1200°C .

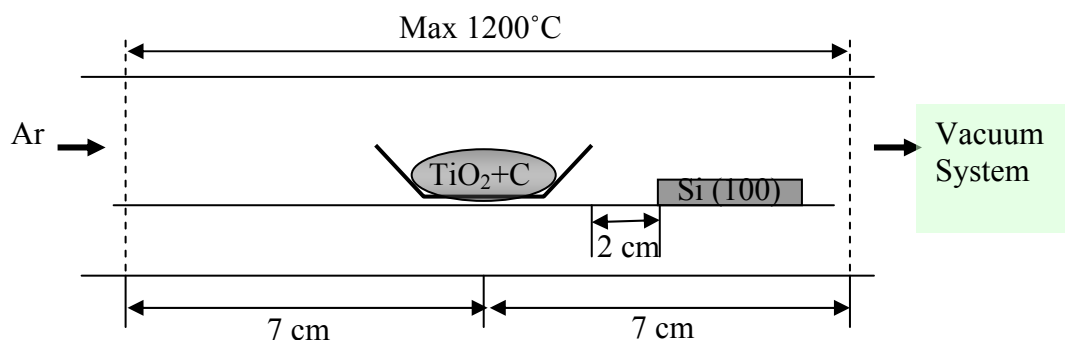


Figure 3.5 A schematic diagram illustrate the synthesis of SiO_x nanowires.

The temperature was gradually increased by 1.4°C/s in all experiments except that for rapid heating rate. To apply rapid heating rate condition, the furnace was first heated up to its maximum temperature 1200°C and then the substrates were inserted directly to the tube.

The argon gas (99.999%) was introduced into the quartz tube at mounted rate at each experiment to transport the growth species from the evaporated areas to condensation places over the substrate surface. While oxygen gas (99.999%) was used as a flowing gas inside the system instead of Ar when required. Experiments were carried out depending upon the variations of experimental conditions.

3.4 Characterization Techniques

After cooling down to room temperature the samples were characterized using field-emission scanning electron microscopy (FESEM), energy-dispersed X-ray spectroscopy (EDX), X-ray diffraction (XRD), high resolution TEM and atomic force microscopy (AFM). The optical properties were studied via photoluminescence spectroscopy system and Fourier transforms Infra-Red (FTIR).

3.4.1 Field Emission Scanning Electron Microscope (FESEM)

The FEI Quanta 200F (FESEM) installed in 2004 was used to capture and magnify the sample images. Electrons are used to view the sample in an electron microscope, which has an effective wavelength of about 0.1 nm, so it allows greater resolution and therefore greater magnification of the sample. Electron accelerating voltage is between 2 to 30 kV. The FESEM resolution is 3.5nm at high vacuum. The vacuum used is up to 20 Torr.

Fig. 3.6 shows one of our FESEM images taken for SiO_x nanowires with 16 kx magnification. This image shows the SiO_x nanowires with their lengths and diameters. The used FESEM device can reach 120 kx maximum magnification. All images can be tilted to see proper images from different angles.

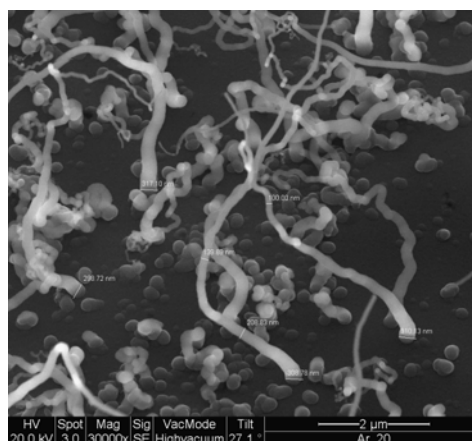


Figure 3.6 FESEM image of SiO_x nanowires grown on pure silicon substrate at 1200°C with 10 sccm Ar gas flowrate for one hour.

3.4.1.1 Energy Dispersive X-Ray (EDX) Analysis

The FEI Quanta 200F (FESEM) is equipped with an Oxford Instruments INCA Energy X-ray detector (EDX) and micro-analysis system. The locations of the EDX peaks are directly related to the particular X-ray “fingerprint” of the elements present. For example, the examined point (b) at the middle of FESEM SiO_x nanowire image in Fig. 3.7 showed the elements of silicon and oxygen present in the EDX spectrum with different weight percentages. Consequently, the presence of a peak, its height, and several other factors, allows the analyst to identify elements within a sample, and with the use of appropriate standards and software.

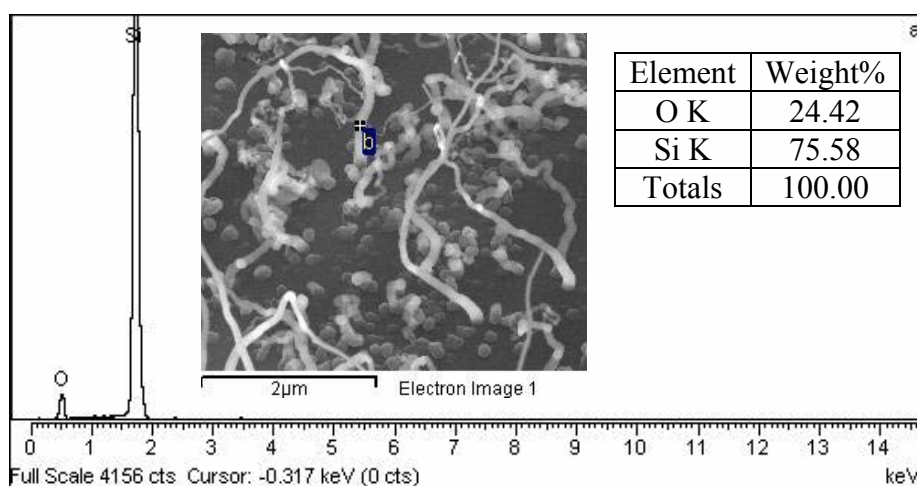


Figure 3.7 EDX spectrum and elements weight percentage of selected spot on the SiO_x nanowire grown at 1200°C with 10 sccm Ar gas flowrate for one hour.

3.4.2 X-ray diffraction (XRD)

XRD is an a non-destructive analytical technique based on observing the scattered intensity of an X-ray beam hitting a sample as a function of scattered angle, polarization and wave length or energy, to study the crystallographic structure, chemical composition and physical properties of materials.

The Siemens D5000 diffractometer used in current study, measures the atomic spacing in crystals using diffraction of approximately monochromatic x-radiation. It can be used to characterize solid samples ranging in size from about 1 millimetre square up to four-inch wafers.

The radiation used is copper k-alpha with a wavelength of 1.5418 angstroms. For each diffracted angle of the incident X-ray there is constructive interference comes out of the crystal plans lattices.

The XRD spectrum shown in Fig. 3.8 shows four high intensity peaks, corresponding to the β -SiC nanowires crystal planes (111), (200), (220) and (311) at $2\theta = 35.75^\circ$, 41.5° , 60.1° and 72.0° respectively.

The first strong intensity peak related to the majority of (111) crystal planes followed by (220), (311) and finally there are small amount of (200) planes. This tells us that our product is poly crystalline of the same material β -SiC. Moreover, thinner XRD peak shows the purity of obtained crystal material and its large size.

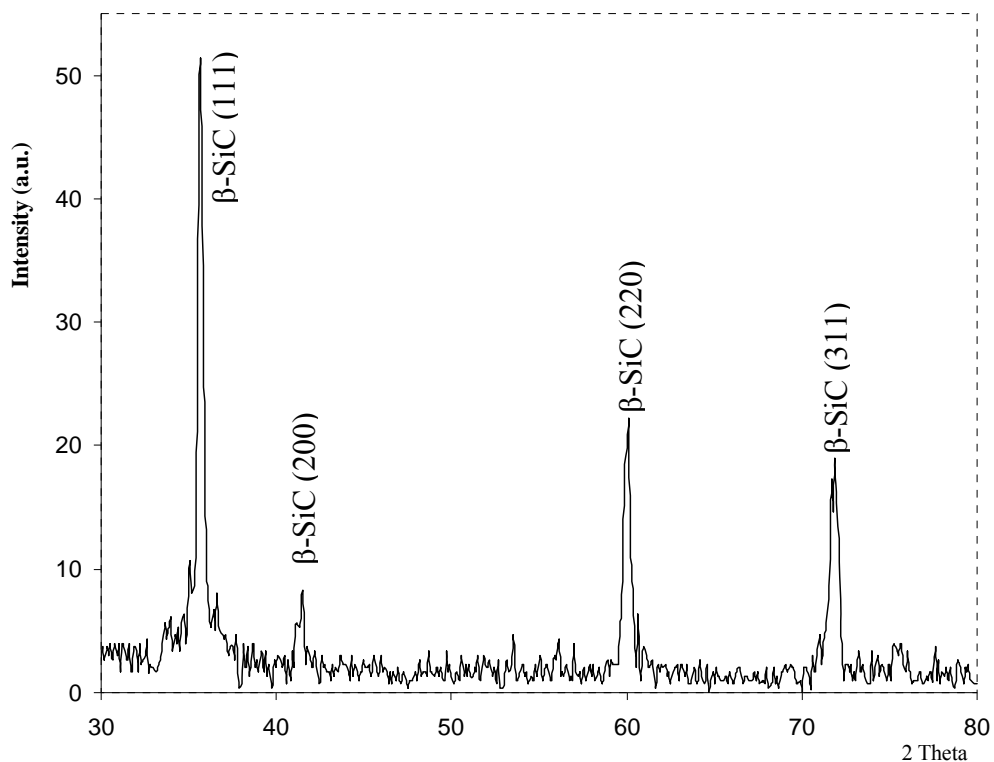


Figure 3.8 XRD spectrum of β -SiC nanowires showing the crystal planes (111), (200), (220) and (311) at $2\theta = 35.75^\circ$, 41.5° , 60.1° and 72.0° respectively, grown under 1200°C with 10 sccm for 1h.

3.4.3 High Resolution Transmission Electron Microscopy

HRTEM used in this study is the JEOL JEM-2010 which is high resolution instrument capable of resolving lattice spacing of approximately 0.14 nm. It is used in our study to investigate the crystal plane structures, which can't be seen in FESEM. The HRTEM is equipped with a sensitive CCD-based camera which is able to generate high quality images with low beam intensity thereby limiting beam damage. The HRTEM with 200 kV accelerating voltage and resolution of about 1.94 Å works under vacuum pressure between 10 to 9 Torr. Fig. 3.9 shows an example of or samples of SiO_x nanowire. The core-shell wire can be seen with HRTEM image. Region A on the core side of wire with darker colour shows the silicon planes, while the outer shell layer, region B, illustrates the amorphous structure of the oxide layer.

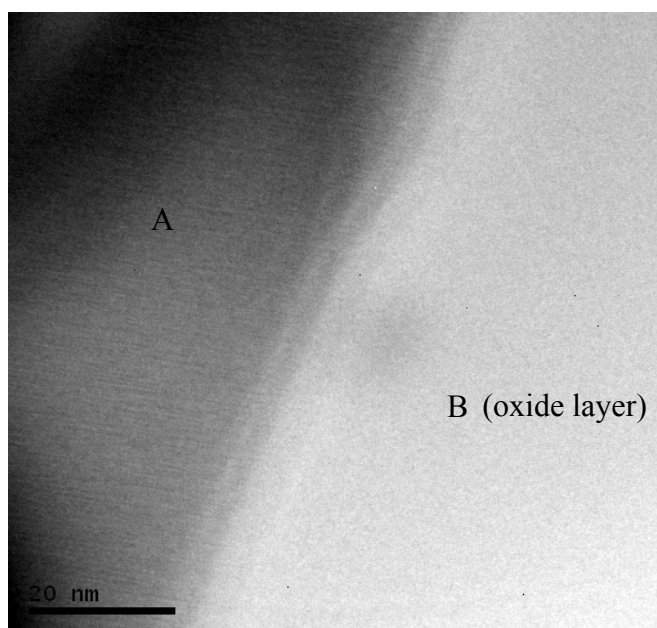


Figure 3.9 HRTEM of (A) core SiO_x NW grown under 1200°C with 10 sccm of Ar flowrate gas for 1h and (B) the outer shell.

3.4.4 Optical Characterization

3.4.4.1 Photoluminescence Spectroscopy System

The PL spectrum provides the transition energies, which can be used to determine electronic energy levels. The PL intensity gives a measure of the relative rates of radiative and nonradiative recombination. Variation of the PL intensity with external parameters like temperature and applied voltage can be used to characterize further the underlying electronic states and bands. Because PL often originates near the surface of a material, PL analysis is an important tool in the characterization of nanostructures on the surfaces. The model used in this study is Jobin Yvon HR 800 UV with energy excitation at 325nm wavelength. For an example, the output PL spectrum taken for our Au-SiO_x nanowires can be seen in Fig. 3.10 the PL spectrum can be divided into two parts, the emission of UV rays at 350 nm and a continuous spectrum of visible light between 420 nm and 600 nm.

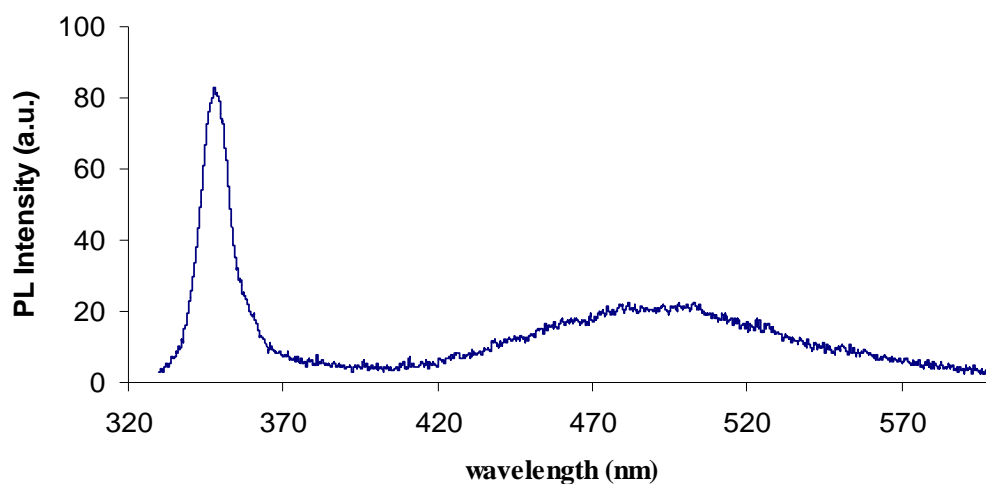


Figure 3.10 Room temperature PL spectrum of Au-SiO_x nanowires grown under 1200°C with 10 sccm for 1h.

These emissions can be related to the number of electron transitions occurred within the excited material, as well as to its band gap. PL spectrum can give informations about the formation of defects of the examined material. Here, the impurities come from the oxygen vacancies that may cause some indirect transitions, which will be discussed in results and discussion chapter.

3.4.4.2 Fourier Transform Infra-Red (FTIR)

In infrared spectroscopy, IR radiation is passed through a sample. Some of the infrared radiation is absorbed by the sample and some of it is passed through (transmitted). The resulting spectrum represents the molecular absorption and transmission, creating a molecular fingerprint of the sample. Like a fingerprint no two unique molecular structures produce the same infrared spectrum. This makes infrared spectroscopy useful for several types of analysis.

The FTIR spectrometer named Spectrum RX1 from PerkinElmer Company was used in our work to investigate the functional groups within the examined material. It can run the samples with range of $7800\text{--}350\text{ cm}^{-1}$, resolution better than 0.8 cm^{-1} . The spectrum shown in Fig. 3.11 illustrates different functional groups presented on the sample. It shows the well-known transversal optical (TO) resonance, the Si–O–Si bond rocking vibrational mode at 477 cm^{-1} , the O–Si–O bond bending mode at 811 cm^{-1} and Si–O asymmetric stretching mode at 1110 cm^{-1} . For each of these atom to atom bond the (TO) resonance give discrete peak.

The other FTIR device was used in this thesis is Nicolet iS10 spectrometer from Thermo Scientific Company. This type of device can read direct from the sample without the need of KBr film or other salt. This technique was applied for β -SiC

nanowires to study their functional groups. Here, the spectrum indicates the transmission radiation in contrast to the absorption one.

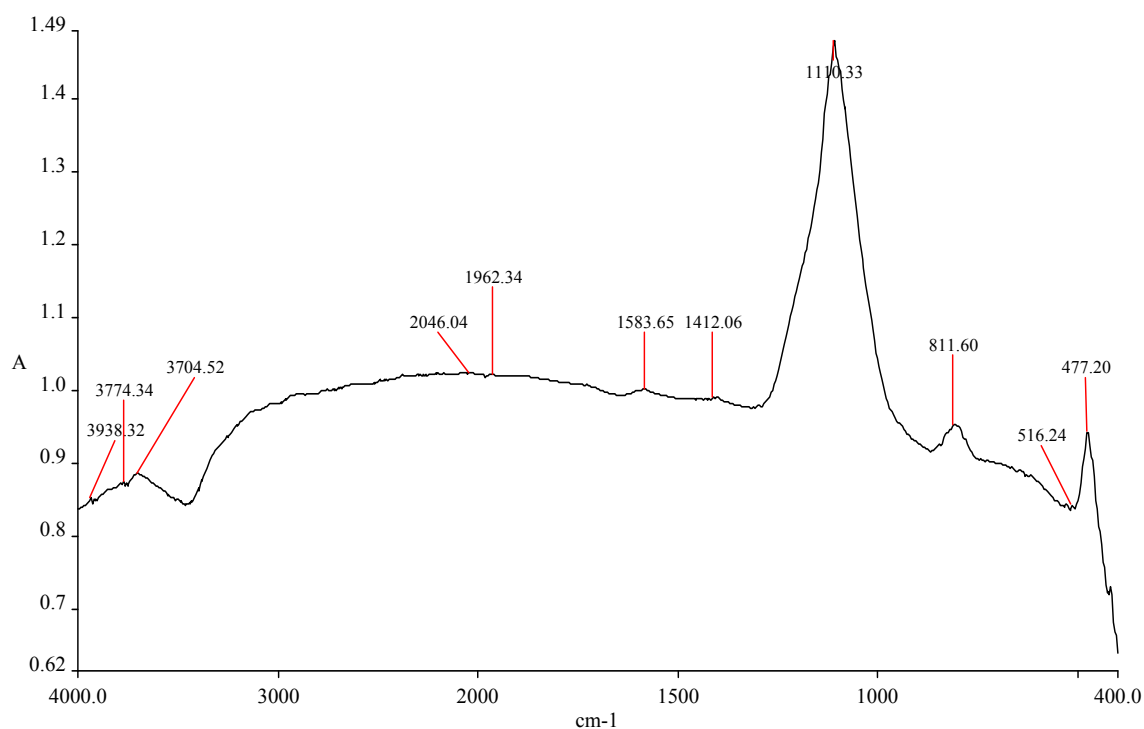


Figure 3.11 Absorption IR spectrum of SiO_x nanowires grown under 1200°C with 10 sccm for 1h.

Chapter 4

Results and Discussions

4.1. Introduction

In the fabrication of silicon oxide nanostructures, the carbo-thermal reaction involving metal oxides mixed in graphite are often used, for example CuO [24] and ZnO [87]. This is because during carbo-thermal chemical reactions graphite can assist the low temperature evaporation of these materials. In this study titanium dioxide with graphite has been used as a precursor to fabricate silicon oxide nanostructures.

The C/TiO₂ ratio was varied to investigate its effect on the yield and shape of the nanostructure. Si substrates coated with Au film catalyst and uncoated have been used.

The SiO_x nanostructures were analyzed using FESEM and EDX for morphology and chemical composition. Also, IR absorption and PL emissions measurements were also conducted.

In another experiment, silicon carbide nanowires have been synthesized using graphite powder and Si substrate and to the best of our knowledge this production method has not been reported before.

4.2. Fabrications of SiO_x Nanostructures without Catalyst

The growth of SiO_x nanostructures was studied using substrates without catalyst, to complement the studies done with Au catalyst. The effect of temperature, deposition time and Ar gas flow rate were studied.

4.2.1. Effect of Temperature on the Growth of SiO_xNWs

Fig. 4.1 shows the FESEM micrograph images of the morphology structure of Si (100) surface after heating at 950°C for 1h under the flow of argon gas with 10 sccm. In Fig. 4.1 (a), holes or pits (dark areas) formed at the centre of the substrate were distributed randomly. Larger diameter pits meet together and formed cracks on the surface as shown in Fig. 4.1(a).

The EDX elemental mass ratio in Fig. 4.1 (a1) shows 90% silicon and 10% oxygen at the center. At the edge the ratio of Si:O is about 1:1. In Fig. 4.1 (b) shows nanowires clearly formed at the edge of the substrate. These wires are long and smooth. The temperature is distributed uniformly over the substrate, so we suggest that the grown silicon oxide nanowires at the edge are not due to temperature variation but may be due to low surface free energy. The surface atoms are highly bonded to each other due to surface tension and more likely to be bonded weakly toward the inside of the substrate. So at the edge, it is likely to form dangling bonds with condensed growth species faster than the other surface places. These dangling bonds works as an anchor for SiO_xNWs which will be discussed in the growth mechanism in details.

The FESEM image of the sample shown in Fig 4.1 (c) with small magnification clearly reveal that no grown SiO_x nanowires before the edge of the sample. Also, the wires are dense and some wires grown vertically on the edge surface.

In general using 950°C as a heating temperature to grow SiO_x nanowires resulted in growths at the areas of the sample edges whereas the rest of the sample is full with pits.

CHAPTER 4 RESULTS AND DISCUSSIONS

Therefore, increasing the temperature from 950°C up to 1200°C is an important parameter to study.

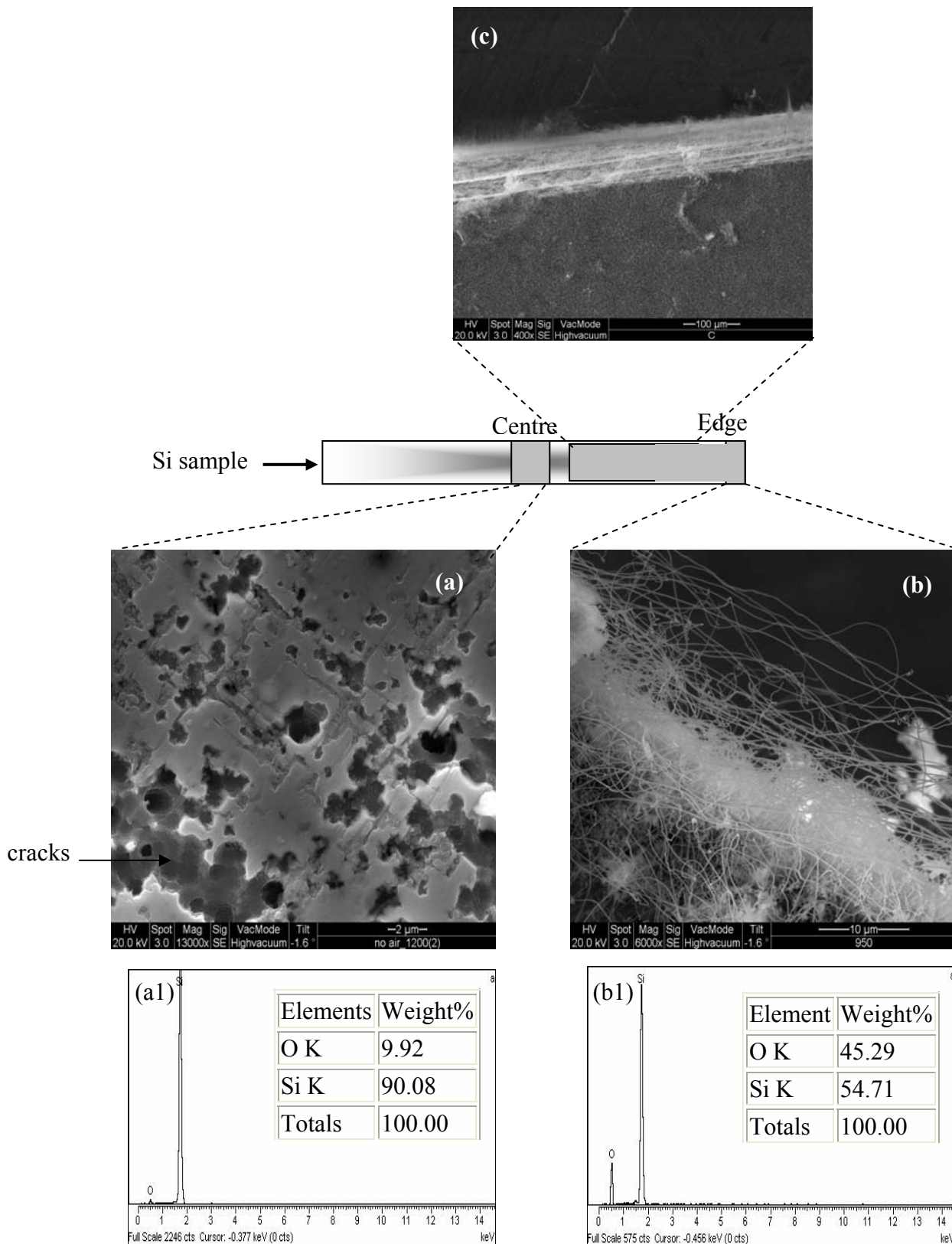


Figure 4.1 FESEM image of sample center (a), edge (b) and (c) in-between. The corresponding EDX spectrum with mass ratios (a1) and (b1) after heating by 950°C for 1h

CHAPTER 4 RESULTS AND DISCUSSIONS

The FESEM images for samples grown at three different temperatures are shown in Fig. 4.2. All images were taken at the centre of the samples. In Fig. 4.2(a), the formations of pits are clearly visible. Sparsely distributed nanowires were visible, formed randomly outside the pits. At a furnace temperature of 1100°C, denser nanowires were visible as shown in Fig. 4.2 (b). Here, the wires were smaller in diameter compared to the sample obtained at 1000°C in Fig. 4.2 (a). Also, the nanowires seem to grow from all over the pits and outside the pits. There is also evidence of long nanowires can be seen around the middle bottom area of the image.

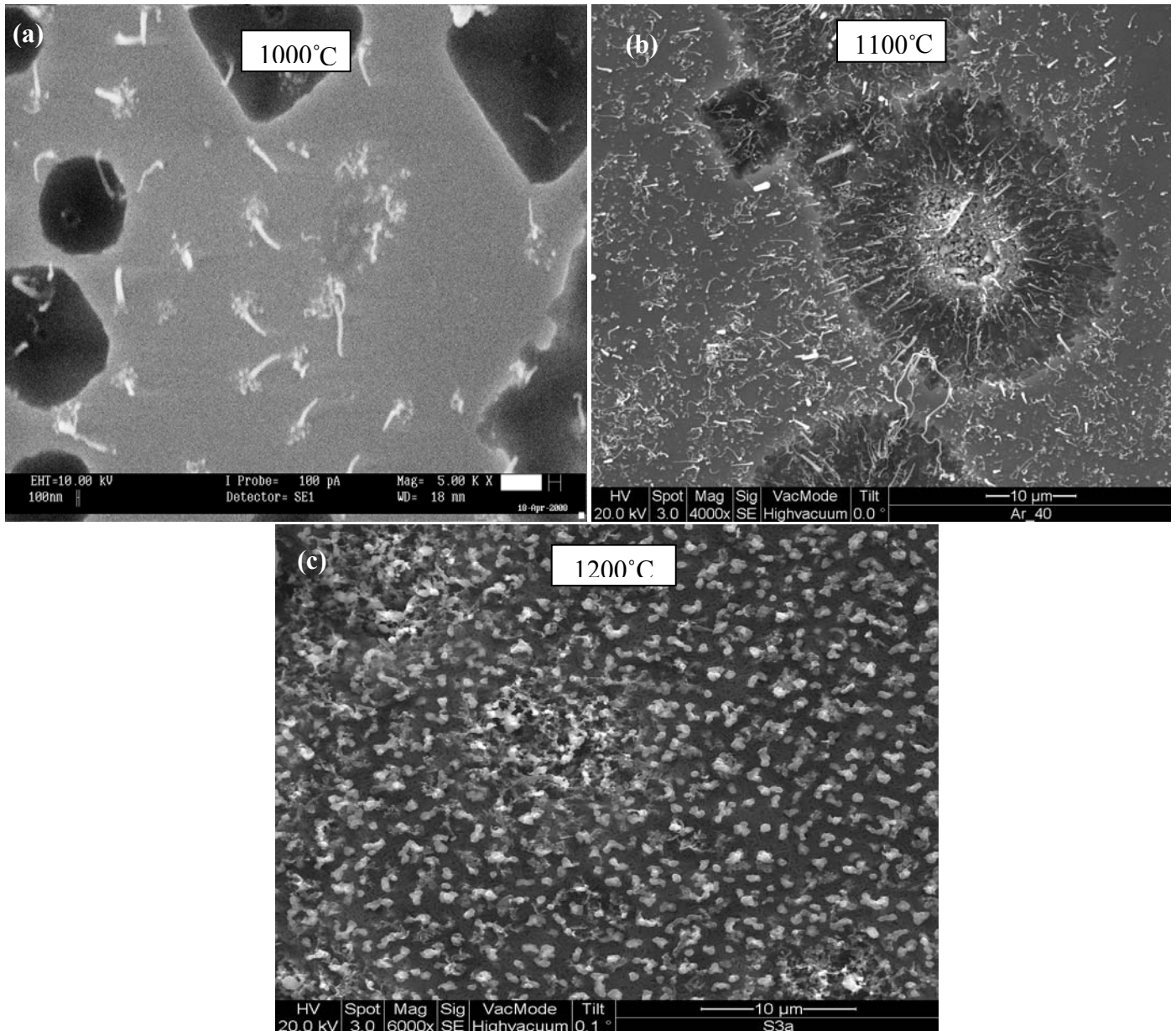
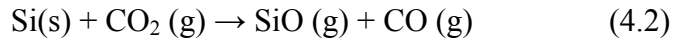
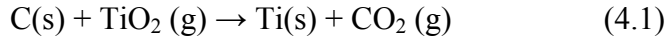


Figure 4.2 FESEM images of SiO_x nanowires grown on pure silicon substrate at (a) 1000°C, (b) 1100°C and 1200°C temperatures with 10 sccm Ar flowrate for one hour.

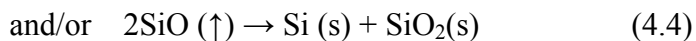
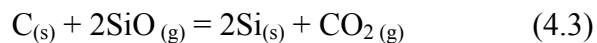
CHAPTER 4 RESULTS AND DISCUSSIONS

When the temperature was increased to 1200°C as shown in Fig. 4.2 (c), stubby structures were formed uniformly covering the whole substrate. The formation of the pits as can be seen in Fig. 4.2 (a) and Fig. 4.2 (b) has been reported before [86]. The formation of pits is due to the evaporation of SiO gas through the reaction in equation (4.1) and (4.2).



From equation (4.1), CO₂ (g) product of the chemical reaction between TiO₂ and solid carbon reacted with silicon on the substrate surface to form SiO gas at temperature > 950°C [86]. To study the effect of Ar flowrate on formation of pits, higher Ar flow rate of 60 sccm and temperature at 1200°C was applied. There were no SiO_xNWs grown near the pits as shown in Fig. 4.3 (a). The tiny rods like structures of SiO_xNWs were formed randomly among the sample surface. The FESEM image of the sample shown in Fig. 4.3 (b) at high magnification reveals one SiO_xNW near one formed pit.

Generally, the formation of SiO_xNWs and the pits can be explained as follows: During Ar flowing process some of solid carbon from the source has been transferred to the surface of the substrate. This is why when Ar flowrate is high as 60 sccm the grown SiO_x nanowires were few and rare. Therefore, most of silicon atoms that involve in the growth process were coming in gas form. And because the only source of silicon is the silicon substrate it self, we believe that the solid substrate silicon evaporated into silicon monoxide in vapor form. Then carbon reacted with silicon monoxide in gas form as in equation (4.3) to form silicon again in solid form when the vapour reached condensation places. Then silicon in solid state is formed and precipitated according to the reactions given in equations (4.3) or (4.4) [85].



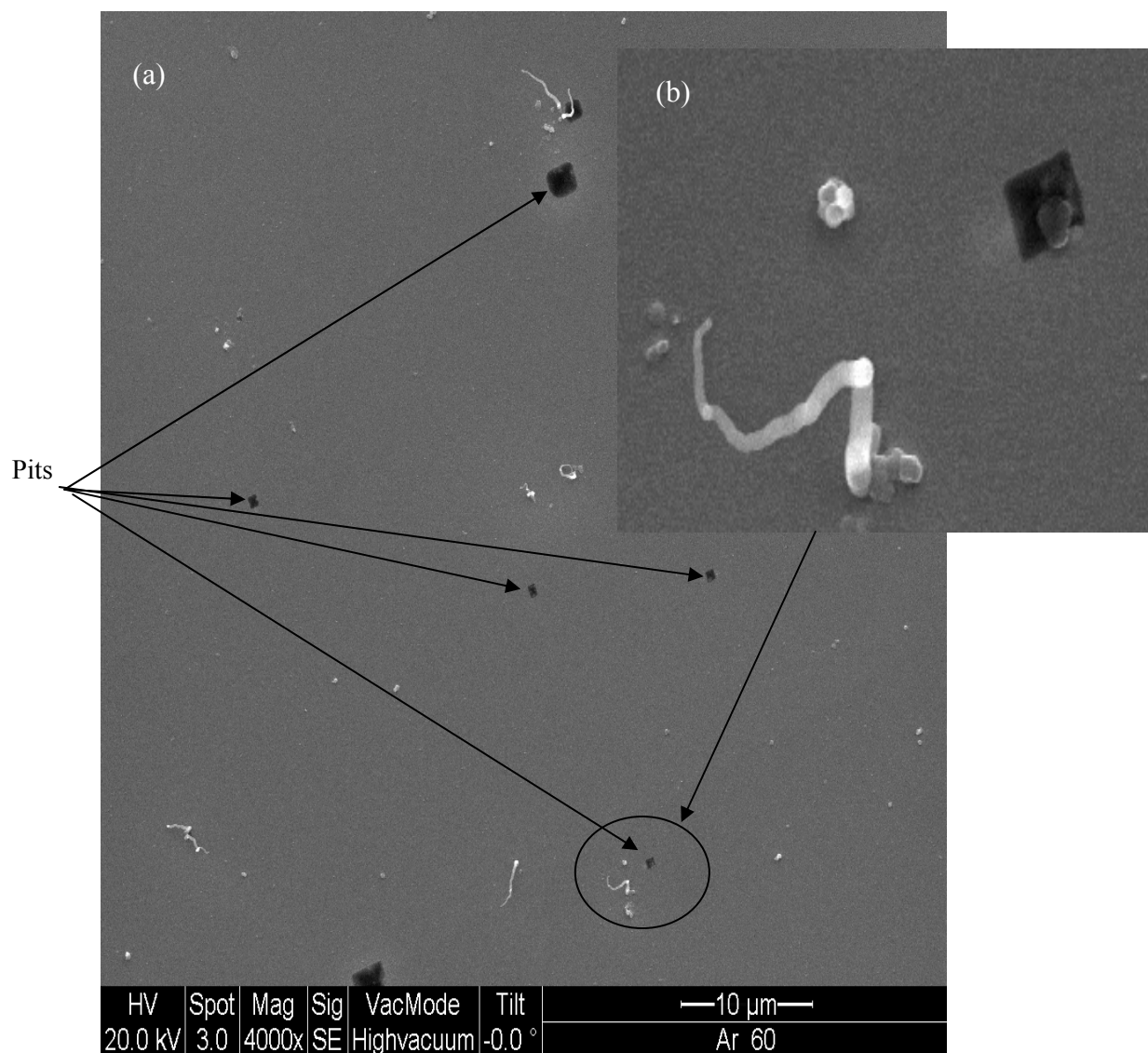


Figure 4.3 FESEM image of (a) pits formation under 60 sccm Ar flow rate at 1200°C for 1h and (b) enlarged image of (a).

4.2.2. Effect of Deposition Time on the Growth of SiO_xNWs

FESEM image of SiO_xNWs in Fig.4.4 (a) shows the initial growth steps on the substrate after being heated up to 1200°C for 5 minutes with argon gas 10 sccm flow rate. The grown wires were horizontal on the sample surface. Higher magnification in Fig.4.4 (b) shows smooth and spherical SiO_x nano-balls. These nano-balls seem to be the growth seeds of the SiO_x nanowires. Here, the evolving SiO_x nanowires from these balls grow in random directions. The result of EDX analysis in Fig 4.4 (c) revealed that these nanostructures were composed of Si and O with the percentage of silicon higher than that of oxygen.

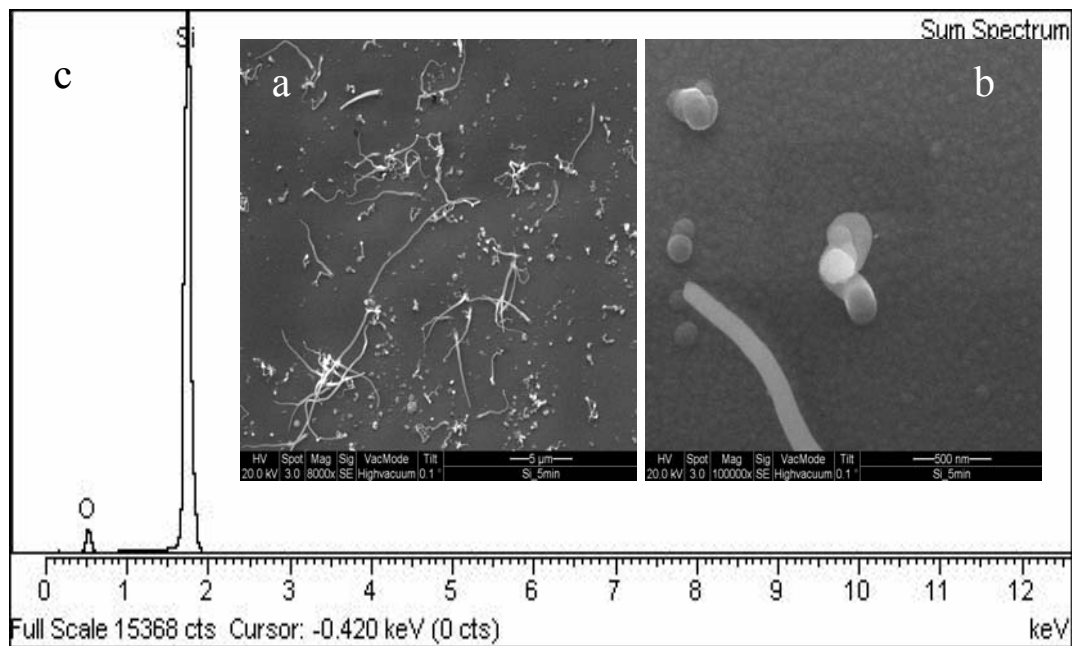


Figure 4.4 FESEM of (a) SiO_xNWs (8k) at 1200°C for 5 minutes, (b) magnified image of the nanoballs (100k) and (c) EDX spectrum of image (a).

CHAPTER 4 RESULTS AND DISCUSSIONS

Another experiment was done for 5, 10, 40 and 60 minutes deposition times. The temperature was kept at 1200°C, the flow rate at 10 sccm.

The results shown in Fig.4.5 reveal the SiO_x nanowires grown at different deposition time. In Fig. 4.5 (a) the sample grown at 5 mins shows short wires with low density and randomly distributed. Also, the SiO_x nano-balls are clearly visible, which can be taken as the initial growth stage.

The FESEM image, in Fig. 4.5 (b), for the sample grown at 10 mins shows long and dense SiO_x nanowires but the sample surface can still be seen. In Fig. 4.5 (c) the synthesized wires at 40 mins were longer and thinner in diameter.

The reduction in the SiO_x nanowires diameter is due to reduction of SiO gas as the deposition time ends. The highest yield of SiO_x nanowires obtained in sample heated for 60 mins in Fig. 4.5 (d). Here, it is hard to see the surface of the sample because it is covered with dense SiO_x nanowires. In general, as the deposition time increases the SiO_xNWs become taller, thinner at the far end of the wires. The length of obtained SiO_xNWs ranged from 2 to tens of microns.

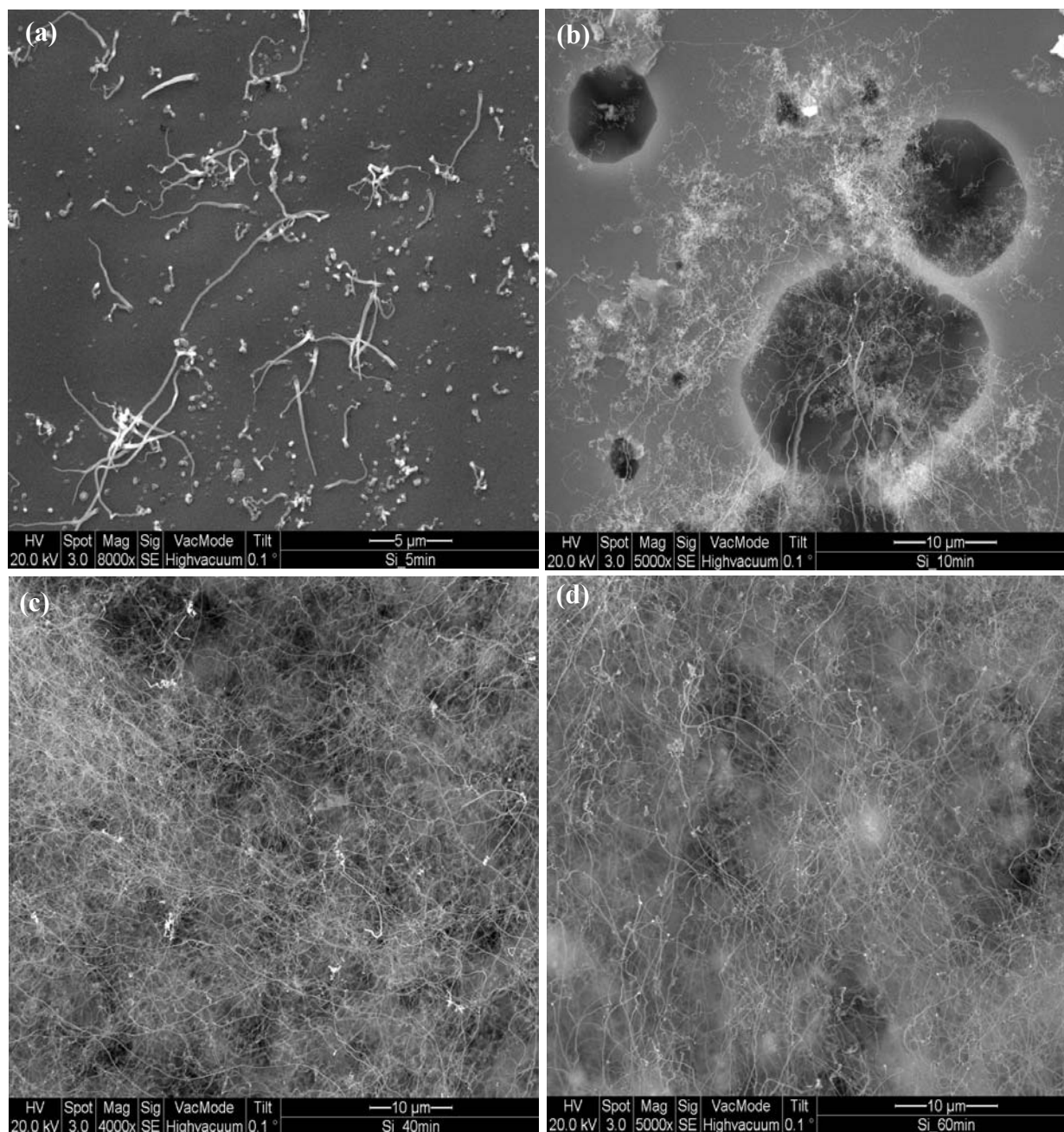


Figure 4.5 FESEM images of SiO_xNWs grown in (a) 5, (b) 10, (c) 40 and (d) 60 minutes under 1200°C temperature with 10 sccm Ar flow rate.

CHAPTER 4 RESULTS AND DISCUSSIONS

Based on our results, the diameter of the SiO_xNWs depends on deposition time. So, as deposition time increases, the SiO_xNW diameter decreases when it is measured at the far end from its base.

For example, the SiO_xNWs diameter was estimated from Fig. 4.6 (a) and Fig. 4.6 (b). The diameters of two SiO_xNWs of a particular length were measured from the FESEM image with same magnification. At the magnification used 1mm equals 34.41nm length of the image scale.

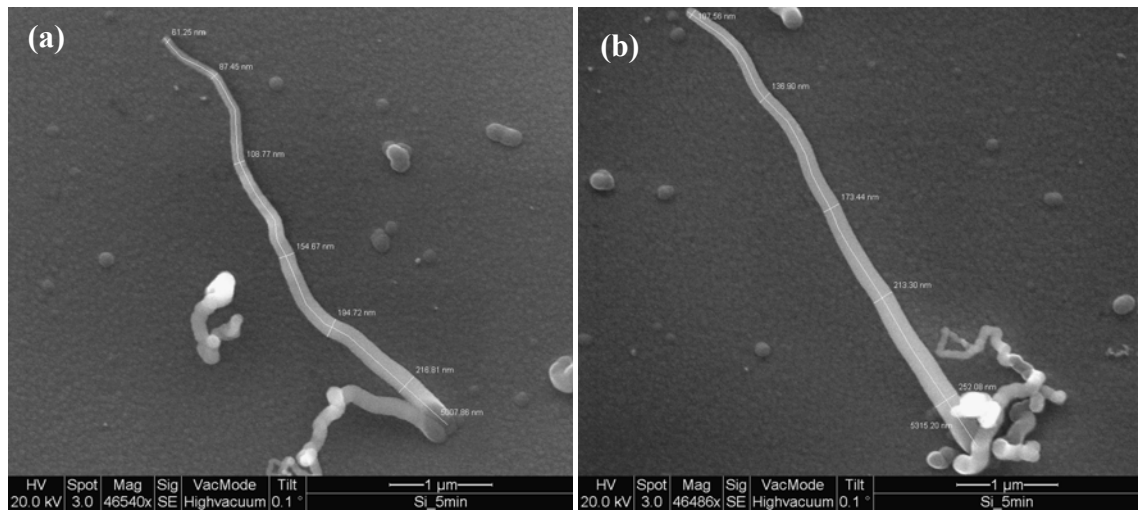


Figure 4.6 FESEM image of two single SiO_xNW (a) and (b) grown on Si(100) substrate for 5 minutes deposition time under 1200°C and 10 sccm flowrate of Ar.

At a specific length of each wire, the corresponding diameter was measured. The measured data for two wires shown in Fig. 4.6 (a) and Fig. 4.6 (b) are listed in table 4.1. The data of measured diameters versus lengths were plotted in Fig. 4.7.

Table 4.1 The SiO_xNW diameters and lengths data.

SiO _x NW in Fig. 4.6 (a)		SiO _x NW in Fig. 4.6 (b)	
SiO _x NWs Diameter	SiO _x NWs Length (μm)	SiO _x NWs Diameter	SiO _x NWs Length (μm)
360	0.2	370	0.3
220	1.0	220	1.1
200	2.3	190	2.2
150	3.7	160	3.5
110	5.3	120	5.4
90	7.5	80	7.2
60	8.3	70	8.5

In Fig. 4.7, we can see the short wire has bigger diameter. At the base of the first wire, the length is about 0.2 μm and the diameter is the highest (about 360 nm). As the wire increase in length the diameter decreases. So at the far end the length of the wire reached 8.3 μm and the diameter is 60 nm. As a results, controlling the deposition time can be one of the important parameter to determine the SiO_xNW diameter and length.

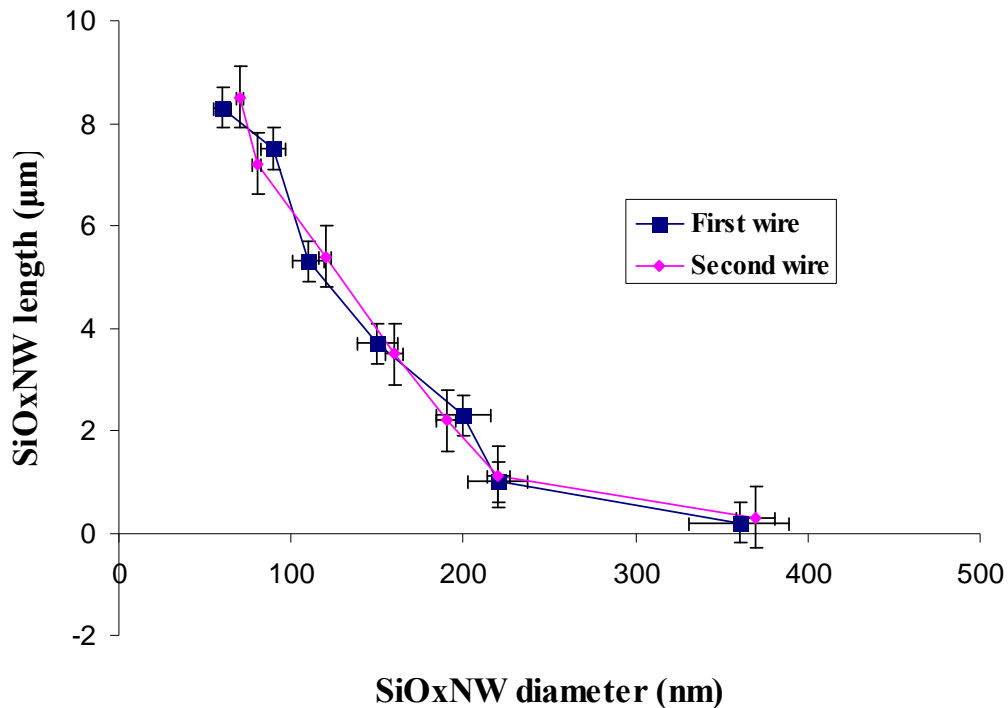


Figure 4.7 Two examples of the variation of SiO_xNWs diameter at different length fabricated for 5 minutes under 1200°C with Ar gas of 10sccm flowrate.

CHAPTER 4 RESULTS AND DISCUSSIONS

The base of the wire in the form of nano-ball with bigger diameter can attract more silicon atoms from SiO gas. This is due to the higher percentage of silicon atoms in gas phase to the silicon atoms inside the nano-balls ($P_{\text{Si (V)}} > P_{\text{Si (L)}}$).

Therefore, more liquid Si atoms start to build the L-S interface and precipitate in solid form beneath this surface.

Fig. 4.8 shows the results of XRD analysis for the samples deposited at different time. It reveals that these nanowires are amorphous. Also the wires are covering the substrate. The amorphous structure of SiO_x nanowires may refer to the oxidation of silicon during growth process. Oxygen atoms may penetrate to the system through connected places either at gas meter or vacuum system connections.

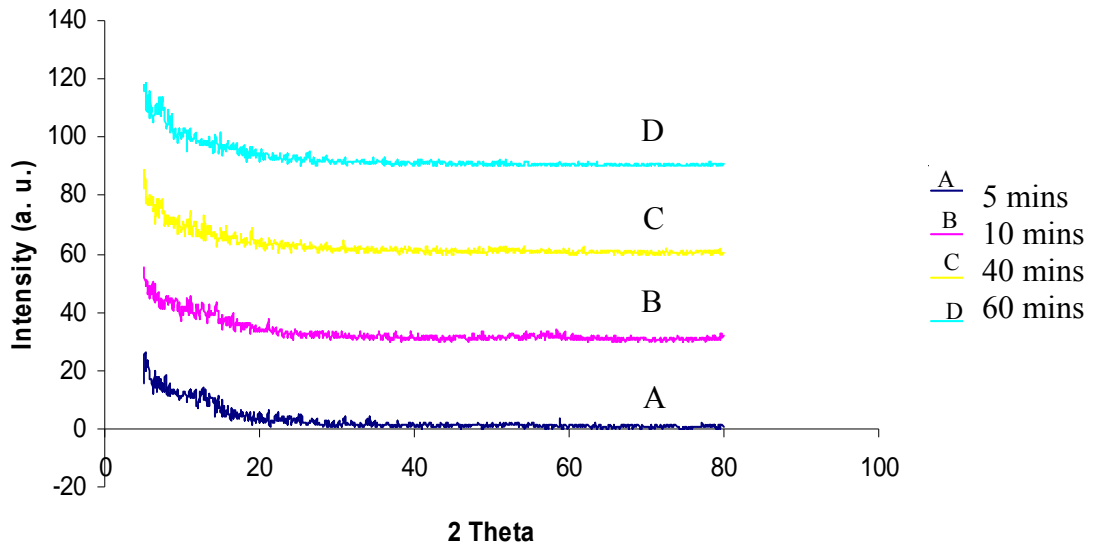


Figure 4.8 XRD spectra of SiO_x NWs for 5, 10, 40, 60 mins deposition time under 1200°C heating temperature with 10sccm Ar flowrate.

4.2.3. Effect of Argon Gas Flow Rate on the Growth of SiO_xNWs

To study the effect of argon gas flow rate, the temperature was kept constant at 1200°C and the deposition time at 30 minutes. In Fig. 4.9 (a-d), the FESEM images taken at 60, 40, 20 and 10 sccm flow rates respectively. For each sample three different magnifications were used such as in Fig. 4.9 (a) 1-3.

Fig. 4.9 (a) shows hardly any wire, pits are visible, very sparse growth at a magnification of 30k. A result of sample grown at 60 sccm Ar flowrate is shown in Fig. 4.9 (a). Here, it is rare to find SiO_x nanowires and the only wire shown in image 3 is short and has 52 nm in diameter at the far end. Also this wire seems to lean down towards the surface. Moreover, small quantities of SiO_x nano-balls are randomly distributed over the sample surface.

In Fig. 4.9 (b) the wires become denser and longer as the flow rate is reduced to 40 sccm. Here, the SiO_x nanowires are anchored to sample surface and they have different lengths depends upon growth starting stage.

In Fig. 4.9 (c) the FESEM of the sample at 20 sccm reveals crowded and taller SiO_x nanowires. Also, the SiO_x nano-balls have bigger diameter as the deposition time increases, which agrees with our previous results. Reducing the Ar flow rate to 20 sccm, the growth of SiO_xNWs increased as evident from Fig. 4.9 (c).

The longest and highest yield of SiO_x NWs has been found when the Ar flowrate is kept at 10 sccm, see Fig. 4.9 (d). Here, the network of SiO_x nanowires seems to be far from the sample surface with smaller diameter of about 44nm.

The decreasing of argon gas flow rate increases the SiO_xNWs lengths and yields. This means that, the higher the flow rate the higher loss of evaporated growth species. This implies that there is silicon or silicon compound available in vapour form, which conforms to our results in the study of the effect of deposition time on the growth of SiO_x nanowires.

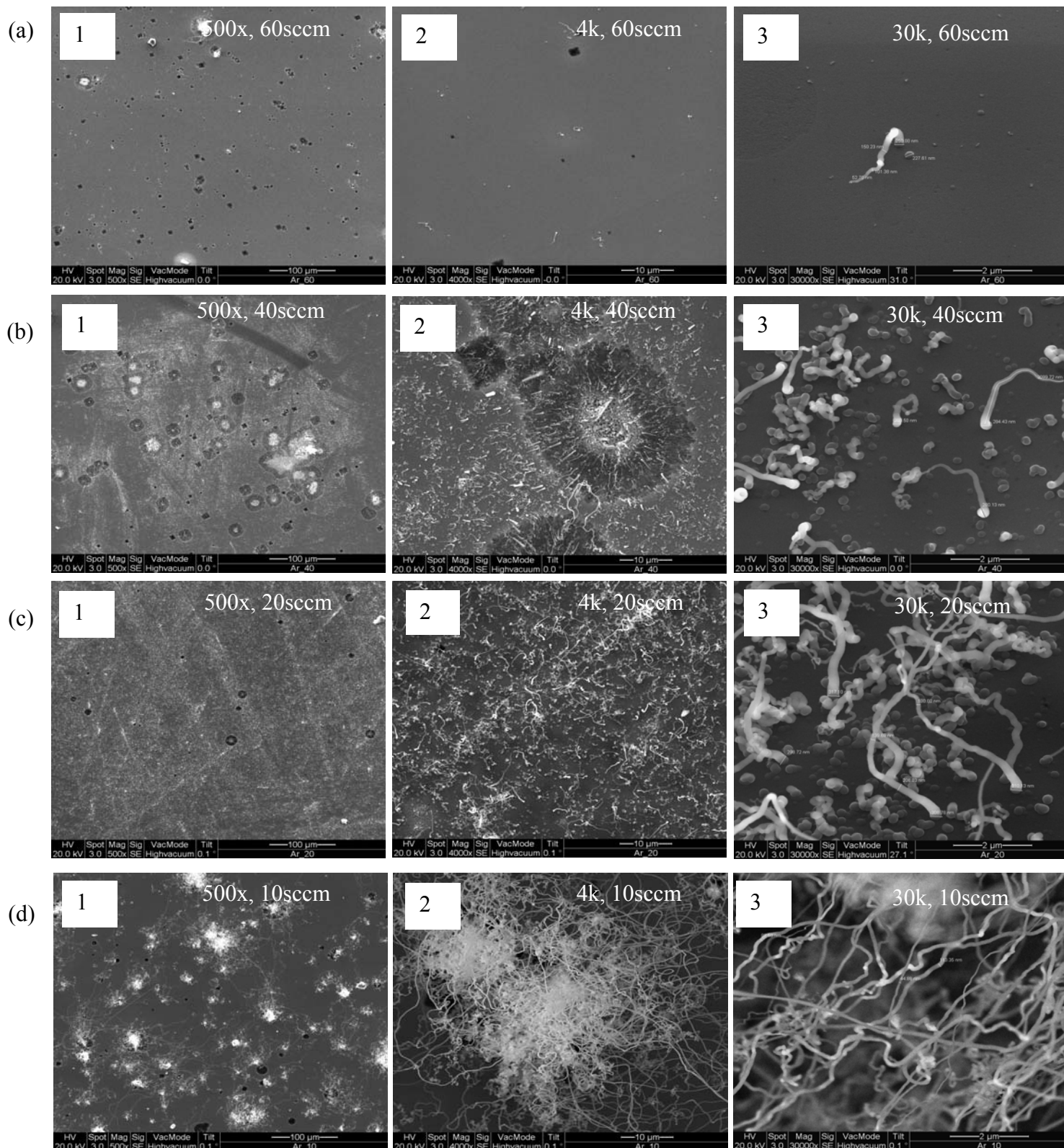


Fig.4.9 FESEM image at different magnifications (1-3) of SiO_x nanowires deposited at Ar flowrate, (a) 60, (b) 40, (c) 20 and (d) 10 sccm using temperature of 1200°C for 1h.

CHAPTER 4 RESULTS AND DISCUSSIONS

Furthermore, when the argon flowrate was less than 10 sccm no growth of SiO_xNWs was observed, which shows the important role of the argon flow rate in growth process. This is because; small amount of Ar flow rate is required to distribute the growth species over the growth sites on silicon substrate as well as the ability to cause temperature fluctuations.

The temperature variation over the Si substrate played an important role in the process of the synthesis of the SiO_x nanowires. So, at low temperature some of evaporated SiO gas will condense and form the wire base, which continue to form SiO_xNWs .

Now consider the one SiO_xNW diameters in Fig. 4.9 (a-3). The diameters decreased along the SiO_x nanowire as we go far from its base or nano-ball.

To study the effect of the Ar flow rates on the SiO_xNWs length and diameter, samples shown in FESEM image with 30kx magnification (number 3) in Fig. 4.9 were chosen and all data of the average length and diameter of the SiO_xNWs were measured using a ruler on a printed image.

For example, in Fig.4.9 (c-3) the wire length is about 2.1 μm (from FESEM measurements), which is equal to 61 mm measured by ruler for the same magnification. This measurement is used on a scale to measure the length of all possible wires for same magnifications (30k), i.e. 1mm is equivalent to 34.41nm.

The collection of data for different argon flow rates, the average nucleation nano-ball diameters and the calculated average SiO_xNWs lengths are in table 4.2.

CHAPTER 4 RESULTS AND DISCUSSIONS

Table 4.2 The collection of data for different argon flow rates, the average nano-ball diameters and the average SiO_xNWs lengths.

Ar flow rate (sccm)	Average nano-ball diameters (nm)	Measurements of average SiO _x NWs length (μm)
60	250	1.8
40	280	3.1
20	310	5.4
10	350	9.7

These data are plotted in Fig.4.10 (a) and (b). The synthesized SiO_xNWs length strongly depends upon the argon flow rate.

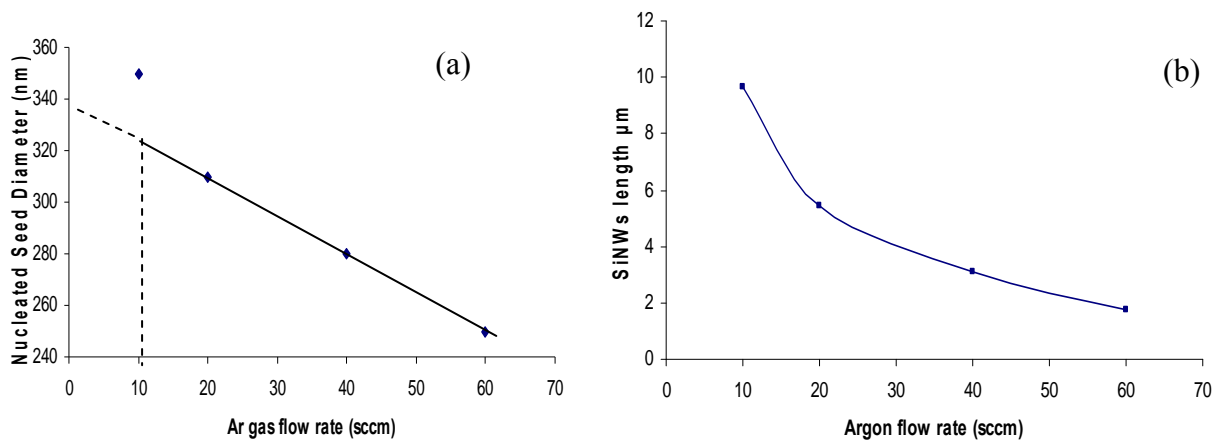


Figure 4.10 Graphs of argon flow rate versus (a) average nucleated seed diameter and (b) average SiO_xNWs length.

The inversely linear relation in Fig. 4.10 (a) between Ar flowrate and wire base or nucleated seed diameter shows the diameter become smaller as the Ar flowrate increased.

Also, it can be seen in Fig.4.10 (a) that the line will cut y-axis at 340 nm and the line slope is -1.5, which lead to an empirical equation (4.5):

$$y = (-1.5)x + 340 \text{ nm} \quad (4.5)$$

Where (y) represents the nano-ball diameter and (x) represents the argon gas flow rate.

That means we can calculate the seed diameter at any given argon gas flow rate and the maximum of seed diameter is 340 nm.

CHAPTER 4 RESULTS AND DISCUSSIONS

Therefore to control the SiO_xNW diameter or length at certain Ar flowrate the other parametric effect (heating temperature, deposition time and heating rate) should kept without change. The relation in equation (4.5) to calculate the nano-ball diameter did not agree with experimental results when argon flow rate is less than 10 sccm because no SiO_x nanowires were obtained. That means, the amount of Ar gas flowrate is not enough to carry the growth species and cause temperature fluctuations.

It clearly showed in Fig.4.10 (b) the exponential increasing of the wires length as the flow rate decreases and the diameter of the ball is decreasing linearly as the argon flow rate increases. Similarly, the diameter of the nano-ball is linearly decreases as the argon flow rate increases. Further more, the SiO_xNWs density; number of nanowires available per cm^2 , for each Ar flow rate has been plotted as in Fig. 4.11.

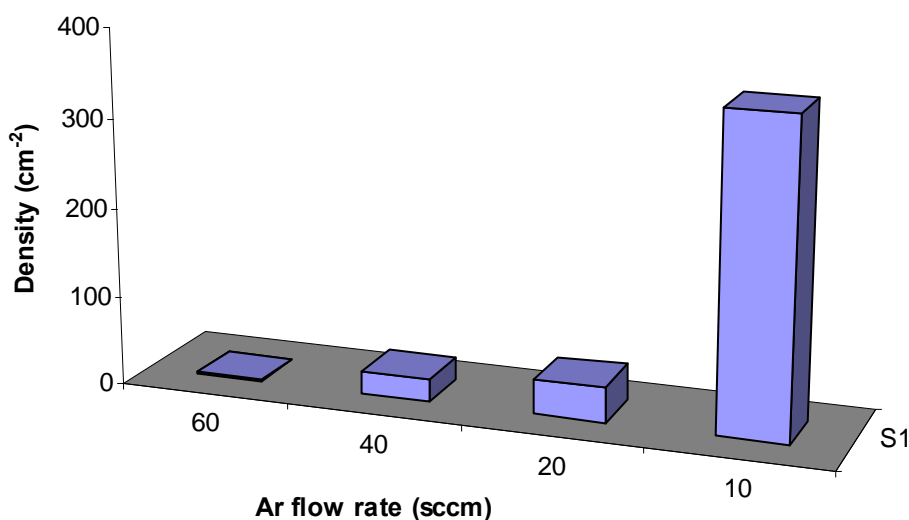


Figure 4.11 A schematic diagram of SiO_xNWs densities at different Ar flow rates

As expected, the highest SiO_xNWs density occurs when the Ar gas has the lowest flowrate at 10 sccm. This is also related to residence time of growth species to accomplish the growth. Therefore, small amount of Ar flowrate increases deposited time, which allows the growth species to move around over the substrate surface and

CHAPTER 4 RESULTS AND DISCUSSIONS

encourage the one dimension growth of SiO_x nanowires. These wires keep forming as long as the growth species available.

The XRD spectrums show all wires are amorphous, Fig. 4.12 (A and C), which can be refer to the high oxidation process during cooling time. Small intensity peaks at $2\theta = 58.1^\circ$ corresponding to Si (310) are shown in Fig. 4.12 (B and D) but this peak not discrete and it has very low intensity so the overall obtained silicon oxide nanowires are amorphous.

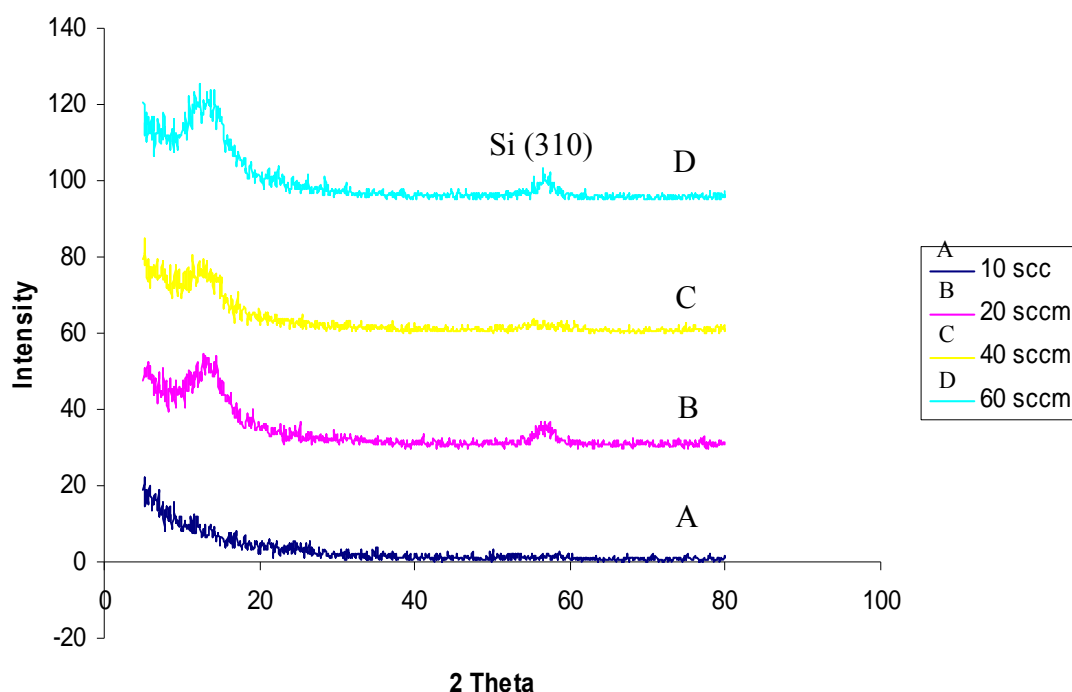


Figure 4.12 XRD spectrums of SiO_x NWs at 10, 20, 40 and 60 sccm flow rates using 1200°C heating temperature and 30 mins deposition time.

4.2.4. Discussion of Non-catalyst Growth of SiO_xNWs

The initial stage of SiO_x nanowires growth starts when the silicon on the surface get oxidized as thin film at the ratio of Si:O of about 1:1. This film starts to form molten SiO_x nano-balls due to the evaporation and condensation of SiO gas as in Fig. 4.13 stage (1).

Then silicon diffuses from Si substrate towards these balls by solid-liquid-solid (SLS) mechanism until the saturation stage occurs inside the nucleated ball as in schematic diagram in Fig. 4.13 (step 2).

The growth should stop at this stage because of equilibrium between amount of silicon oxide inside the ball and those coming from the substrate silicon, but the growth continuously for long wires because of the continuous evaporation of silicon monoxide (SiO) gas. This gas is responsible in supplying the growth by Si feed stock, which then condenses at lower temperature sites due to temperature fluctuations and dissolved in the agglomerated balls of mixed Si and SiO_x alloy through the vapour-liquid-solid (VLS) mechanism.

The SiO_xNW nuclei could form on low energy sites of silicon wafers such as defects. Defects, such as stacking faults in the nucleation sites, will enhance the one-dimensional growth. Therefore, when the pressure or concentration of the SiO vapour is enough and the temperature increases, the Si and O start to condense into the nano-balls forming SiO_xNWs, which start growing up from the ball or forming a root (step 3). Then, the wire starts to grow from the surface of the substrate as it absorbed more growth species (step 4). The reduction of SiO_xNWs diameters caused by the amount of growth species Si and O available in vapour form, which decreased gradually until stop at the tip of the wire.

This is why the tip or the end of the wire has smallest diameter. Zhang et. al. [180] found that the most energetically favourable small clusters are silicon monoxide (SiO)

i.e., Si to O ratio of 1:1. The evaporated SiO clusters deposited on a substrate would be anchored due to their high reactivity at Si sites. Non-bonded reactive silicon atoms in the same cluster are now exposed to the vapour with their available dangling bonds directed outward from the surface. They act as nuclei that absorb additional reactive silicon oxide clusters and facilitate the formation of SiO_xNWs .

Depending on oxygen assisted growth mechanism (OAG), the percentage of oxygen played an important role in the SiO_xNWs formation. The smaller the O atoms ratio, the higher the reactivity between the formed dangling bonds and the transported vapour. Here, OAG controls the percentage of the evaporated silicon monoxide gas from the substrate which then changed into solid silicon at condense places to form the silicon oxide nanowires. The latter mechanism points out that there are two phases of initial source of silicon. The first one is solid from the substrate and the second is SiO vapour after carbothermal reactions as shown in equation (4.2).

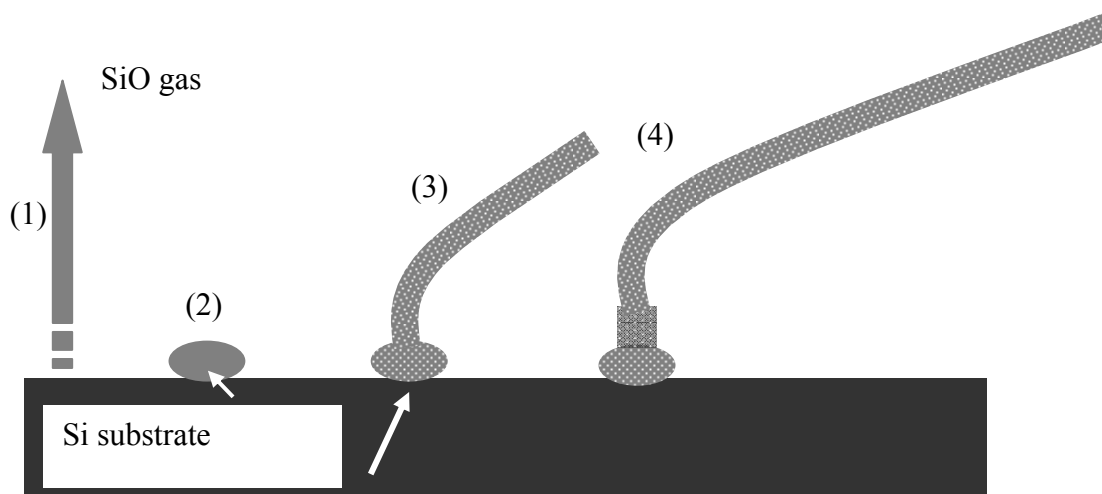


Figure 4.13 A schematic diagram of non-catalytic growth of SiO_x nanowires by SVLS mechanism.

4.2.5. Summary

The obtained SiO_x nanowires diameters were about from 60 nm to 300 nm and several microns in length. Pits formed on the silicon substrate surface maybe due to the evaporation of silicon monoxide at $>900^\circ\text{C}$. Increasing temperature and deposition time and decreasing the flowrate increases the growth yield of SiO_xNWs . The wires diameters were reduced as the length of the wires increased and the highest density of SiO_x nanowires obtained was at 10 sccm flow rate. No wires obtained when lowering the flowrate less than 10sccm. The XRD results show the amorphous nature of these wires.

4.3. Fabrications of Silicon Oxide Nanostructures on Au Coated Si Substrate

In the fabrication of SiO_xNWs using gold as catalyst, 270 nm layer of gold was deposited on Si substrates using a dc sputter coater. Annealing of Au thin film played a role in the growth of SiO_x nanostructures with the control of the growth parameters process.

The sample shown in Fig. 4.14 present Au coated Si substrate annealed at 450°C for 1h using argon as the ambient gas. Here, the gold layer and silicon at the surface will be mixed in an Au-Si alloy.

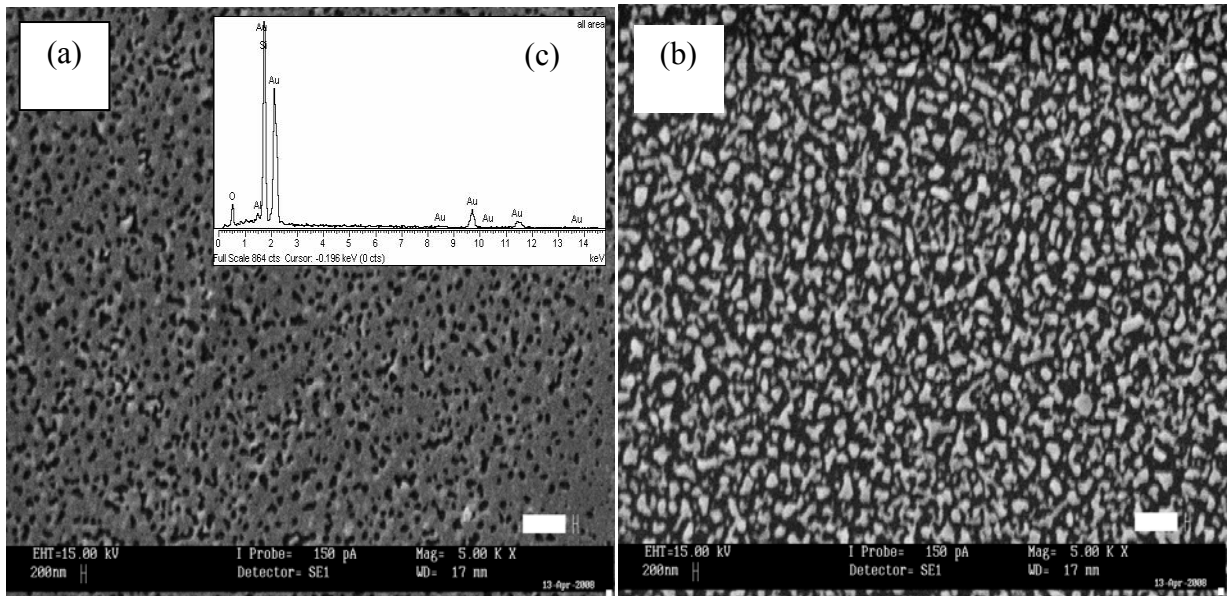


Figure 4.14 FESEM of gold thin film over Si substrate heated at (a) 450°C and (b) 550°C temperatures.

The Au-Si alloy described by Massalski et al. [70] presents a deep eutectic temperature, which is the indication of a strong attractive interaction between Au and Si in the liquid state, in contrast with the strong repulsive interaction between Au and Si in the solid state.

The temperature for SiO_xNW formation must be above the eutectic point as liquid droplets can form under this condition. From the phase diagram studied by Massalski et al. [70] the melting (T_m) temperatures for Au and Si are 1046°C and 1414°C respectively. But both Au and Si at certain percentage of Si reach a eutectic alloy

CHAPTER 4 RESULTS AND DISCUSSIONS

temperature around 363°C. The gold catalyst has very low eutectic temperature with silicon, when comparing to other metals. So the Au-Si alloy melted faster at the higher temperature employed.

This is clearly visible in sample shown in Fig. 4.14 (b) when the temperature is elevated up to 550°C. Here, the molten alloy seems to be distributed in undefined manner to small Au-Si alloy nanoparticles. These Au-Si nanoparticles are less in density than that shown in Fig. 4.14 (a).

More spherical and smaller Au-Si alloys are due to the effect of temperature on the liquidity of the alloy. So the EDX spectrum in Fig. 4.14 (c) shows gold, silicon and oxygen elements existed in the sample which indicates that these alloys oxidized during cooling down.

4.3.1. Parametric Studies of SiO_x Nanostructures on Au Coated Si Substrate

Parametric study of the synthesis of SiO_x nanostructures was to determine the best condition for the growth of SiO_x nanostructures.

Equal proportion of TiO₂+C mixture in a porcelain boat was placed at the furnace centre inside the horizontal quartz tube. Then Au coated silicon substrate was loaded at 2 cm apart from boat.

Next, the system was flushed with Ar gas for two minutes and then kept at 10 sccm Ar flowrate. The temperature was then elevated from room temperature until 1200°C or as required with a 1.5°C/sec heating rate. Upon reaching the desired temperature, the substrate was kept inside the chamber for 1h, as described in section (3.1).

4. 3.1.1. Effect of Temperature on the Growth of SiO_x Nanowires

To study the effect of furnace temperature on the growth of SiO_xNWs on Au coated Si substrates, the deposition temperature was varied at 900°C, 1000°C, 1100°C and 1200°C.

FESEM images in Fig. 4.15 show different samples obtained at different temperatures. Fig. 4.15 (a) shows the sample at 900°C. Visible Au nanoparticles as spherical balls surrounding with shell of oxide silicon layers are indicated from the corresponding EDX spectrum. The Au nanoparticles seem to be distributed uniformly over the sample. Then, the FESEM image of obtained sample shown in Fig. 4.15 (b) reveals thick SiO_x nanowires in a connected network orientation at 1000°C. Also for each Au-Si alloy nanoparticles, two or more branches of SiO_x nanowires were formed but with shorter length.

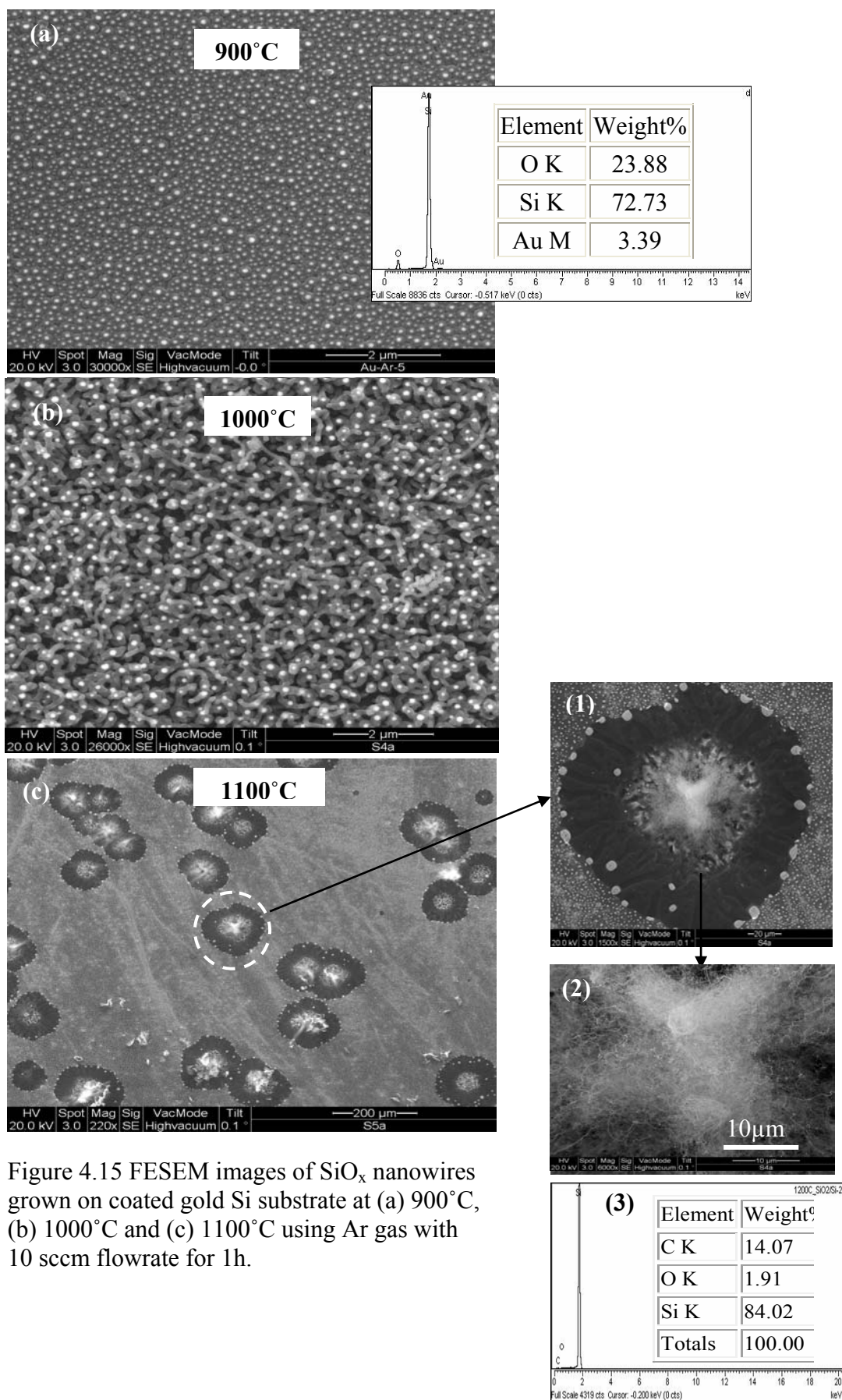


Figure 4.15 FESEM images of SiO_x nanowires grown on coated gold Si substrate at (a) 900°C, (b) 1000°C and (c) 1100°C using Ar gas with 10 sccm flowrate for 1h.

CHAPTER 4 RESULTS AND DISCUSSIONS

The sample shown in Fig. 4.15 (c) shows SiO_x nanowires grown at 1100°C. Here, the morphology of the sample looks like island shape which is randomly distributed on the sample. Also, it good to mention that the magnification of the FESM image shown in Fig. 4.15 (c) is too small around 220x and that because we want have to a general picture of the morphology of the sample.

Also, the grown SiO_x nanowires were high in yield around these islands; see inset (1) of Fig.4.15 (c). In the middle of the island, Fig. 4.15 (c), down magnified image (2), high growth of fine and complicated SiO_x nanowires network were visible.

Based on EDX analysis shown in Fig shown in Fig. 4.15 (c) spectrum (3), there was no gold detected in the SiO_xNWs located at the center of these islands. So at the centre of the island the SiO_x nanowires grown direct from the substrate without assistance of Au-Si alloy, which can occur in such a temperature as discussed in non-catalyst growth of SiO_x nanowires section.

On the other hand, the growth of SiO_xNWs at the islands surroundings were according to the base of the growth of SiO_x nanowires. Magnified FESEM images in Fig. 4.16 (a) and 4.16 (b) show clearly the Au-Si alloy and the attached growth of SiO_x nanowires.

The EDX spectrum in Fig.4.16 (c) shows the high mixture of Au and Si atoms. Also, Fig.4.16 (b) shows the Au-Si alloy or nucleated balls, responsible for the first growth step, surrounded by thin layer of SiO_x.

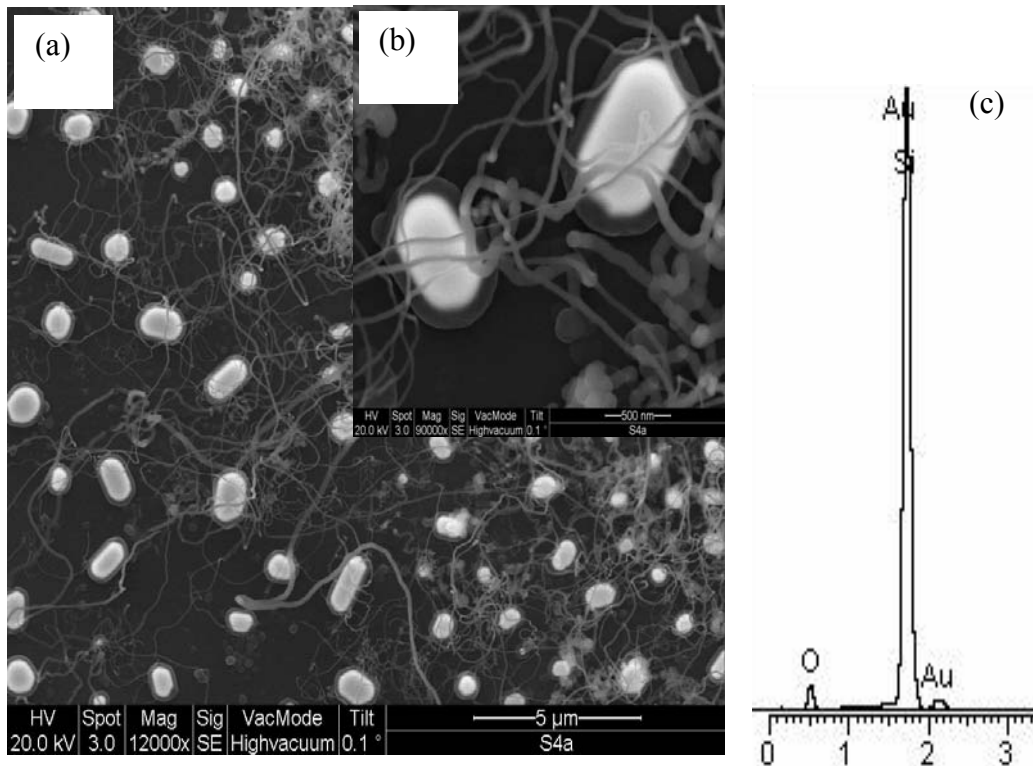


Figure 4.16 FESEM of (a) SiO_x nanowires grown at 1100°C from base Au-Si alloy (b) enlarge image of two Au-Si alloys with attached SiO_xNWs and (c) EDX spectrum of image (a).

The EDX spectrum in Fig.4.17 (a1) taken at point b in image (a2), nucleated ball, shows high concentration of gold on the centre of ball around 50%.

While it was reduced to about 5% at the surrounding as in Fig.4.17 (b1) at point c in image (b2) which shows that the Au particles does not exist within the obtained SiO_xNWs.

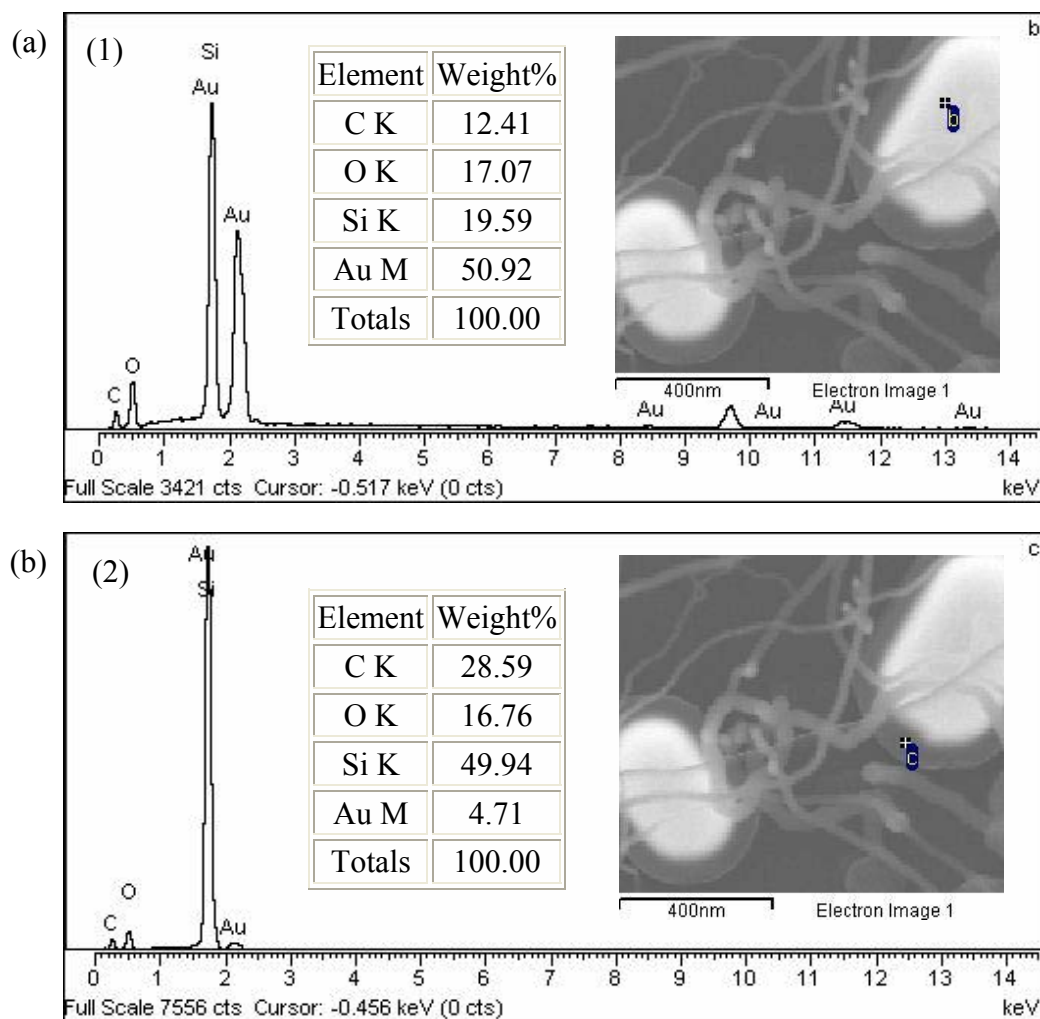


Figure 4.17 EDX spectrum of (a) FESEM image a2, centre of the nucleated ball and (b) EDX spectrum of FESEM image b2, the ball surrounding SiO_x layer.

4.3.1.1.1. Silicon Oxide Nanostructures observed at Temperature 1200°C

To study the different SiO_x nanostructure morphologies formed, the temperature was set at 1200°C under 10 sccm Ar flowrate for 1h deposition time.

The obtained nanostructures are shown in Fig.4.18 (a), which can be divided into two shapes of nanostructures, nanowires and nanofibers. Nanofibers are hollow wires like structures, which looked like transparent tubes. The grown SiO_x nanowires in Fig.4.18 (a) were vertical with a spherical ball at the end of the wire.

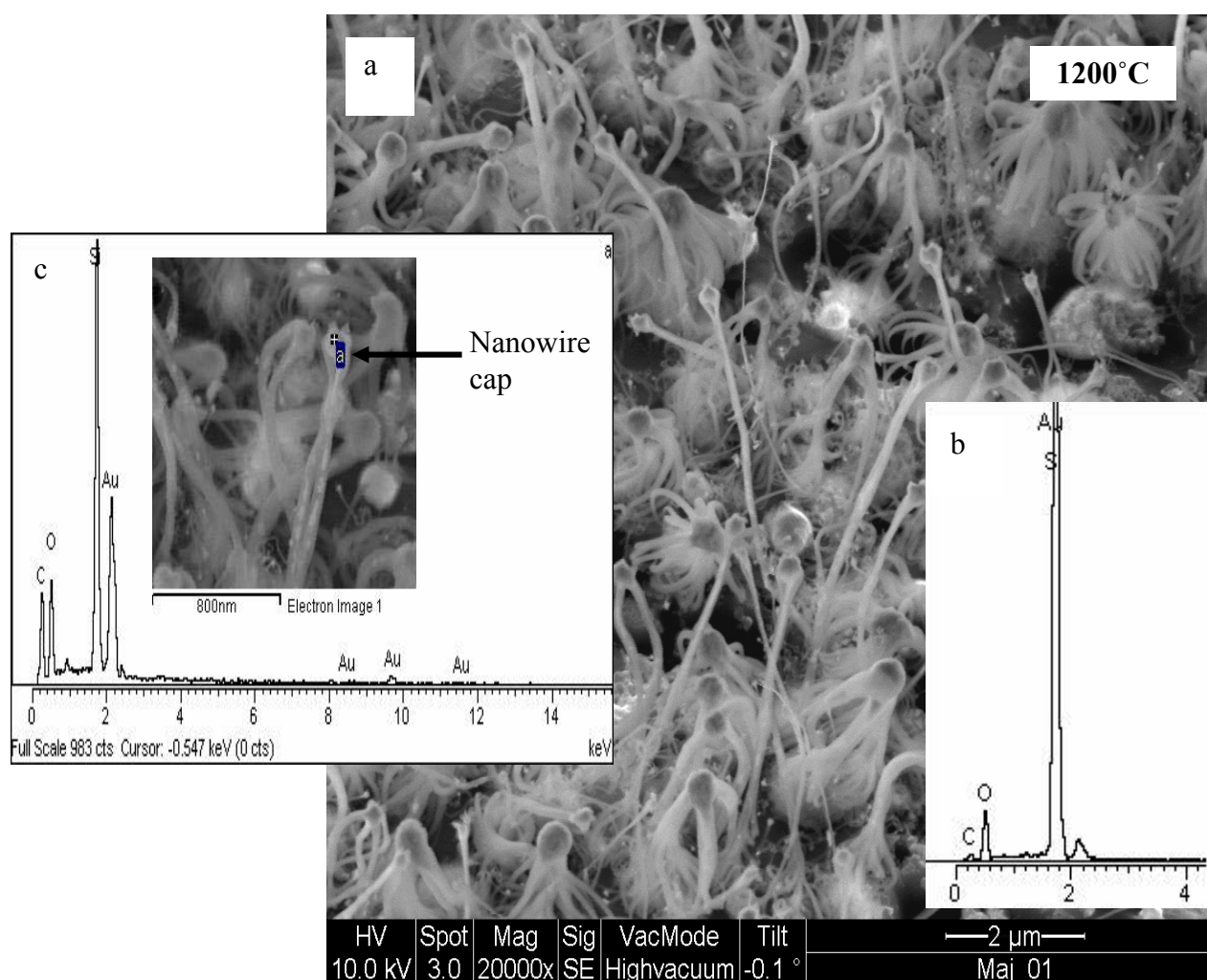


Figure 4.18 FESEM of (a) SiO_x nanostructures grown at 1200°C under 10 sccm Ar flowrate and 1h deposition time, (b) EDX spectrum of sample (a) and (c) EDX spectrum of one nanowire's cap (see inset image).

CHAPTER 4 RESULTS AND DISCUSSIONS

The obtained SiO_x NWs were smooth with a cap of Au-Si alloy on the top of the wires. The measured diameters of SiO_x NWs measured in FESEM are between 20 nm to 240 nm. These wires were 190 nm to several microns in length.

The EDX spectrum shown in Fig.4.18 (b) revealed that the nanostructures consist of Si, O, Au (the catalyst) and carbon, which might come from the graphite powder.

Fig. 4.18 (c) shows the magnified image of one SiO_x nanowire with EDX spectrum taken at the spherical nanowire cap, which reveals Si and Au as two elements existing on the cap.

The Au-Si alloy located at the SiO_x NW cap, which indicates the important function of this alloy and specially gold in the growth of standing SiO_x nanowires. Here, the Au-Si alloy or cap controls the wire diameter because the precipitation of silicon accorded at the bottom of the Au-Si alloy makes the wires grow downward and pushing the cap upward with same wire diameter.

The FESEM image of sample shown in Fig.4.19 reveals high magnification of smooth selected SiO_x nanowire. Here, the SiO_x nanowire is embedded with gold which can be seen clearly in Fig. 4.19 (a) and Fig. (b).

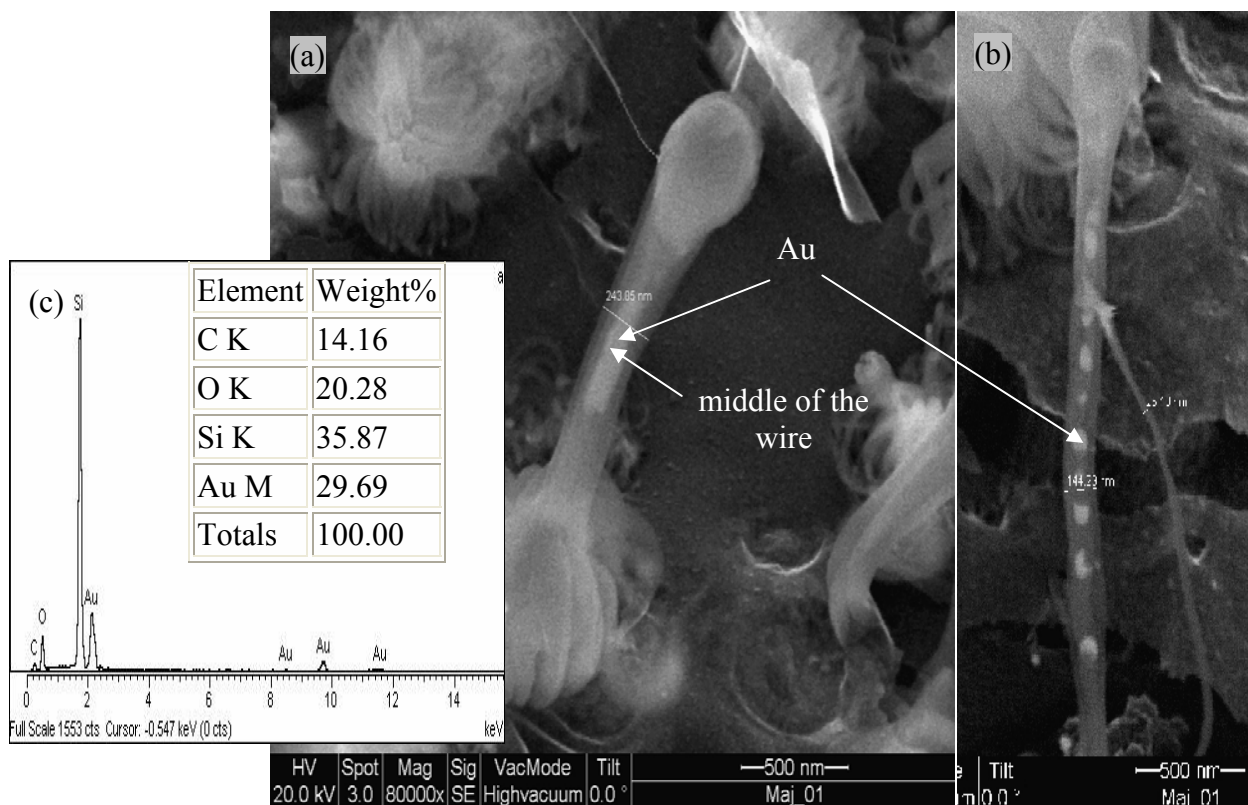


Figure 4.19 FESEM image of SiO_x nanowires embedded with gold (a) and (b) at 1200°C under 10 sccm Ar flowrate and 1h deposition time, (c) the EDX spectrum at the middle of the wire indicated by arrow.

The nanowires with embedded Au show a unique morphology. Some solid gold rod-like nanostructures were distributed uniformly at the core of silicon oxide nanowires.

The EDX spectrum in Fig.4.20 (c) showed about 30% gold confirmed the existence of Au at the wire core. This phenomenon can be explained as follows. The Au-Si alloy attracted growth species (Si and O) from SiO gas which is available at 1200°C , and hence, silicon precipitated toward the bottom of the Au-Si alloy. Continuous precipitation forms the SiO_xNW beneath the Au-Si alloy and pushes it upward. So some of Au nanoparticles of Au-Si alloy remains at the surface of the standing SiO_xNW s during the synthesis process. Then, the Au nano-particle which was attached to the surface of Si nanowire moves due to heat, together with the motion of the oxide layer of the wire to reduce the surface area and thus the surface energy. As the annealing

CHAPTER 4 RESULTS AND DISCUSSIONS

temperature was slightly below the melting point of Au, the Au nanoparticles would be in a semi-liquid state.

The silicon nanowire is an amorphous structure soft enough to allow the diffusion of Au nanoparticles into the core of the nanowire.

Fig. 4.20 (a) shows SiO_x nanofibers grown at 1200°C . The nanofibers can be divided into two shapes, the comet-like objects with long tails and the tree-like objects. The SiO_x nanofibers were grown beneath the nanowires with diameter between 10 nm to 30 nm and around 50 nm to several microns in length.

In Fig.4.20 (b) an enlarged image of comet-shaped nanofibers can be seen. The SiO_x nanofibers of comet like structures were larger in diameter near or closer to the Au-Si alloys than at the far end of the nanofibers.

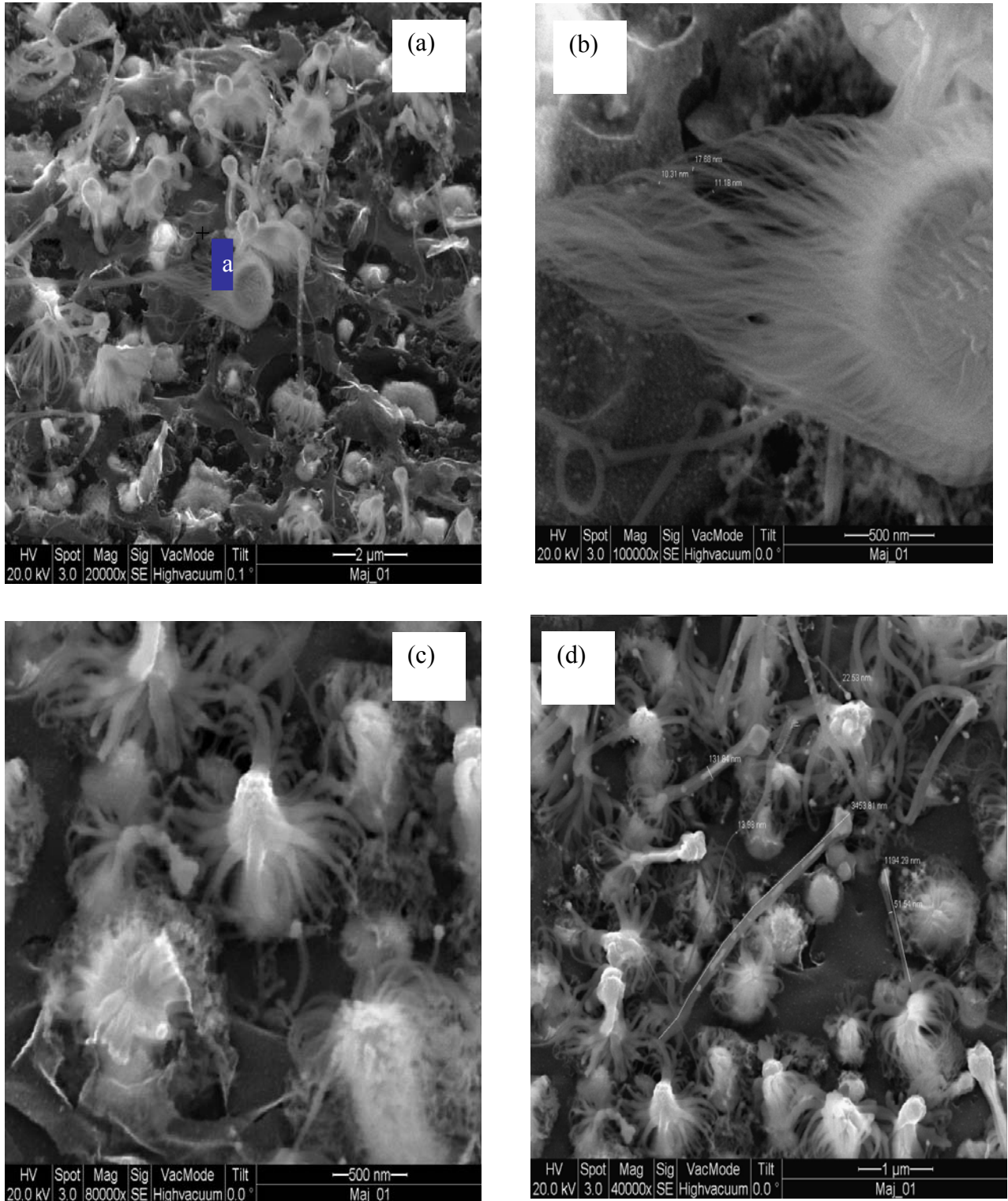


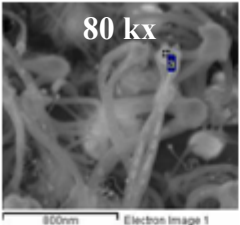
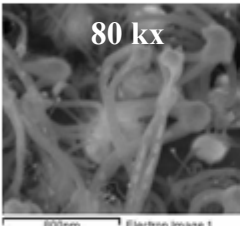
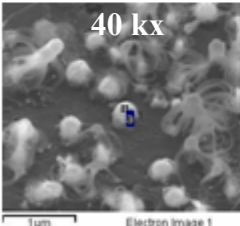
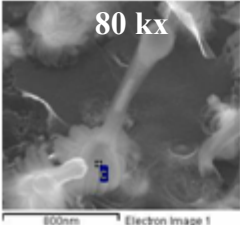
Figure 4.20 FESEM of SiO_x comet-like objects low and high magnifications at 1200°C under 10 sccm Ar flowrate for 1h deposition time (a) and (b), (c) tree-like nanostructure attached to a rod (white), (d) SiO_x nanowires tree-roots base formation.

CHAPTER 4 RESULTS AND DISCUSSIONS

Furthermore, tree-like structures; in Fig.4.20(c), reveals hollow nanotubes attached to the tip of the short rod. Fig.4.20 (d) shows SiO_x nanowire base having tree-like nanofibers or tree roots. These nanostructures have spherical tips with very long tails unlike that obtained by Chen et al. [181], which have very small spherical tops and long tails. Chen et al. evaporated pure silicon powder as a source of silicon at 1100°C to get the SiO_x nanofibers.

The data taken from EDX spectrum applied at different spots on the grown SiO_x nanostructures summarized in table 4.3. The Si:O ratio measured was not constant even in the same wire or fibre. The percentage of gold changed in the same wire or fiber depending on the examined spot area. And it depends upon the wire growth stage, more explanation can be found at section 4.3.2.1.

Table. 4.3 The Si:O mass ratio for different spots on the SiO_x nanostructures.

Spot No	Site image	Au (%)	Si(%)	O (%)	Si:O
1		4.46	16.46	25.65	1:1.56
2		2.90	18.00	27.24	1:1.5
3		14.02	17.56	43.21	1:2.5
4		9.24	30.66	60.10	1:2

CHAPTER 4 RESULTS AND DISCUSSIONS

In addition, another test was done using 1200°C under 10 sccm Ar flowrate for 1h deposition time by placing the Au coated silicon substrate at 6 cm inside the tube furnace instead of 2 cm.

Different morphology of SiO_x nanostructure was obtained. These nanostructures look like balloon cage, which named nano-cages. Nano-cages shown in Fig. 4.21 (a) and Fig. 4.21 (b) are different in shape from the obtained zinc oxide nano-cages [182] because of the hexagonal structure of ZnO. Our SiO_x nano-cages are smooth with rounded shape ending with a spherical ball at the top.

To the best of our knowledge; this is first time to produce the SiO_x nano-cages, which shows the important of our work.

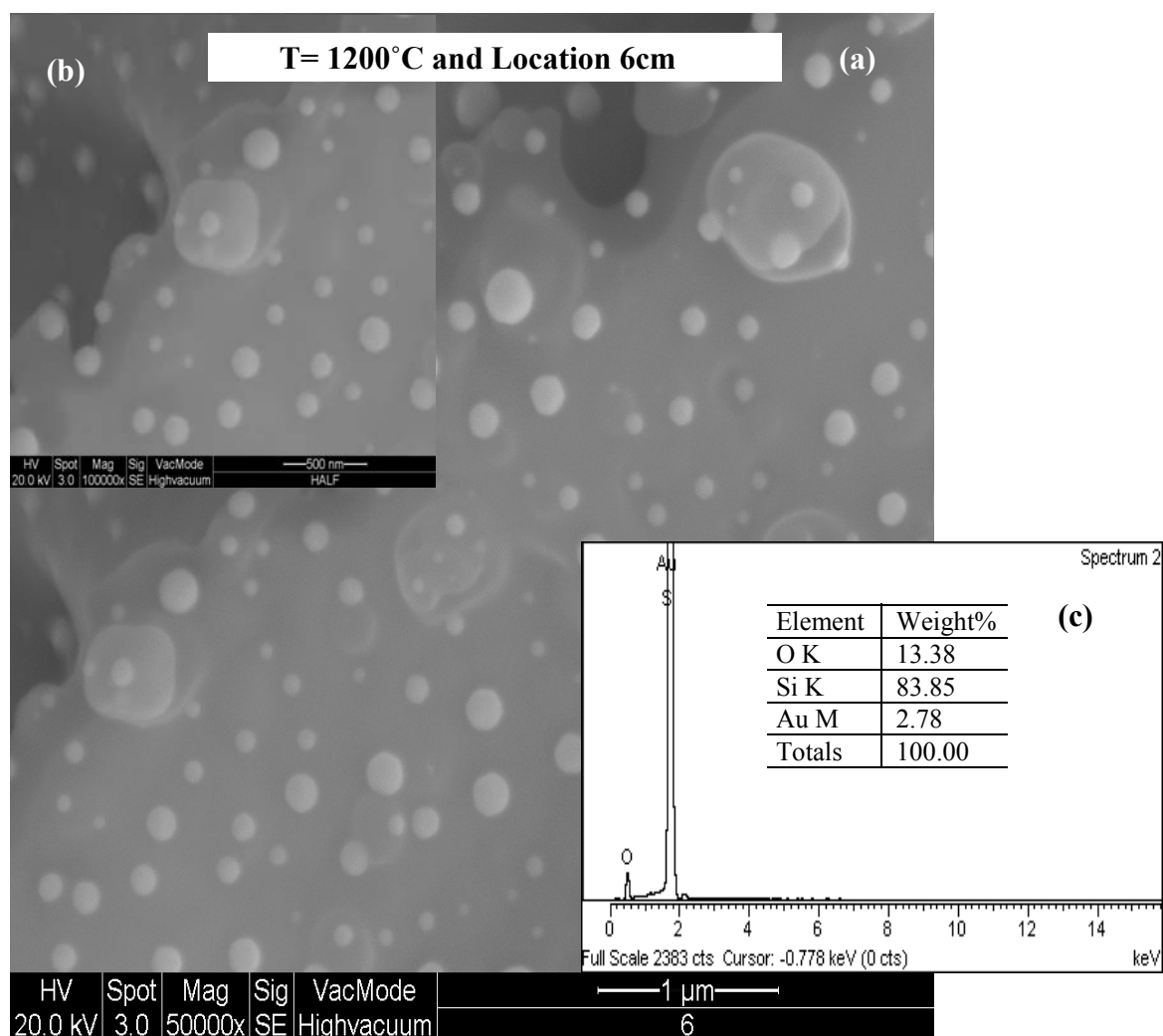


Figure 4.21 FESEM of (a, b) SiO_x nano-cages obtained on Au/Si substrate at 6cm apart from the furnace centre at 1200°C and under 10 sccm Ar flowrate for 1h, (C) EDX spectrum of SiO_x nano-cages.

CHAPTER 4 RESULTS AND DISCUSSIONS

The EDX spectrum in Fig. 4.21 (c) shows that the nano-cages consist of silicon with small amounts of oxygen and gold. The distance from the furnace centre cause reduction in temperature over the substrate surface, which may be responsible for the formation of such a unique morphology.

The XRD analysis technique was applied for three different samples, the cleaned (SiO_2/Si) substrate, the Au coated substrate before experiment and the resultant SiO_x nano-cages. In Fig 4.22 (B), XRD spectrum peaks referred to gold with (111) phase at 38.2° , (200) at 44.4° and (220) at 64.6° .

While, no peak can be observed in the XRD spectrum shown Fig. 4.22 (C), which is taken for the grown SiO_x nano-cages. Therefore, the obtained SiO_x nano-cages are amorphous, which is due the oxidation process during cooling period.

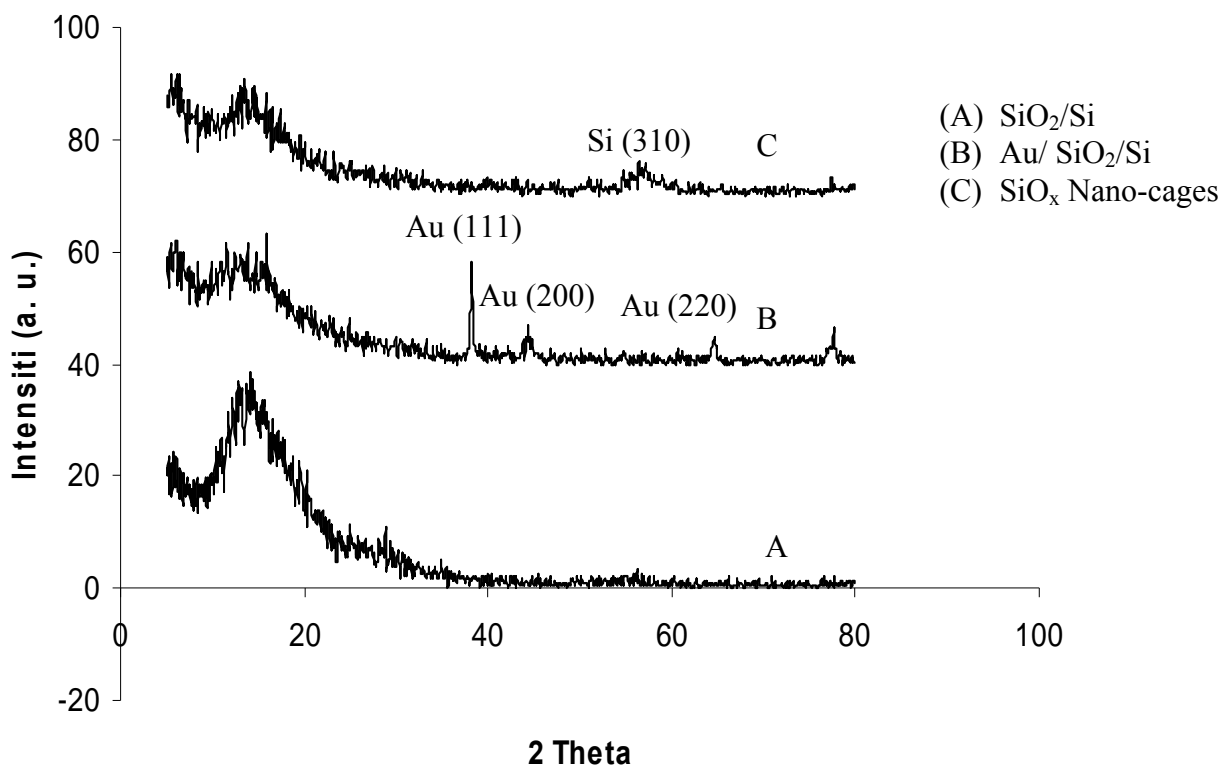


Figure 4.22 XRD spectra of (A) SiO_2/Si , (B) $\text{Au}/\text{SiO}_2/\text{Si}$ and (C) SiO_x Nanowires at 1200°C heating temperature for 1h.

4.3.1.2. Effect of Oxygen and Argon Gases on the Growth of SiO_xNWs

In this experiment, the effect of O₂ and Ar on the growth of SiO_xNWs was investigated. The deposition temperature kept at 1200°C under 10 sccm Ar or O₂ gas flowrates was conducted for 5 mins to 8 mins.

The obtained SiO_xNWs using Ar gas shown in Fig 4.23 (a) image (1) to Fig. 4.23 (d) image (1). In contrast, there is no growth at all when oxygen was used.

Fig.4.23 (a) image (2) to Fig. 4.23 (d) image (2) reveals that there are only Au spherical balls on the surface. So large amount of O₂ introduced to the system hindered the nanowires growth.

The EDX spectrum for sample shown in Fig.4.23 (b) image (2) indicates that these balls mainly consist of gold. These balls do not have the ability to grow wires because it never reached the supersaturation stage where the alloy gains more Si atoms from the vapour. And this is because there were not enough SiO in gas form. This result agrees with the previous reported studies [24, 58, 91] that a higher proportion of O₂ in the gas flow could suppress the growth of SiO_xNWs. Paulose et. al. [58] indicated that a higher proportion of O₂ in the gas flow favours surface oxidation of the silicon wafer, which may prevent the formation of Au–Si alloys and thereby the nanowire growth.

CHAPTER 4 RESULTS AND DISCUSSIONS

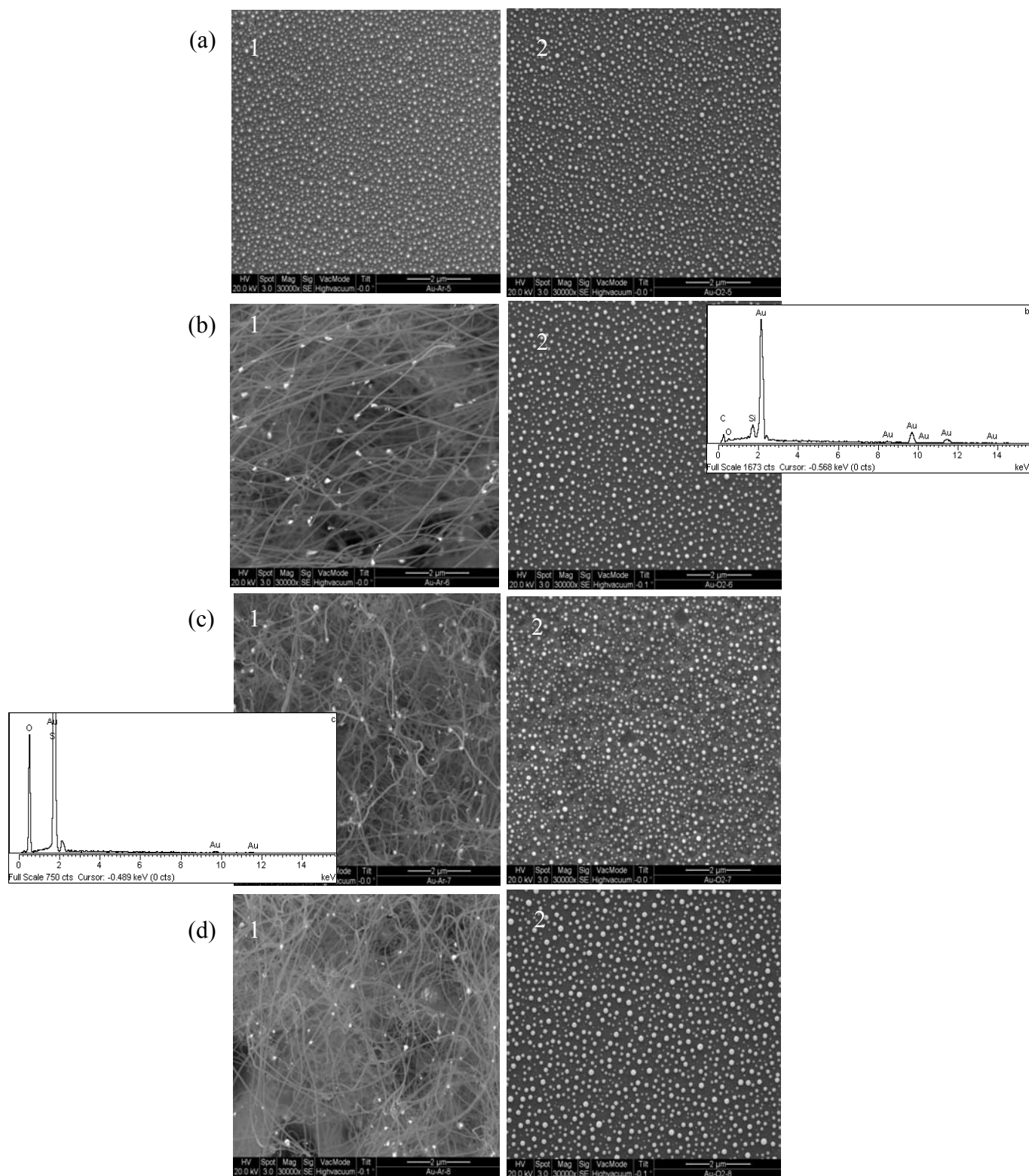
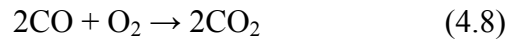


Figure 4.23 FESEM image of SiO_x nanowires grown at 1200°C under 10 sccm Ar flowrate for 5, 6, 7 and 8 mins deposition time for (a) image (1) to (d) image (1) and using oxygen gas for (a) image (2) to (d) image (2).

CHAPTER 4 RESULTS AND DISCUSSIONS

To explain how oxygen hinders the growth of SiO_x nanowires, the carbo-thermal reaction should be discussed. Carbon played an important role in enhancing the silicon oxide evaporation from the substrate, but in the presence of oxygen, carbon oxidized before reaching high temperatures. Carbon was oxidized through the following reactions: [183]



Carbon becomes oxidized to gas at 1200°C. Therefore, the carbo-thermal reaction (4.1) will not occur. Based on our results a condition where oxygen depletion favors the growth of SiO_xNWs. In a condition of excess oxygen, SiO₂ layer were formed instead.

4.3.1.3. Effect of (TiO₂: C) Mass Ratio on the Growth of SiO_xNWs

In this experiment the temperature was kept at 1200°C under 10 sccm Ar flowrate and 1h deposition time. The TiO₂:C mass ratio was changed as follows; 1:1, 1:2, 1:3 (increasing carbon mass with 1g each time) and 2:1, 3:1 (increasing titanium dioxide mass 1g each time). The FESEM shown in Fig.4.24 illustrates these five ratios with inset images at 12000 xs.

Fig. 4.24 (a) shows SiO_x nanowires grown at 1:1 TiO₂:C mass ratio. These wires were seen to grow in some parts of the substrate.

In Fig. 4.24 (b) the grown area become bigger and it covers the entire sample surface, for the sample synthesized at 1:2 TiO₂:C mass ratio. Here, the SiO_x nanowires formed with very high growth yield. The FESEM image of sample shown in Fig. 4.24 (c) reveals the grown SiO_x nanowires with relatively less growth yield. This is because increasing carbon should enhance the one dimension growth of SiO_x nanowires as stated by Li et. al. [24].

However, there is a limitation of adding carbon to the mixture.

It was discovered that the best TiO₂:C ratio was 1:2, as in Fig.4.24 (b). This means, the amount of carbon controls the growth yield, as the carbon mass increases in the total mixture the resultant SiO_x nanowires become higher in yield but only to certain limit. This is due to availability of C(s) involved in the formation of SiO_xNWs through equation (4.3).

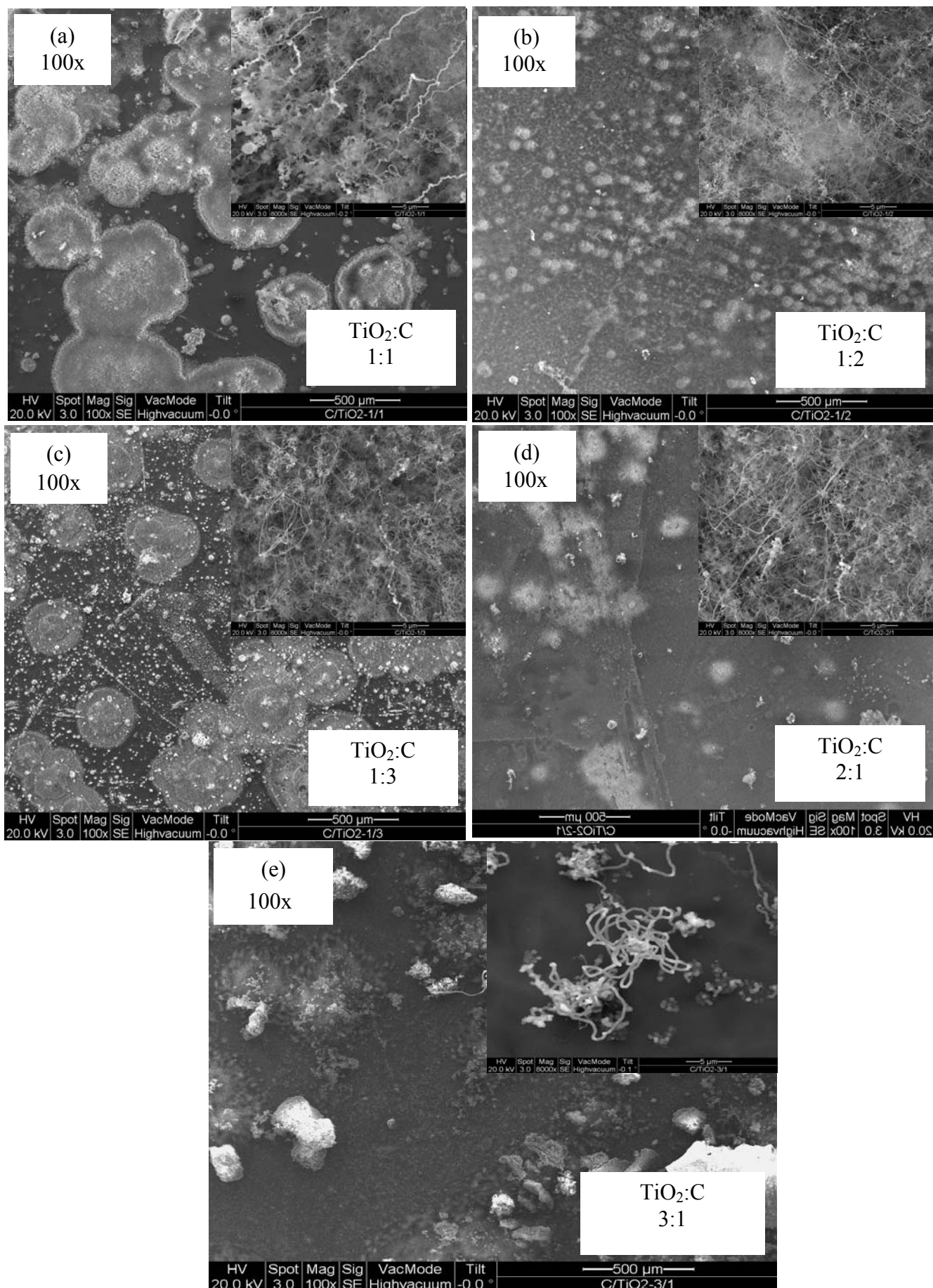


Figure 4.24 FESEM (100x mag.) of SiO_xNWs with inset images at 12k mag. at 1200°C under 10 sccm Ar flowrate for 1h deposition time using $\text{TiO}_2:\text{C}$ mass ratios at (a)–(c) 1:1-1:3 and (d)-(e) 2:1-3:1 respectively.

4.3.1.4. Effect of Argon Flowrate on the Growth of SiO_xNWs

The FESEM image in Fig.4.25 shows the growth of SiO_x nanowires synthesized at 1200°C under different Ar gas flowrates and deposited for 1h.

Fig. 25 (a) shows the sample grown at 40 sccm Ar flowrate. Here, the sample surface can be seen and density of the SiO_x NWs was relatively low in density.

While in Fig. 4.25 (b) the synthesis process was carried with 30 sccm of Ar flowrate and the grown SiO_xNWs seem to be denser. Also, bright dots were visible at the end of the grown SiO_xNWs. These dots represented the Au-Si alloys, which pull the wires upward during the growth process.

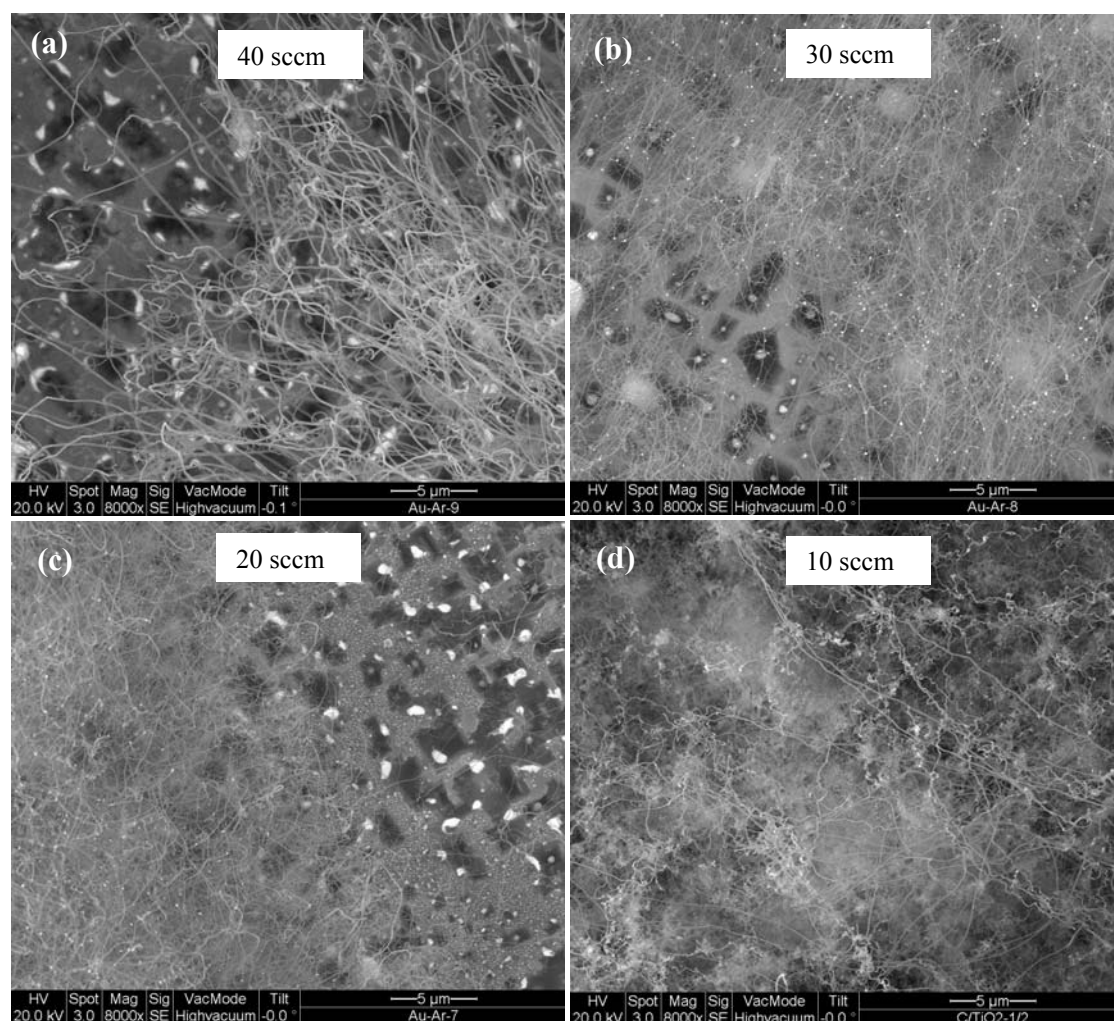


Figure.4.25 FESEM image of SiO_xNWs at (a) 40, (b) 30, (c) 20 and (d) 10 sccm flow rates with 1200°C heating temperature for 1h deposition time.

CHAPTER 4 RESULTS AND DISCUSSIONS

The FESEM image of the sample in Fig. 4.25 (c) shows the SiO_xNWs grown at 20 sccm Ar flowrate. The SiO_xNWs were denser with Au-Si alloys as wire caps. Also, in the growth region the sample surface could not be seen, because of the SiO_xNWs were overlapped.

In Fig. 4.25 (d) the obtained SiO_xNWs were fabricated at 10 sccm of Ar flowrate. Here, the ultra long SiO_xNWs covered the sample surface and the Au-Si alloys not can be seen, which gives clear idea about the length of the grown wires.

The effect of Ar gas on the growth of SiO_xNWs can be explained as follows. There are no other sources of silicon other than the substrate itself, the SiO in gas form is the source of Si atoms for the growth, as pointed out by Gundiah et. al. [97]. This leads to suggest that the argon gas flow rate affect the residence time of SiO gas. Therefore, when the argon gas flowed with high rates the residence time for the growth element is low, which reduce the ability for the growth reactions to occur especially during temperature fluctuations which are due to Ar flow.

The temperature fluctuations changed the surface temperature slightly, which allow the condensation of SiO gas. Therefore, long residence time can produce very long wires as in Fig.4.25 (d), because of the continuous condensations of the growth species.

Fig. 4.6 shows the XRD spectrum of Au coated Si substrate and the sample deposited at 10 sccm, which is typical of all the deposited samples. For Au coated Si substrate shown in Fig 4.26 (a), the prominent peaks are Au (111) at 38.2° , (200) at 44.4° and (220) at 64.6° . This spectrum was taken after sputtering Au layer onto the Si substrate and before it placed inside the furnace.

Fig. 4.26 (b) shows the XRD spectrum of SiO_xNWs which indicates the amorphous nature of the sample, similar to the results obtained without catalyst. Also, no peaks are visible for gold which due to the coverage of SiO_xNWs over the spot investigated. This is because Au-Si alloy is distributed at the far ends of these wires and they become

small in size. So, when the X-ray beam hits the sample with ultra long and amorphous SiO_xNWs , it did not give any diffraction patterns.

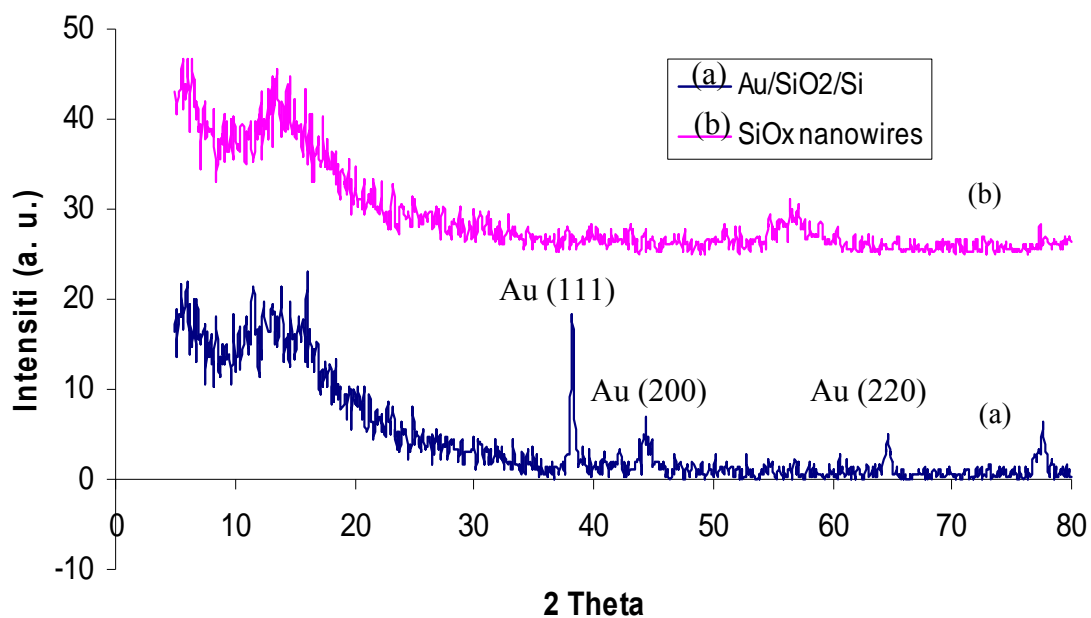


Figure 4.26 XRD spectrum for (A) Au coated Si substrate and (B) SiO_xNWs grown at 1200°C under 10 sccm Ar flowrate for 1h deposition time.

4.3.1.5. Effect of Deposition Time on the Growth of SiO_xNWs

The deposition time needed to accomplish the growth of SiO_xNWs has been tested for five periods which are 10, 20, 40, 60 and 80 minutes.

Fig. 4.27 shows the FESEM image of samples obtained for different deposition times at 1200°C under 10sccm Ar flowrate. FESEM image shown in Fig. 4.27 (a) was deposited 10 mins which shows no growth of SiO_xNWs.

The deposition time was increased to 20 mins and the results shown in Fig. 4.27 (b), but also no grown SiO_xNWs were visible.

In Fig. 4.27 (c) the deposition time was increased to 40 mins and the SiO_xNWs can be seen at low density under high magnification. Here, the sample surface is visible and the grown SiO_xNWs were sparse.

In Fig. 4.27 (d) the fabricated SiO_xNWs at 60 mins were in a random network. These wires were dense and covered the substrate surface.

The FESEM of sample shown in Fig. 4.27 (e) illustrates the grown SiO_xNWs at 80 mins deposition time. This large deposition time yielded in long and dense SiO_xNWs. This result agrees with our prediction of the effect of deposition time on the growth species over the substrate, which then precipitates during condensation part. Also, this result is similar to the effect of Ar gas flowrate where the deposition time of growth species played an important role to enhance the SiO_xNWs fabrication.

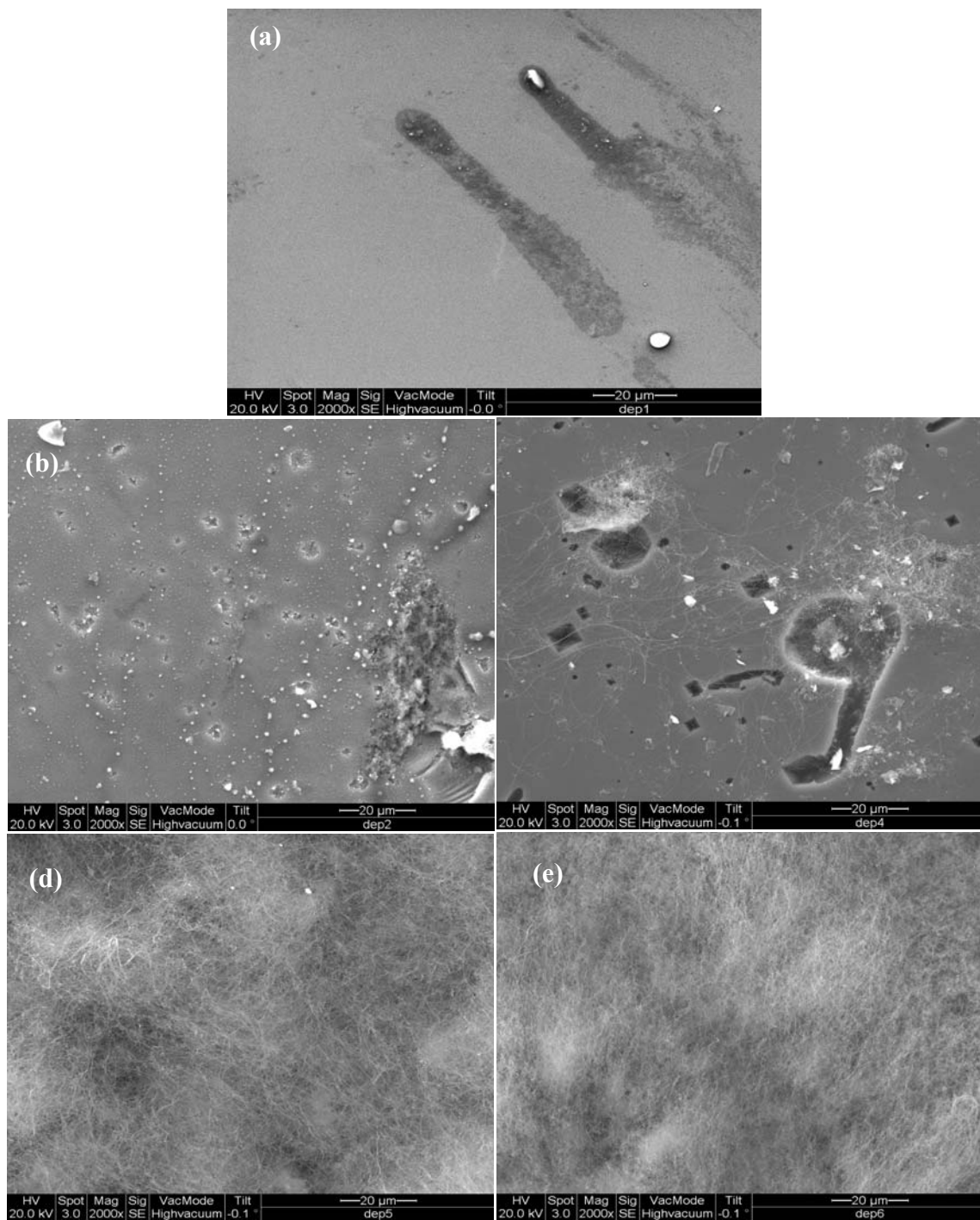


Figure 4.27 FESEM of SiO_x nanowires grown at 1200°C for (a) 10 (b) 20 (c) 40 (d) 60 and (e) 80 minuts deposition time under 10sccm Ar flow rate.

4.3.1.6. Effect of Gold Layer Thickness on the Growth of SiO_xNWs

Si substrate with Au layers of different thickness was prepared by varying the sputtering time of the sputter coater at 20, 30, 40, 60 and 80 seconds.

Fig. 4.28 shows the FESEM of SiO_xNWs grown on silicon substrates coated with Au of different thicknesses. The SiO_xNWs shown in Fig. 4.36 (a) were grown on from the Au-Si alloys. Here, arrows are used to indicate the Au-Si alloys locations. These alloys have high percentage (86%) of gold as reveals in EDX spectrum in Fig. (a1). The Au-Si alloys were at the bottom or base of the SiO_xNWs. Therefore, the Au-Si alloys are the preferred locations of the growth process of the SiO_xNWs. The FESEM image of sample shown in Fig.4.28 (b) reveals the obtained SiO_xNWs were random.

On the other hand, the FESEM image in Fig. 4.28 (c) shows the grown SiO_xNWs were more aligned with bright dots at their ends. These dots were the Au-Si alloys which can be explained by VLS growth mechanism. The VLS mechanism relates the grown wire diameter to the Au-Si alloy diameter. So at 40 second sputtering time we can obtain a nearly definite diameter for all wires by controlling both of heating temperature and deposition time as well as the Ar flowrate. In addition, the length of these wires seems to be almost the same and this due to the timing of solidification of the Au-Si alloy at the wires ends. On the other hand, increasing the sputtering time up to 60 and 80 seconds give rise of very long and dense wires as in Fig. 4.28 (d) and (e). Here, the wires are sliding with different lengths. Therefore, the place of Au-Si alloys at the base or tip of the SiO_xNWs is governed by the thickness of the Au deposited layer and proper temperature. As results, Au sputtered time at 40 sec was preferred to fabricate standing SiO_xNWs with Au-Si spherical balls at their far end. Also, as the thickness of the layer gold increased the obtained SiO_x nanowires increased in quantity in different directions over the sample surface.

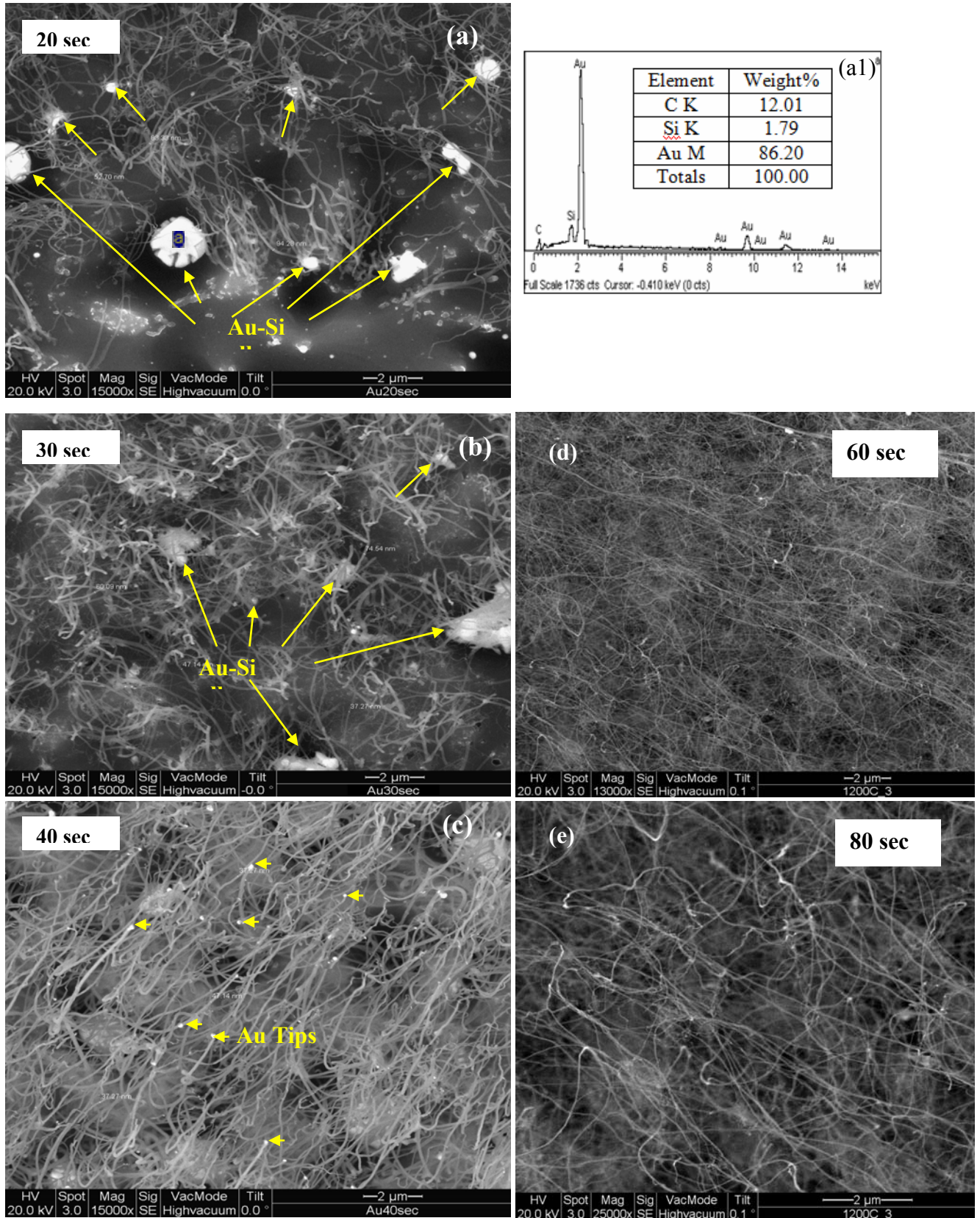


Figure 4.28 FESEM of SiO_xNWs grown using Au coated silicon substrate deposited at (a) 20, (b) 30, (c) 40, (d) 60 and (e) 80 seconds, the wires were grown out from the Au-Si alloys for (a) and (b) as in (a1) while in (c) the nanowires have Au tips at the far end of the standing wire.

CHAPTER 4 RESULTS AND DISCUSSIONS

The data of sputtering times, Au layer thicknesses and the measured average diameters of SiO_xNWs are listed in table 4.4.

The sputtering time readings were taken from 20 to 80s sputtering time and the relative thickness of the deposited Au layer was calculated from the equation (4.9) [164].

$$D = K \cdot I \cdot V \cdot t \quad (4.9)$$

Where D is the thickness of the coated layer. K is an experimentally determined constant depending on the metal being sputtered and the gas being used based on a distance of approximately 5 cm between the target and the specimen. K is approximately 0.17 for gold used in conjunction with argon. I is the plasma current, V is the voltage applied (1 kV), and t is the sputtering time in seconds.

For example, the obtained Au thickness for 20 second sputtering time is calculated as follows: I=20mA, K_{Au}=0.17, V=1kV, so from equation 3.1 the thickness is:

$$D = (0.17)(20)(1)(20) = 68 \approx 70 \text{ \AA}$$

Table 4.4 The data of sputtering time, Au layer thickness and the estimated average SiO_xNWs diameter.

Sputtering Time (s)	Au deposited layer thickness (Å)	Average SiNWs diameter (nm)
20	70	120
40	140	55
60	200	45
80	270	35

CHAPTER 4 RESULTS AND DISCUSSIONS

The data are plotted in Fig. 4.29. The curve shows high reduction of wire diameter from 120 to 55 nm when the Au layer thickness increased from 70 to 140 Å which is equal to the sputtering time from 20 to 30s. Then the curve slope becomes very small and the change is not that much. The lowest diameter could be obtained is around 35 nm.

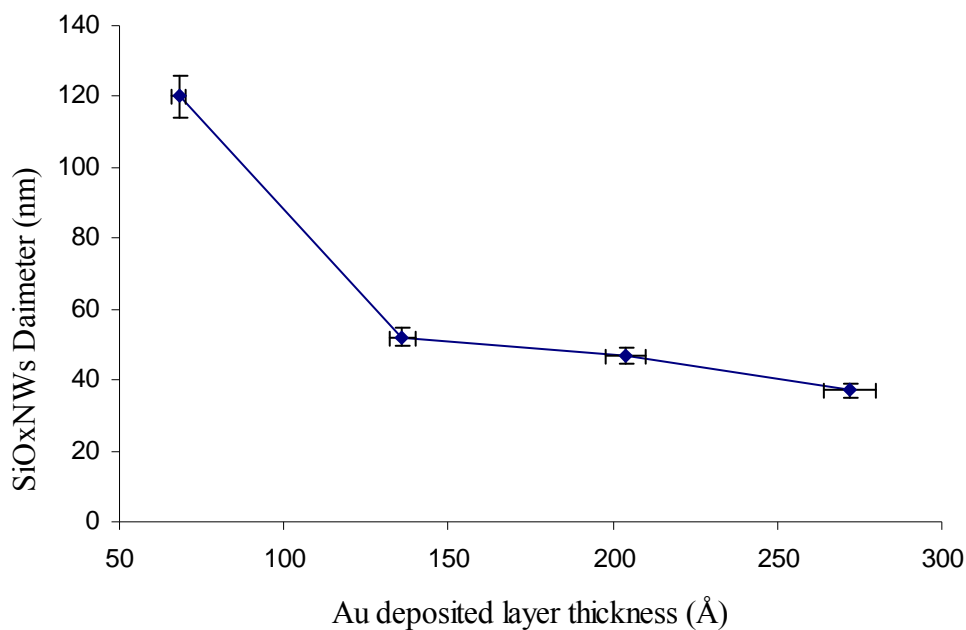


Figure 4.29 Au thickness layer versus average SiO_xNWs diameter

4.3.1.7. Effect of Rapid Heating Rate on the Growth of SiO_xNWs

In this experiment, deposition of SiO_xNWs was obtained under rapid heating. This is done by heating the furnace up to 1200°C and hence the substrate was directly inserted to the quartz tube before it was sealed and vacuumed. The system was then works for 8 mins deposition time under 10 sccm Ar flow.

The FESEM image of sample shown in Fig. 4.30 shows SiO_xNWs grow vertically around circular shapes and look like nanocake. This morphology is unique and to the best of our knowledge no similar nanostructures were synthesized before.

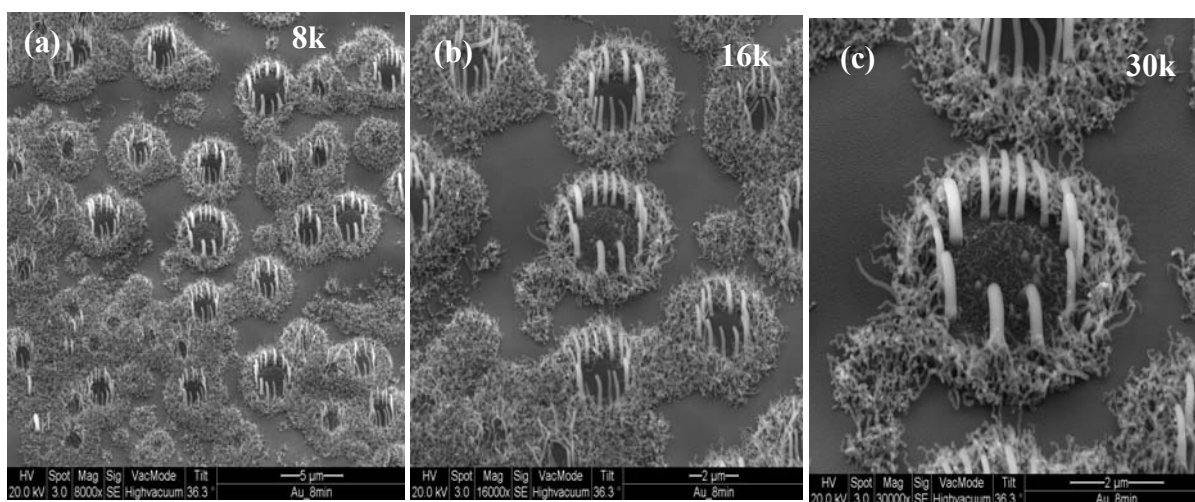


Figure.4.30 FESEM of SiO_x Nanocakes grown on Au coated Si substrate which was inserted directly to the furnace at 1200°C with 10 sccm Ar flowrate for 8 mins, (a) 8k, (b) 16k and (c) 30k.

The obtained SiO_x nano-cakes seem to be grown directly from the sample substrate as evident from Fig.4.30 (a). At higher magnifications, Fig. 4.30 (b) and Fig. 4.30 (c), there is no growth on the middle of the SiO_x nanocakes or circle.

In Fig.4.31 (a) and (b) the EDX spectrums of inset images show no gold at all for these two images of the same sample. The SiO_x nanowires are smooth circulated aligned on the surface of the sample. This can be explained as follows.

CHAPTER 4 RESULTS AND DISCUSSIONS

When the temperature is raised rapidly the gold layer melted before it reacts with silicon from the silicon substrate to form Au-Si alloys. This Au liquid molten layer moved from place to another on the surface of the Si substrate due to its high mobility. Therefore, at the substrate edges this layer poured to the quartz tube. The small Au dots found on the tube evident this suggestion.

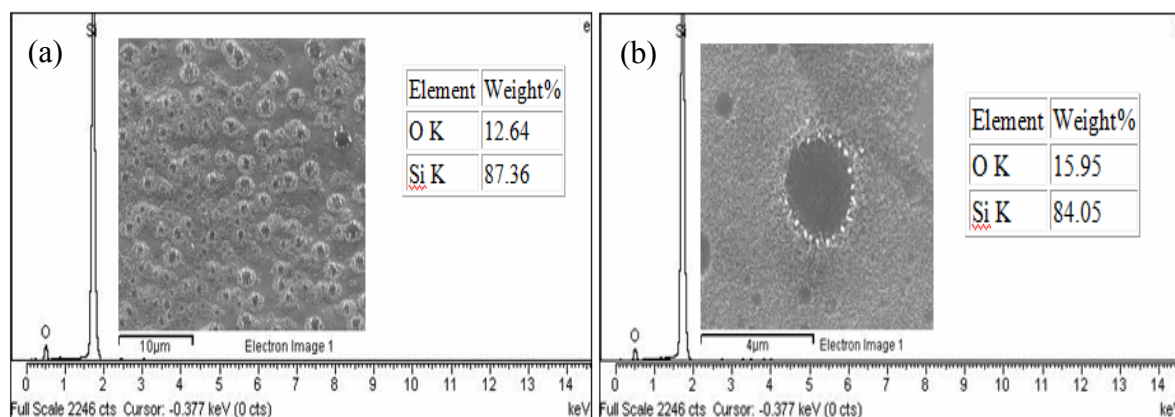


Figure 4.31 EDX spectra of SiO_x nano-cakes grown on Au coated Si substrate which was inserted directly to the furnace at 1200°C with 10 sccm Ar flowrate for 8 mins, (a) low magnification (8k) and (b) high magnification (30k).

The XRD spectrum in Fig. 4.32 shows the SiO_x nano-cakes are amorphous. This is due to the oxidation process during cooling period. Oxygen may penetrate from outside the system or when the sample gets exposed to air during characterization.

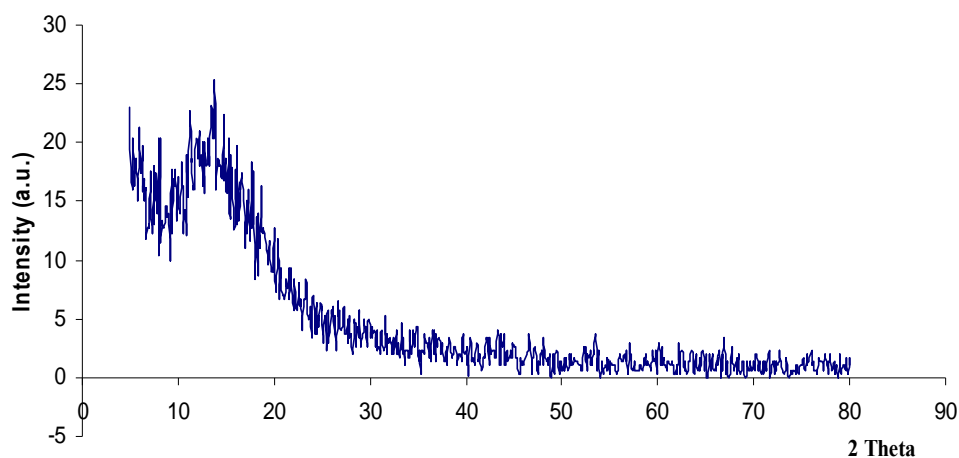


Figure 4.32 XRD spectrum of SiO_x nano-cakes grown on Au coated Si substrate which was inserted directly to the furnace at 1200°C with 10 sccm Ar flowrate for 8 mins.

4.3.2. Catalytic Growth of SiO_x Nanostructures

The obtained wires can be classified into two types upon their morphology; tip growth and root growth, depending upon the location of Au nano-balls whether it's on tip or root.

4.3.2.1. Tip Growth Process of SiO_xNWs Grown on Au coated Silicon substrate

In Fig. 4.33 a schematic diagram of SiO_x nanowires growth model. Here, in the first step, tip growth mechanism starts when the deposited Au layer collapsed forming spherical balls with diameter of hundreds of nanometres due to the effect of surface tension of the molten Au layer.

As the temperature increased, Au balls became smaller due to high surface tension. The Au catalyst served as a nucleation seed for the subsequent nanowires growth at the appropriate temperature, from 900°C to 1200°C. Thus, the heating step explains the Au balls formation.

When the temperature drops down (natural cooling) in the condensation area, the Au balls formed alloys with silicon on the surface of the Si substrate at the eutectic temperature point between gold and silicon around 363°C measured by Massalski [70].

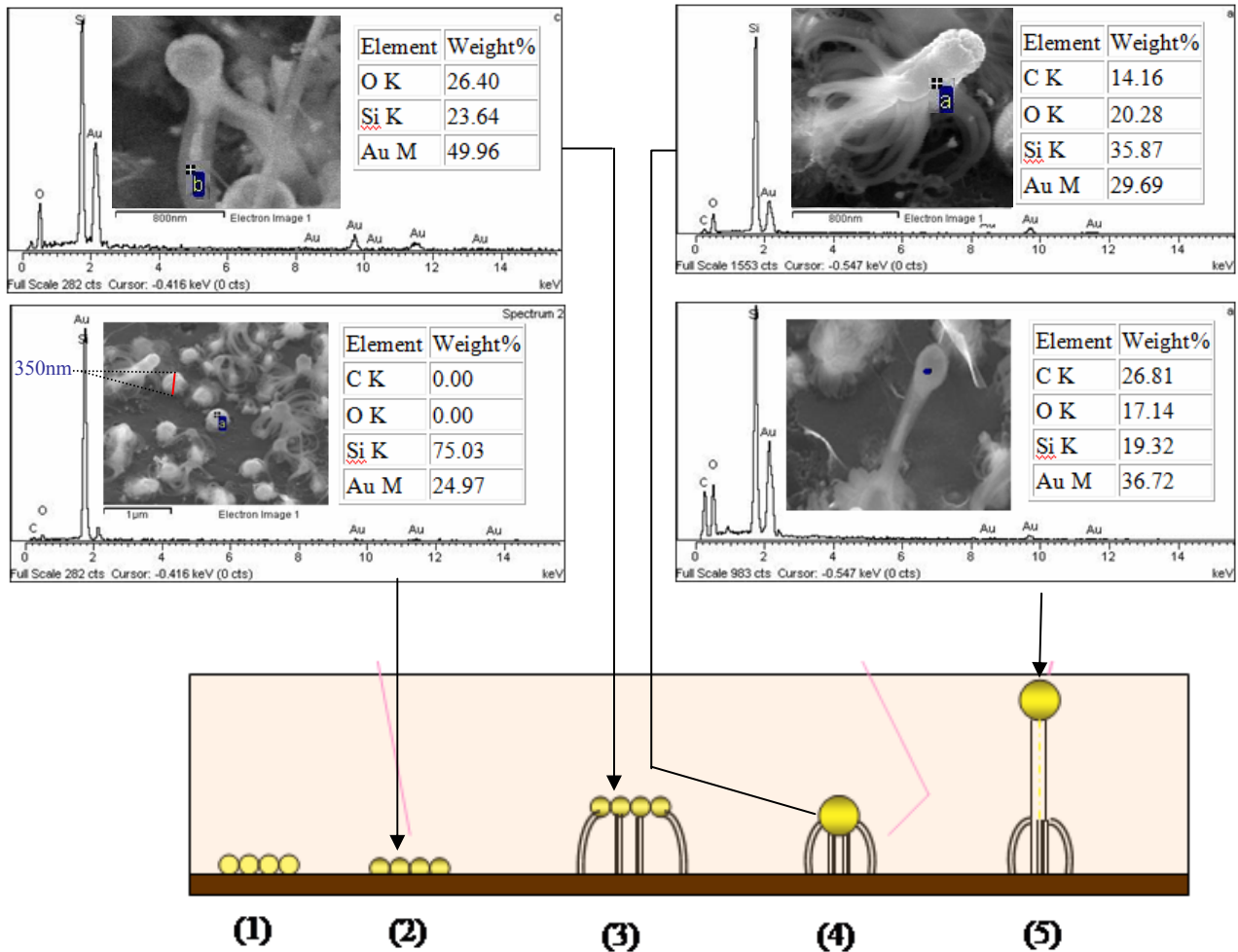


Figure 4.33. A schematic diagram of SiO_x nanostructures growth mechanism.

Hence, in stage (2), silicon diffused into the droplet from the oxide layer of the substrate. Then, more and more silicon diffused and dissolved into the droplet until supersaturated where the excess silicon started to precipitate towards the bottom of the droplet and the SiO_x nanowires start to form.

In step (3), if the growth of SiO_x nanowires continued beneath the Au-Si alloys, comet and tree-like SiO_x nanofibers formed. Whereas, if the furnace temperature is not enough to continue the growth process, this process will stop and the final shape will look like tree roots or comet shape.

CHAPTER 4 RESULTS AND DISCUSSIONS

In stage (4), increased in deposition time will enhanced the Au-Si alloys to aggregate and form bigger alloy or ball which pulled the wires upward and formed SiO_x nanowires with Au-Si cap at the end of the wire, see stage (5).

Furthermore, Fig. 4.33 (5) shows the formation of SiO_x NWs embedded with Au nano-particles which could be explained as follows: the nano-particles are formed in vapour phase surrounded by ambient Ar gas. Such Au-containing nano-particles from the source material are assumed regularly attached to the surface of a SiO_x NW, and then “sink,” or even completely submerge into the SiO_x NW. If the growth temperature is sufficiently high, Au nano-particles are then in liquid phase and the surface tension between droplet- SiO_x NW interfaces drives the Au-containing nano-particles into the SiO_x NWs.

It is convenient to explain the tip growth of SiO_x NWs by solid-liquid-solid (SLS) mechanism, which suggested that silicon atoms diffused from silicon substrate to Au balls to form the Au-Si alloys in liquid state. This is because it solved the need of silicon in vapour form to grow the SiO_x NWs especially in our experiment because no silicon gas source was used.

Here, the SLS mechanism implies that the Au-Si alloys attract silicon atoms from silicon substrate by diffusion and at saturation stage between silicon and gold, silicon precipitated towards the bottom of these alloys and one dimension growth of SiO_x NWs formed. But SLS mechanism still poorly understood when the Au-Si alloy reach the saturated stage. This balanced situation should eliminate the absorption of Si atoms from the substrate, which did not happen due to Bahloul et al [86]. So, we suggest the carbo-thermal reactions, which is responsible of silicon monoxide evaporation from the substrate.

Carbon monoxide and carbon dioxide react with a source of silicon to form the nanostructures. Silicon monoxide (SiO) was suggested to be the only source of silicon

CHAPTER 4 RESULTS AND DISCUSSIONS

in gas phase as in equation (4.2). Therefore, the SiO may react with C or CO to generate more stable SiO₂ as in equations (4.3) and/or (4.4).

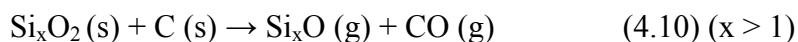
The resultant solid Si and SiO₂ will be responsible in providing the Si feed stock to the growth sites areas. This implies that first phase is in vapour form then it condense into the Au-Si alloys, liquid form, and then precipitated and formed solid silicon nanowires, solid state.

This mechanism is called vapour-liquid-solid (VLS) mechanism. Here, silicon may come by both SLS and VLS mechanisms as follows. First, gold nano-particles attracted silicon from the silicon substrate to form the Au-Si alloy and hence the diffusion of silicon stopped at saturation stage and the percentage of silicon is balanced to gold. that is because in phase diagram in Fig. 2.10 both Au and Si should reach certain percentage to lower their eutectic temperature. Therefore, to accomplish the SiO_xNWs growth more silicon atoms were needed. These atoms come from the vapour of SiO that condensed into the Au-Si alloy to form the supersaturation stage and establishing the one dimension growth of these wires.

The two initial phases, solid or vapour, of silicon give rise for solid-vapour-liquid-solid (SVLS) mechanism as will be discussed in root growth group. The SVLS mechanism was proved theoretically by Bahloul et al [86].

4.3.2.2. Root Growth of SiO_xNWs

The formation of SiO_xNWs in the presence of carbon can be explained as follows. Silicon is generally covered by an oxide layer. The oxide layer gets reduced by carbon into silicon sub-oxide by the reactions (4.10)



In our temperature range (from 1000 to 1200 °C) the available form of oxide silicon is silicon monoxide (SiO) where x equals one in Si_xO (g) as in equation (4.11)



Then, the solid silicon and silica condenses forming the structure of the wires. The Au-Si alloy balls have large diameter due to low annealing temperature this time. The large Au ball diameter cannot rise and form SiO_x nanowires as in the tip growth because these balls are too heavy. Here, the silicon or silica starts to precipitate on the Au ball surface. This is due to the percentage of Si atoms to gold. Therefore, the resultant wires start to form on the surface when they reach supersaturated stage.

Fig. 4.34 shows a schematic diagram of the SVLS mechanism stages of SiO_xNWs. Stage (1), the Au particles formed in spherical objects or nano-balls during high temperature and at the same time SiO gas evaporated from silicon substrate.

In stage (2), the Au nano-balls attracted silicon from both silicon substrate and SiO vapour to form Au-Si alloys.

In stage (3) a silicon oxide layer formed around the Au nano-ball as result of silicon precipitation inside the alloy.

Finally, in stage four, more precipitation of silicon atoms made the Au-Si alloy supersaturated and the excess silicon atoms aggregated and arranged to build one dimension silicon nanowires. These wires get oxidized during cooling period or when exposed to air.

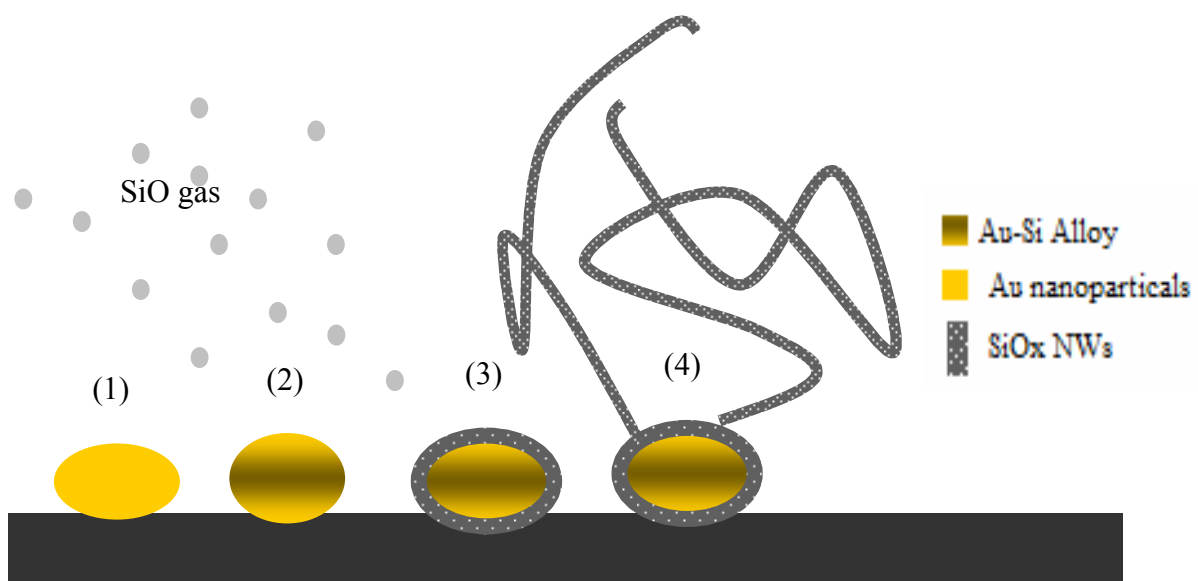


Figure 4.34 A schematic drawing for root growth group of SiO_xNWs by SVLS mechanism.

4.3.2.3. Growth Model of SiO_x Nano-cages

The growth model of SiO_x nano-cages is shown in Fig. 4.35. In the first stage, the Au-Si alloy forms by gathering Si atoms through SLS mechanism. At supersturation the silicon starts to precipitate around the molten Au-Si alloy and hence get oxidized as illustrated in stage (2).

The outer oxidised layer gets solidified before the molten Au-Si core due to the low temperature of melting eutectic Au-Si. As the SVLS mechanism provide more silicon atoms, the wire become taller as shown in stage (3).

Finally, in stage (4), the molten core cannot sustain because of gravity and then goes down again to the surface of the substrate.

The last step can be also contributed to the supersaturation condition, which required percentage of Au to Si atoms. This condition happened only at the boundaries not inside the wire, so the nano-cage walls started to form before the core gets solidified.

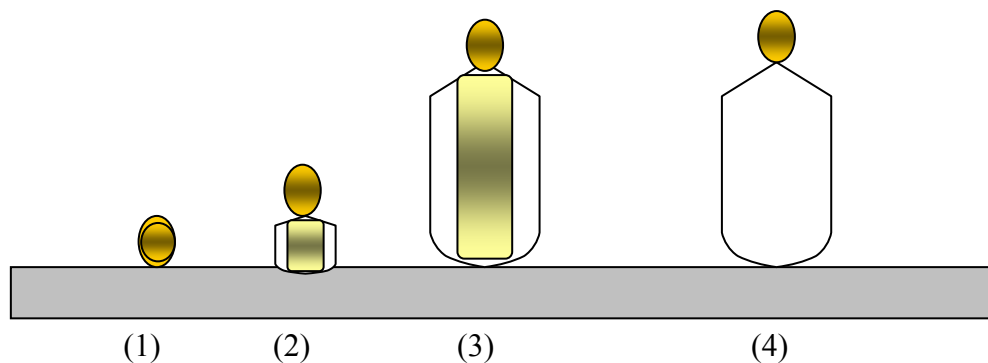


Figure 4.35 A schematic diagram of SiO_x nano-cages growth model by assistance of SVLS mechanism.

4.3.2.4. Growth Model of SiO_x Nanocakes

Our growth model shown in Fig. 4.36, explains the three growth steps of SiO_x nanocakes formation. Firstly, the Au coated silicon substrates faced high heating temperature rate, which made the formation of the Au nano-balls very fast, so the diffusion of Si atoms to these balls can not reach a sufficient percentage to form nucleation stage or supersaturation.

Secondly, the liquid Au nanoballs and at the same time the SiO_x nanowires start to form by SLS mechanism on the non-catalytic part through diffusion of silicon from the substrate in the places where are no gold nano balls formed. Thirdly, the SiO_xNWs formed around the Au nanoballs. This circle shape gives rise for this unique morphology of SiO_x nanocakes.

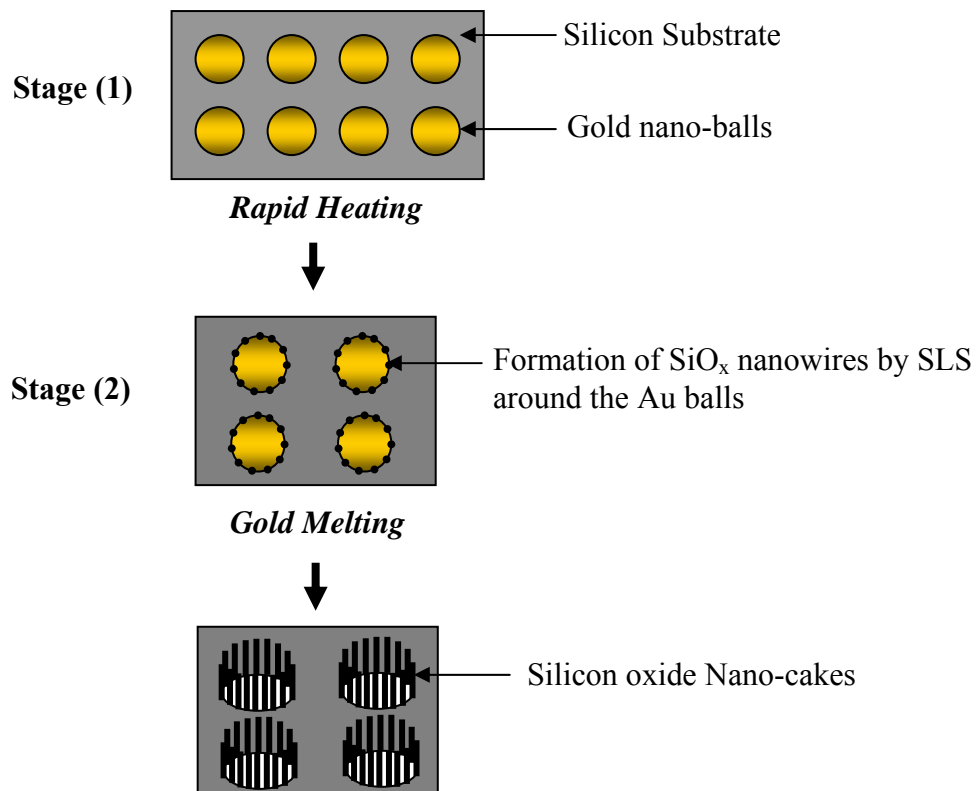


Figure 4.36 A schematic model of SiO_x nanocakes growth at 1200°C with rapid heating rate. Growth steps: Stage (1) formation of Au nanoballs, stage (2) Formation of SiO_xNWs by SLS and stage (3) Formation of SiO_x nanocakes.

4.3.3. Summary

All the results can be summarized as follows: In the tip growth group, the SiO_x nanowires were 13 nm to about 243 nm in diameters and 194 nm to several microns in length.

From FESEM these wires were embedded with gold at 1200°C. And the obtained SiO_x nanofibers look like comet and tree roots in shape, which grown beneath the nanowires with diameter between 8 nm to 30 nm and around 50 nm to 2.5 μm in length.

In root growth group, the average lowest diameter found to be 37 nm at 68 Å gold layer thickness and as the layer become thicker, the SiO_x nanowires diameter become bigger. The obtained nanostructures with different experimental conditions are amorphous based on XRD results.

The best growth conditions for SiO_xNWs found to be as follows. The thicker Au layer involved in the synthesis of SiO_xNWs should obtain at 140 Å which equal to 40 sec sputtering time. Also, the temperature should be elevated up to 1200°C and the best $\text{TiO}_2\text{:C}$ mass ratio found to be at 1:2. Increasing the deposition time will increase the yield of grown wires. Whereas, the decreasing of argon flow rate not less than 10 sccm, gives the highest growth yield.

The unique morphology of SiO_x nanocages, were obtained when the substrate placed 6 cm far from the mixed $\text{TiO}_2\text{:C}$ powders boat.

For the first time SiO_x nanocakes were fabricated using rapid heating rate and kept at temperature of 1200°C for 8 minutes deposition time.

4.4. High Resolution Transmission Electron Microscopy Characterizations

The samples were prepared by ultrasonic agitation of the SiO_x nanostructures in ethanol for 5 minutes to remove the grown nanostructures from the substrate surface and then a small drop of ethanol containing SiO_x nanostructures was deposited on TEM copper grids, which was heated to 60°C .

Fig. 4.37 shows high resolution transmission electron microscopy (HRTEM) image of SiO_x nanowire with Au-Si nano-ball on its tip. This result shows that the silicon nanowires were grown by normal VLS mechanism, where the Au-Si nanoball at the top of the wire.

The SiO_xNW was moving during capturing due to charging effect which happened with non-conductive elements and compounds. This motion affected the quality of the image.

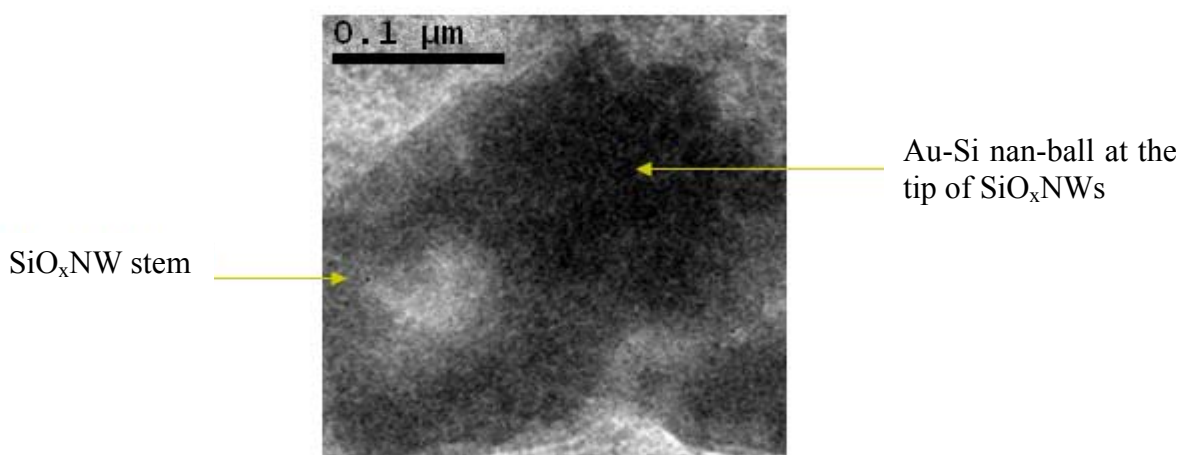


Figure 4.37 HTEM image of Au- SiO_x nanowire tip and stem grown at 1200°C with 10 sccm of Ar flowrate gas for 1h.

In Fig. 4.38 (a) the HRTEM image shows SiO_xNWs without any attached Au-Si nanoballs. These wires have many branches on the stem and tip, which grow to form new wires during growth process.

The HRTEM image shown in Fig. 4.38 (b) did not show any spherical tip at high resolution on the tip area of SiO_xNW .

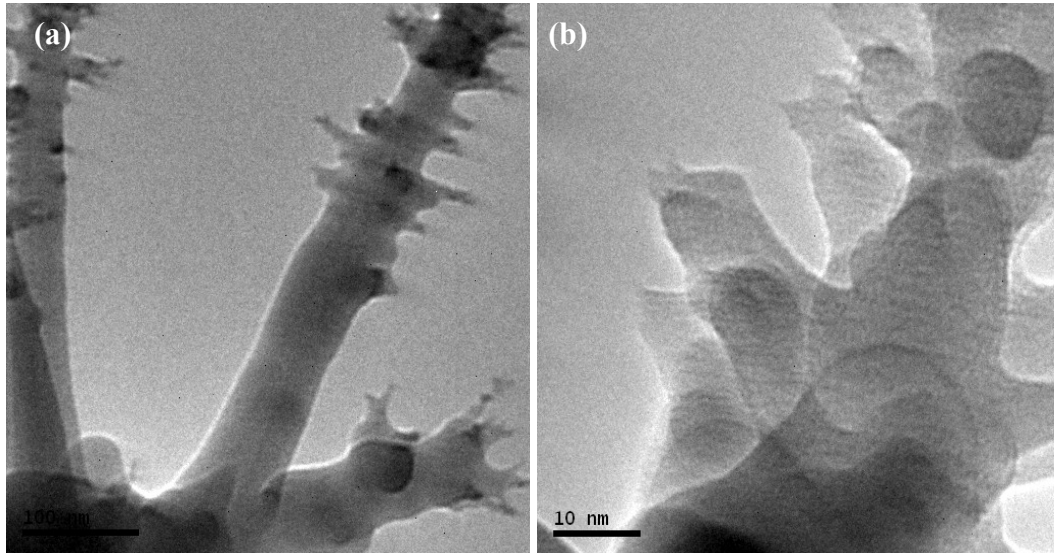


Figure 4.38 HRTEM image of (a) SiO_xNWs grown at 1200°C and under 10 sccm Ar flowrate gas for 1h (b) magnified image of the tip of the wire.

Fig. 4.39 shows two areas of SiO_xNW stem the core, area A; surrounding shell and area B, the core indicates that these wires are solid not hollow tubes as expected. The core area indicates small layers of amorphous silicon. As results our grown SiO_xNWs were in core- shell orientation.

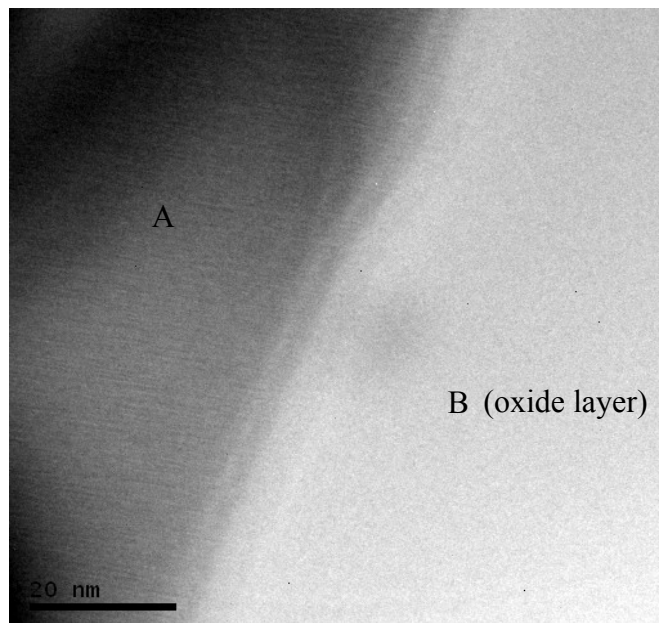


Figure 4.39 HRTEM of (A) core SiO_xNW grown under 1200°C with 10 sccm of Ar flowrate gas for 1h and (B) the outer shell.

4.5. Optical Properties of Silicon Oxide Nanostructures

4.5.1. Photoluminescence of SiO_x Nanostructures

The photoluminescence (PL) spectrum of SiO_x nanowires was measured at room temperature using He-Cd laser (325nm) (3.8 eV) as an excitation source. Figure 4.40 shows a typical PL spectrum of SiO_x nanowires deposited on Au coated silicon substrate.

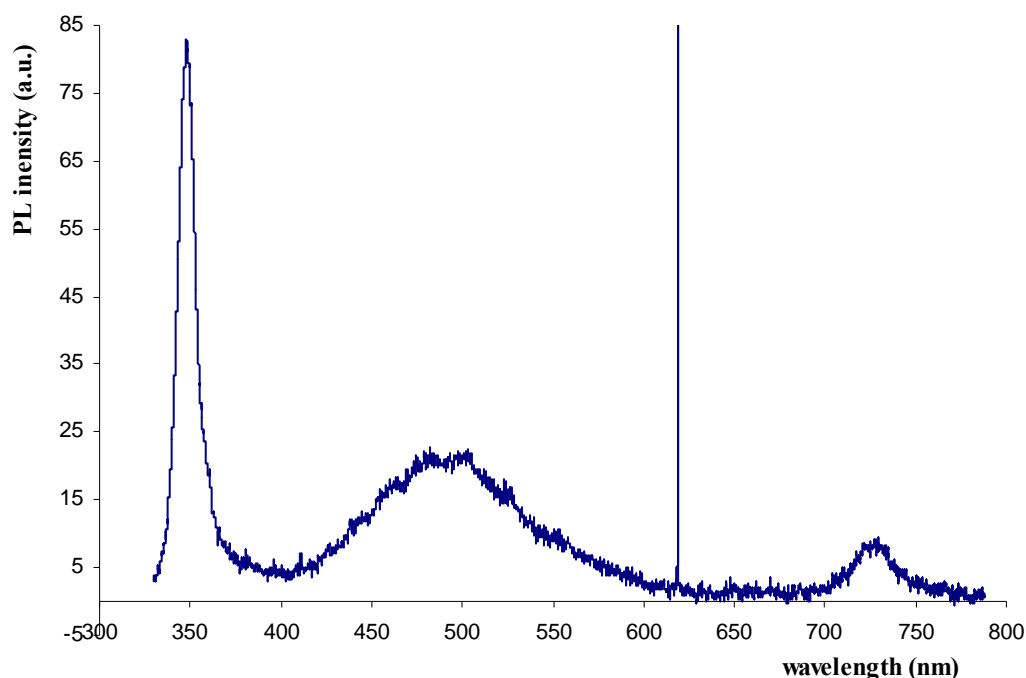


Figure 4.40 Room temperature PL spectrum of Au-SiO_x nanowires grown at 1200°C with 10 sccm of Ar flowrate gas for 1h recorded with excitation at 325nm.

The PL spectrum shown in Fig. 4.40 reveals a broad emission band from 333 to 790 nm. The broad band is composed of UV peak centred at 350 nm (3.54 eV), one wide peak in the blue and green regions (400–600 nm) and red band centered at 730 nm. Also, the vertical line at 612 nm is referred to the wave length of absorbed photon from the device.

Our UV emission can be attributed to the silicon oxide to silicon interface layers inside the SiO_xNW which become oxidized at high temperature. Lin et al. [127] reported UV light emission with a wavelength around 360–370 nm from porous silicon prepared by

CHAPTER 4 RESULTS AND DISCUSSIONS

high temperature oxidation, and it was believed that the UV light emission occurred in the luminescence centres in silicon oxide. Kanashima et al. [128] reported that photoluminescence peaks at 3.4–3.5 eV for the silicon oxide film were observed, and they believed that the PL peaks at 3.4–3.5 eV originated from oxygen excess defects.

In addition, there exist large quantities of different types of unsaturated bond in the large volume fraction interface in the nanostructures, which produce some defect energy level in the energy gap, and cause new luminescence bands.

The blue emission in our work may be attributed to natural oxygen vacancies. Usually, blue emission peaks position occur in the range of 414–470 nm and it have been previously observed in the PL spectrum of SiO_x nanowires by Yu at al. and Liu at al. [22,37], which was due to neutral oxygen vacancy or oxygen deficiency-related diamagnetic defect centers [22].

Also, the similar green emission peak at 540 nm has also been reported from the SiO_x nanowires [39], which has been due to neutral oxygen vacancies [123]. We believe that both blue and green light emissions from the SiO_x nanostructures in the present study can be attributed to the above-mentioned defects arising from oxygen deficiency, presumably being generated during the high temperature synthetic process.

4.5.1.1. Effect of Temperature on the PL of SiO_x Nanostructures

Fig.4.41 shows two PL spectrums of SiO_xNWs grown at 1200°C and 1100°C under 10sccm Ar flowrate for 1h. For those SiO_xNWs grown at 1200°C, three bands including two blue bands centred at 465 nm (2.67 eV) and 482 nm (2.57 eV) and one green band centred at 502 nm (2.47 eV) were visible. There were no peaks observed in the UV and red bands. While, the PL spectrum of the SiO_xNWs grown at 1100°C, a low intensity broad band with out identified peaks were obtained.

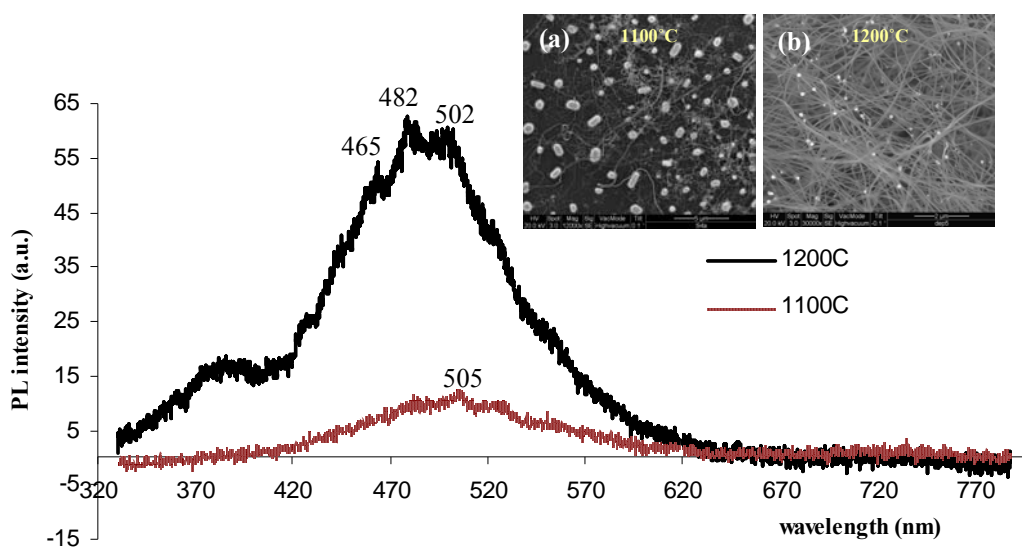


Figure 4.41 Room temperature PL spectra of SiO_xNWs grown at 1200°C and 1100°C under 10sccm Ar flowrate for 1h.

In Fig. 4.41 (a), the FESEM image of SiO_xNWs grown at 1100°C seems to be less dense. The related PL spectrum in Fig. 4.41 was less intense. The FESEM image in Fig. 4.41 (b) shows SiO_xNWs grown at 1200°C. Here, the SiO_xNWs are denser look like a completed network.

The PL spectrum with thick line indicates the higher intensity emission peaks in blue and green regions as mentioned. In general, for high density SiO_xNWs the relative resultant PL spectrum should be high in intensity and versa versa.

4.5.1.2. Effect of Au Catalyst on the PL of the SiO_x Nanostructures

In Fig.4.42 the UV band in the PL spectrum is the same for both catalytic and non-catalytic SiO_x nanowires centred at 350 nm (3.54 eV). The PL intensity peak is low for SiO_xNWs deposited without Au catalyst. In contrast, the blue and green emission peaks were higher in non-catalytic growth, because the grow yield is higher with smaller diameter.

In catalytic growth, the Au nano-balls can be used to control the diameter of the grown wires. Therefore, the regions where SiO_xNWs growth sites occur are reduced.

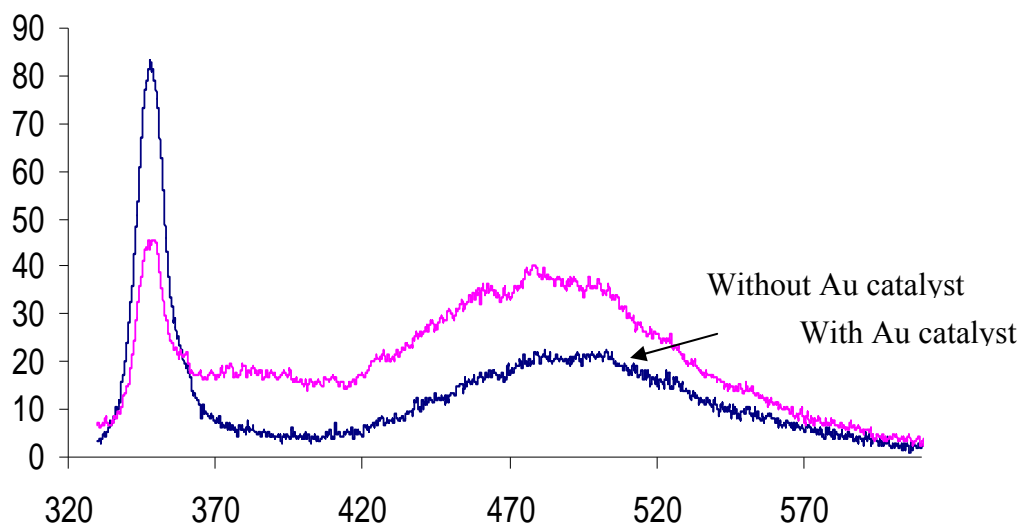


Figure 4.42 Room temperature PL spectrums of catalytic and non-catalytic SiO_x nanowires grown under 1200°C with 10 sccm of Ar gas flowrate for 1h.

4.5.1.3. Effect of Annealing Temperature on the PL of SiO_x Nanostructures

The PL of SiO_x nanowires grown assisted by catalyst gold before and after annealing are shown in Fig 4.43. The sample was annealed at 1000°C for 30 minutes. The results reveal that no UV emission peak after annealing and the intensity of the three peaks become less by about 10 units.

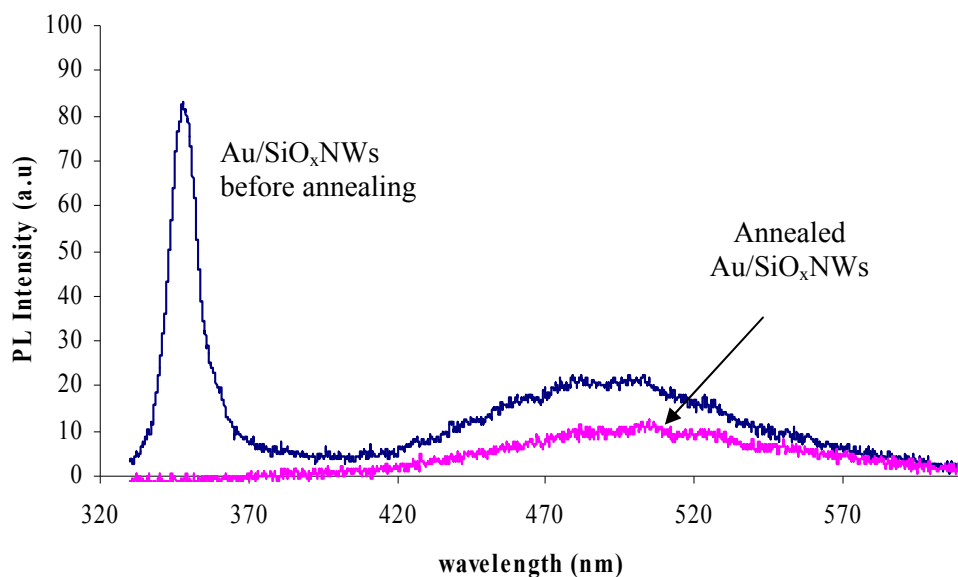


Figure 4.43 Room temperature PL spectrum of Au-SiO_x nanowires grown at 1200°C under 10 sccm of Ar gas flowrate for 1h with excitation at 325nm recorded before and after annealing.

Here, the annealed temperature would release the local stress formed during growth of the nanowires and decrease the amount of defects; then the PL peak's intensity would be reduced due to the decrease of emitting centres.

4.5.2. Discussion on PL of SiO_x NWs

The process of charge transfer widens the band gap directly by emptying the occupied density of state (DOS) below fermi energy, E_f . It has been shown that electronegative elements such as oxygen and nitrogen possess the special ability to widen the band gap by producing the holes below E_f through charge transportation during bond formation [25], which explain the continues transitions in the broad band.

To understand the cause of this irradiative recombinations we have to point out to the red or weak emission of SiO_xNWs [100], which can be referred to the nonbridging oxygen hole centres (NBOHCs, $\equiv\text{Si}-\text{O}\cdot$) [119].

Unlike bulk Silica, the SiO_x nanowires have very large surface to volume ratio, which allows the molecules (oxygen, hydrogen, hydroxide and water) to be adsorbed and diffused to SiO_x nanowires during growth process as well as when the sample is exposed to air. There are two radicals that may form intrinsic defects:

- a) The hydroxyl radicals $\equiv\text{Si}-\text{O}-\text{H}$
- b) The peroxy linkage $\equiv\text{Si}-\text{O}-\text{O}-\text{Si}\equiv$ [120]

These intrinsic defects may change to be (NBOHCs, $\equiv\text{Si}-\text{O}\cdot$) by breaking the original bond as in Fig. 4.44.

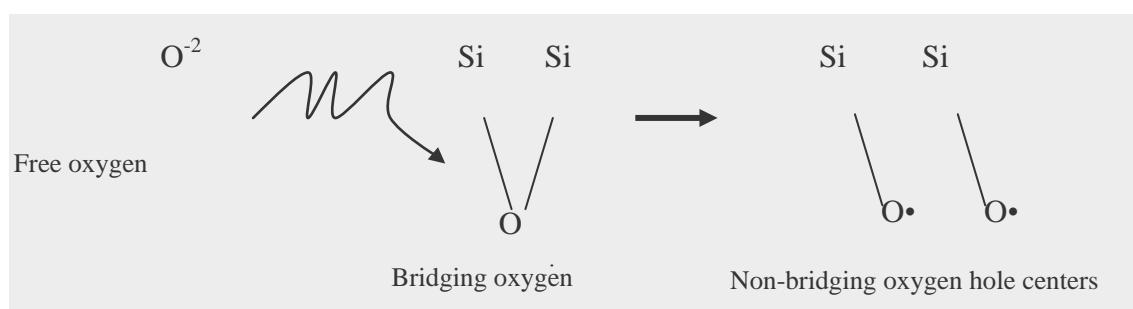


Figure 4.44. The formation of non-bridging oxygen centers

CHAPTER 4 RESULTS AND DISCUSSIONS

It is possible for NBOHCs to be induced by the high-energy photon (3.8 eV) excitation in our PL measurement to form $\equiv\text{Si}-\text{O}\cdot \rightarrow \equiv\text{Si}\cdot + \text{O}$.

The emission of the blue light has been suggested due to oxygen deficient centres (ODCs) such as neutral oxygen vacancies $\equiv\text{Si}-\text{Si}\equiv$ [123,136] and some intrinsic diamagnetic defect centres, such as the twofold coordinated silicon lone pair centres ($=\text{Si}$: i.e. $\equiv\text{Si}-\text{O}-\text{Si}-\text{O}-\text{Si}\equiv$) and self trapped excitons (STEs) [122,123].

Our strong UV emission band is agreed with porous silicon prepared by high temperature oxidation [127] UV emission, and it was believed that the UV light emission occurred in the luminescence centres in silicon oxide.

4.5.3. Fourier Transform Infrared Spectroscopy Characterization of Silicon Oxide Nanostructures

Fourier Transform Infrared Spectroscopy (FTIR) can examine various covalent bond types of the obtained SiO_xNWs . The IR absorption properties are investigated by studying the vibration modes of Si–O on the surface of the amorphous SiO_x nanowires. To study the function groups of the SiO_x nanowires grown on Au coated Si substrate, the sample was scratched out.

The scratched sponge-like silicon oxide nanowires were mixed with high-purity potassium bromide (KBr) thin film salt to make a measurement pellet. The IR beam hits the prepared film with spectral resolution of 0.5 cm^{-1} in the range of $400\text{--}4000\text{ cm}^{-1}$. In Fig. 4.45, the absorption spectra of these samples are presented.

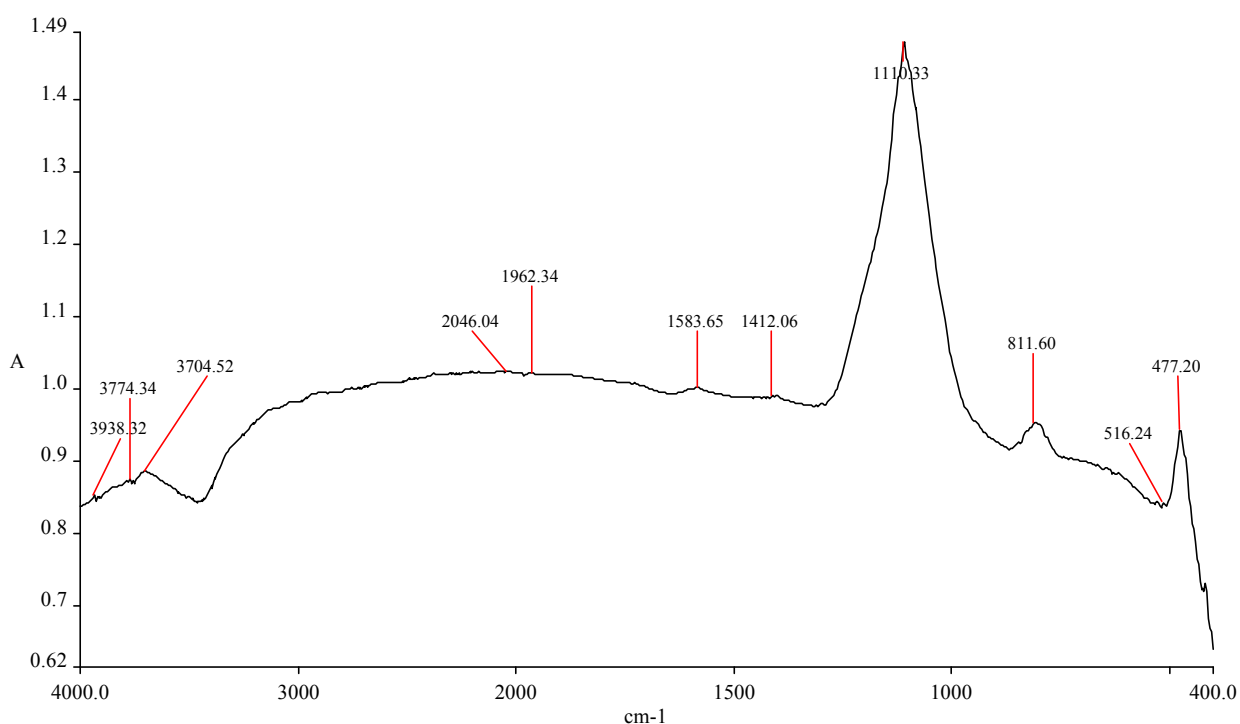


Figure 4.45 Absorption IR spectrum of non-catalytic SiO_x nanowires grown under 1200°C with 10 sccm of Ar flowrate gas for 1h.

CHAPTER 4 RESULTS AND DISCUSSIONS

Here, the absorbed spectrum shows the well-known transversal optical (TO) resonance, the Si–O–Si bond rocking vibrational mode (477 cm^{-1}) [193], the O–Si–O bond bending mode (811 cm^{-1}) [194] and Si–O asymmetric stretching mode (1110 cm^{-1}) [195]. And the strongest absorption peak locates at the higher frequency side of 1110 cm^{-1} which pointed to Si–O asymmetric stretching mode. All the bond types and related wavenumber are listed in table 4.5.

Table 4.5 FTIR data of SiO_xNWs , the bond types, vibration modes and related wavenumber.

Bond types	Vibration modes	Wavenumber ($1/\lambda$) cm^{-1}
Si–O–Si (single)	Rocking	477
O–Si–O (single)	bending	811
Si–O (single)	asymmetric stretching	1110

The obtained SiO_xNWs grown on Au coated Si substrate at 1200°C under various Ar flowrate for 1 h deposition time with different locations on Si substrates.

The Ar flowrate were changed from 60 to 10 sccm. Samples at different flowrates were examined by FTIR beam.

The absorption spectra for all these six samples are illustrated in Fig. 4.46. Here, the IR spectrum peaks shown in Fig. 4.46 (f) to Fig. 4.46 (c) at ($475\text{-}477\text{ cm}^{-1}$) can be related to S–O stretching mode.

The reported peaks for samples with high Ar flow rates have lower intensities. This can be related to density of the grown SiO_xNWs on the sample which synthesized at related Ar flow rate.

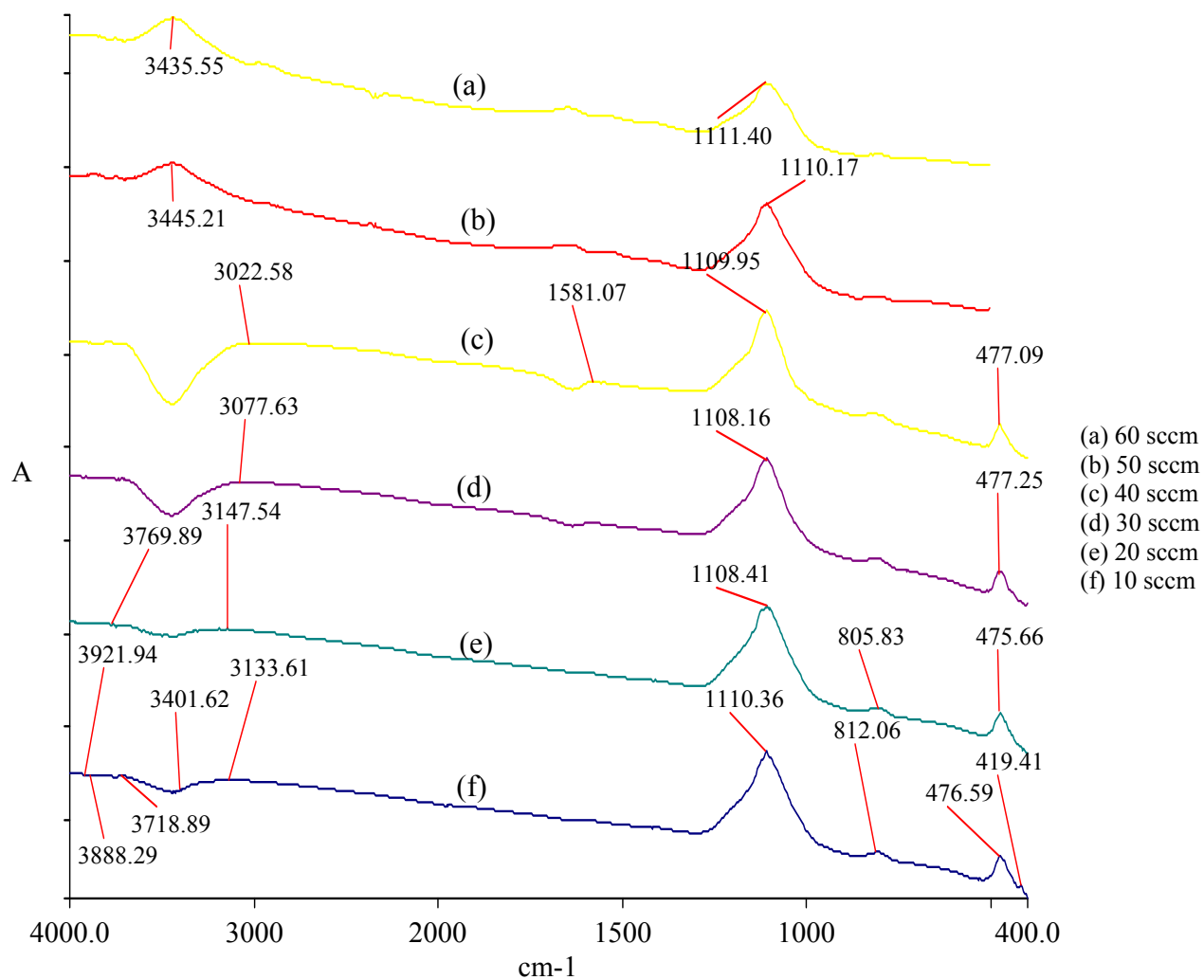


Figure 4.46 IR spectra of SiO_xNWs grown at 1200°C deposited for 1h at Ar flowrates (a-f) 60, 50, 40, 30, 20 and 10 sccm respectively.

4.6. Growth of Beta-Silicon Carbide Nanowires

4.6.1. Introduction

We have successfully fabricated beta silicon carbide (β -SiC) nanowires on pure silicon substrate. We used carbon powder as shown in Fig. 4.47. The source-substrate distance was varied because it changes the temperature for different substrate at different locations.

In this experiment the carbon boat and 5 substrates were placed inside the chamber and then Ar gas was introduced to the chamber at 10 sccm flowrate. The chamber was evacuated and the temperature was raised up to 1200°C at 1.5°C/sec. After the temperature reached 1200°C all the system left for one hour and then cooled to room temperature.

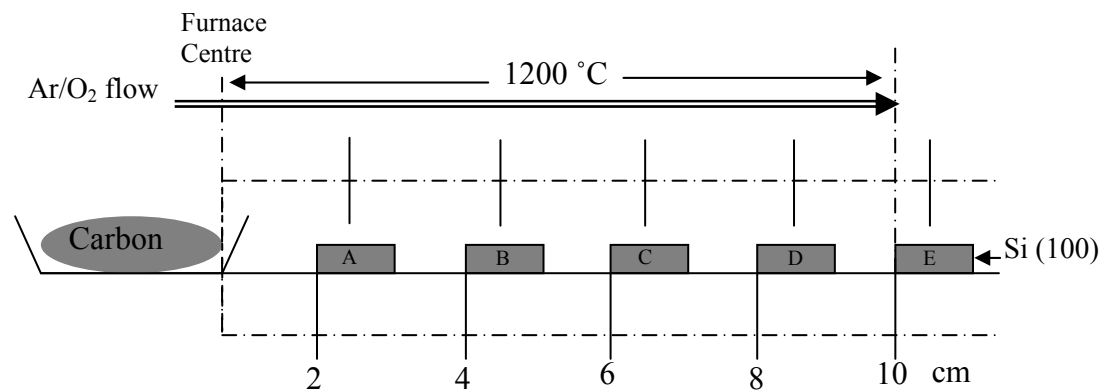


Figure 4.47 A schematic diagram of experiment setup for SiC fabrication at certain positions using Ar /O₂.

The XRD spectra in Fig. 4.48 are for locations A-E at 2, 4, 6, 8 and 10 cm apart from the furnace centre where the porcelain boat containing carbon powder is located.

Spectrum A and B seem to be the same in their patterns, which refer to beta silicon carbide (β -SiC) nanowires, as it will be discussed later. At location 6 cm in Fig. 4.48 (C), the spectrum shows one strongest and very sharp peak at $2\theta = 56.1$ degrees corresponding to Si (111). While no peaks are shown on D and E, amorphous SiO_x nanowires seem to be the only nanostructures that exist.

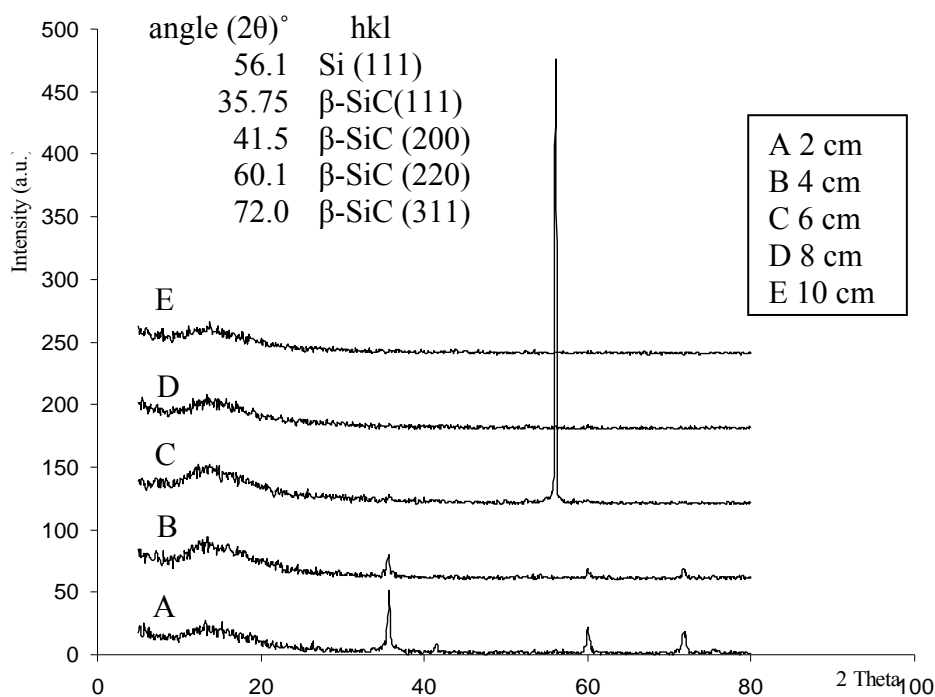


Figure 4.48 XRD spectra for as prepared samples (A-E) at 2, 4, 6, 8 and 10 cm locations from the furnace centre respectively grown at 1200°C with 10 sccm Ar gas flowrate for 1h.

Fig. 4.49 shows the FESEM image of β -SiC nanowires in samples A and B at 2 and 4 cm locations which shows that, sample A has higher yield than sample B.

The EDX mass ratio in Fig. 4.49 (A) shows that these wires consisted of silicon, carbon and oxygen. The mass ratio of carbon to oxygen (C:O) intensities in sample A is bigger than 1, but in (B) it is less than 1. The percentage of silicon is almost same in both locations. The magnified FESEM in Fig.4.49 (C) gives an estimation that these wires seems to be in same length.

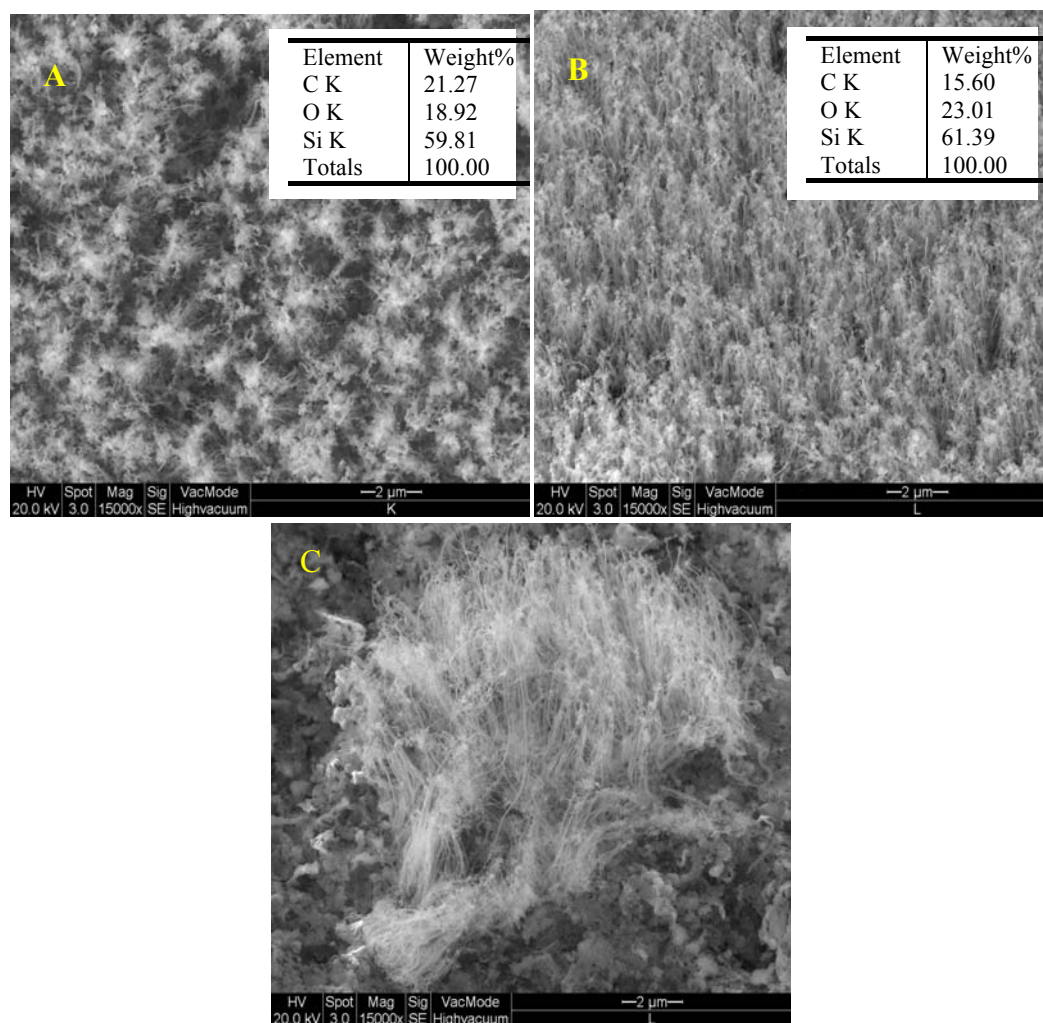


Figure 4.49 FESEM image of β -SiC nanowires at (A 2cm) and (B 4cm) locations from the furnace centre grown at 1200°C with 10 sccm flowrate for 1h; with inset image of EDX element mass percentages for A and B. (C) is magnified image (15k)

The typical XRD spectrum in Fig. 4.50 shows β -SiC nanowires found at 2 and 4 centimetres. The diffraction peaks positions in the pattern can be indexed to β -SiC with the cubic structure. The strong peak of β -SiC (111) at 35.75° become weaker as the distance increase. This is may be due to the reduction in the synthesized wires. Patterns with less intensity found at $2\theta=41.5^\circ$, 60.1° and 72° can be indexed to (200), (220) and (311) facets. The intensity of these peaks reduced as the location of the examined substrates placed away from the furnace centre.

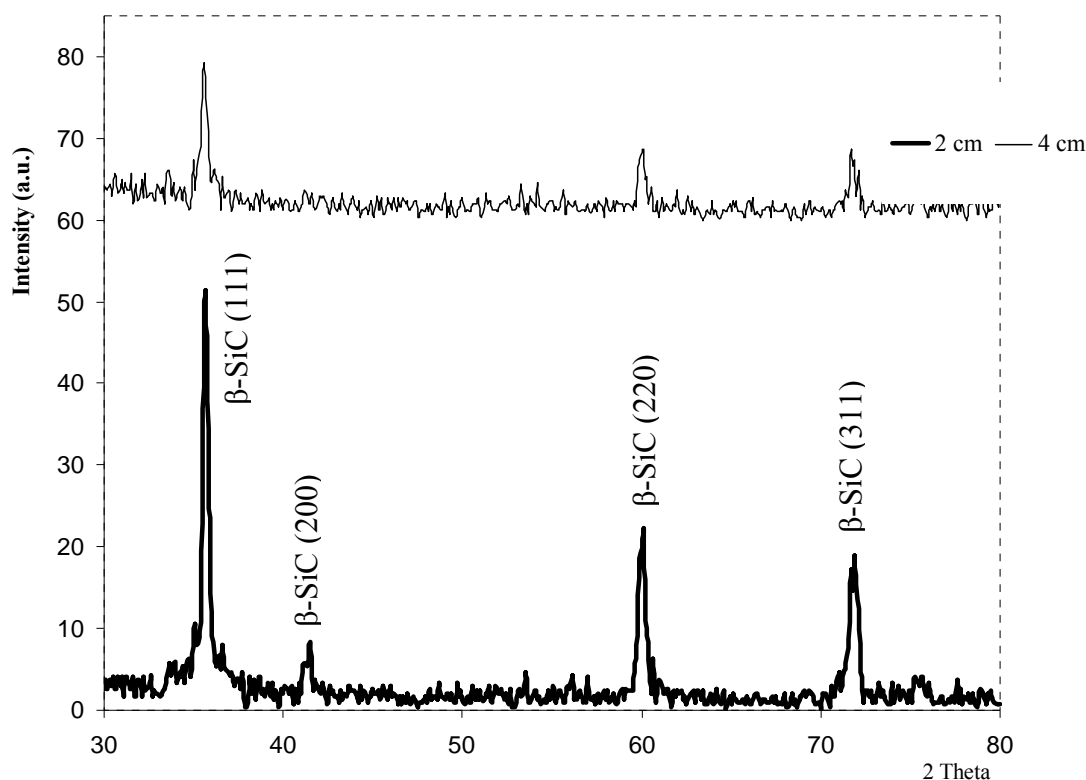


Figure 4.50 XRD spectrum for β -SiC nanowires grown at 2cm and 4cm locations respectively at 1200°C with 10 sccm flowrate for 1h.

To examine the alignment of obtained β -SiC nanowires, sample B at location 4cm was tilted and magnified as shown in Fig. 4.51. The alignment of these wires may be due to growth starting time and the uniform distribution of the growth species.

In Fig. 4.51 (A) we can see the aligned nanowires become denser near the edge. The tilted image with 35° in Fig. 4.51 (B) shows the wires with almost the same length.

While in C we can not see nanowires grown in the sample unless near the edge.

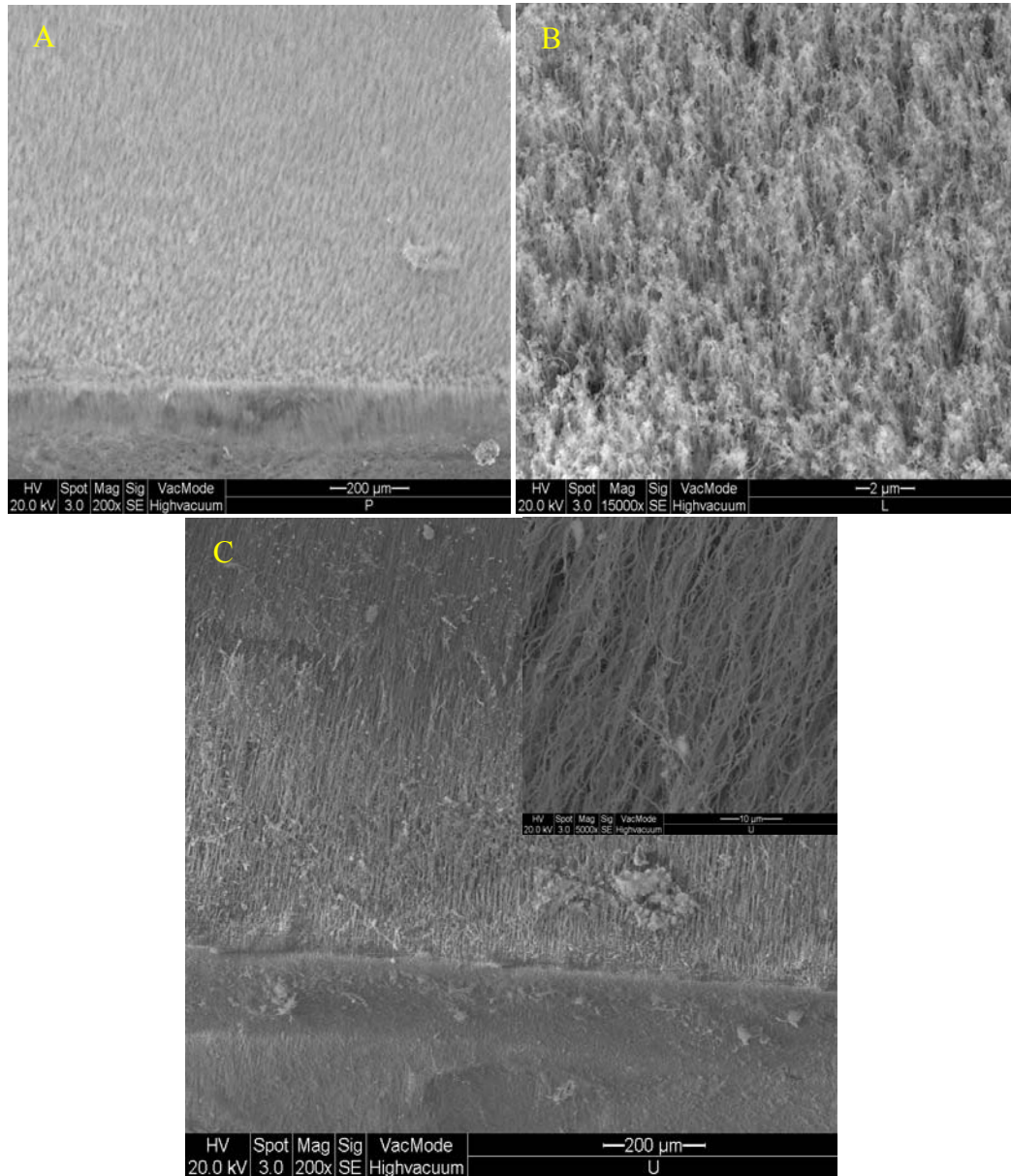


Figure 4.51 FESEM of aligned β -SiC nanowires obtained at location B, 4cm apart from the furnace centre at 1200°C with 10 sccm flowrate for 1h.

Fig. 4.52 reveals that the diameter of the obtained β -SiC nanowires changed with the location of the substrates of 2 and 4 cm. The largest diameters found were on the nearest substrate as in (A) Fig. 4.52. This confirmed that as the Si source is higher the growth continue rapidly. The important factor here is the temperature, which controls the evaporation and condensation of the SiO gas.

Even the location in B is double of A but still gave both small and large SiC nanowires of diameters ranging from 40 to 500 nm. Most β -SiC nanowires have big diameter with in clusters.

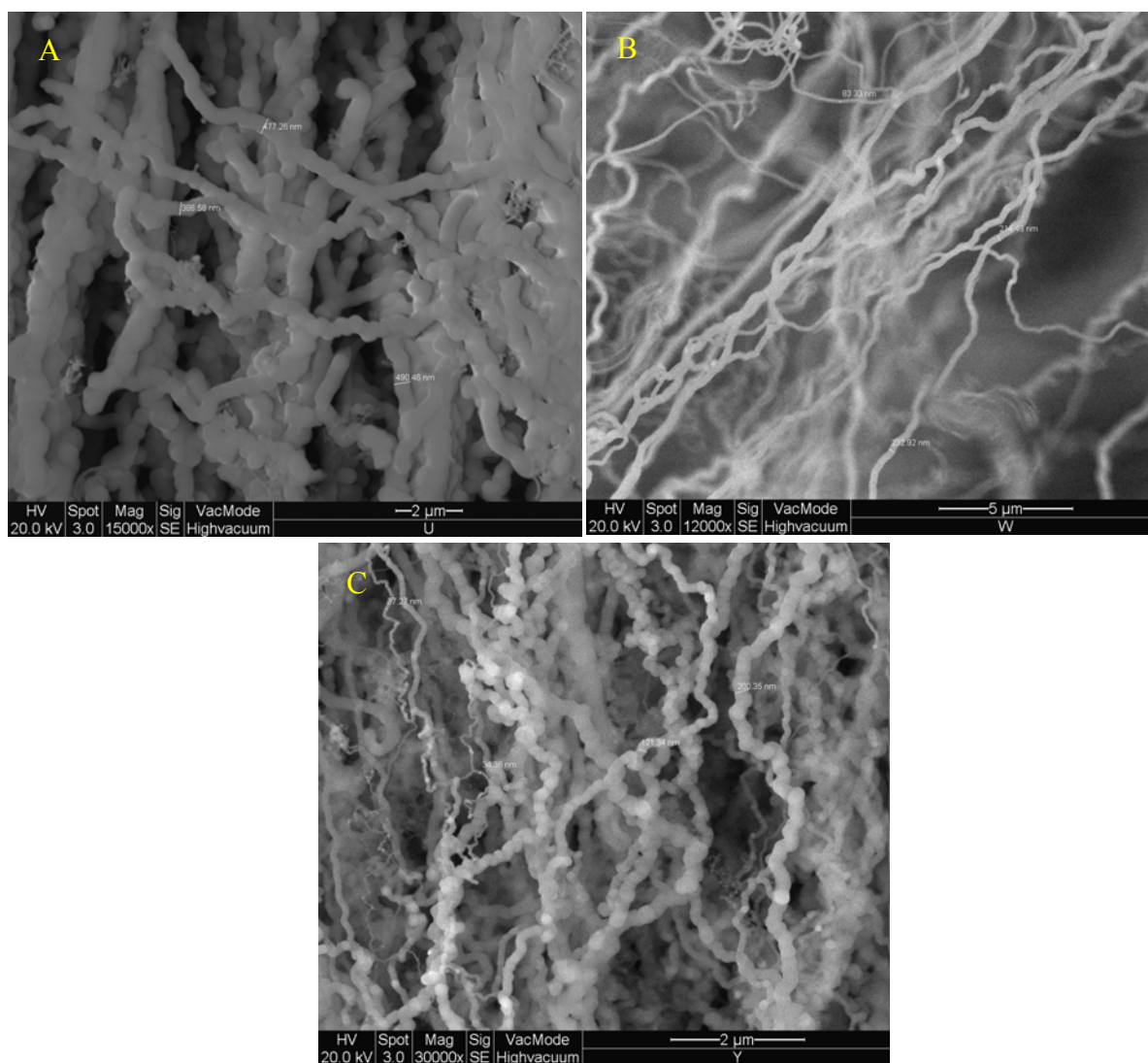


Figure 4.52 FESEM of β -SiC NWs diameters at (A=2cm and B= 4cm) at 1200°C in 10 sccm Ar flowrate gas for 1h. (C) enlarged image of B.

4.6.2. Parametric Studies on the Growth of β -SiCNWs.

O₂ was used instead of Ar to study their effect on the growth of β -SiC nanowires. The effect of heating rate on the growth of SiC nanostructures has been studied. These parameters were chosen for different substrate locations because we want to know the best growth conditions.

4.6.2.1. Effect of the Substrate Location on the Growth of β -SiCNWs with Ar gas flow.

The effect of substrate location from the boat containing graphite using Ar gas on the growth of β -SiC nanowires for A-E samples (2-10 cm) can be seen in Fig. 4.53. In all sample locations, the β -SiC nanowires were grown at different yields.

At high temperature zone the yield is high and at the far location the formation of the wires occurs only near the edge as in E (1 and 2) Fig. 4.53. The wires were not aligned, which may be due to defects in the grown wires as mentioned in literature. These defects were affected by temperature fluctuations.

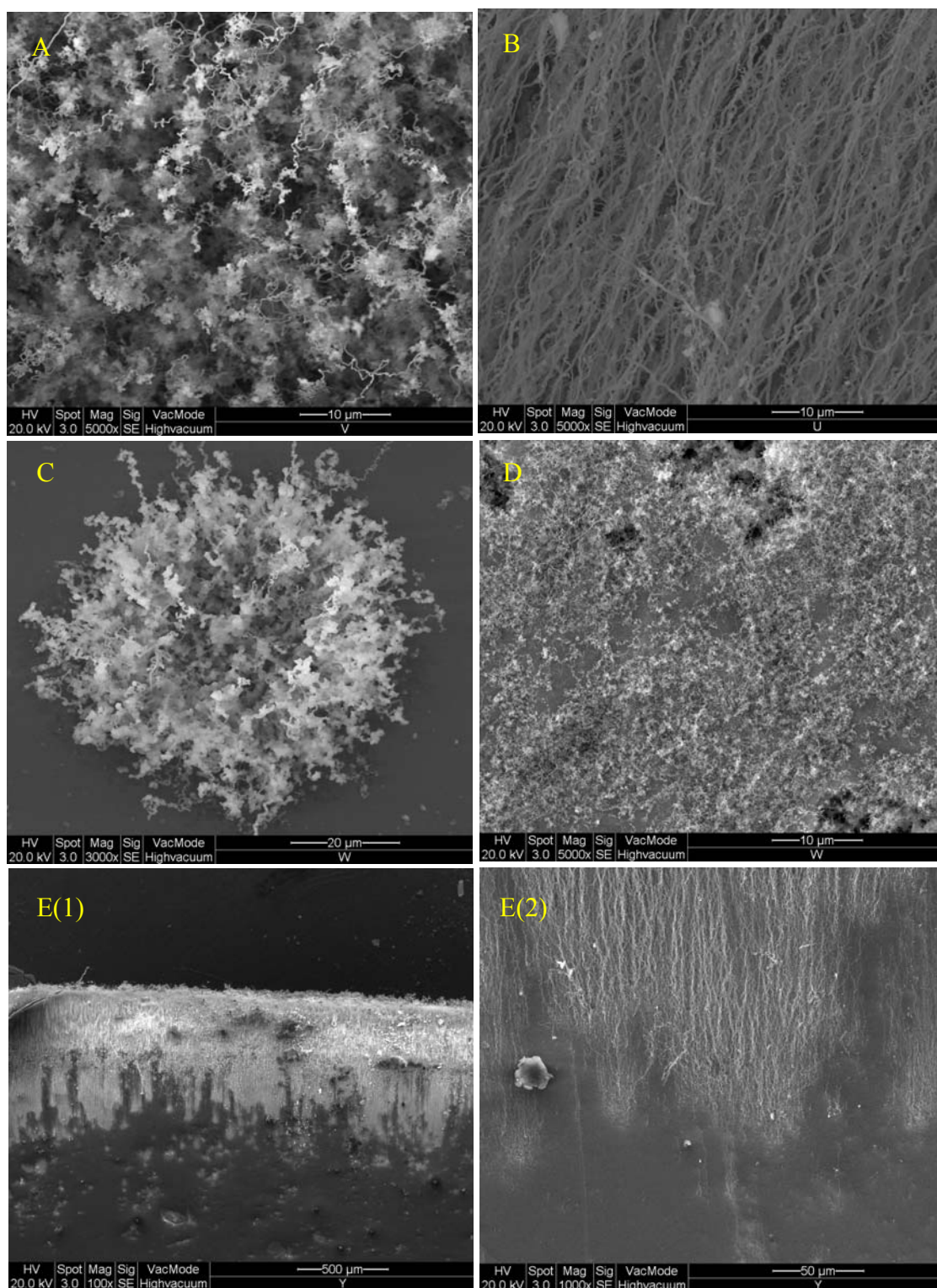


Figure 4.53 FESEM of β -SiC nanowires grown at (A-E), 2 -8 cm locations respectively, and (E (1, 2) at 10 cm from the furnace centre at 1200°C with 10 sccm Ar flowrate for 1h.

The XRD spectra in Fig. 4.54 shows different peaks for β -SiC nanowires obtained at different locations. Peaks intensities become lesser as the position of the substrate shifted away from the furnace centre. When the peaks of (220) and (311) planes present the SiC nanowires have three different crystal facets directions which is can be seen in Fig. 4.53 (B) and (C).

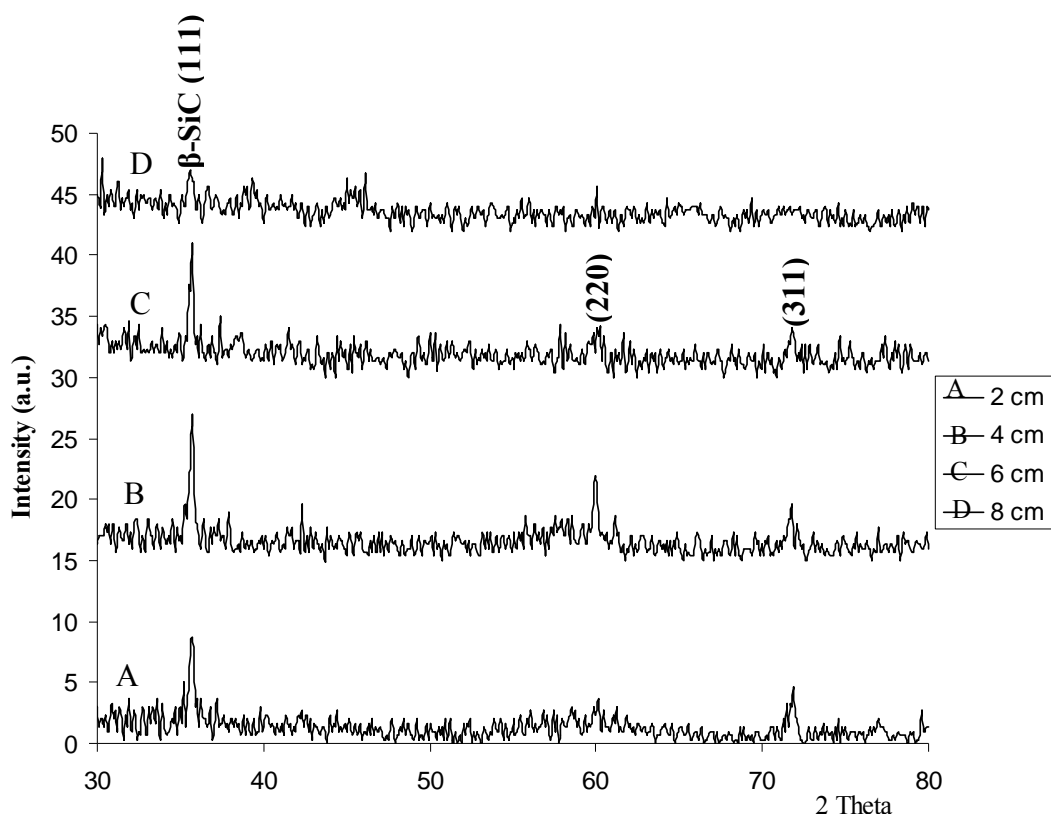


Figure 4.54 XRD spectra of β -SiC nanowires at (A-B, 2-8 cm from the furnace centre) using Ar as an ambient gas at 1200°C for 1h.

4.6.2.2. Effect of the Substrate Location on the Growth of β -SiCNWs with O_2 gas flow

The effect of oxygen gas on the growth of β -SiC nanowires has been studied. As shown in Fig.4.55 there is no growth of β -SiC nanowires at location 2 cm near the carbon boat and when the location of the substrate is shifted away from the centre such as at location C, D and E, dense and complicated networks of wires were formed.

CHAPTER 4 RESULTS AND DISCUSSIONS

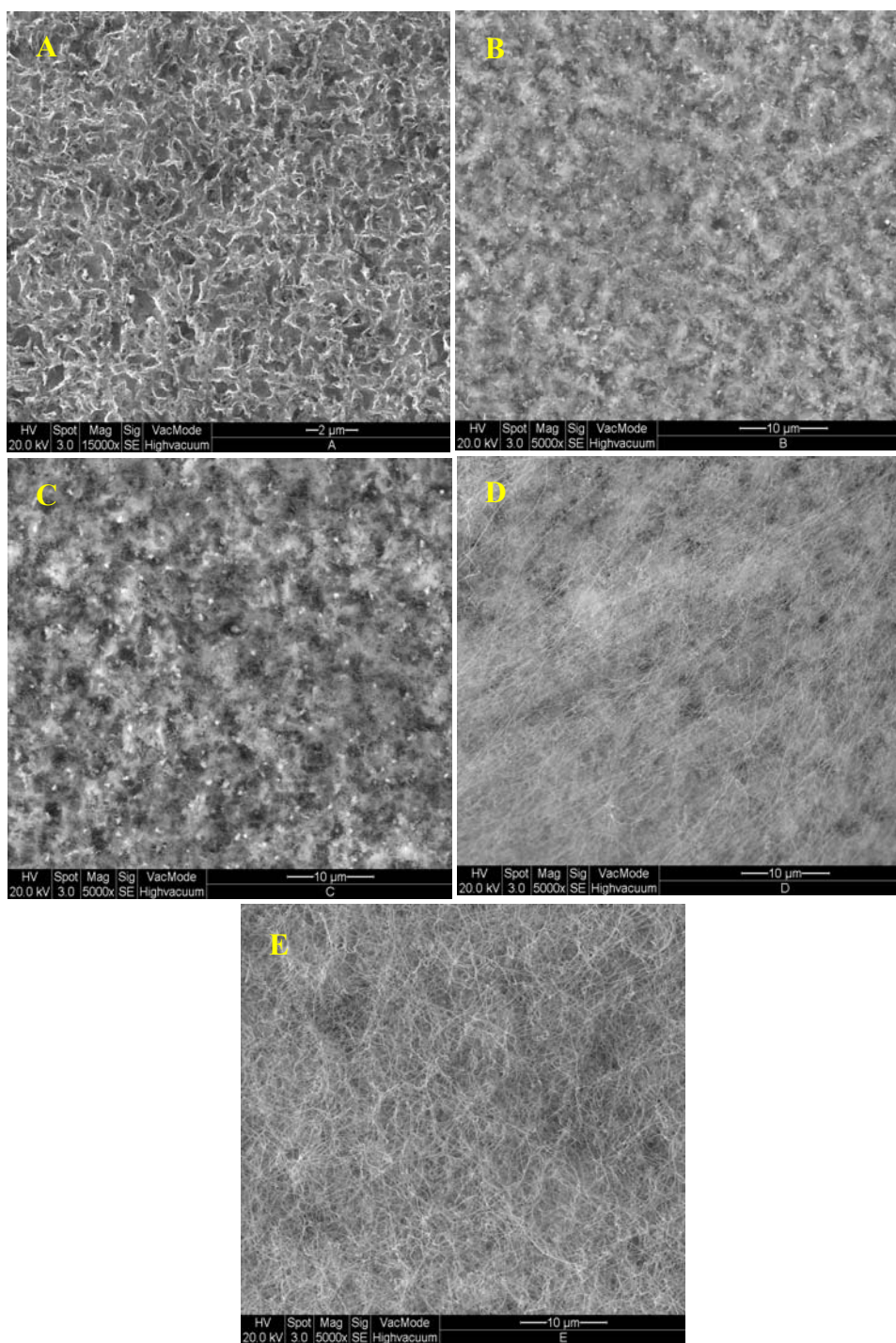


Figure 4.55 FESEM of substrate locations from the graphite boat at (A-D), (2 -8 cm) and E at 10 cm using 10 sccm of O_2 flowrate gas at 1200°C for 1h.

CHAPTER 4 RESULTS AND DISCUSSIONS

Also, It can be seen from Fig. 4.55 that the growth starts at 4 cm and continue with high yield as the distance increases.

The XRD spectrum taken for four samples at different locations are shown in Fig. 4.56.

The peak of β -SiC (111) is strong whereas (200), (220) and (311) peaks are weak. Also (111) peak becomes smaller as the distance increases.

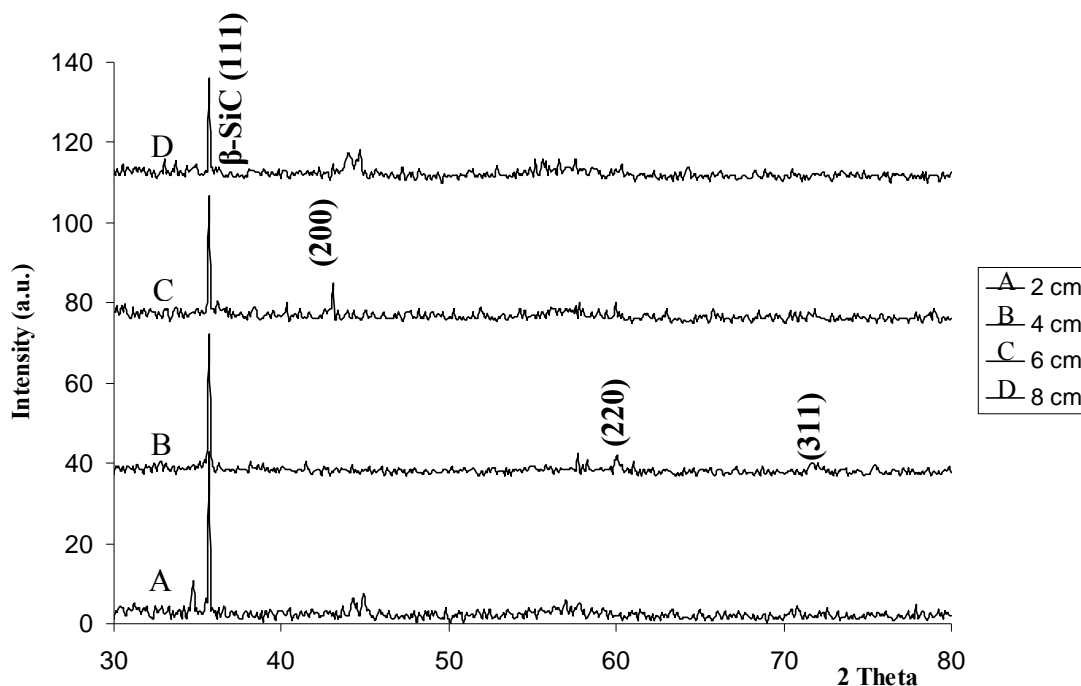


Figure 4.56 XRD spectra of β -SiC nanowires using 10 sccm of O_2 flowrate gas at locations 2cm, 4cm, 6cm and 8cm at 1200°C for 1h. heatitemperature.

4.6.2.3. Effect of Rapid Heating Rate on the Growth of β -SiCNWs

In this experiment, the furnace was first heated up to 1200°C and the carbon boat and the prepared substrates were loaded direct inside it. The substrate was placed 6 cm apart from the carbon boat. Then the system was evacuated for one hour and the Ar gas was introduced to the system. Then when the system cooled to room temperature, the samples were taken for characterization. The obtained β -SiC nanowires are in bunch arrangement. The nano-bunches are randomly distributed over the substrate surface and the nanowires are not aligned as can be seen in Fig. 4.57 (A and B).

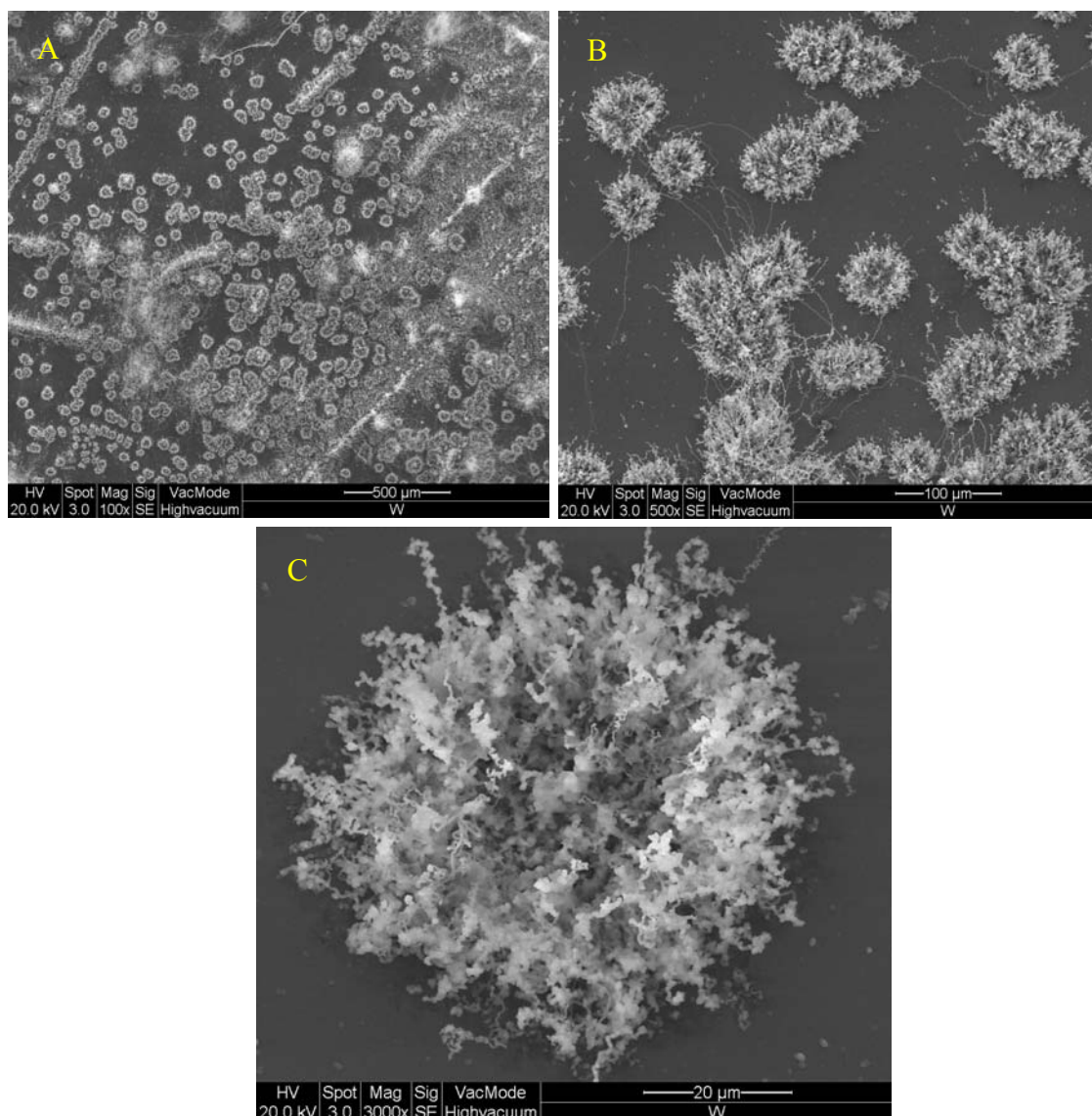


Figure 4.57 (A-C) FESEM of β -SiC bunch-like nanostructures (with 0.1k, 0.5 and 3k magnifications, respectively) grown with rapid heat rate by loading the silicon substrates directly to the furnace centre at 1200°C and 10 sccm of Ar flowrate for 1h.

CHAPTER 4 RESULTS AND DISCUSSIONS

In Fig. 4.57 (c) the crowded wires are grown in different directions but from same area. The formation of such unique morphology is not well understood, and it needs more investigations.

The edge of the all the examined samples shows unique morphology. The highest β -SiC nanowires yield and ultra- longer wires found on the edge of different samples as in Fig. 4.58 (A-D).

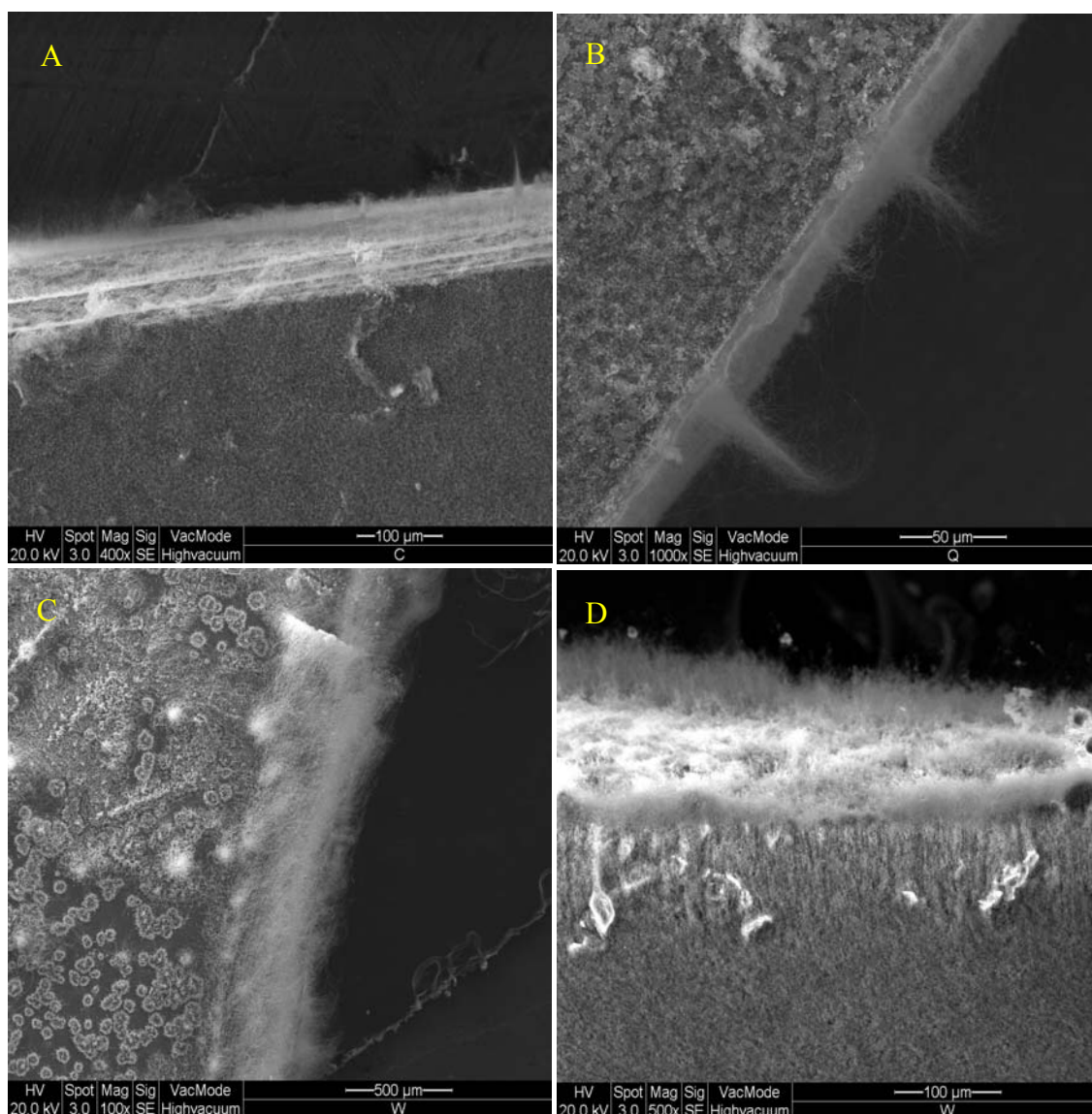


Figure 4.58 FESEM image of ultra-long β -SiC nanowires obtained at the sample edge. The sample was prepared at 1200°C with 10 sccm of Ar flowrate for 1h.

CHAPTER 4 RESULTS AND DISCUSSIONS

The intense growth of wires in the edge areas referred to the low surface energy of such places where the bonded forces between the surface atoms and the interior ones are weak. This phenomenon occurs even on the edges of some samples which do not have growth on their surfaces.

4.6.3. Growth Mechanism of β -SiCNWs

To understand the mechanism growth of β -SiC nanowires, we need to discuss about the carbon effect on this process. Carbon burns to produce many moles of CO over the substrate surface atmosphere. CO can easily react with evaporated SiO to form β -SiC nanowires at lower temperature near surface, which is explained with equations in the coming discussion part.

The β -SiC nanowires follows the OAG self catalysed mechanism because in the non-catalytic the growth is governed by oxygen to make availability of growth species. In the first place the carbon gets oxidized to form the vapour of CO and then enhancing the evaporation of SiO from the substrate as illustrated in Fig. 4.59. When these species reach the substrate surface they react by forming β -SiC, which was deposited on the surface due to temperature fluctuations and anchored to the silicon surface atoms as in stage (1) and with more condensation the SiC nanowires start to evolve and making 1D growth, see stage (2).

Then more SiO vapour give rise to long β -SiC nanowires through the reaction with CO, stage (3). As obtained from the XRD most of the wires are in (111) direction, which explained the nature of their alignment. Because there is some carbon powder left on the boat, we believe that SiO gas is responsible for the stopping of the β -SiC nanowires growth, which stopped to evaporate during cooling time.

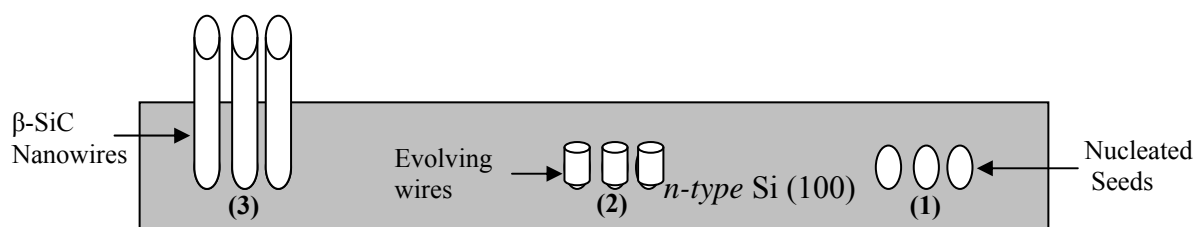


Figure 4.59 A schematic diagram showing the OAG mechanism of SiC nanowires growth.

4.6.4. Fourier Transform Infrared Spectroscopy Characterization of β -SiCNWs

FTIR spectrum shown in Fig. 4.60 represents sharp transmitted peaks of SiCNWs samples fabricated at 2, 4 and 6 cm under 10 sccm Ar flowrate and deposited with 1200°C for 1h. A transmitted peak at 798 cm^{-1} for sample located at 2cm from the furnace centre indicates the transversal optic (TO) mode (Si–C stretching vibration) [196]. Also, the other two peaks of locations 4 and 6 centimetres at 810 and 820 cm^{-1} are referred to the same mode [197]. The peak at 820 cm^{-1} has less intensity than the peaks taken from samples at 2 and 4 cm locations. All peaks show significant asymmetry vibration mode due to the polycrystalline nature of the SiC nanowires.

The FTIR spectrum of SiCNWs grown at 6 cm shown in Fig 4.60 shows weak peak at 1090 cm^{-1} which is visible and can be attributed to the stretching vibration of Si–O [195]. Therefore, we conclude that most wires grown on the sample at 6 cm is SiO_xNWs .

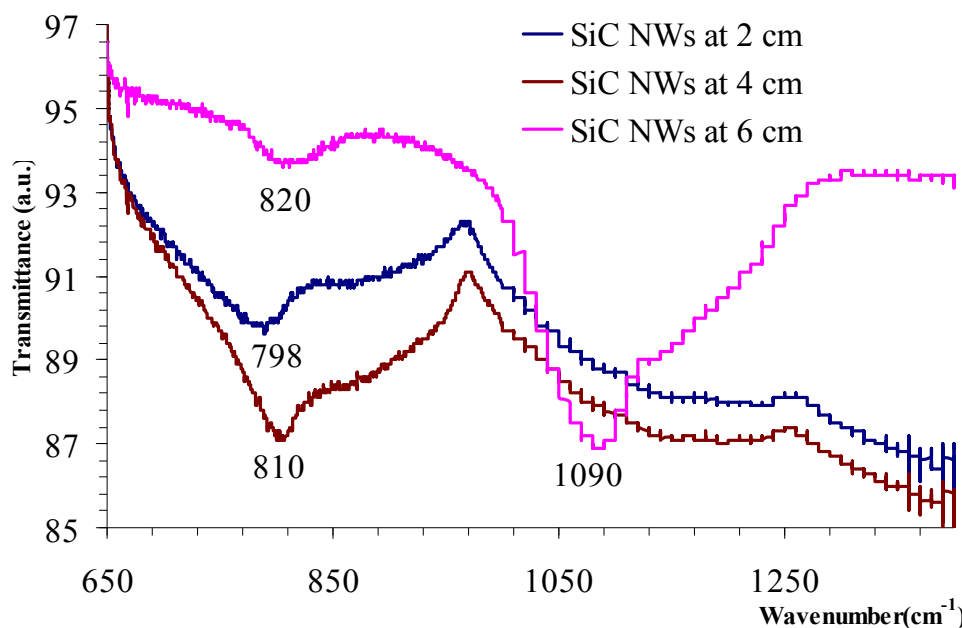


Figure 4.60 FTIR spectra peaks of β -SiC nanowires are corresponding to Si–C stretching vibration at 798, 810 and 820 cm^{-1} and stretching vibration of Si–O for samples grown at 2, 4 and 6 cm locations.

4.6.5. Summary

The β -SiC nanowires were successfully fabricated using simple carbo-thermal evaporation without catalyst. The obtained β -SiC nanowires found to be denser in samples at 2cm location under Ar flow gas. When introducing oxygen gas as ambient gas instead of argon, no growth occurred at location A (2 cm) and the wires growth began at location B (4 cm) and consequently, the growth density increases at location with further distance. The majority of crystal planes were β -SiC (111) with some other less intensity planes of (200), (220) and (311).

The obtained β -SiC nanowires were aligned and with diameters ranged between 40 to 500 nm. Rapid heating rate enhanced the growth of β -SiC nanowires in some surface sites before other places, which results in a bunch like shape.

Strong stretching vibration mode of Si-C at 798, 810 and 820 cm^{-1} were found by the FTIR analysis which evident the existence of SiCNWs with high yield at 2, 4 and 6 cm far from the furnace centre. Another peak at 1090 cm^{-1} found only for the sample placed 6 cm away which can be attributed to the stretching vibration of Si-O.

4.7. General Discussion on the Growth of SiO_x Nanostructures

In the non catalytic growth of silicon oxide nanowires, the formation of carbon dioxide at 1200°C can assist the growth by reacting with the oxide layer over the silicon substrate. We believe that the amorphous silicon oxide was the key factor which significantly enhances the nucleation of one dimensional growth of the SiO_x nanowires. This indicated that the vapour phase generated by thermal evaporation of the solid source (Si+SiO₂) mainly consisted of SiO. The formation of SiO was due to the reaction of Si and CO₂. The nucleation of nano-particles may involve different decompositions of the Si oxide vapour phase at a relatively low temperature of 930 °C as shown in equation (4) inside Fig. 4.61. The evaporation process of silicon oxide (SiO) from the oxide layer formed many pits on the surface as in Fig. 4.61.

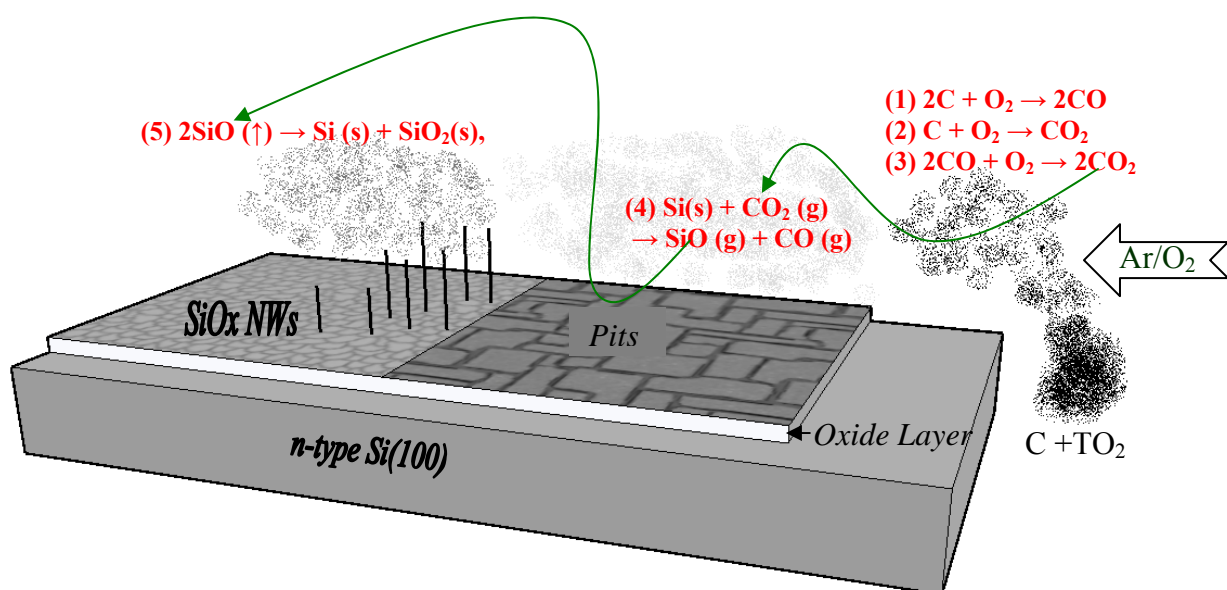


Figure 4.61 A schematic drawing of non-catalytic growth of SiO_x nanowires via carbo-thermal reactions.

Therefore, as much SiO vapour was transferred by Ar or O₂ gases, high yield growth was obtained.

Our results in studying the Ar flow rates effect on the growth of SiO_xNWs confirmed that there is no growth occurred at high rates of argon. But gas flow is important to

CHAPTER 4 RESULTS AND DISCUSSIONS

achieve the growth because no wires obtained at flow rate less than 10 sccm. The role of Ar other than working as carrying gas is the generation of temperature fluctuations over the substrate surface. These fluctuations are important to allow the SiO gas to condense into solid silicon or silica, see Fig. 4.61. All XRD results show the amorphous structure of the obtained wires. At high temperatures (1000-1200°C) these wires get oxidized, so the oxide layer around these wires results in amorphous structure.

In addition the obtained nanowires are sliding over the surface without uniform direction, which is due to gravity. So after nucleation, the wire evolved and as the wire length increased, the wire becomes heavier. As a result, this wire will incline down as illustrated clearly in Fig.4.6. The stronger standing wires are the shorter one with bigger diameter.

Furthermore, the diameter is very small at the far end of the wire; because of amount of SiO feed stock start to stop at the end of the process.

High PL intensity for the non-catalytic growth is due to the formation of oxygen vacancies inside the amorphous SiO_x nanowires. The SiO_x nanowires without catalyst easily can form defects of hydroxyl radicals ($\equiv\text{Si}-\text{O}-\text{H}$) and the peroxy linkage ($\equiv\text{Si}-\text{O}-\text{O}-\text{Si}\equiv$) [120]. As a result, these defects forms non-bridging oxygen hole centres (NBOHCs, $\equiv\text{Si}-\text{O}\cdot$). This unstable bond may react with coming oxygen atoms and break the bonds. Breaking bonds in such a wire increases the natural oxygen vacancies, which is the reason for the PL higher intensity in the case of non catalytic wires. Moreover, this phenomena doesn't happen with Au SiO_x nanowires because the nature of gold, which cannot react with oxygen event at high temperature.

The FTIR strongest absorption peaks located at the higher frequency of 1110 cm⁻¹ in all samples, which indicates that the main bond or mode available is the Si-O asymmetric stretching mode. Higher frequency absorption of IR spectrum in nanowires is because

these wires have a strong surface tension to cause the distortion and the shortening of Si–O bond length. And this will produce higher intensity at higher frequency.

However if we consider the structural characteristics of nanostructures and nanowires, the differences on IR spectrum are very obvious. And there are a lot of point defects such as vacancy and broken bonds of Si–O on these interfaces. Therefore, these could also bring the strong absorption intensity at higher frequency as in [184].

In catalytic growth of SiO_x nanowires the Au balls formation allowed a space for the SiO evaporation this evaporation causes pits (deep holes) on the substrate surface. Pits formation according to Yu-Chiao et al. [87] is due to annealing of Si substrate at 1100 °C for 2 minutes at a flow rate of 100 sccm and it enhanced the growth of SiO_xNWs mainly around these pits. Even in the Au-coated Si substrate, the formation of the pits is due to heating at a temperature of 1000-1200°C in the Ar flow with [24] or with out graphite powder [58].

We suggest the formation of pits in coated substrate is due to the high stress induced by Au thin film in the Si surface and the growth of SiO_xNWs is controlled by the so-called solid–liquid–solid (SLS) mechanism. For non–coated substrates, the formation of pits is due to out-diffusion of Si from the substrate, where Si diffuses into the SiO_x droplets or spherical alloy to induce nucleation and growth of SiO_xNWs, i.e., the SLS mechanism.

Catalytic growth parameters of the SiO_x nanowires depends on a series of experimental conditions, such as substrate coating (Au) thickness, the presence of graphite powder, the substrate temperature, the oxygen gas effect, and the growth time. Temperature is one of the most important factors that influence the nanowires formation. Li at al. [24] suggested that the optimum growth conditions are a substrate temperature of 1000°C, an Ar flow of 250 sccm, and an O₂ flow of 5 sccm and the ratio of the Ar and O₂ flow rates played a very important role in the growth of the nanowires. In this work, the minimum temperature was 1000°C and the Ar flow rate should not be less than 10 sccm. Time

CHAPTER 4 RESULTS AND DISCUSSIONS

dependence of SiO_x nanowires formation have been studied by [24], which shows how the nanowires grow as a function of time under the optimum growth conditions, which agreed with our result as well.

Moreover, our results on the effect of the C/TiO_2 ratio on the growth of SiO_x nanowires are agreed with Zhang et. al. [43] study because they pointed out that increasing carbon concentration the CuO/carbon powders maximized the SiO_x nanowires yield. Deposited gold layer was found to be important by forming the spherical Au-Si alloys at high temperatures. These alloys or balls can control the diameter size of the wire if the temperature is kept at 1200°C for 1h. Here, high temperature makes the radius of the Au balls small. The larger the whisker diameter, the faster is its growth rate. This growth phenomenon is attributed to the well-known Gibbs–Thomson effect, i.e., the decrease of supersaturation as a function of the whisker diameter [185], so when the diameter of the nanowire decreases the curvature of the droplet at the tip of the wire decreased. The decreasing stops the intake of Si vapor at the vapor-liquid interface due to this effect.

Moreover, the carbo-thermal reactions controlled by CO_2 enhanced the SiO to evaporate from the Si substrate. When the temperature goes down due to Ar gas flowrates causing the fluctuations in temperatures over silicon surface, the vapour of SiO condenses. Then, the pressure of silicon atoms in the vapour form (SiO) is more than the silicon atoms inside the Au-Si alloy, i.e. $P_{\text{Si (V)}} > P_{\text{Si (L)}}$, so the silicon start to penetrate and sink inside the alloy. More atoms get adsorbed more atoms precipitate at the bottom of the alloy, which increase the concentration of Si. On the other hand the diffusion of Si atoms comes from the substrate as SLS mechanism suggested. At equilibrium, no more atoms adsorbed or diffused and hence the building of the wire takes over forming super saturation stage. Tip growth (Au-Si ball at top of the wire) and root growth is determined by the radius of alloy and the effect of heating temperature and time.

CHAPTER 4 RESULTS AND DISCUSSIONS

In tip growth, when the Au-Si alloy move up far from substrate some of the gold particles gets solidified because the percentage of silicon is too small. This solidification accrues at different condensation temperatures which causes the embedded phenomena. All the operation and carbo-thermal reactions in the catalytic growth process can be summarized in Fig. 4.62.

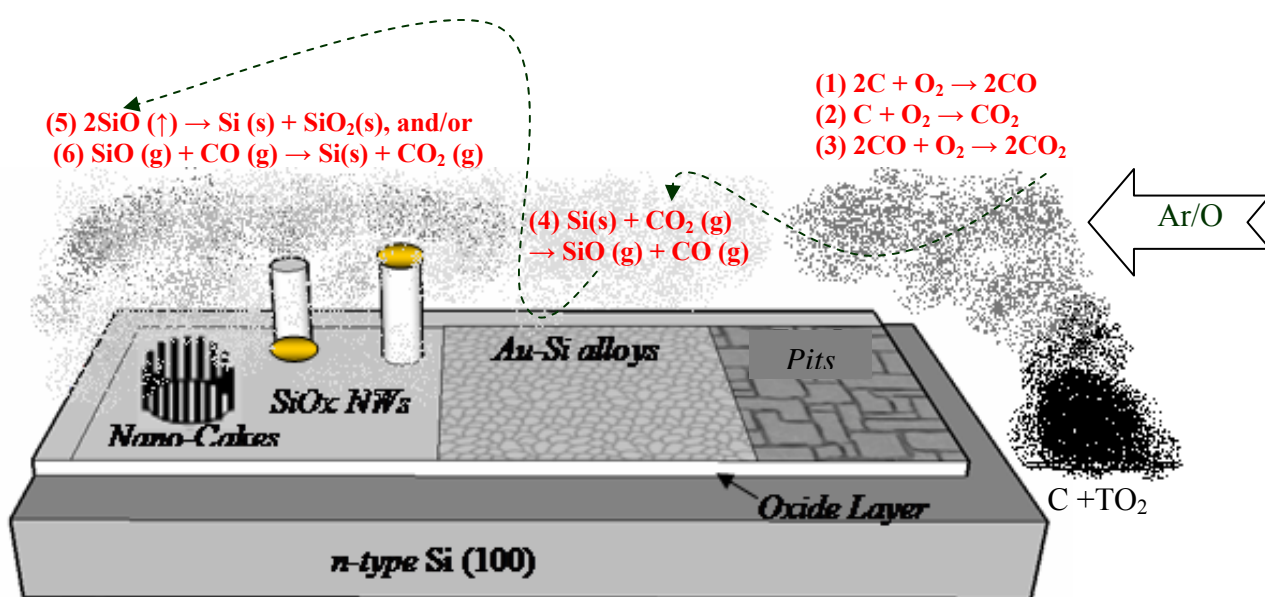


Figure 4.62 A schematic drawing of catalytic SiO_x nanowires (tip, root) growth and the relative carbo-thermal suggested reactions.

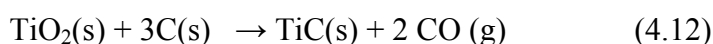
The obtained embedded SiO_x nanowires were directly grown on coated substrate by thermal evaporation at 1200°C in an Ar ambient atmosphere with no additional Si source materials. Our results shown in Fig. 4.19 reveals that most wires are embedded with different gold masses, which can be related to the wire diameter, temperature fluctuations and growth speed. Bigger wire can contain bigger gold particles.

At faster cooling rate (the up and down temperature fluctuations), more gold nanoparticles solidified. In addition, the growing speed controls the length of these embedded wires. This is due to the relaxation on the condensation rate of Si species that reduces the precipitation Si atoms to the wire and hinders the growth for a very tiny

time. Even when the growth rate is small some silicon atoms continue to build the wire, which get oxidized from penetrated oxygen atoms towards the system. On the other hand, the percentage of Si in the mixture of Au-Si alloy is important to establish the supersaturation stage, which is responsible for establishing the growth. So if the percentage of silicon is less than 19% of the total mixture, gold will be in liquid phase at 1100°C and above as reported in [70].

Therefore, the molten gold from the Au-Si alloy start to replace the empty gaps as the wires rising upward. This replacement occurred as empty spaces found, which may happen many times in one wire. So this explains the formation of many unattached Au particles in the same wire.

The effect of TiO₂/C mass ratio on growth yield of SiO_x nanowires found to be high when increasing carbon percentage in the mixture. So as the carbon percentage increases, the ability to form CO₂ will increase. This CO₂ may results through oxidization of carbon by residual oxygen as in equations (1-3) in Fig. 4.60 or from the chemical reaction with titania at 1200°C. It has been shown by Transit et al [186] that the carbothermal reduction of titanium dioxide, anatase or rutile, following the global equation:



This reaction is rapid at temperatures higher than 1000°C and their rates are limited by the volumetric diffusion of oxygen inside the oxide grains [187]. We believe that carbothermal reactions played an important role in the synthesis of SiO_xNWs using titanium oxide powder. This is because the effect of oxygen in titania on the resultant carbon monoxide as in equation (4.12). Then, the CO gas will react with SiO gas to produce SiNWs. Therefore, CO gas should be in high percentage than CO₂ during the condensation. For an example, Li at al. [24] and Yu-Chiao at al.[87] referred the reason behind the growth of SiO_x nanowires on Au-coated Si substrate to carbothermal

reduction of ZnO and CuO respectively. We can conclude that these materials (TiO_2 , ZnO and CuO) do not evaporate to form nanostructures of their type, but it provides the system with CO which may convert to CO_2 in reaction (3) in Fig 4.62. On the other hand evaporating silicon powder mixed with graphite by Carter et al [61] who found the effect of Ar- CO_2 and Ar-CO- CO_2 flow gases over Ni-Si and Co-Si substrates at 1130°C lead to rapid growth of crystalline SiO_2 nanofibers. This argument seems to be poorly explained because the evaporation temperature of silicon is 1414°C at atmospheric pressure and therefore the source behind their growth is the substrate itself not the silicon powder. Another study of Saulig-Wenger et al. [91] reported that the silica nanowires were grown by direct thermal treatment of a commercial silicon powder in the presence of graphite. From their point of view the mixture of carbon and silicon powder were used as source of silicon to accomplish the growth process and they did not observe any SiO_x nanowires by silicon powder separately without carbon [24]. So we believe that the carbon is important to enhance the production of silicon monoxide gas from the silicon substrate not from the silicon powder and this is why no growth result when there is no carbon is used.

Many other papers reported that the growth of SiO_x nanowires can occur without using Si or/ and SiO powders, i.e. the main source is the substrate itself. For example, Chan and his co-workers [181] have grown comet-like SiO_x nanostructures by heating pure silicon powder at 1100°C for 30 minutes via Fe catalyst without specifying certain pressure. By pointing to the VLS as the growth mechanism, Si should be in gas form, which is unattainable under these experimental conditions.

Our comet and tree like nanofibers, conform that the production of such a novel morphology can be occur at 1200°C temperature and 150mTorr. On the other hand, the comet shape nanofibers have large head with smaller tails. The diameter of the nanofibers is smaller at their ends which is deferent from. Djamila et al. [86] and his co-

workers works. They reported that the presence of SiO in the gaseous phase is necessary but not the only sufficient condition for the formation of nanowires.

Our PL results for SiO_x nanowires shows blue emission which can be ascribed to the neutral oxygen vacancy ($\equiv\text{Si}-\text{Si}\equiv$) and twofold-coordinated silicon lone-pair centres ($\equiv\text{Si}-\text{O}-\text{Si}\equiv$) [99] and [119]. It believed that the UV light emission occurred in the luminescence centres in silicon oxide thin film [120]. In addition, there exist a large quantity of different types of unsaturated bond in the large surface to volume in the nanostructures, which create some new energy levels below fermi level in the energy gap, and cause some new luminescence bands.

On the other hand, the annealing process lowers the PL spectrum intensity of SiO_x nanowires, which makes the wires gain more oxygen and reduces the lack of oxygen vacancies therefore, reduces the intrinsic defects. Looking at PL and FTIR results we can state that the PL at 3.54 eV band corresponds to the twofold coordinated Si lone pair centers originating from the formation of strain bonds ($\equiv\text{Si}-\text{O}-\text{Si}\equiv$) when mechanical stress is applied on the silica [188, 189]. The 3.3 eV band may be correlated with the formation of the Si-O-C due to the reaction between $\equiv\text{Si}-\text{O}\cdot$ defects and carbon atoms during nanowire growth, which has been reported in carbon doped silica [190, 191]. Analysis of bonding configurations from FTIR confirms the existence of Si-O-C and ($\equiv\text{Si}-\text{O}-\text{Si}\equiv$) bonds on these wires as mentioned by Socrates et al [192]. The presence of this type of single bonds can be related to the PL recompilation that accrues due to the effect of oxygen vacancies. This free oxygen can change the bridging oxygen between to two Si atoms to be non bridging oxygen or terminating oxygen and hence the single Si-O bonds were formed.

4.8. General Discussion on the Growth of β -SiCNWs

Based on XRD results, we have produced β -SiC nanowires from graphite powder at 1200°C. The obtained β -SiC nanowires have different yields depending on the substrate location. The highest growth yield obtained at location 2 and lowest at 4 and 6 centimetres respectively. The key factor is the use of carbon and varying substrate locations. In the synthetic process, when temperature rises gradually, the carbon monoxide is generated due to the oxidation of carbon as in equation (1) inside Fig. 4.63.

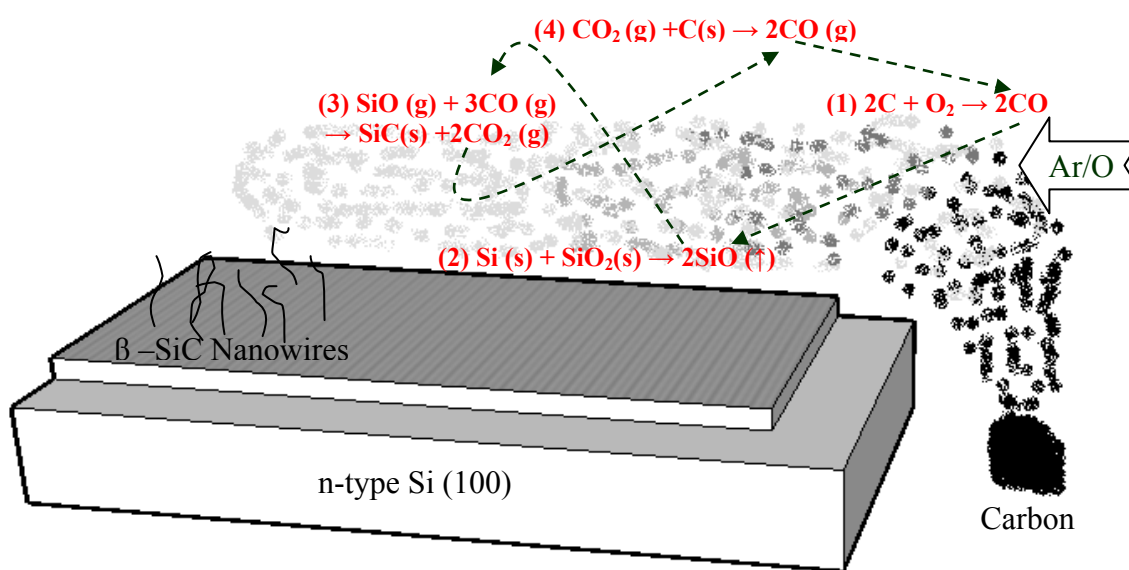


Figure 4.63 A schematic drawing of the formation process of β -SiC nanowires and the relative carbo-thermal suggested reactions.

At the same time and at temperatures more than 950°C SiO vapour is produced from oxide layer as in equation (2) inside Fig. 4.63. SiO vapour reacts with CO to form β -SiC nanowires occurring in the mole rate of 1:1 as in equation (3).

Then to continue the growth process of β -SiC nanowires more CO vapour is needed. Reaction (4) inside Fig. 4.63 recycles the process by releasing CO again. So CO plays a key role in the whole reaction process. As soon as the feedback current occurs, the CO vapour is synthesized continuously.

The location of the substrates inside the tube furnace found to be important because it effects the morphology and the yield of the grown SiC nanowires. When the substrate is

CHAPTER 4 RESULTS AND DISCUSSIONS

near to the carbon boat, the obtained β -SiC nanowires are high in yield and more aligned than the substrates at further distance.

The effect of rapid heating rate changed the shape of grown wires orientation. The shape is unique because the wires were grown in bunch orientation in a semi organized manner. This orientation may be due to the pits occurred in the surface of the silicon substrate which works as favourite growth places to accomplish the fabrication of β -SiC nanowires before other places. We believe that nanowires of SiO_x and β -SiC grow to gather with out catalyst in our system, because both of them depends upon SiO gas as the most important source of silicon.

So to control the type of produced materials, the initial heated mixture (titania and graphite in case of SiO_x NWs and graphite only in the production of β -SiC) should be chosen correctly. Even these powders are not the source involved in the production of the growth species, but it has an effect on the resulted material.

Chapter 5

5.1 Conclusion

Silicon oxide nanostructures and β -type silicon carbide nanowires were synthesized by simple carbo-thermal evaporation method using non-catalytic and catalytic growths.

In the non catalytic growth, the SiO_x nanostructures obtained having dimensions of 60 nm to 300 nm in diameter and several microns in length. The formation of cracks on the silicon substrate surface was found to be at $T > 900^\circ\text{C}$ which is due to the evaporation of silicon monoxide. The diameter of the wire decreases forwards the end. the highest density of SiO_x nanowires was obtained at 10 sccm flow rate.

Using catalytic process the SiO_x nanowires were 13 nm to about 243 nm in diameters and 194 nm to several microns in length. From FESEM images the SiO_x nanowires obtained at 1200°C are embedded with gold. And the obtained nanofibers (comet and tree shape) were 8 nm to 30 nm in diameter and around 50 nm to $2.5\mu\text{m}$ in length.

In root growth part, the average lowest diameter found to be 13 nm for catalytic growth at 68 \AA gold layer thickness and as the layer become thicker, the SiO_x nanowires become random. Standing SiO_x nanowires with gold at their far end were obtained at 40 s sputtering time of gold over silicon substrate. The existence of pits may be due to the high stress induced by Au thin film in the Si surface. It was found that increasing the temperature, C: TiO_2 ratio and deposition time increases the out come yield of the SiO_x nanostructures. The highest yield is obtained at 10 sccm Ar flow rate. The nanocakes which unique morphology is obtained at 1200°C deposited for 8 minutes. These nano-

CHAPTER 5 CONCLUSIONS

cakes circuited SiO_x nanowires are aligned with almost same height. The obtained nanostructures under different experimental conditions are amorphous based on XRD results.

The best yield is obtained at 10 sccm argon flow rate, temperature more than 1000°C in catalytic and $\geq 900^\circ\text{C}$ in non catalytic growth process.

HRTEM images shows SiO_x nanowires have a solid core with a with spherical cap at their ends.

The PL broad band of the obtained SiO_x nanowires at 1200°C have a UV peak at 350 nm (3.54 eV), one wide peak in the blue and green regions (400-600 nm) and red band at 730 nm. There were two blue bands at 465 nm (2.67 eV) and 482 nm (2.57 eV) and one green band at 502 nm (2.47 eV) in the wide peak. The above PL centres of SiO_xNWs synthesized at 1200°C found to be higher in intensity than the PL of SiO_xNWs obtained at 1100°C . The blue and green regions bands were due to oxygen vacancies during growth process at high temperature. The UV peak disappeared after annealing at 1000°C for 1h and the rest three peaks decreases.

The PL intensities for the green and blue bands are higher for non-catalytic growth of SiO_x nanowires comparing with catalytic results while the UV emission has small intensity. The FTIR spectra for SiO_xNWs showed three chemical bonds and their related vibration modes, the Si–O–Si bond rocking vibrational mode (477 cm^{-1}), the O–Si–O bond bending mode (811 cm^{-1}) and Si–O asymmetric stretching mode (1110 cm^{-1}). The strongest absorption peak locates at the higher frequency side of 1110 cm^{-1} which pointed to Si–O asymmetric stretching mode.

CHAPTER 5 CONCLUSIONS

The β -SiC nanowires were successfully fabricated using simple carbo-thermal evaporation without catalysts. The grown β -SiC nanowires were aligned with almost same height. The highest growth yield of β -SiC nanowires obtained at locations 2, 4 and 6 centimetres far from furnace centre. The obtained crystal planes of β -SiC are (111), (200), (220) and (311). The obtained β -SiC nanowires have diameter ranged between 40 to 500 nm. When introducing oxygen gas instead of argon, no growth occurred at location A (2 cm) and the wires growth began at location B (4 cm) and consequently, the growth density found to be decreased at further distance from the furnace centre. The obtained β -SiC nanowires were aligned and with diameters ranged between 40 to 500 nm. The edges of samples have very long SiC nanowires.

Strong stretching vibration mode of Si-C at 798, 810 and 820 cm^{-1} were found for SiCNWs obtained at 2, 4 and 6 cm far from the furnace centre. Another peak at 1090 cm^{-1} is found only for the sample placed 6 cm away which can be attributed to the stretching vibration of Si-O.

5.2 Suggestions for Future Research

As mentioned in conclusion the usage of graphite to achieve the SiO_x nanostructures is still new and a lot of research can be done. Here we suggest four ideas for studies in future work with silicon oxide nanostructures.

- (1) More catalysts should be examined other than gold especially those with small eutectic temperature with silicon and study the parametric effects on the growth of SiO_x nanostructures.

CHAPTER 5 CONCLUSIONS

- (2) The phenomena of embedded SiO_x nanowires is interesting as it increases the conductivity of the wires, so these embedded wires can be used as interconnection wires between two silicon substrates and this is important in electronic devices.
- (3) The PL SiO_x nanostructures seem to be important in optical devices applications and the PL emissions should be distinct at specific wavelengths and to do so the diameter of the wire need to be modified and should be very small.

On other hand, our production of β -SiC nanowires with simple carbo-thermal process can be developed to form single crystal, which may give important optical properties due to its optical band gap. Finally, doping these wires may increase their electronic and PL abilities.

REFERENCES

- [1] S. De Franceschi et al., Appl. Phys. Lett. 83, 344 (2003)
- [2] T. Mårtensson et al., Nano Lett. 4, 1987 (2004)
- [3] C. Thelander et al., Nano Lett. 5, 635 (2005)
- [4] H. Klauk, Nature 451, 533 (2008)
- [5] X. Wang et al., Science 316, 102 (2007)
- [6] A. Fontcuberta i Morral et al., Small 19, 1347 (2007)
- [7] X. Duan, Y. Huang, Y. Cui, J. Wang and C. M. Lieber, Nature. 409, 66 (2001).
- [8] Y.N. Xia, P.D. Yang, Y.G. Sun, Y.Y. Wu, B. Mayers, B. Gates, Y.D. Yin, F. Kim and H.Q. Yan, Adv. Mater. 15, 353 (2003).
- [9] J. Sha, J.J. Niu, X.Y. Ma, J. Xu, X.B. Zhang, Q. Yang and D.R. Yang. Adv. Mater. 14, 1219 (2002).
- [10] J.J. Niu, J. Sha, Y.W. Wang, X.Y. Ma and D.R. Yang. Microelectron. Eng. 66, 65 (2003).
- [11] Y. Cui and C.M. Lieber. Science. 291, 851 (2001).
- [12] X.T. Zhou, J.Q. Hu, C.P. Li, D.D.D. Ma, C.S. Lee and S.T. Lee. Chem. Phys. Lett. 369, 220 (2003).
- [13] S.F. Hu, W.Z. Wang, S.S. Liu, Y.C. Wu, S.L. Song and T.Y. Huang. Solid State Commun. 125, 351 (2003).
- [14] M. Macucci, B. Pellegrini, G. Pennelli and M. Piotta. Microelectron. Eng. 61–62, 701 (2002).
- [15] W.G. Moffat, The Handbook of Binary Phase Diagrams, Genium Publishing Corp, Schenectady, New York, (1990).
- [16] J.O. Besenhard, in: T. Besenhard (Ed.), Handbook of Battery Materials, Wiley-VCH, Weinheim, 363 (1999).

CHAPTER 5 CONCLUSIONS

- [17] W.J. Weydanz, M. Wohlfahrt-Mehrens, R.A. Huggins, J. Power Sources 81–82 237 (1999).
- [18] Y. Cui, Q.Q. Wei, H.K. Park, and C.M. Lieber, Science 293, 289 (2001).
- [19] M. Paulose, C.A. Grimes, O.K. Varghese, and E.C. Dickey, Appl. Phys. Lett. 81, 153 (2002).
- [20] T. Qiu, X.L. Wu, X. Yang, G.S. Huang, and Z.Y. Zhang, Appl. Phys. Lett. 84, 3867 (2004).
- [21] P. Jena, S.N. Khanna, B.K. Rao, Physics and Chemistry of Finite System: From Clusters to Crystals, vols. I and II, Kluwer Academic Publishers, Boston, (1992).
- [22] D.P. Yu, Q.L. Hang, Y. Ding, H.Z. Zhang, Z.G. Bai, J.J. Wang, Y.H. Zou, W. Qian, G.C. Xiong, S.Q. Feng, Appl. Phys. Lett. 73, 3076 (1998).
- [23] Zhu Y Q, Hsu W K, Terrones M, Grobert N, Terrones H, Hare J P, Kroto H W and Walton D R M J. Mater. Chem. 8, 1859 (1998).
- [24] Li S H, Zhu X F and Zhao Y P., J. Phys. Chem. B 108, 17032 (2004).
- [25] M. Ruff, H. Mitlehner, and R. Helbig, IEEE Trans. Electron Devices 41, 1040 (1994).
- [26] H. Morkoc, S. Strite, G. B. Gao, M. E. Lin, B. Sverdlov, and M. Burns, J. Appl. Phys. 76, 1363 (1994).
- [27] G. Cicero, A. Catellani, and G. Galli, Phys. Rev. Lett. 93, 016102 (2004).
- [28] C.C. Tang, S.S. Fan, H.Y. Dang, J.H. Zhao, C. Zhang, P. Li, Q. Gu, J. Cryst. Growth 210, 595(2000).
- [29] Z.J. Li, H.J. Li, X.L. Chen, A.L. Meng, K.Z. Li, Y.P. Xu, L. Dai, Appl. Phys. A 76, 637(2003).
- [30] M. Lu, M.K. Li, H.L. Li, X.Y. Gao, J. Mater. Sci. Lett. 22, 1107 (2003).
- [31] W. Yang, H. Araki, A. Kohyama, S. Thaveethavorn, H. Suzuki, T. Noda, Mater. Lett. 58, 3145 (2004).

CHAPTER 5 CONCLUSIONS

- [32] A.I. Kharlamov, N.V. Kirillova, S.N. Kaverina, *Theor. Exp. Chem.* 38 (2002) 232.
- [33] Z.X. Yang, Y.J. Wu, F. Zhu, Y.F. Zhang, *Physica E* 25 (2005) 395.
- [34] Iijima S. *Nature*; 354:56–8 (1991).
- [35] H. Takikawa, M. Yatsuki, T. Sakakibara, *Jpn. J. Appl. Phys.* 38, L401 (1999).
- [36] X.C. Wu, W.H. Song, K.Y. Wang, T. Hu, B. Zhao, Y.P. Sun, J.J. Du, *Chem. Phys. Lett.* 336, 53 (2001).
- [37] Z.Q. Liu, S.S. Xie, L.F. Sun, D.S. Tang, W.Y. Zhou, C.Y. Wang, W. Liu, Y.B. Li, X.P. Zou, G. Wang, *J. Mater. Res.* 16, 683 (2001).
- [38] W.B. Hu, Y.Q. Zhu, W.G. Xu, *Sci. China Ser. B* 45, 389 (2002).
- [39] J.Q. Hu, Y. Jiang, X.M. Meng, C.S. Lee, S.T. Lee, *Chem. Phys. Lett.* 367, 339 (2003).
- [40] G. Che, B.B. Lakshmi, C.R. Martin, E.R. Fisher, R.S. Ruoff, *Chem. Mater.* 10, 260 (1998).
- [41] C.N.R. Rao, M. Nath, *Dalton Trans.* 1, 1 (2003).
- [42] B.B. Lakshmi, C.J. Patrissi, C.R. Martin, *Chem. Mater.* 9, 2544 (1997).
- [43] M. Zhang, Y. Bando, K. Wada, *J. Mater. Res.* 15, 187 (2000).
- [44] S.O. Obare, N.R. Jana, C.J. Murphy, *Nano Lett.* 1, 601 (2001).
- [45] C.M. Chan, M.A. Van Hove, and E.D. Williams, *Surface Sci.* 91,440 (1980).
- [46] G. Binnig, H. Rohrer, Ch. Gerber, and E. Weibel, *Phys. Rev. Lett.* 50, I20 (1 983).
- [47] R. Schlier and H. Farnsworth, *J. Chem. Phys.* 30, 9 17 (1 959).
- [48] R.M. Tromp, R.J. Hames, and J.E. Demuth, *Phys. Rev. Lett.* 55, 1303 (1 985).
- [49] R.M. Tromp, R.J. Hames, and J.E. Demuth, *Phys. Rev. Lett.* B24,5343 (1986).
- [50] H. Yan, Xing, Y., Hang, Q., Yu, D., Wang, Y., Xu, J., Xi, Z. and Feng, S., *Chem. Phys. Lett.* 323, 224–228 (2000).
- [51] Y. H. Tang, Y. F. Zhang, N. Wang, W. S. Shi, C. S. Lee, I. Bello, and S. Lee, T., *J. Vac. Sci. Technol. B.* 19, 317–319 (2001).

CHAPTER 5 CONCLUSIONS

- [52] S. Jin, Q. Li, and C. Lee, *Phys. Status Solidi A—Appl. Res.* 188, R1–R2 (2001).
- [53] Peng, X. S.; Wang, X. F.; Zhang, J.; Wang, Y. W.; Sun, S. H.; Meng, G. W.; Zhang, L. D. *Appl. Phys. A*, 74, 831(2002).
- [54] Dai, L.; Chen, X. L.; Zhou, T.; Hu, B. Q. *J. Phys.: Condens. Matter.* 14, L473 (2002).
- [55] Dai, L.; Chen, X. L.; Jian, J. K.; Wang, W. J.; Zhou, T.; Hu, B. Q. *Appl. Phys. A*, 76, 625 (2003).
- [56] Meng, G. W.; Peng, X. S.; Wang, Y. W.; Wang, C. Z.; Wang, X. F.; Zhang, L. D. *Appl. Phys. A*, 76, 119 (2003).
- [57] Wang, Z. L.; Gao, R. P.; Cole, J. L.; Stout, J. D. *Adv. Mater.* 12, 1938 (2000).
- [58] Paulose M, Varghese O K and Grimes C A J. *Nanosci. Nanotechnol.*, 3, 341 (2003).
- [59] Wang, Y. W.; Liang, C. H.; Meng, G. W.; Peng, X. S.; Zhang, L. D. *J. Mater. Chem.*, 12, 651(2002).
- [60] Chen, Y.-J.; Li, J.-B.; Dai, J.-H. *Chem. Phys. Lett.*, 344, 450 (2001).
- [61] Carter, P.; Gleeson, B.; Young, D. J. *Oxid. Met.*, 56, 375 (2001).
- [62] Zhang, Z. J.; Ramanath, G.; Ajayan, P. M.; Goldberg, D.; Bando, Y. *Adv. Mater.*, 13, 197 (2001).
- [63] Zheng, B.; Wu, Y. Y.; Yang, P. D.; Liu, J. *Adv. Mater.* 14, 122 (2002).
- [64] Wang, J. C.; Zhan, C. Z.; Li, F. G. *Solid State Commun.*, 125, 629 (2003).
- [65] Ma, R.; Bando, Y. *Chem. Phys. Lett.*, 377, 177 (2003).
- [66] Th Stelzner, G Andr'a, EWendler, WWesch, R Scholz, U G'osele, and S Christiansen, *Nanotechnology.* 17, 2895–2898 (2006).
- [67] A. Cho, *Science.* 299, (14 March 2003), 1684-1685 (2003).
- [68] M.M. Schubert, S. Hackenberg, A.C.v. Veen, M. Muhler, V. Plzak, and R.J. Behm, *Journal of Catalysis.* 197, 113-122 (2001).

CHAPTER 5 CONCLUSIONS

- [69] G. Schmid and B. Corain, *European Journal of Inorganic Chemistry*. 3081-3098, (2003).
- [70] T. B. Massalski, H. Okamoto, P. R. Subramanian, and L. Kacprzak, (ASM International, materials Park, OH 1990).
- [71] T.C. Wong, C.P. Li, R.Q. Zhang, S.T. Lee, *Appl. Phys. Lett.* 84, 407 (2004).
- [72] R.V. Kumar, Y. Koltypin, X.N. Xu, Y. Yeshurun, A. Gedanken, I. Felner, *J. Appl. Phys.* 89, 6324 (2001).
- [73] J.H. Liang, C. Peng, X. Wang, et al., *Inorg. Chem.* 44, 9405 (2005).
- [73] R.S Wagner , W.C. Ellis, *Appl. Phys. Lett.* 4, 89 (1964); R.S. Wagner, R.S., W.C. Ellis, S.M. Arnold, K.A. Jackson, *J. Appl. Phys.* 35, 2993(1964).
- [74] J-Y. Yu, S-W. Chung, J.R. Heath, *J. Phys. Chem. B.* 104, 11864 (2000).
- [75] A.M. Morales, C.M. Lieber, *Science.* 279, 208 (1998).
- [76] X. Duan, C.M. Lieber, *Adv. Mater.* 12, 298 (2000).
- [77] J. Westwater, D. P. Gosain, and S. Usui, *Phys. Status Solidi A-Appl. Res.* 165, 37-42 (1998).
- [78] S. Helveg, C. Lopez-Cartes, J. Sehested, P. Hansen, B. Clausen, J. Rostrup-Nielsen, F. Abild-Pedersen, and J. Norskov, *Nature.* 427, 426-429 (2004).
- [79] J. D. holmes, K. P. Johnston, R. C. Doty, and B. A. Korgel. 287, 1471-1473 (2000).
- [80] Yu D P, Xing Y J, Hang Q L, et al., *Physica E.* 9(3), 305–309 (2001).
- [81] Zhang Z, Fan X H, Xu L, et al., *Chemical Physics Letters.* 337(1), 18–24 (2001).
- [82] D.P. Yu, Y.J. Xing, Q.L. Hang, H.F. Yan, J. Xu, Z.H. Xi and S.Q. Feng. *Physica E.* 9, 305 (2001).
- [83] W.K. Burton, N. Cabrera, F.C. Frank, *Nature* 163, 398 (1949).
- [84] A.H. Cottrell, *Dislocations and Plastic Flow in Crystals*, Oxford University Press, London, 1963.

CHAPTER 5 CONCLUSIONS

- [85] Wu X C, Song W H, Wang K Y, Hu T, Zhau B, Sun Y P and Du J J Chem. Phys. Lett. 336, 53 (2001).
- [86] Djamila Bahloul-Hourlier and Pierre Perrot, Journal of Phases Equilibrium and diffusion. 28, 2 (2007).
- [87] Yu-Chiao Lin and Wen-Tai Lin, Nanotechnology, 16, 1648–1654 (2005).
- [88] Jie J, Wang G, Chen Y, Han X, Wang Q, Xu B and Hou J G, Appl. Phys. Lett. 86, 031909 (2005).
- [89] Park B T and Yong K, Nanotechnology. 15, 365 (2004).
- [90] Liu L, Zhang T J, Cui K and Dong Y D, J. Mater. Res. 14, 4062 (1999).
- [91] Saulig-Wenger K, Cornu D, Chassagneux F, Epicier T and Miele P J. Mater. Chem. 13, 3058 (2003).
- [92] Y. Zhu, W. Hsu, M. Terrones, N. Grobert, H. Terrones, J. Hare, H. Kroto, and D. Walton, J. Mater. Chem. 8, 1859–1864 (1998).
- [93] K.H. Lee, S.W. Lee, R.R. Vanfleet, W. Sigmund, Chem. Phys. Lett. 376, 498 (2003).
- [94] Z.L. Wang, R.P. Gao, J.L. Cole, J.D. Stout, Adv. Mater. 12, 1938 (2000).
- [95] S.W. Karine, D. Cornu, F. Chassagneux, T. Epicier, P. Miele, J. Mater. Chem. 13, 3058 (2003).
- [96] Y.Q. Zhu, W.K. Hsu, M. Terrones, N. Grobert, H. Terrones, J.P. Hare, H.W. Kroto, D.R.M. Walton, J. Mater. Chem. 8, 1859 (1998).
- [97] Gundiah, F.L. Deepak, A. Govindaraj, C.N.R. Rao, Chem. Phys. Lett. 381, 579 (2003).
- [98] N. Wang, Y.F. Zhang, Y.H. Tang, C.S. Lee, S.T. Lee, Appl. Phys. Lett. 73, 3902 (1998).
- [99] N. Wang, Y.H. Tang, Y.F. Zhang, C.S. Lee, S.T. Lee, Phys. Rev. B 58, 16024 (1998).

CHAPTER 5 CONCLUSIONS

- [100] N. Wang, Y.H. Tang, Y.F. Zhang, C.S. Lee, S.T. Lee, Chem. Phys. Lett. 299, 237 (1999).
- [101] Y.F. Zhang, Y.H. Tang, N.Wang, C.S. Lee, I. Bello, S.T. Lee, Phys. Rev. B. 61,4518 (2000).
- [102] W.S. Shi, Y.F. Zheng, N.Wang, C.S. Lee, S.T. Lee, Adv. Mater. 13, 591 (2001).
- [103] S.C. Lyu, Y. Zhang, H. Ruh, H.J. Lee, C.J. Lee, Chem. Phys. Lett. 367, 717 (2003).
- [104] H.Y. Peng, X.T. Zhou, N. Wang, Y.F. Zheng, L.S. Liao, W.S. Shi, C.S. Lee, S.T. Lee, Chem. Phys. Lett. 327, 263 (2000).
- [105] N. Wang, B.D. Yao, Y.F. Chan, X.Y. Zhang, Nano Lett. 3, 475 (2003).
- [106] R. Q. Zhang, T. S. Chu, H. F. Cheung, N.Wang, S. T. Lee, Material Science and Engineering. 16, 31-35 (2001).
- [107] S. T. Lee, N.Wang, C. S. Lee, Material Science and Engineering A. 286, 16-23 (2000).
- [108] Lin YM, Rabin O, Cronin SB, Ying JY, Dresselhaus MS. Appl. Phys. Lett; 81, 2403–5 (2002)
- [109] Q. hu, S. verghese, R. Wyss, T. schapers, j. delalamo, S. feng, K. Yakubo, M. Rooks, M. Melloch, et al. semicond. Sci. Technol. 11, 1888-1894 (1996).
- [110] Y. F. Zhang, Y. H. Tang, C. Lam, N. Wang, C. S. Lee, I. Bello, and S. T. Lee, J. Cryst. Growth. 212, 115-118 (2000).
- [111] Y. Tang, Y. Zhang, N. Wang, C. Lam, X. Han, I. Bello, and S. Lee, J. Appl. Phys. 85, 7981-7983 (1999).
- [112] R. S. Yang, Y. Ding, and Z. L. Wang, Nano Lett. 4, 1309-1312 (2004).
- [113] T. Guo, P. Nikolaev, A. G. Rinzler, D. Tomanek, D. T. Colbert, and R. E. Smalley, J. Phys. Chem. 99, 10694-10697 (1995).

CHAPTER 5 CONCLUSIONS

- [114] G. Pacchioni, L. Skuja, and D.L. Griscom, 'Defects in SiO₂ and Related Dielectrics: Science and Technology', Kluwer Academic Publishers, Dordrecht, (2000)
- [115] R.A.B. Devine, J-P. Duraud and E. Doory'ee, 'Structure and Imperfections in Amorphous and Crystalline Silicon Dioxide', Wiley, Chichester, (2000).
- [116] D.L. Griscom, J. Ceram. Soc. Japan. 99, 923 (1991).
- [117] L. Skuja, M. Hirano, H. Hosono, and K. Kajihara, Phys. Stat. Sol. (c). 2, 15 (2005)
- [118] M. Stapelbroek, D. L. Griscom, E. J. Friebele, and G. H. Sigel Jr., J. Non-Cryst. Solids. 32, 313 (1979).
- [119] O'Reilly E P and Robertson, J. Phys. Rev. B. 27, 3780 (1983).
- [120] Tomozawa M, Li H and Davis K M, J. Non-Cryst. Solids. 179, 162 (1994).
- [121] Kalceff M A S, Phys. Rev. B. 57, 5674 (1998).
- [122] Trukhin A N, Skuja L N, Boganov A G and Rudenko V S, J. Non-Cryst. Solids. 149, 96 (1992).
- [123] Nishikawa H, Shiroyama T, Nakamura R, Tohmon R, Ohki Y, Nagasawa K and Hama Y Phys. Rev. B. 45, 586 (1992).
- [124] D.P. Yu, Z.G. Bai, J.J. Wang, Y.H. Zou, W. Qian, J.S. Fu, H.Z. Zhang, Y. Ding, G.C. Xiong and S.Q. Feng. Phys. Rev. B. 59, p. 2498 (1999).
- [125] H. Li, G.W. Zhou, D.P. Yu, X.J. Huang, L.Q. Chen, Z. Zhang, unpublished.
- [126] G.W. Zhou, H. Li, H.P. Sun, D. P Yu, Y.Q. Wang, L.Q. Chen and Z. Zhang. Appl. Phys. Lett. 75, 2447(1999).
- [127] Lin J, Yao G Q, Duan J Q and Qin G G Solid State Commun. 97, 221(1996).
- [128] Kanashima T, Okuyama M and Hamakawa Y Appl. Surf. Sci. 79/80, 321(1994).
- [129] M. Ruff, H. Mitlehner, and R. Helbig, IEEE Trans. Electron Devices 41, 1040 (1994).

CHAPTER 5 CONCLUSIONS

- [130] H. Morkoc, S. Strite, G. B. Gao, M. E. Lin, B. Sverdlov, and M. Burns, J. Appl. Phys. 76, 1363 (1994).
- [131] G. Cicero, A. Catellani, and G. Galli, Phys. Rev. Lett. 93, 016102 (2004).
- [132] G. W. Robert and F. Davis, Proc. of the Inter. Conf. in SiC and Relat. Mater. 93, Washton DC, USA, November 1-3, 1993, Inst. Phys. Conf. Ser. 137, 1 (1994)
- [133] J. J. Berzelius, Ann. Phys. Lpz. 1, 169 (1824)
- [134] A. H. Cowles and E. H. Cowles, U. S. Pat. 319945 (1885)
- [135] A. G. Acheson, England Patent 17911(1892)
- [136] G. Meng, L. Zhang, C. Mo, S. Zhang, Y. Qin, S. Feng, and H. Li, J. Mater. Res. 13, 2533 (1998)
- [137] H. Dai, E. W. Wong, Y. Lu, S. Fan, and C. M. Liber, Nature, 375, 769 (1995)
- [138] S.K. Andersson and M.E. Thomas, Infrared Phys. Technol. 39, p. 223 (1998).
- [139] Accuratus company, <http://www accuratus.com/silicar.html> [viewed 10/12/2008].
- [140] Z.L. Wang, Z.R. Dai, R.P. Gao, Z.G. Bai, J.L. Gde, Appl. Phys. Lett. 77, 3349 (2000).
- [141] Y.H. Gao, Y. Bando, K. Kurashima, T. Sato, J. Mater. Sci. 37, 2023(2002).
- [142] Y.H. Mo, M.D. Shajahan, Y.S. Lee, Y.B. Hahn, K.S. Nahm, Synth. Met. 104, 309 (2003).
- [143] H.C. Lo, D. Das, J.S. Hwang, K.H. Chen, C.H. Hsn, C.F. Chen, L.C. Chen, Appl. Phys. Lett. 83, 1420 (2003).
- [144] Wikipedia, http://en.wikipedia.org/wiki/Silicon_carbide#Properties [viewed 10/11/2008].
- [145] C.C. Tang, S.S. Fan, H.Y. Dang, J.H. Zhao, C. Zhang, P. Li, Q. Gu, J. Cryst. Growth 210, 595(2000).

CHAPTER 5 CONCLUSIONS

- [146] Z.J. Li, H.J. Li, X.L. Chen, A.L. Meng, K.Z. Li, Y.P. Xu, L. Dai, *Appl. Phys. A* 76, 637(2003).
- [147] M. Lu, M.K. Li, H.L. Li, X.Y. Gao, *J. Mater. Sci. Lett.* 22, 1107 (2003).
- [148] W. Yang, H. Araki, A. Kohyama, S. Thaveethavorn, H. Suzuki, T. Noda, *Mater. Lett.* 58, 3145(2004).
- [149] A.I. Kharlamov, N.V. Kirillova, S.N. Kaverina, *Theor. Exp. Chem.* 38, 232(2002).
- [150] Z.X. Yang, Y.J. Wu, F. Zhu, Y.F. Zhang, *Physica E* 25, 395(2005).
- [151] W.Y. Yang, H.Z. Miao, Z.P. Xie, L.G. Zhang, L.N. An, *Chem. Phys. Lett.* 383, 441(2004).
- [152] Shi W, Zheng Y, Peng H, Wang N, Lee CS, Lee ST. *J Am Chem Soc*,;83:3228 – 30 (2000).
- [153] Liang CH, Meng GW, Zhang LD, Wu YC, Cui Z. *Chem Phys Lett*;329:3238 (2000).
- [154] Han W, Fan S, Li Q, Liang W, Gu B, Yu D. *Chem Phys Lett*;265:374–8 (1997).
- [155] Deng SZ, Wu ZS, Zhou J, Xu NS, Chen J, Chen J. *Chem Phys Lett*;356:511–4 (2002).
- [156] Deng SZ, Wu ZS, Zhou J, Xu NS, Chen J, Chen J. *Chem Phys Lett*;364:608– 11(2002).
- [157] Tang CC, Bando Y, Sato T, Kurashima K, Ding XX, Gan ZW, Qi SR. *Appl Phys Lett*;80:4641–3 (2002).
- [158] Wenger KS, Cornu D, Chassagneux F, Ferro G, Epicier T, Liele P. *Solid State Commun*;124:157–61(2002).
- [159] Pan Z, Lai HL, Au FCK, Duan X, Zhou W, Shi W, Wang N, Lee CS, Wong NB, Lee ST, Xie S. *Adv Mater*; 12:1186–90 (2000).
- [160] Kim HY, Park J, Yang H. *Chem Commun*, 256–7 (2003).

CHAPTER 5 CONCLUSIONS

- [161] Wu ZS, Deng SZ, Xu NS, Chen J, Zhou J, Chen J. Appl Phys Lett; 80:3829–31 (2002).
- [162] Quorum Technologies, http://www.sputtercoater.com/Manuals/Current_Technical_Briefs/TB-SPUTTER.pdf [viewed 20/12/2008].
- [163] Wikipedia, http://en.wikipedia.org/wiki/Sputter_deposition [viewed 26/11/2008].
- [164] Structure Probe, Inc (1999-2009), The SPI Sputter Coater Handbook, http://www.emal.engin.umich.edu/handbooks/pdfs/sputter_coater.pdf [viewed 11/07/2008].
- [165] M.A. Sutton & N. Li & D.C. Joy & A.P. Reynolds & X., LiExperimental Mechanics. 47, 775–787 (2007).
- [166] J.Y. Yu, S.W. Chung and J.R. Heath, Journal of Physical Chemistry B. 104, 11864-11870 (2000).
- [167] Wikipedia, http://en.wikipedia.org/wiki/Energy_dispersive_X-ray_spectroscopy [viewed 21/10/2008].
- [168] Corrosion Testing Laboratories, Inc.(1995-2007), Energy Dispersive X-ray Spectrometer (EDS), <http://www.corrosionlab.com/facilities/eds.htm> [viewed 20/12/2008].
- [169] B. C. Cullity, Elements of X-ray Diffraction, addison-wesley, (1956).
- [170] Spence, John C. H.. Experimental high-resolution electron microscopy. New York: Oxford U. Press. (1988)
- [171] Central Facility for Electron microscopy (CFEM) , University of Nebraska, <http://www.unl.edu/CMRAcfem/hires.htm> [viewed 29/11/2008].
- [172] Thermo Nicolet, USA, <http://mmrc.caltech.edu/FTIR/FTIRintro.pdf> [viewed 2/1/2009].
- [173] T. Furukawa, W.B. White, J. Non-Cryst. Solids. 87, 38–39 (1980).
- [174] C.T. Kirk, Phys. Rev. B. 38, 1255(1998).

CHAPTER 5 CONCLUSIONS

- [175] J.R. Martinez, F. Ruiz, Y.V. Vorobiev, F. Perez-Robles, J. Gonzalez-Hernandez, *J. Chem. Phys.* 109, 7511(1998).
- [176] C.J. Brinker, G.W. Scherer, *J. Non-Cryst. Solids.* 70, 301(1965).
- [177] Fisk University, Nashville, USA, http://www.fisk.edu/~aburger/Published03_06/Instruments/SPEX_riplemate/spex_riplemate.html [veiwed 27/10/2008].
- [178] R.R. Chang, R. Iyer, D.L. Lile, *J. Appl. Phys.* 61, 1995–2004 (1987).
- [179] Carbolite co., Range of Tube furnaces, www.dynalabcorp.com/files/Tube%20Furnace.pdf [viewed 20/2/2009].
- [180] R.Q. Zhang, T.S. Chu, H.F. Cheung, N.Wang, S.T. Lee, *Phys. Rev. B.* 64, 113304 (2001).
- [181] Y.J. Chen, J.B. Li, Y.S.Han, Q.M.Wei, J.H. Dai, *Appl. Phys. A.* 74, 433–435 (2002).
- [182] Snure, Michael; Tiwari, Ashutosh *Journal of Nanoscience and Nanotechnology*, Volume 7, Number 2, February, 481-485(5) (2007).
- [183] CRC Handbook of Chemistry and Physics, 59th ed.; CRC Press:Boca Raton, FL, (1978).
- [184] Q. Hu, Quanli Hu , Hiroshi Suzuki, Hong Gao, Hiroshi Araki, Wen Yang, Tetsuji Noda, *Chemical Physics Letters.* 378, 299–304 (2003).
- [185] (a) E.I. Givargizov, *Highly Anisotropic Crystals*, Springer, New York, 1987; (b) E.I. Givargizov, *J. Cryst. Growth.* 31, 20 (1975).
- [186] P. Tristant, PhD Thesis, University of Limoges, France (1992).
- [187] P. Tristant and P. Lefort, *J. Chim. Phys.*, 90, 91 (1993).
- [188] Munekuni, S. et al. *J. Appl. Phys.* 70, 5054–5062 (1991).
- [189] Yu, D. P. et al. *Appl. Phys. Lett.* 73, 3076–3078 (1998).
- [190] He, H., Wang, Y. & Tang, H. *J. Phys. Condens. Matter* 14, 11867–11874 (2002).
- [191] Zhao, J. et al. *Appl. Phys. Lett.* 73, 1838–1840 (1998).

CHAPTER 5 CONCLUSIONS

- [192] Socrates, G. Infrared Characteristic Group Frequencies (Wiley, Bristol, 1980).
- [193] Rübeler H., Schröder B., Fuhs W., Krauskopf J., Rupp T. and Bethge K., *Physica Status Solidi B* **139**, 131(1987).
- [194] Hayashi S., Kawata S., Kim H.M. and Yamamoto K., *Jpn. J. Appl. Phys.* **32**, 4870 (1993).
- [195] Lowe-Webb R.R., Lee H., Ewing J.B., Collins S.R., Yang W., and Sercel P.C., *J. Appl. Phys.* **83**, 2815(1998).
- [196] K. Okada, H. Kato and K. Nakajima, *J Am Ceram Soc* **77** 6 (1994).
- [197] N. Keller, C. Pham-Huu, S. Roy, M.J. Ledoux, C. Estournes and J. Guille, *J Mater Sci* **34** 13 (1999).

List of Publications

Published Papers

- [1] **Majid. S. Al-Ruqeishi**, Roslan Md Nor, Yusoff Mohd Amin, Khalifa Al-Azri, (2009) Carbon assisted growth and photoluminescence of silicon nanowires fabricated without a catalyst, *Silicone* DOI 10.1007/s12633-009- 9024-0 available on-line.
- [2] **Majid. S. Al-Ruqeishi**, Roslan Md Nor, Yusoff Mohd Amin, Khalifa Al-Azri, (2009) Synthesis of Amorphous SiO_x Nanowires and Nanofibers by Thermal Evaporation with Gold as Catalyst. *Malaysian Journal of Science*, 28 (3). pp. 309-314. ISSN 13943065
- [3] **Majid. S. Al-Ruqeishi**, Yusoff Mohd Amin, Wong, Relative Thermoluminescence Response of TLD-100, TLD-200 and GE-Doped Optical Fiber to 8,05 keV X-ray, (2008) *Malaysian Journal of Science*, 27 (2): 91 – 95
- [4] **MS Al-Ruqeishi**, RM Nor, YM Amin and K Al- Azri, Amorphous SiO_x Nanowires and Aligned Nano-Cakes: Growth Mechanism and Photoluminescence, *NANOSCIENCE AND NANOTECHNOLOGY Book Series: AIP Conference Proceedings Vol. 1136*, 414-419 (2009)
- [6] **Majid.S.Al-Ruqeishi**, Roslan Md Nor, Yusoff Mohd Amin, Khalifa Al-Azri, SYNTHESIS OF SiO_x NANOWIRES AND NANOFIBERS BY DIRECT HEATING OF *n-type* SILICON (100) SUBSTRATE WITH GOLD AS CATALYST, Third International Meeting on Frontiers of Physics (IMFP 2009), Labuan, Malaysia, 12-16 January (2009).
- [7] **Majid.S.Al-Ruqeishi**, Roslan Md Nor, Yusoff Mohd Amin, Khalifa Al-Azri, ATMOSPHERIC PRESSURE GROWTH AND CHARACTERIZATION OF SILICON NANOWIRES BY DIRECT HEATING WITHOUT CATALYST, Times square, Kuala Lumpur, Malaysia, August (2008).

Submitted Papers

- [1] **Majid. S. Al-Ruqeishi**, Roslan Md Nor, Yusoff Mohd Amin, Khalifa Al-Azri, Direct synthesis of β -Silicon Carbide nanowires from graphite only without a catalyst, (2010) *Journal of Alloys and Compounds*, ref. JALCOM-D-10-00444.
- [2] **Majid. S. Al-Ruqeishi**, Roslan Md Nor, Yusoff Mohd Amin, Khalifa Al-Azri, Synthesis and Photoluminescence of SiO_x Nanowires and Aligned Nanocakes, (2010) *Physica E*, PHYSE-D-10-00113.

Oral presentations papers

- [1] **Majid.S.Al-Ruqeishi**, Roslan Md Nor, Yusoff Mohd Amin, Khalifa Al-Azri, Amorphous SiO_x Nanowires And Aligned Nano-Cakes : The Growth Mechanism And Photoluminescence, NANO-SciTech 2008, Universiti Teknologi MARA (UiTM) and Nagoya Institute of Technology (NIT), Japan, November (2008).

Posters

- [1] **Majid.S.Al-Ruqeishi**, Roslan Md Nor, Yusoff Mohd Amin, Khalifa Al-Azri, SYNTHESIS OF SiO_x NANOWIRES AND NANOFIBERS BY DIRECT HEATING OF *n-type* SILICON (100) SUBSTRATE WITH GOLD AS

CHAPTER 5 CONCLUSIONS

CATALYST, The 2nd International Conference on Functional Materials & Devices (ICFMD-2008), *Times Squar,e Kuala Lumpur*, Malaysia, 16th to 19th June.

- [2] **Majid.S.Al-Ruqeishi**, Roslan Md Nor, Yusoff Mohd Amin, Khalifa Al-Azri, The Nanophysics workshop, SYNTHESIS OF SiO_x NANOWIRES AND NANOFIBERS BY DIRECT HEATING OF n-type SILICON (100) SUBSTRATE WITH GOLD AS CATALYST, 27-28 May 2008, Physics Department, Faculty Science, UM, , 50603 Kuala Lumpur, Malaysia.